Multi-scale Modeling of a Natural Circulation Loop in Support of the Scaling Problematic within the VVUQ Framework

Haifu Huang

To cite this version:

Haifu Huang. Multi-scale Modeling of a Natural Circulation Loop in Support of the Scaling Problematic within the VVUQ Framework. Engineering Sciences [physics]. Aix Marseille University, 2023. English. NNT : 2023AIXM0356 . tel-04578457

HAL Id: tel-04578457
https://amu.hal.science/tel-04578457

Submitted on 16 May 2024

NNT/NL : 2023AIXM0001/001ED353

THÈSE DE DOCTORAT

Soutenue à Aix-Marseille Université
le 31 octobre 2023 par

Haifu HUANG

Multi-scale Modeling of a Natural Circulation Loop in Support of the Scaling Problematic within the VVUQ Framework

Discipline
Sciences pour l'Ingénieur

Spécialité
Mécanique et physique des fluides

École doctorale
ED 353 Sciences pour l'ingénieur : Mécanique, Physique, Micro et Nanoélectronique

Laboratoire/Partenaires de recherche
Institut Universitaire des Systèmes Thermiques Industriels (CNRS/AMU)
Laboratoire d'Etudes et de Modélisation des Systèmes (CEA|IRESNE|DER|SESI)

Composition du jury

Francesco D'AURIA University of Pisa	Rapporteur
Jose-Luis MUÑOZ-COBO PolytPolytechnical University of Valencia	Rapporteur
Jean BACCOU IRSN	Président du jury
Jeremy GALPIN Framatome	Examinateur
Stephane MIMOUNI EDF	Examinateur
Maria Giovanna RODIO CEA	Examinatrice
Marc MEDALE AMU & CNRS	Directeur de thèse
Nicolas ALPY CEA	Co-encadrant/Invité
Jorge PEREZ MANES CEA	Co-encadrant

Affidavit

Je soussigné, HUANG Haifu, déclare par la présente que le travail présenté dans ce manuscrit est mon propre travail, réalisé sous la direction scientifique de Marc MEDALE, dans le respect des principes d'honnêteté, d'intégrité et de responsabilité inhérents à la mission de recherche. Les travaux de recherche et la rédaction de ce manuscrit ont été réalisés dans le respect à la fois de la charte nationale de déontologie des métiers de la recherche et de la charte d'Aix-Marseille Université relative à la lutte contre le plagiat.

Ce travail n'a pas été précédemment soumis en France ou à l'étranger dans une version identique ou similaire à un organisme examinateur.

Fait au CEA Cadarache, le 12 juillet 2023

Huang Haifu

Liste de publications et participation aux conférences

Liste des publications réalisées dans le cadre du projet de thèse :

1. H. Huang, J. Mañes Perez, N. Alpy, and M. Médale, ‘CFD for Natural Circulation Flows : Numerical Investigations with TrioCFD for a Pitchfork Bifurcation in the Framework of System Scaling Uncertainty Quantification’, presented at the Computational Fluid Dynamics for Nuclear Reactor Safety (CFD4NRS-9), Texas A&M University, USA : OECD Nuclear Energy Agency (NEA), Feb. 2023.

Participation aux conférences et écoles d’été au cours de la période de thèse :

1. H. Huang, ‘Modélisation Multi-échelles en Convection Mixte sur la Base d’Etudes d’Effets Falaises (SFR)’, presented at the TrioCFD Seminar, CEA-Saclay, Oct. 07, 2021.
2. CEA/EDF/INRIA numerical analysis summer school, ’Certification of errors in numerical simulations’, EDF Saclay Lab, June 27 – July 1, 2022
3. H. Huang, J. Mañes Perez, N. Alpy, and M. Médale, ‘Multiscale CFD Simulations for a Single-Phase Flow Stability under Natural Circulation in the Framework of System Scaling Uncertainty Evaluation’, presented at the 13th International Topical Meeting on Nuclear Reactor Thermal Hydraulics, Operation and Safety (NUTHOS-13), Hsinchu, Taiwan, Sep. 07, 2022.
4. H. Huang, J. Mañes Perez, N. Alpy, and M. Médale, ‘CFD for Natural Circulation Flows : Numerical Investigations with TrioCFD for a Pitchfork Bifurcation in the Framework of System Scaling Uncertainty Quantification’, presented at the Computational Fluid Dynamics for Nuclear Reactor Safety (CFD4NRS-9), Texas A&M University, USA : OECD Nuclear Energy Agency (NEA), Feb. 2023.

Executive summary

This research work is part of the quest to improve the safety of nuclear power plants, specifically focusing on single-phase natural circulation (NC), a critical physical process for the removal of residual heat. This process is significant in the context of passive safety systems and is particularly relevant given the ongoing projects involving low-power modular reactors, such as Advanced and Small Modular Reactors, as well as its implementation in advanced 'Gen3+' power reactor designs (e.g., the AP1000). The work seeks to solve non-linear equations that model the coupling between the fluid mechanics of the coolant (accounting for buoyancy, viscosity, and the centrifugal effect with bends) and the transport of thermal energy between a heat source and sink. This problem solution typically allows for the description of key parameters, including the potential onset threshold for flow, beyond which the mass flow-rate of the coolant dynamically establishes itself, and the stability of the established regime.

The research employs TrioCFD, a thermohydraulic simulation tool developed at CEA, to conduct what are termed as high-fidelity (LES) and best-effort (URANS) simulations. These simulations incorporate various levels of turbulence modelling in the core and boundary layers, with the flow profiles in NC differing from those of pressure-driven flows. Regarding VVUQ (Verification, Validation, and Uncertainty Quantification) and scaling considerations (scale effects, refer as transposition in ASN Guide 28), an initial perspective (potentially too schematic) is to place high-fidelity (HF) simulations within the context of validation, and best-effort (BEF) simulations within the context of scaling. This involves using HF for generating reference data at a reduced scale, and BEF for simulating a system as it applies to the actual reactor scale, or a part thereof in the context of multi-scale/multi-fidelity calculations.

The process of scaling between the validation range and real-world reactor applications might face challenges due to physical distortions (incomplete similarity) and distortions in numerical resolution (which can occur even in complete similarity). The advantage of a CFD approach over a system-code approach is its lower dependency on closure laws, rendering it more resistant to physical distortions. This research investigates the evolution of modelling uncertainties in high-fidelity simulations concerning physical distortion effects. This methodology also appears extendable to the URANS approach (BEF), thereby introducing the notion of scaling uncertainties associated with physical modelling.

Beyond the aspects of physical modelling, the quality of numerical solution remains a central concern in the qualification of such approaches. As previously mentioned, the scaling may also experience distortions in numerical solution. To address this, the simulations delve into the details, examining various numerical solution schemes available in TrioCFD, as well as different efforts in spatial and temporal discretizations.

These efforts impact the balance between CPU cost and accuracy of a target quantity of interest, known as the Figure of Merit (FoM). The research explores the evolution of numerical uncertainties in relation to physical distortion effects, thereby introducing also the notion of scaling uncertainties, this time tied to numerical solution. Given the diverse types of modelling uncertainties, this study primarily focus on these two key aspects: numerical uncertainties, which encompasses uncertainties in the numerical solution, and physical modelling uncertainties, which deals with uncertainties related to input parameters.

The bibliographic analysis provides an inventory of scaling techniques and offers a state-of-the-art on natural circulation loops (NCLs) designed to support water nuclear reactor fleets, incorporating past scaling techniques. The DSS technique, a recent scaling method, uniquely offers quantitative (distortion metrics) and synthetic (phase space) comparisons for various scaling solutions. Interestingly, the measure of physical distortion, essential for identifying the best scaling solution, relies on simulations that are simultaneously being assessed for quality concerning distortion effects linked to scaling. This paradox highlights the complexity of the scaling challenge and suggests a methodological inflection to be explored further.

More pragmatically, within the simulation resources of the thesis work, 4th-gen reactor coolants, typically like liquid metals (liquid sodium in this context), introduce a deviation in local physical mechanisms due to their properties. These changes must guide predictive modelling choices when accurately scaling NCLs. HF simulations conducted in our approach serve not just a means to frame the validation range with reference data but also serve as a guide for mastering the scaling. A detailed understanding of the physical mechanisms provides a foundation for a critical analysis of their sensitivity to scaling effects, and hence, to the risks involved in modelling them through calibrated closure laws in the validation domain.

The chosen loop application configuration (HHHC -Horizontal Heating, Horizontal Cooling- loop) is based on nuclear R&D literature. It represents a threshold configuration where the numerical noise will initiate the flow beyond which a sufficient thermal power threshold is crossed. This flow can occur in either a clockwise or counterclockwise direction, depending on factors such as the orientation of the mesh. According to our experience, this feature is accurately reproduced by our simulations, unlike with system codes. Specifically, the choice of numerical scheme impacts the intensity of the numerical noise, to which synthetic noise can be added to accelerate the onset of natural circulation, only if the established regime is of first interest. Following the CFD analysis, a critical Rayleigh number (Ra_c) is determined, establishing a dimensionless scaling law for the onset of flow in a HHHC loop, as in the case of infinite plates (referred to as the Rayleigh-Bénard convection).

The study, conducted in 2D due to CPU budget constraints and thus methodologically focused, employs a comprehensive VVUQ approach for HF and BEF simulations of NCLs. This involves understanding the physical phenomena (as part of PIRT), physical modelling, its numerical simulation, along with steps for verification, validation, and uncertainty management. Recommendations are given on the types of numerical schemes to implement, after having thoroughly investigated various alternatives. The modelling uncertainty is addressed by examining both the uncertainties related to the numerical solution and the model uncertainties. The former is addressed using the Grid Convergence Index (GCI) method and Direct Numerical Simulations (DNS) specifically for low Reynolds number cases. Model uncertainty is tackled using the Polynomial Chaos Expansion (PCE) method, facilitated by the CEA's URANIE uncertainty platform. This platform simplifies the generation of surrogate models for quantile calculations, sensitivity analysis, and calibration.

Furthermore, as highlighted earlier, the methodology is extended to include aspects of scaling, or transposition, as it's termed. Before initiating the modelling process, the validity framework for employing the Boussinesq approximation according to physical scales is established. This sets the stage for its effective utilisation in the scaling context, particularly concerning the temperature range. Following this, the work explores the evolution of both numerical and modelling uncertainties in relation to physical distortion effects. These effects include the Dean number of the flow related to the geometric stiffness of the bends and the Reynolds number, as well as temperature differences between heat source and sink. This introduces the concept of scaling uncertainties.

From the specific cases studied through LES, it becomes clear that only the uncertainty tied to the numerical solution is significantly affected by physical distortions. This indicates the high level of direct flow resolution, illustrated by an indicator of the minimal portion of the flow modeled by a closure law for turbulent cascade (quantified as the solved eddy ratio for LES), thereby qualifying it as a predictive approach. Concerning the evolution of this numerical uncertainty, with geometric bend stiffness and temperature as scaling axes, it is observed that its amplitude can vary in complex and opposite ways depending on the specific FOM considered. Specifically, steady-state flow is largely influenced by the final Reynolds number, which decreases as the bend stiffness increases (due to higher pressure losses resulting in a reduced mass flow-rate). On the other hand, the half-flow time (half-time) is predominantly governed by the Dean number, which conversely increases as the bend curvature tightens.

While the scaling effect does impact numerical solution uncertainties, its relationship can only be meaningfully defined in the simplest cases. When distortions are coupled—both numerical and physical—modelling evaluation and distortion measurements become interdependent. When considering the scaling methodology for CFD, evaluating this interdependence, which is strong and/or correlatable or not, helps decide if a full reassessment at the reactor scale is worth the high computational cost, or if numerical best practices learned at a smaller scale could be applied instead. For future studies employing URANS method with wall functions (being the only computationally feasible approach for reactor system scenarios) might indicate a more significant loss of predictive capability due to distortion effects with a higher fraction of modeled eddies. This is especially the case when considering the unique characteristics of velocity and temperature profiles in the boundary layers of liquid sodium under NC, compared to standard models derived from forced convection scenarios. Pursuing research on BEF simulation for scaling investigation seems to be the logical short-term continuation of the research that has been conducted.

In conclusion, it must be emphasized that the successful defense of the scaling process requires a nuanced understanding of the underlying physical mechanisms. From our standpoint, HF calculations should be an integral part of the approach, even if they might not be directly applicable at the reactor scale. These calculations offer insights that are difficult to obtain through facilities and serve as a means to evaluate the risks associated with scaling, especially if performed across various distorted scenarios. This aligns with the request by ASN Guide 28, which stresses the importance of deep physics expertise. Undertaking these simulations is not just about computational resources but also demands numerical expertise for performing HF computations of the relevant governing equations, a fact underscored by our chosen case analysis. As such, the comprehensive approach detailed for this specific case serves as a valuable guideline. Its effectiveness would benefit significantly from further software advancements, with the aim of automating the entire process, named **MUQCFD** (**M**odelling **U**ncertainty **Q**uantification for **CFD**).

In the long-term view, complementing the short-term proposals concerning URANS (BEF) approach, main suggestions are put forth to advance our understanding of scaling uncertainty metrics. The diminishing predictive accuracy of simulations, whether due to physical distortions (from incomplete similarities) or numerical distortions (even for complete similarity), could be integrated into the validity range. HF calculations could serve as benchmark reference points in this context. The focus shouldn't be solely on obsessively optimizing the uncertainty ranges of the input parameters of the model closure laws to cover the outcomes of two scaling-affected experiments. Instead, it should measure the changes in the uncertainties of a model calibrated on one experiment when applied to a second experiment at a different scale. The objective is to manage the evolution of these uncertainties. This approach incorporates key elements from the scaling studies carried out during the thesis research and aligns with ASN Guide 28, which requires justification of a tool's predictive capability. In this context, the DSS technique might prove instrumental in suggesting distorted configurations that remain in the validity range, especially considering anticipated distortions for the reactor scenario. This approach also sketches out a proposal to the paradox that has been raised, offering a way to measure the impact of distortions on the accuracy of simulations created for this very purpose. The proposed approach, which requires further refinement, is named **MUSQ** (**M**odelling **U**ncertainties with **S**caling **Q**uantification).

Keywords: Multi-Scale Modelling, Scaling, VVUQ, Natural Circulation Loop, CFD, DNS, LES, URANS

Résumé exécutif

Ce travail de recherche s'inscrit dans la quête d'amélioration de la sûreté des centrales nucléaires en se focalisant sur la circulation naturelle (CN) monophasique, un processus physique clé de l'évacuation de la chaleur résiduelle de systèmes de sûreté passifs, mis en avant par l'actualité des projets de réacteurs modulaires de basses puissances (Advanced et Small Modular Reactors) et déjà mise en oeuvre dans des conceptions avancées "Gen3+" de réacteurs de puissance (eg. pour l'AP1000). Il s'attache à résoudre des équations non-linéaires modélisant le couplage entre la mécanique du fluide caloporteur (force motrice de flottabilité, contrainte visqueuse résistive et effet d'inertie centrifuge en présence de coudes) et le transport d'énergie thermique qu'il assure entre une source et un puit de chaleur. Cette résolution permet typiquement de décrire des grandeurs d'intéret dont le seuil éventuel de démarrage de l'écoulement, au-delà la dynamique d'établissement du débit massique du caloporteur, et la stabilité du régime établi. TrioCFD, code de thermohydraulique développé au CEA, est utilisé pour les simulations qualifiées ici de haute-fidélité (LES) et de best-effort (URANS) : elles intègrent des niveaux différents de modélisation de la turbulence à cœur et de couches limites, les profils de ces dernières en CN différant de ceux d'un écoulement de type "pressure driven". Vis a vis du VVQI et de la transposition (effets d'échelles), une première vue (trop schématique comme il le sera rediscuté) est d'inscrire la haute-fidélité dans le cadre de la validation et le best-effort dans le cadre de la transposition en constituant respectivement des moyens de calcul de données de référence à échelle réduite et de simulation d'un système pour le cas réacteur (ou d'une partie d'un système dans le cadre d'un calcul multi-échelles).

La transposition entre le domaine de validation et d'application réacteur rencontre possiblement des effets de distorsions physiques (similitude incomplète) et de distorsion de la résolution numérique (engagée y compris en cas de similitude complète) : l'intéret d'une approche CFD est de réduire (en regard d'une approche code système) la dépendance à des lois de fermeture sur-mesure et donc de mettre en œuvre une approche s'accommodant mieux sur le principe des effets de distorsions physiques. L'évolution de l'incertitude de modélisation de l'approche haute-fidélité vis-a-vis d'effets de distorsion physique est ainsi investie dans le cadre du travail de thèse et la méthodologie apparaît applicable au cas d'une approche URANS pour laquelle l'impact de la transposition se pose effectivement, esquissant donc la notion d'incertitude de transposition liée à la modélisation physique.

Outre ces aspects de modélisation physique, la qualité de la résolution numérique est bien sûr une question centrale de la qualification pour de telles approches et la transposition rencontre un possible effet de distorsion de la résolution numérique. Les simulations investissent ainsi différents schémas de résolution disponibles dans

TrioCFD et différents efforts de discrétisation spatiales et temporelles, dont dépend l'équilibre entre le coût du calcul et la précision d'une grandeur cible (en anglais, Figure of Merit - FoM, dont des exemples ont été donnés ci-avant). Les travaux investissent l'évolution de l'incertitude numérique en fonction d'effets de distorsion physique, esquissant donc la notion d'incertitude de transposition, cette fois liée à la résolution numérique. Étant donné les divers types d'incertitude de modélisation, cette étude se concentrera principalement sur ces deux aspects clés : l'incertitude numérique, qui englobe les incertitudes dans la résolution numérique, et l'incertitude de modélisation physique, qui traite des incertitudes liées aux paramètres d'entrée.

L'analyse bibliographique propose un inventaire des techniques de transposition et fait un point d'état de l'art des boucles de circulation naturelle (NCLs) construites en soutien au parc nucléaire des réacteurs à eau et dont la conception a constitué une application des techniques précitées de mise à l'échelle. La DSS, technique de transposition la plus récente, présente notamment l'intérêt de comparer quantitativement (métrique de distorsion) et synthétiquement (espace de phases), différentes solutions de mise à l'échelle. Il est souligné dans l'analyse que la mesure de distorsion physique qui sert à identifier la meilleure solution de mise à l'échelle, s'appuie sur des simulations dont on cherche aussi à qualifier la qualité vis a vis d'effets de distorsions associés : ce paradoxe apparaît révélateur de la complexité du sujet de la transposition et inspire une voie d'inflexion méthodologique exposée en perspective.

Il ressort également, et plus pragmatiquement dans le cadre des moyens de simulation des travaux de thèse, que les fluides caloporteurs associés à la 4ième génération de réacteurs nucléaires, typiquement les métaux liquides (sodium liquide dans le cadre des travaux de thèse), introduisent par leurs propriétés une inflexion des mécanismes physiques locaux, dont doivent tenir compte sur le principe les choix de modélisation pour une approche prédictive en transposition des NCLs. Les simulations de haute-fidélité menées constituent dans notre démarche, non-seulement une possibilité pour fournir au domaine de validation des données de référence mais aussi un support à la maîtrise de la transposition : la compréhension fine des mécanismes physiques donne une assise à une analyse critique de leur sensibilité à des effets d'échelle et donc aux risques de leur modélisation par des lois de fermeture calibrées dans le domaine de validation. La configuration applicative de boucle choisie HHHC (Horizontal Heating & Horizontal Cooling), s'appuie sur la littérature du domaine de R&D nucléaire : elle constitue une configuration originale, à seuil, où le bruit numérique va, une fois ce seuil franchi (par augmentation de la puissance thermique), déclencher l'écoulement qui peut alors avoir lieu en sens horaire ou antihoraire. Ces caractéristiques conceptuelles sont reproduites par nos simulations, contrairement au code système. Notamment, l'orientation du maillage détermine le sens de l'écoulement, le choix du schéma numérique affecte l'intensité du bruit numérique auquel peut être superposé un bruit synthétique pour accélérer le démarrage de la CN si l'on s'intéresse en premier lieu au régime établi. A l'issue d'une étude de transposition, une valeur de nombre de Rayleigh critique, correspondant au seuil de déclenchement de l'écoulement, est établie. Ceci concrétise la possibilité d'une loi d'échelle adimensionnée dans une boucle HHHC, comme cela est connu dans le cas de deux plaques infinies (appelé convection de Rayleigh-Bénard).

L'étude (menée en 2D pour des raisons de budget CPU et dont la portée est donc méthodologique) déploie une démarche complète de VVQI pour la réalisation des calculs de haute fidélité et best-effort (BEF) des NCLs. Elle comprend la compréhension des phénomènes physiques, la modélisation physique, sa simulation numérique, la vérification, la validation, et la gestion des incertitudes. Des recommandations sont données sur le type de schéma à mettre en œuvre, après avoir investigué en détail les alternatives. La quantification de l'incertitude de la simulation implique l'examen de l'incertitude de la solution numérique et de l'incertitude du modèle. La première est abordée par le biais de la méthode de l'Indice de Convergence de Grille (GCI) et des simulations numériques directes (DNS) pour des cas à faibles nombres de Reynolds. L'incertitude du modèle est traitée en utilisant la méthode du chaos polynomial (PCE) via la plateforme d'incertitude du CEA, URANIE, qui facilite la génération de modèles de substitution pour les calculs de quantiles, l'analyse de sensibilité, et l'étalonnage.

Comme mentionné précédemment, la démarche est étendue aux aspects de transposition. Avant la modélisation, le cadre de validité de l'hypothèse de Boussinesq selon des échelles physiques est établi et permet donc d'inscrire sa bonne utilisation dans un cadre de transposition, en particulier en terme de plage de température. Ensuite, les travaux investissent l'évolution de l'incertitude numérique et de modélisation en fonction d'effets de distorsion physique (nombre de Dean de l'écoulement associé à la raideur géométrique des coudes et au nombre de Reynolds, écart de température des sources et puit de chaleur) esquissant donc la notion d'incertitude de transposition. Il ressort du cas d'espèce traité par LES que l'incertitude associée à la résolution numérique est la seule significativement impactée par un effet de distorsion physique, ce qui témoigne du haut niveau de résolution directe de l'écoulement (une étude fréquentielle de la cascade turbulente est prise comme indicateur de la faible part de l'écoulement modélisée par une loi de fermeture), qui en fait une approche prédictive. Concernant l'évolution de l'incertitude de résolution numérique avec - la raideur géométrique des coudes et les températures pour paramètres d'échelle - il est illustré que son amplitude peut, de manière complexe, évoluer de façon opposée selon la FOM considérée. En effet, le débit en régime permanent est fonction du nombre de Reynolds final et décroît lorsque le rayon de courbure des coudes décroît (les pertes de charge plus élevées entraînent un débit massique plus faible), tandis que le temps de demi-écoulement dépend principalement du nombre de Dean qui est lui au contraire plus fort lorsque le rayon de courbure diminue.

Tandis que l'effet d'échelle a un impact sur l'incertitude de résolution numérique, sa relation ne peut être significativement définie que dans les cas les plus simples. Lorsque les distorsions sont couplées — à la fois numériques et physiques — l'évaluation du modèle et les mesures de distorsion deviennent interdépendantes. Lors de la considération de la transposition pour la CFD, l'évaluation de cette interdépendance (forte et/ou corrélée) aide à décider si une réévaluation complète à l'échelle du réacteur vaut le coût computationnel élevé, ou si les meilleures pratiques numériques apprises à une échelle plus petite sont suffisantes. Il peut être attendu du même type d'étude abordée en URANS avec loi de paroi (la seule des deux approches raisonnablement applicable en terme de CPU à un système du cas réacteur) que la perte de prédictivité de la modélisation sous un effet de distorsion soit plus importante puisque les profils de vitesse et température dans les couches limites en CN du sodium liquide donnés par l'approche LES montrent leur spécificité par rapport aux lois standards provenant d'écoulement en convection forcée : ce point d'investigation apparaît constituer une suite logique à court terme aux travaux de recherches qui ont été menés.

En conclusion, il est rappelé que la défense de la transposition passe par une compréhension fine des mécanismes physiques et qu'à ce titre, les calculs haute-fidélité sont - de notre point de vue - à intégrer dans la démarche bien qu'ils soient non applicables à l'échelle réacteur : ils fournissent des détails auxquels une instrumentation a difficilement accès et constituent un moyen de juger des risques de transposition (d'autant plus si on les réalise pour différents cas distordus) s'incrivant pleinement en phase avec la demande du guide 28 de l'ASN quant à une expertise de la physique. Les réaliser n'est pas seulement un gage en terme de budget cpu à obtenir auprès d'un programme, mais nécessite une expertise numérique pour les mettre en œuvre de façon maîtrisée, comme l'analyse du cas applicatif choisi a permis d'en faire l'ardue expérience. A ce titre, la démarche complète déroulée sur ce cas applicatif, apparait comme une 'guideline' utile dont la mise en œuvre gagnerait en efficacité si les développements logiciels complémentaires identifiés étaient réalisés (avec comme objectif d'automatiser le processus complet, nommé **MUQCFD** - **M**odelling **U**ncertainty **Q**uantification for **CFD**).

Finalement, en perspective à long terme, complémentairement à la proposition à court terme faite précédemment vis-à-vis de l'approche URANS, des propositions de principe sont faites pour progresser sur une métrique d'incertitude de transposition : la perte de prédictivité de la simulation sous l'effet de distorsion physique (similitude incomplète) et/ou numérique (engagée aussi en cas de similitude complète) pourrait être intégrée au domaine de validité, avec possiblement comme points de référence des calculs haute-fidélité. L'analyse devrait s'attacher, pour ce qui est de l'incertitude de modélisation, non pas à optimiser à toute force la gamme d'incertitudes des paramètres d'entrée des lois de fermeture du modèle pour s'assurer de couvrir les résultats issus de deux expériences (calibration) présentant un effet d'échelle, mais plutôt à prendre une mesure de l'évolution du changement de l'incertitude du modèle calibré sur une expérience, lorsqu'on le soumet à une seconde expérience d'échelle différente, avec pour objectif d'en montrer une évolution maîtrisée. Cette démarche, qui reprend donc des éléments de principe des études de transposition menées pendant le travail de thèse, nous parait là-aussi s'incrire dans le sens de la demande du guide 28 de l'ASN qui requière de justifier de la capacité d'un outil à rester prédictif. Dans ce cadre, la technique DSS pourrait s'avérer efficace pour proposer des configurations distordues à intégrer au domaine de validité, d'intérêts par rapport à la nature des distorsions attendues pour le cas réacteur. Cette voie esquisse aussi une réponse au paradoxe soulevé en associant des mesures de l'impact de distorsions sur la précision de simulations réalisées pour en juger. La démarche proposée, qui nécessite des affinements ultérieurs, est nommée **MUSQ** (**M**odeling **U**ncertainty with **S**caling **Q**uantification).

Abstract/Résumé

To enhance safety, nuclear plants in the design phase rely on passive mechanisms like Natural Circulation (NC) for the removal of residual heat. Employing TrioCFD, a tool developed at CEA, simulations are carried out using liquid sodium as the coolant in a "horizontal heating - horizontal cooling" loop based on literature. Both High-Fidelity (HF via LES) and Best-Effort (BEF via URANS) approaches are used, thus showcasing differing levels of turbulence and boundary layer modelling.

This methodological study, carried out in 2D on a configuration with a threshold effect, analyzes the physical mechanisms and deploys a VVUQ process. It starts by determining the validation range for the Boussinesq approximation (thereby framing its applicability for scaling). Modelling uncertainties envelop both numerical solution uncertainties, tackled by the Grid Convergence Index, and physical modelling uncertainties, managed through Polynomial Chaos Expansion via CEA's URANIE platform. The study extends to scaling issues and focuses on the uncertainty evolution in relation to physical distortion effects, sketching out the notion of scaling uncertainties. From the cases computed using LES, it emerges that only the numerical solution uncertainties are significantly impacted by physical distortion. This underscores the high predictive resolution of the LES approach. It can be expected that URANS studies with wall laws (the approach reasonably CPU-efficient for reactor-scale case) would experience a degradation in predictability due to distortion effects. Since the velocity and temperature profiles in the NC boundary layers of liquid sodium given by LES show their specificity compared with the standard laws from forced convection flows, this point of investigation appears to be a logical follow-up of the research.

In conclusion, an in-depth understanding of physical mechanisms is essential when tackling the challenges of scaling. HF analyses provide insights sometimes unattainable otherwise and contribute to risk evaluation, in line with ASN Guide 28. In perspective, the study, in terms of modelling uncertainties, proposes that focus should not merely be on minimizing input parameter uncertainties of closure laws to cover two experiments with scale effects, but rather on measuring the change in the uncertainty of the calibrated model in one experiment when it is subjected to a second experiment of a different scale. To control evolution of modelling uncertainties, this approach also appears to align with the request made in ASN guide 28, which requires proof of a tool's predictability. In this light, the Dynamical System Scaling technique could offer original suggestions for configurations to include in the validity range. Finally, the proposed methodology, which requires further refinements, is denoted as MUSQ (Modelling Uncertainties with Scaling Quantification).

Résumé

Pour accroître la sûreté, les centrales nucléaires en conception s'appuient sur des mécanismes passifs tels que la circulation naturelle (CN) pour l'évacuation de la chaleur résiduelle. Dans ce contexte, via TrioCFD (outil du CEA), des simulations avec du sodium liquide comme caloporteur, sont menées sur une boucle de type "horizontal heating - horizontal cooling" issue de la littérature. Des approches haute-fidélité (HF via LES) et best-effort (URANS) sont employées, mettant donc en jeu des niveaux différents de modélisation de la turbulence à cœur et de couches limites.

L'étude, méthodologique puisque réalisée en 2D sur une configuration présentant un effet de seuil, analyse les mécanismes physiques et déploie un processus de VVQI. Elle commence par déterminer le domaine de validation de l'approximation de Boussinesq (cadrant son applicabilité pour la transposition). L'incertitude de modélisation englobe celle de la solution numérique, abordée par l'Indice de Convergence de Grille et celle de modélisation physique, traitée par la technique d'Expansion du Chaos Polynômial, via URANIE - plateforme du CEA. Les travaux sont étendus aux aspects de transposition et investissent ainsi l'évolution de l'incertitude numérique et de modélisation en fonction d'effets de distorsion physique (nombre de Dean, écart des températures) esquissant donc la notion d'incertitude de transposition. Il ressort du cas d'espèce calculé par LES que l'incertitude associée à la résolution numérique est la seule significativement impactée par un effet de distorsion physique, ce qui témoigne du haut niveau de résolution directe de l'écoulement, qui en fait une approche prédictive. Il peut être attendu du même type d'étude abordée en URANS avec loi de paroi (la seule des deux approches raisonnablement applicable en terme de CPU à un système du cas réacteur) que la perte de prédictivité de la modélisation sous un effet de distorsion soit plus importante. Puisque les profils de vitesse et température dans les couches limites en CN du sodium liquide donnés par LES montrent leur spécificité par rapport aux lois standards provenant d'écoulement en convection forcée, ce point d'investigation apparaît constituer une suite logique à l'étude menée.

L'analyse illustre qu'une compréhension fine des mécanismes physiques est primordiale pour les défis de la transposition : les analyses HF fournissent des détails parfois inaccessibles autrement et contribuent à évaluer les risques, conformément à une des demandes du Guide ASN 28. En perspective, l'analyse devrait s'attacher, en termes d'incertitude de modélisation, non pas à optimiser à toute force la gamme d'incertitudes des paramètres d'entrée des lois de fermeture du modèle pour s'assurer de couvrir les résultats issus de deux expériences présentant un effet d'échelle, mais plutôt à prendre une mesure de l'évolution de l'incertitude du modèle calibré sur une expérience, lorsqu'on le soumet à une seconde expérience d'échelle différente, avec pour objectif d'en montrer une évolution maîtrisée : cette démarche s'inscrit aussi dans le sens de la demande du guide 28 qui requière de justifier de la capacité d'un outil à rester prédictif. Dans cette optique, la technique Dynamical System Scaling pourrait être originalement exploitée pour suggérer des configurations à intégrer au domaine de validité. La démarche proposée, qui nécessite des affinements ultérieurs, est nommée MUSQ (**M**odeling **U**ncertainty with **S**caling **Q**uantification).

Acknowledgements

To everyone and everything that have shaped who I am today. I would like to express my deepest gratitude for their influences on my journey. Here, I am going to extend special thanks to those who have helped me during the thesis process.

To my CEA tutors, **Nicolas Alpy** and **Jorge Perez**, without you, I would not have achieved what I have. **Nico**, your wisdom, prudence, thoughtfulness, and meticulous nature have been invaluable. You have been not only an academic mentor but also a guide in life. I will never forget the times your ideas flowed freely, your extensive talks during meetings, your attention to detail towards results and the care when I lost myself in self doubt. I think I would like to become an engineer-researcher like you!

Jorge, your helpfulness, humility, and communication skills have made you the most timely "911". You've always been there when I needed the most, be it academically, personally, or even during challenging situations, such as several accidental crimes;) I appreciate all the moments of discussion we've had in all forms. You are more than just a tutor, but also a dear friend to me. See you next time in Valencia, when I regain the courage ;-)

As my thesis director, **Marc Médale**, thank you for your professional knowledge and meticulous attitude. Your high standards and efficiency in scientific research have constantly impressed me. I will miss the crème brûlée at the school restaurant and several discussions we had in IUSTI.

Over these three years, I have gained a wealth of knowledge from CEA inhouse SCTs. My thanks go to **Nabil**, **Jérémy**, **Pierre Ledac**, **Pierre-Emmanue Angeli**, **Yangzi Song** for TRUST/TrioCFD; and to **Rudy Chocat** and **Salomon** for Uranie. The training I received, like those from Salome **Christophe Bourcier**, Statistic **Amandine Marrel**, TH winter school **Dominique Bestion**, and more. As well as the knowledge I gathered from various GTs and seminars, have been truly enriching, such GT-VVQI under **Simon Li**, Seminar of scaling under **Vincent Faucher**, seminar VVUQ of multi-physics under **Claire Vaglio-Gaudard**, etc.

Before beginning my PhD, I want to sincerely thank my internship supervisors - **Claire Vaglio-Gaudard**, **Christoph Doderlein**, **Paolo Olita**. Your support helped me to complete my internship smoothly despite the Covid. Under **Manuel Saez**'s recommendation, I embarked on my doctoral journey. A special thank you goes to **Bertrand Mercier** for recommending me since the internship. I also appreciate the administrative help from **Manon Ori** throughout my internship and PhD journey. My gratitude extends to **Ophélie Lorito**, **Delphine Rojo**, **Emma Butty** and other HR staffs like **Céline Foricher**, and to the wonderful restaurant staffs who allowed me to enjoy a variety of French foods in the most refined ways and the most punctual staff the drivers!

Thank you, **Sacha Ranc**, for tolerating my lifestyle and sharing the humour over the past three years. Despite experiencing confinement and more, I look forward to meeting you somewhere else in the world again! To my fellow PhD students in the lab, **Guillerme**, **Charly**, and **Idris**, our shared journey of research and discussions over the past three years have been beneficial in countless ways. Especially, my dear Brazilian friend one of Guillerme, thank you for the best humour and long live capybara!

I cannot forget to mention my good comrade, **Gabriel Sarazin**, the hardest worker in France. You show me how to work hard while keeping a good sense of humor. I admire your perseverance, high standards and crazy physical fitness. The days of working late, covoiturage (best and fast driver ever known), grocery shopping, extraordinary cooking skill etc. will be lasting in my memory, along with all the other helps you provided!

I am grateful to all my direction for their timely reviews of my work, including **Manuel Saez**, **Nicolas Maurand**, **Edwige Richebois**, **Gerard Mignot**, **Marie-Sophie Chenaud**, **Patrick Dumaz** and more. In life, I thank all the Chinese doctoral students at CAD - **Congjin Ding**, **Yifan Peng**, **Shuqi Xu**, **Linkai Wei**, **Ma Xiaoshu**, **Siyue Peng**, and Queen of chimie in Marcoule **Elise Guerinoni** and more, for making my doctoral life full of fun. To my roommates over the years, especially my Brazilian roommate **Magno** and my French maman **Hélène**, your care and shared experiences over the past three years have been invaluable.

Lastly, I want to express my gratitude to my family for their unwavering support and for tolerating my occasional bad temper. The support from my parents, the help from my siblings (**Jiujin** & **Meimei**), and the unconditional love from my grandparents have been upmost of everything. Papi, you will live forever in my memory with the breeze through the sunset harbour. Also, my dear cousin **Liying** (just married when I start writing this acknowledgement), and my mentor of many years, **Spyros**, your presence in my life has been something special.

Last but certainly not least, I wish to express my profound gratitude to my previous institute **IFCEN**, my current school institute **IUSTI** and my current company **CEA**, along with all other hosts who have been involved in this journey. Their patience and the knowledge have been invaluable. It is thanks to them that I have been able to grow and shape myself into the professional I am today. Additionally, I extend my heartfelt thanks to all the reporters and jury members for their patience and for taking the time to review my work.

Thank you, everyone and everything, for being a part of my journey.

Haifu HUANG 黄海富
21 July - 22 August 2023
at Aix-en-Provence, France & Fuzhou, China

Contents

List of Figures

List of Tables

Acronyms

Terms	**Description**
ABC	**A**pproximation **B**ayesian **C**omputation techniques for calibration
AHX	sodium-**A**ir **H**eat e**X**changer in ASTRID
AMG	**A**lgebraic **M**ulti**G**rid
AMR	**A**dvanced **M**odular **R**eactors
ANOVA	**AN**alysis **O**f **VA**riance
ASTRID	**A**dvanced **S**odium **T**echnological **R**eactor for **I**ndustrial **D**emonstration
BCS	**B**ayesian **C**ompressive **S**ensing for PCE
BE	**B**est-**E**stimate and **B**est-**E**ffort
BEF	**B**est-**EF**fort
BEPU	**B**est **E**stimate **P**lus **U**ncertainties
BES	**B**est-**ES**timate
BIC	**B**oundary and **I**nitial **C**ondition
CAD	**C**omputer-**A**ided **D**esign
CEA	French **A**tomic **E**nergy **C**ommission
CFD	**C**omputational **F**luid **D**ynamics
CFL	**C**ourant–**F**riedrichs–**L**ewy number
CI	**C**onfident **I**nterval
CLI	**C**ommand **L**ine **I**nterface (PETSc solver)
CSAU	**C**ode **S**caling **A**pplicability and **U**ncertainty
DNS	**D**irect **N**umerical **S**imulation
DHX	**D**irect **H**eat e**X**changer
DoE	**D**esign **o**f **E**xperiments
DoF	**D**egrees **o**f **F**reedom
DSS	**D**ynamic **S**ystem **S**caling approach
DTW	**D**ynamic **T**ime **W**arping
EoS	**E**quation **o**f **S**tate
F(R)HF(R)P	**F**ull(**R**educed)**-H**eight **F**ull(**R**educed)**-P**ressure
FoM	**F**igure **o**f **M**erit
FSA	**F**ractional **S**caling **A**nalysis
GCI	**G**rid **C**onvergence **I**ndex
GCP	**P**reconditioned **C**onjugate **G**radient
GMRES	**G**eneralized **M**inimal **RES**idual
H2TS	**H**ierachical, **2** **T**iered **S**caling approach

HF	**H**igh-**F**idelity
HHHC	**H**orizontal **H**eating **H**orizontal **C**ooling
HPC	**H**igh **P**erformance **C**omputing
IBICGSTAB	**I**mproved **STAB**ilized **Bi**-**C**onjugate **G**radient
ITF	**I**ntegral **T**est **F**acility
LARS	**L**east **A**ngle **R**egre**S**sion for PCE
LASSO	**L**east **A**bsolute **S**hrinkage and **S**election **O**perator for PCE
LBLOCA	**L**arge **B**reak **L**oss **Of** **C**oolant **A**ccident
LES	**L**arge **E**ddy **S**imulation
LEVM	**L**inear **E**ddy-**V**iscosity **M**odel
LHS	**L**atin **H**ypercube **S**ampling
LMN	**L**ow **M**ach **N**umber
MC	**M**onte **C**arlo method
MUQCFD	**M**odelling **U**ncertainty **Q**uantification for **C**omputational **F**luid **D**ynamics
MUSQ	**M**odelling **U**ncertainties with **S**caling **Q**uantification
MUSCL	**M**onotone **U**pstream-centered **S**chemes for **C**onservation **L**aws
NCL	**N**atural **C**irculation **L**oop
Nisp	**N**on-**I**ntrusive **S**pectral **P**rojection
NLEVM	**N**on-**L**inear **E**ddy-**V**iscosity **M**odel
OLS	**O**rdinary **L**east **S**quares **R**egression for PCE
OMP	**O**rthogonal **M**atching **P**ursuit for PCE
PCE	**P**olynomial **C**haos **E**xpansion
PETSc	**P**ortable, **E**xtensible **T**oolkit for **Sc**ientific **c**omputation
PIRT	**P**henomena **I**dentification and **R**anking **T**able process
PSD	**P**ower **S**pectral **D**ensity
P-V	**P**ower-**V**olume scaling method
QoI	**Q**uantity **o**f **I**nterest
RANS	**R**eynolds-**A**veraged **N**avier-**S**tokes
SA	**S**ensitivity **A**nalysis
SCT	**S**cientific **C**omputing **T**ool
SET	**S**eperate **E**ffect **T**est
SFR	**S**odium-cooled **F**ast **R**eactor
SGS	**S**ub**G**rid-**S**cale
SMR	**S**mall **M**odular **R**eactors
SRS	**S**imple **R**andom **S**ampling
TRUST	**TR**io**U** **S**oftware for **T**hermohydraulics
UDL	**U**niform **D**iameter **L**oop
UMAE	**U**ncertainty **M**ethodology based on **A**ccuracy **E**xtrapolation
URANS	**U**nsteady **R**eynolds-**A**veraged **N**avier-**S**tokes
VDF	**F**inite **V**olume **D**ifferences
VEF	**F**init **V**olume **E**lements
VVUQ	**V**erification, **V**alidation & **U**ncertainty **Q**uantification
WALE	**W**all-**A**dapting **L**ocal **E**ddy-viscosity

Glossary

ASN Guide No. 28 (ASN and IRSN 2017)

"Qualification of scientific computing tools used in the nuclear safety case"

In this guide, the qualification of an SCT implies recognition by the licensee that an SCT is able to provide results that are usable for a nuclear safety case(*). This recognition is established on the basis of data produced by verification, validation, quantification of uncertainties and transposition operations. These operations are part of an overall process ensuring that the SCT is capable of calculating the variables of interest with the uncertainties appropriate to the requirements, within the intended scope of utilisation.

This guide presents the ASN and IRSN recommendations for these operations and this process. Its purpose is to provide a coherent set of recommendations to be implemented in order to ensure that an SCT is qualified in accordance with ASN's requirements. It aims to facilitate the preparation and assessment of the files establishing the qualification of the SCTs, by specifying the contents of the file to be produced by the licensee for transmission to ASN.

Best-Effort (BEF) or Lower-Fidelity simulation

One of fidelity levels, as listed in Table 2.6, lies between Best-Estimate and High-Fidelity simulations. In this context, refer to URANS appraoch with wall functions.

Distortions

- **Physical distortion**: the discrepancy of physical phenomena lies between the scales before the modelling and simulations.
- **Numerical distortion**: Even with complete similarity, this distortion may exist due to inconsistencies in the modeling and simulation process during scaling.

Figures of Merit (FoMs)

- Flow-Rate: The quantity evaluates the time-averaged velocity fields, assuming constant density.
- Half-Time: The time taken to reach half of the established flow rate (difference).
- Frequency/Power Density by PSD: The frequency and power density are measured from fields using Power Spectral Density techniques.
- Warping Cost by DTW: This cost measures the similarity between two time sequences using Dynamic Time Warping techniques.

High-Fidelity (HF) or Higher-Fidelity simulation

One of fidelity levels, as listed in Table 2.6, refers to LES appraoch in this context.

Modelling uncertainties

The sources of modeling uncertainties are listed in Figure 2.3. This work will primarily focus on the following two:

- **Numerical Solution Uncertainties**: Using the GCI method, uncertainties due to discretization will be quantified, following **ASME 2009**.
- **Physical Modeling Uncertainties**: Using the meta-modeling method, uncertainty arising from turbulence models will be quantified using the PCE method, in accordance with OECD recommendations (**NEA/CSNI 2016**)

MUQCFD

Denoted as "Modeling Uncertainty Quantification for CFD", the module developed in this work (see flowchart in Figure 6.1) calculates the FoMs and computes the related uncertainties at expected fidelity levels for given scales.

MUSQ

Outlined in the perspective (see flowchart in Figure 6.2), the methodology, denoted as "Modeling Uncertainty with Scaling Quantification", aims to offer a comprehensive approach to addressing ASN requests as detailed in **ASN and IRSN 2017**.

Qualification

Described in **ASN and IRSN 2017**: Recognition by the licensee that an SCT is able to provide results that are usable for a nuclear safety case.

Scaling/Transposition

Widely known as scaling, **ASN and IRSN 2017** refers to it as the process of transposition of the validation cases to the intended scope of utilization.

Scientific Computing Tool (SCT) - *Outil de calcul scientifique (OCS)*

Described in **ASN and IRSN 2017**: SCTs are software performing numerical simulation of physical phenomena. They consist of one or more solvers and may comprise pre- and post-processors:

- the solvers are designed by means of several successive steps:
  - formulation of physical modelling hypotheses, generally leading to a system of equations;
  - definition of algorithms for numerical resolution of these equations;
  - implementation of these algorithms;
- the pre-processors can be used to introduce the calculation data (mesh, physical characteristics, etc.);

— the post-processors are used to exploit the calculation results, more specifically in graphic form.

In this work, the primary SCTs used include Salomé, Trust/TrioCFD, and URANIE, along with the external processors already embedded.

Scope of utilisation - *Champ d'utilisation*

Described in **ASN and IRSN** 2017: All the situations or scenarios studied in the safety case and that are to be substantiated using this SCT.

Utilisation range - *Domaine d'utilisation*

Described in **ASN and IRSN** 2017: Variation range for the characteristic geometrical or physical variables (pressure, temperature, flowrate, power, etc.) for the scenarios of the intended scope of utilisation.

Validation

Described in **ASN and IRSN** 2017: Validation consists in ensuring that an SCT can satisfactorily simulate the physical phenomena within the validation range.

Validation range - *Domaine de validation*

Described in **ASN and IRSN** 2017: Variation range for the characteristic geometrical or physical variables (pressure, temperature, flowrate, power, etc.) for which the SCT results are considered to be satisfactory.

Validity range - *Domaine de validité*

Described in **ASN and IRSN** 2017: The validity range is the result of the possible adaptation of the validation range following transposition, for the intended application.

Verification

Described in **ASN and IRSN** 2017: Verification consists in ensuring that the SCT functions as required (correct computing and numerical performance, correct numerical results).

Latin letter	Description
A	flow area, m^2
$\boldsymbol{A_w}$	wetted flow area(DL), m^2
a	dimensionless flow area
b	exponent in the friction factor equation
$\boldsymbol{C_p}$	specific heat, $J/(kgK)$
Cs	SGS coefficient in LES Smagorinsky model
Cw	SGS coefficient in LES WALE model
D	diameter, m
d	dimensionless diameter
f	friction factor
$\boldsymbol{f_s}$	scaled factor
g	acceleration due to gravity, m/s^2
$\boldsymbol{Gr_m}$	modified Grashof number
H	height, m
h	enthalpy, kJ/kg
K	loss coefficient
L	length
l	dimensionless Length
m	mass, kg
$\boldsymbol{\dot{m}}$	mass flow rate, kg/s
N	number of pipe segments
$\boldsymbol{N_G}$	geometric number
$\boldsymbol{Nu_m}$	modified Nusselt number
p	pressure, bar or coefficient in friction factor equation
$\boldsymbol{p_{gci}}$	apparent order by GCI method
Pr	Prandtl number
prdt	turbulent Prandtl number
Q	power,W
q	heat flux, W/m^2
R	flow resistance
$\boldsymbol{R_k}$	radius of elbow bent
Re	Reynolds number
s	coordinate along the loop, m
S	dimensionless coordinate around the loop (s/H)
$\boldsymbol{St_m}$	modified Stanton number
Δs	heater/cooler length,m
t	time, s
T	temperature,K
$\boldsymbol{\Delta T_r}$	reference temperature difference in the definition of Gr_m
U	heat transfer coefficient
u	velocity, m/s

V	volume, m^3
Vk	Von Karman coefficient
z	elevation,m
Z	dimensionless elevation (z/H)

Subscript	Description
0	reference
c	cooler
cl	cold leg
e	equivalent/effective
h	heater
hl	hot leg
i	i-th, ititial
R	ratio between model and prototype
r	reference
ss	steady state
t	total

Grec letter	Description
$\boldsymbol{\beta_T}$	thermal expansion coefficient, $1/K$
$\boldsymbol{\gamma}$	parameter defined as $\sum_{N_i}^{i} \frac{l_i}{a_i}$
$\boldsymbol{\theta}$	dimensionless temperature
$\boldsymbol{\lambda}$	thermal conductivity, $W/(m \cdot K)$
$\boldsymbol{\lambda_A}$	affine parameter of β
$\boldsymbol{\lambda_B}$	affine parameter of ω
$\boldsymbol{\Pi}$	ratio M/P for H2TS
$\boldsymbol{\mu}$	dynamic viscosity, $kg/(m \cdot s)$
$\boldsymbol{\rho}$	density, kg/m^3
$\boldsymbol{\tau}$	dimensionless time
$\boldsymbol{\tau_s}$	process action for DSS
$\boldsymbol{\nu}$	kinematic viscosity, m^2/s
$\boldsymbol{\Omega}$	effect parameter for DSS

1. Introduction

> 千里之行，始于足下。
>
> - 老子

> A journey of a thousand miles begins with a single step.
>
> - Laozi (571–471 BCE, Philosopher)

Sommaire

1.1. Motivation

The primary motivation of this thesis work is to pave the way for a possible response and to address in details the challenges posed by the French Nuclear Safety Authority (ASN) Guide 28, issued in 2017 and titled 'Qualification of scientific Computing Tools (SCTs) used in the nuclear safety case' (**ASN and IRSN 2017**). Besides the classic VVUQ (Verification, Validation, Uncertainty Quantification), this guide requests the defense of scaling-transposition (term used in the guide) issues when using SCTs in safety cases. It aims to discern how the outcomes of SCT validation correlate with the target utilisation range. This process can be broken down into two stages:

- Initially, a comparison is made between the validation cases, such as experimental prototypes or BNI data, and the intended scope of utilisation for the specific facility. This involves examining the impact of geometrical and physical disparities on main physical phenomena and influential parameters. If the impact is very slight, or even non-existent, this step may be sufficient;
- A secondary step, as necessary, evaluates the models ability to remain predictive, considering the differences between the SCTs validation and utilisation range. This may involve extra experimental data, sensitivity analyses, or expert evaluations, especially focusing on the justification for transposing adjustments and uncertainties.

An essential aspect of scaling is ensuring that modelling decisions in safety studies align with those in validation cases. Discrepancies mandate revising validation case simulations or evaluating their effects on safety studies. Conclusively, the SCTs validity range is ascertained after the scaling.

For the designated safety cases, a reactor safety demonstration requires the analysis of complex problems related to accident scenarios. Without some simplifications, experiments or reference calculation solving the exact equations cannot reproduce the full-scale case at respectively, a reasonable financial and CPU costs. Hence, only experiments at reduced-scale or high-fidelity (HF)) computations aiming at providing reference data at reduced scale are feasible. However, this necessary downscaling process could introduce some physical distortions compared to full scale. Connectively, selected SCTs tools are applied at full scale to perform the VVUQ process. Pragmatically, SCTs should apply time and/or space-averaging of the equations, which introduce modelling closure laws (**Bestion, D'Auria et al. 2017**). Modelling uncertainties from the validated range may be changed for upscaling, depending on the physical complexity to be described, that can be partially distorted between both scales, in spite of the downscaling technics.

Hence physical distortions and modelling uncertainties can actually be coupled which introduce a scaling uncertainty. Furthermore, the uncertainty of a targeted Figure of Merit (FoM) depends on the spatial and temporal discretization efforts and the numerical scheme, which must again be compatible with computational time resources. Widely used 1D-sytem approaches assume that the numerical solution errors have a lower order of magnitude regarding the closure laws or modelling errors, which can be easily out of validation range especially for natural circulation stability (**Ambrosini et al. 2004**). Currently, an increasing number of HF simulations are being applied at the reactor scale (**Gerschenfeld et al. 2017**), which could reduce the weight of closure laws and increase the predictability of the codes, thus its scaling capability (scalability). In such a new paradigm, the role of numerical resolution error is increased so that the question could partly shift from the scalability of closure laws to the scalability of numerical resolutions. However, for the actual reactor scale, only best-effott/best-estimate (BE=BEF+BES) simulations are feasible: as such, the natural circulation in a loop (NCL) of a sodium flow, which is the subject of this research work, is a particular case for which the reliability of the CFD closure laws of the BE approach is still debatable.

As a conclusion, in the context of code qualification for nuclear safety regarding natural circulation, the uncertainty that needs to be characterized and upscaled to demonstrate the reliability of reactor case simulations, involves a complex coupling of numerical, physical modelling and physics distortion components. The recent requests from ASN in Guide 28 underline the point, while CFD offers new possibilities and challenges: both encourage further methodological investigations.

1.2. Natural Circulation in Nuclear Passive Systems

Importantly, passive systems, including those driven by natural circulation (NC), play a key role in enhancing the safety and efficiency of next-generation reactors. This category comprises Advanced Modular Reactors (AMRs), advanced Pressurized Water Reactors (APWRs), and 4th generation reactors (**IAEA 2005**). For instance, the AP1000, a state-of-the-art design by Westinghouse for advanced PWRs, utilizes NC for residual heat removal in emergency scenarios, using buoyancy-driven flows to cool the core. This innovative approach not only bolsters safety but also amplifies reliability. The reactor features multiple NCLs, labeled from NC1 to NC5 as illustrated in Figure 1.1. Interactions within these loops might lead to intricate and occasionally unpredictable oscillations in parameters such as pressure, fluid velocity, and void fraction (**D'Auria 2023**).

Further emphasizing the universal significance of NC in the nuclear was the ASTRID reactor project —a 1500MWth Sodium-cooled Fast Reactor (SFR) pool type model. ASTRID concept has two distinct systems, RRA and RRB, to remove heat from its core. Both systems engage primary sodium via an in-vessel Direct Heat eXchanger (DHX), depicted in Figure 1.2. These systems, while sharing the same core function, differ

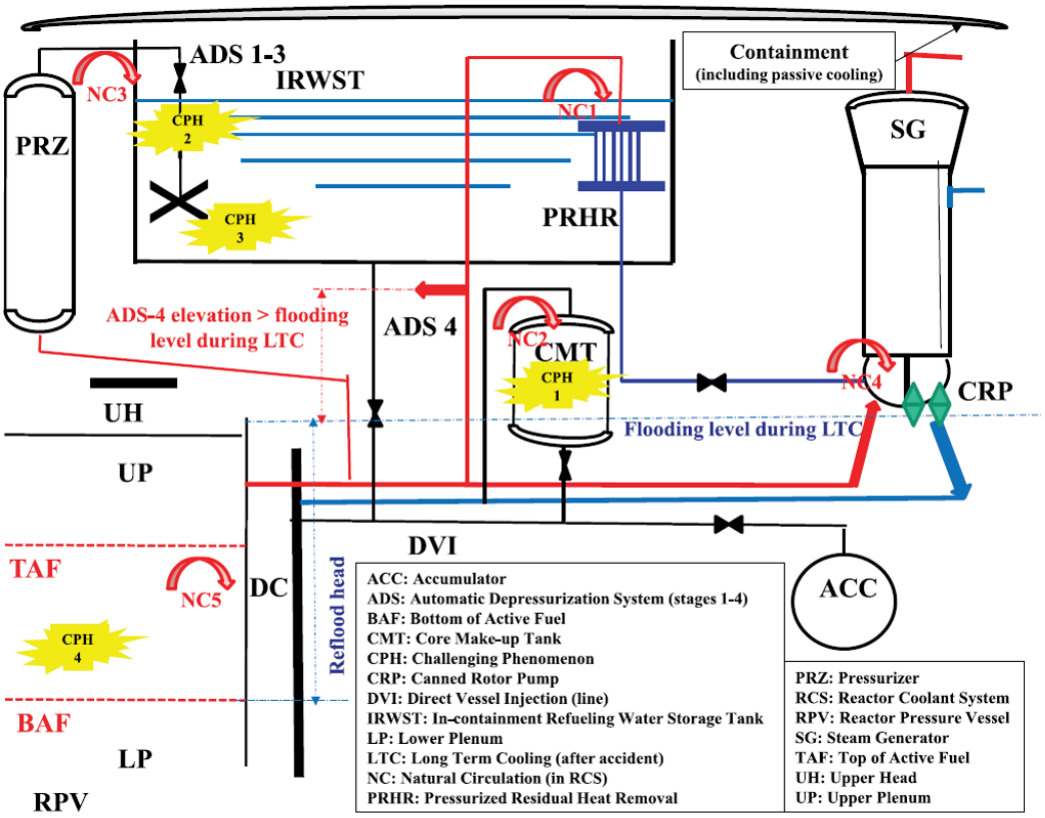

Figure 1.1. – Selected safety systems that are part of the AP1000 design with acronym definitions (**D'Auria 2023**).

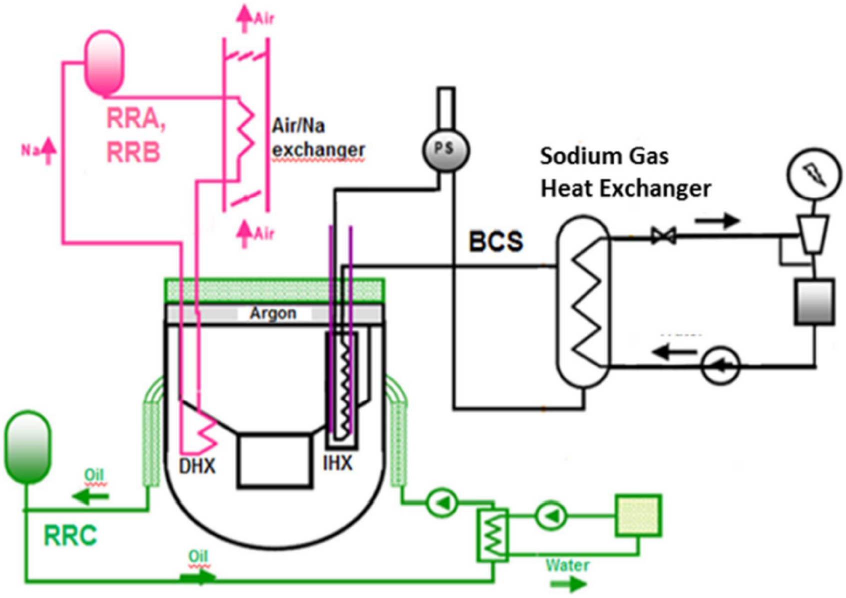

Figure 1.2. – Presentation of ASTRID Decay Heat Removal Systems: RRA, RRB and RRC (**Hourcade et al. 2018**).

in their operational modes. RRA requires electrical power, whereas RRB operates primarily on NC. This distinction significantly impacts the loop design, especially in the design of the sodium-Air Heat eXchanger (AHX). While RRA necessitates an active air fan, RRB is solely dependent on the natural convection of sodium and air (**Hourcade et al. 2018**). Although the ASTRID project was halted, R&D in SFRs continues to be a priority, not only in France but also globally: as such, within the CEA, other initiatives are underway, including new startups like Hexana [1] and Otrera [2], which focus on AMRs using sodium as a coolant.

Therefore, ensuring the fine operation of NCL safety systems that use sodium coolant is still vital for reactor licensing. Sodium in NCL presents unique challenges compared to water, especially in CFD modelling when accounting for geometric changes like elbows. Conducting multiple experiments with high-temperature liquid sodium is time-consuming and expensive. As a result, the RANS (Reynolds-Averaged Navier-Stokes) approach in CFD is often favored for studying sodium's thermohydraulic flow, given its efficiency relative to DNS (Direct Numerical Simulation) and LES (Large Eddy Simulation). However, the common Reynolds-analogy hypothesis, which assumes a constant turbulent Prandtl number (Prt=0.85-0.9), is ill-suited for sodium due to its unique thermal properties and low Prandtl numbers. This challenge is especially critical in NC scenarios, where heat exchange is tightly coupled with flow dynamics. This underscores the need for the development of advanced models specifically for sodium in the context of NC.

Specifically, sodium flow, especially downstream of an elbow, can manifest anisotropic turbulence patterns, such as Dean vortices and thermal plumes with heat transfer. This adds complexity to the modelling process and introduces concerns regarding scaling. In summary, while one-dimensional codes may not capture all the nuances of NCL systems with sodium, CFD methods demand a balance between accuracy and efficiency for further scaling issue.

1.3. Scaling Problematic for Scientific Computation Tools Qualification

Scaling is not a new issue for thermal-hydraulics applied to nuclear safety (**Bestion, D'Auria et al. 2017**). As has been highlighted, concern on scaling issue has been however recently reinforced by ASN on SCT qualification. Within the neutronics scientific field, the issue has been the topic of recent works (**Martinez 2017**; **De Saint Jean et al. 2017**), which is focused on the scalability of the uncertainties related to nuclear data between the validation and the utilisation range in reactor case. In the thermal-hydraulics domain, the non-linearity and wide spectrum of interacting scales raise different issues and require different scaling approaches comparing to neutronics (however, both could for sure share smartly some statistical technics for uncertainty

---

[1] https://www.hexana.fr/

[2] https://otreraenergy.fr/

propagation). Indeed, validation, in addition to scaling in thermal-hydraulics, has to deal with a wide range of physical parameters, geometrical configurations, closure laws, etc., which relate to a broad spectrum of flow and heat transfer regimes.

To address scaling issues effectively, both reference data for validation and scaling procedures for distortion measurement are essential. A parallel challenge comes from "project flexibility" that runs parallel to the ASN's request. It reflects the growing number of changeable projects, which demand the use of existing data (mostly not custom-tailored) and validation of their scaling distortion with current objective. Moreover, the flowchart 1.3 questions also how CFD codes, specifically HF and BEF simulations, can supplement the experiments plus system code approaches to meet these diverse requirements, including those set by the ASN's SCT qualification.

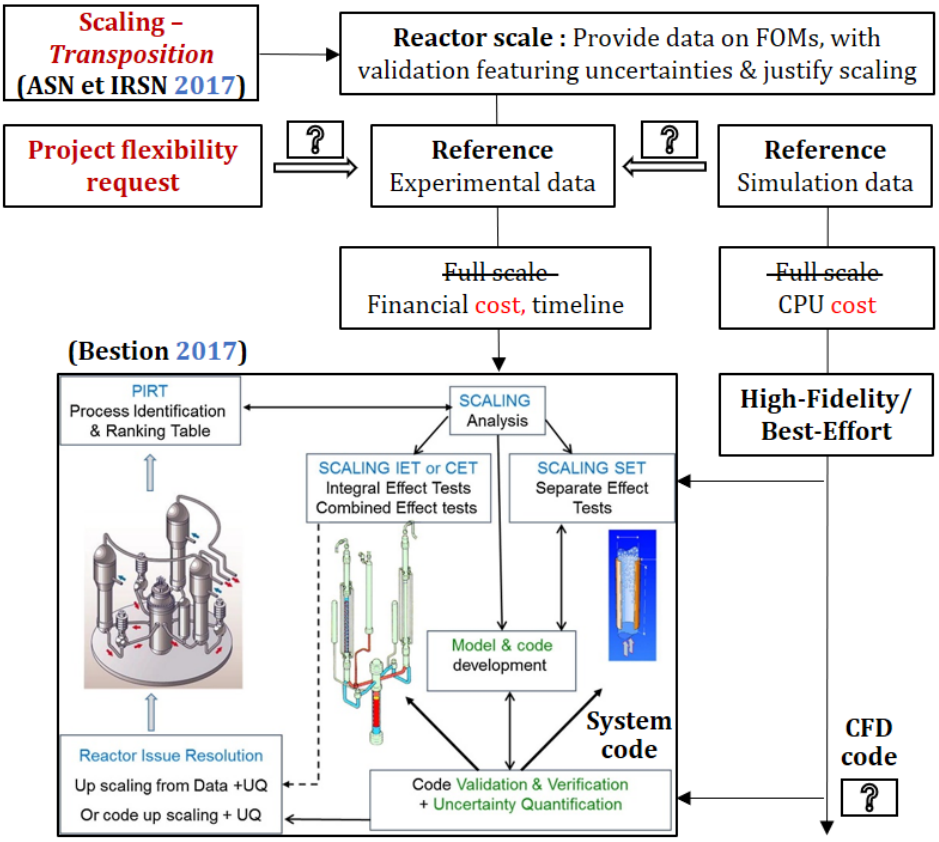

Figure 1.3. – Illustration of scaling procedures of complex reactor issue.

For complex reactor studies, **Bestion** 2017 offers a robust experimental framework and code prediction. To counter these challenges, the methodology integrates elements like PIRT (Process Identification and Ranking Table) analysis, scaling assessments, and the selection of Integral Effect Tests (IET), Combined Effect Tests (CET), and Separate Effect Tests (SET). The process further involves selecting a suitable SCT (mostly system codes), followed by its verification and validation. Ultimately, the SCT is used to address safety concerns while assessing prediction uncertainties. Given that experiments cannot affordably replicate all physical conditions and numerical tools can't solve exact equations, the industry often relies on scaled-down experiments and approximate equations. These methods are susceptible to errors from imperfect closure laws and numerical inaccuracies in question. Advances in computing are shifting the focus from 1D-system codes, which required multiple validations, to HF and BEF simulations via CFD codes. While still resource-intensive, these simulations offer both time and cost benefits. This shift not only presents new challenges, like numerical resolution and expertise, but also allows for more tailored solutions and the use of past test data, providing a broader approach to scaling issues.

1.4. Objective, Scope and Organization of the Thesis

The study seeks to investigate how high-fidelity (HF) and best-effort (BEF) simulations can be synergistically integrated to tackle the scaling challenges outlined in ASN Guide 28, specifically within the context of a NCL featuring sodium flow.

To provide a practical guideline with detailed implementation for addressing scaling problems, it is imperative to begin with the PIRT process. Chapter 2 focuses on a literature review, covering scaling methodologies and the state-of-the-art in NCLs. From this inventory, one can pinpoint the crucial physical phenomena for simulation, the SCTs for use, and the models to be chosen. The various methods for down-scaling, particularly the advanced one Dynamical System Scaling (DSS), are presented and analyzed in detail in Chapter 2. However, they are not employed within the framework of this thesis. Instead, we will deliberately introduce physical and geometrical distortions to methodically study their impact on modelling uncertainties.

Thus, Chapter 3 is directed towards varying fidelity level computations for NCL with sodium flow, using a CEA thermohydraulics tool, TrioCFD, based on the TRUST platform. This chapter encompasses geometry configurations, physical modelling, numerical modelling, and a comprehensive VVUQ process. In the subsequent Chapters 4 and 5, numerical uncertainties and physical modelling uncertainties are chosen from modelling uncertainties for investigation. For the former, the Richardson extrapolation-based method, GCI (Grid Convergence Index), will be employed for various FoMs (Figures of Merit) concerning NCL onset and establishment. For the latter, the meta-modelling technique, PCE (Polynomial Chaos Expansion), will be implemented using the CEA statistical platform URANIE with different turbulence models of TrioCFD. The uncertainties will be quantified using the aforementioned methods and examined separately in the context of scaling effects.

In conclusion, primary insights from the conducted CFD simulations, modelling uncertainties, and scaling considerations are presented. Thanks to the module MUQCFD (Modelling Uncertainty Quantification for CFD), the FoMs and uncertainties can be obtained for the up-scaling analysis. For the outlooks, a comprehensive roadmap of the MUSQ methodology (Modelling Uncertainties with Scaling Quantification) will be detailed, paving the way for further research.

2. Literature Review

知之为知之，不知为不知，是知也。

- 孔子

To know what you know, and what you do not know, that is true knowledge.

- Confucius (551–479 BCE, Philosopher)

Sommaire

2.1. Scaling under the Framework of Codes Qualification

Experiments aiming to recreate safety-related thermal-hydraulic (TH) phenomena must simplify to accommodate constraints of budget, logistics, and safety. However, such simplification can lead to distortions compared to the ideally-scaled experiment that would precisely mimic the behaviour of the reference plant. Such distortions arise from differences in parameters like volume, power, temperature, pressure, velocity, geometry, fluid nature, and scaling-related distortions in geometry including macroscopic size ratios and local geometric variations, etc.

Many potential sources of distortion exist, sun as heat losses, loop pressure drops and conductivity etc., belong to **physical distortion**. Such distortion escalates as the thermal-hydraulic behaviour diverges from the original, ultimately limiting the accuracy of the scaled facilities in representing the prototype physics. As such, scaling distortions are an unavoidable limitation in TH codes, particularly under transient and non-developed flow conditions (**D'Auria and Galassi 2010**).

Meanwhile, due to high costs and complexity of experimental facilities, the application of modellings and simulations bring in the **numerical distortion**. As computing power grows, this affordable approach also helps to verify the feasibility of projects before any full-scale construction. Reflecting this trend, **ASN and IRSN** 2017 demands a code qualification procedure that incorporates the process of scaling, referred as to *transposition* in French. This process involves the following two steps:

- " a first step consisting in identifying the geometrical (scale effect) and physical differences between the validation cases (for instance, experimental mock-ups or data collected from the basic nuclear installations (BNI) itself) and the intended scope of utilisation for the facility in question. The impact of these differences on the principal physical phenomena and the influential parameters are evaluated. This is typically done through a physical analysis. If the impact is minimal or non-existent, this initial step might be enough."
- " a second step involves assessing the capability of the models to remain predictive (or penalising), taking into account the differences identified between the validation range of the SCT and the utilisation range. This evaluation could rely on additional experimental data, sensitivity calculations, or expert assessments. Importantly, this includes justifying the transposition of the adjustments and the uncertainties."

This section primarily aims to discuss the scaling problematics for the qualification of SCTs. It starts with an introduction to the principles of similarity and scaling. After discussing the methods to scale down a prototype, a comparative analysis will be conducted to identify the most effective methodology. Then, a summary of both experimental and theoretical advances using these techniques will be provided. For the scaling uncertainty aspect, we will further examine the origin of the scaling process within the general Best Estimate Plus Uncertainties (BEPU) methodologies. Finally, the section will address the identification of modelling uncertainties under scaling.

2.1.1. Similarity and Scaling

In the nuclear domain, it is often difficult to completely preserve all the similarities (scaling groups) between the small-scale model and the prototype. For example, in horizontal flows with a free surface (separated flow, wavy flow, etc.), both the Reynolds and Froude numbers cannot be preserved because they require different velocity scales. Under such conditions, scaling distortions are inevitably present (**Bestion, D'Auria et al.** 2017). Therefore, we will explore the complete and incomplete similarity cases, along with the methods for identifying dimensionless numbers, which are fundamental to the field of fluid dynamics and play an essential role in experimental and computational research.

2.1.1.1. Complete and Incomplete Similarities

In engineering, designing, constructing, and operating new systems can raise human or financial risks and technical issues, especially when there's insufficient knowledge or the governing equations are unknown, insoluble, or non-validated experimentally. To mitigate these risks, preliminary experiments are conducted on scaled models.

If specific conditions are fulfilled, dimensional analysis enables the transposition of results from one scale to another, which is particularly useful in fluid flow situations. **Bonnefoy** 2021 presents the difference between the complete and incomplete similarities:

Complete Similarity: It is said that two systems are similar, or in complete similarity, when the following conditions are met:

- all dimensionless numbers are identical;
- the dimensionless boundary conditions are identical;
- the dimensionless initial conditions are identical.(for non-stationary systems)

From the first condition, it can be deduced that the geometric shape is invariant: in complete similarity, the two systems are similar to each other. Among all invariances, some authors distinguish geometric similarity (invariance of length ratios), kinematic similarity (invariance of speed ratios), and dynamic similarity (invariance of force ratios).

Incomplete Similarity: We speak of incomplete similarity when at least one similarity condition is not met. This situation is encountered in particular when:

- the materials imposed by the similarity are too inconvenient to use or simply do not exist;
- the stresses cannot be controlled. For example, the intensity of the gravitational force is the same regardless of the size of the system (except in free fall, centrifugation, etc.);
- a phenomenon is negligible at one scale and predominant, or at least influential, at another scale. For example, the effect of surface tension is important for a millimetric systems, but is negligible for systems of much greater sizes (metric and above).

2.1.1.2. Identification of Dimensionless Numbers

Dimensionless analysis offers a method for reducing complex physical problems to the simplest (that is, most economical) form prior to obtaining a quantitative answer (**Sonin** 2001). The identification of dimensionless numbers is an essential step in the study of similarity and scaling. The Buckingham's Pi Theorem (**Buckingham** 1914) provides a method for deriving sets of dimensionless parameters from the given variables, even if the form of the equation is still unknown. The theorem indicates that any physical law can be expressed as an identity involving only dimensionless combinations (ratios or products) of the variables linked by the law. For experimental purposes, different systems that share the same description in terms of these dimensionless numbers are equivalent.

When the governing equations are available, they are directly used to derive the dimensionless numbers. This approach often leads to a more precise and comprehensive identification of the relevant dimensionless groups, helping in the establishment of similarity and the development of scaling laws (**Kunes** 2012). Despite the scientific significance and widespread use of dimensionless numbers, discovering new dimensionless numbers and their relationships (i.e., scaling laws) from experiments remains challenging, especially for a complex physical system lacking complete governing equations. Using dimensionless numbers can considerably simplify a problem by reducing the number of variables that describe the physical process, thereby reducing the number of experiments or simulations required to understand and design the physical system (**Xie et al. 2022**). In summary, the concepts of similarity, scaling, and dimensionless numbers play a crucial role in fluid dynamics research, providing a critical framework for experimental design and data analysis.

2.1.2. State-of-the-Art on Scaling Methodologies

2.1.2.1. Quasi-Static Scaling Methods

Quasi-static scaling methods are pivotal techniques used in the field of engineering and physics for the purpose of simulating and analyzing system behaviors. These methods, which include Power-Volume, Ishii, H2TS, and FSA, are often used to create scaled-down models of physical systems, allowing us to conduct experiments and make observations that would be difficult, costly, or risky to apply at full scale.

Power-to-Volume (P-V) method

Balancing length, time, and force scales is essential when designing test facilities for macroscale objectives. This typically leads to full-height, full-pressure designs using Power-to-Volume (P-V) scaling. The latter method, proposed by **Nahavandi et al. 1979**, conserves heat flux and velocity, thereby ensuring kinematic similarity. This approach, with modifications to suit local specifics, has been utilized by facilities for Pressurized Water Reactor (PWR) such as PKL, LSTF, and BETHSY (see Table 2.3).

However, when the P-V scaling method is applied to a test facility with an area scale that is too small (typically when scaling the number of parallel channels is not an option), major phenomena can be significantly distorted. In particular, the system's pressure drops and heat losses, along with the accumulated heat of test facility structures, become excessive in the smaller scale facility. Additionally, the aspect ratio (length to diameter) increases due to the reduced area under full-height conditions, resulting in inadequate simulation in the test facility for multidimensional flow phenomena (**Bestion, D'Auria et al. 2017**).

This scaling approach offers advantages like **prototypical height and pressure** but can result in **shape distortion and limited component representation**. To mitigate these drawbacks, Separate Effect Tests (SETs) may be necessary, involving testing specific components separately or verifying heat and mass transfer correlations through targeted tests.

Three level scaling (Ishii)

The approach introduced by **Ishii 1998** ensures dynamic similarity for single-phase and certain two-phase flows, essential for addressing natural circulation incidents prevalent in design-based accidents. Its key attribute is allowing designers to control the height scale, thus minimizing surface-to-volume distortion compared to the power-to-volume scaling method. This approach also better conserves multidimensional phenomena in small-scale facilities due to a closer aspect ratio to the prototype. However, the reduced scales for time and flow velocity due to the diminished length scale result in unavoidable distortion of local thermal hydraulic phenomena. This three levels scaling method encompasses:

— A **global-scaling analysis** maintaining the flow of both single and two-phase natural circulation by applying similarity rules based on fluid continuity, momentum, and energy governing equations. It also focuses on preserving the general similarity parameters of the system overall behavior and determining the requirements for geometric similarity, time scale, and the similarity of the main thermal hydraulic parameters.

— **Boundary flow and inventory scaling** that are crucial for multi-component systems, where accurate scaling of intercomponent junctions is essential.

— **Local phenomenon scaling** to ensure their preservation, thereby completing the overall system similarity.

Hierarchical Two-Tiered Scaling (H2TS) Method

Developed by the US-NRC technical program group in the early 1990s, the H2TS methodology (**Zuber** 1991), a descendant of Ishii's method, **Ishii et Jones** 1976, offers a systematic process for scaling analysis. The H2TS process is a hierarchical scaling method. Initially, the system is broken down into subunits like subsystems, geometries, and processes. Subsequently, the appropriate scaling level for each phenomenon is determined.

It employs top-down (T-D) analysis to derive time ratios from conservation equations of mass, energy, and momentum, while bottom-up (B-U) analysis is used for specific phenomena. The goal is to develop time ratios for transfer processes of interest and to establish similarity criteria by matching time ratios between the scaled facility and the project scale (**Frepoli** 2019). Any potential deviations are assessed for their significance, and if necessary, adjustments are made to the physical geometry, fluid properties, and operating conditions of the model (**Muñoz-Cobo et al.** 2018).

Notably, this method was employed for AP600 and AP1000 design certification, and its relevance persists, as evidenced by its recent use in the NuScale Integral System Test NIST-1 facility (**Houser et al.** 2013). Through these years, H2TS has been applied to the design of several integral system test facilities, including the APEX (**Vertes** 1989) and the MASLWR test facility (**Modro** 2002), among others. It can also be beneficial for the scaling analysis of SET facilities.

Fractional Scaling Analysis (FSA) Method

The Fractional Scaling Analysis (FSA) methodology, formalized by **Zuber et al.** 2007, is an evolution of the H2TS approach. It reduces the eight hierarchical levels of H2TS to three: System, Components, and Processes. FSA simplifies analysis through the concepts of the fractional rate of change (FRC) and the agents of change (AOC). It allows for scaling time-dependent processes in complex, interacting systems, an essential characteristic for simulating intricate accident scenarios. Additionally, FSA can analyze directly at the chosen hierarchical level given necessary initial conditions, boundary conditions, and data **Dzodzo** 2016.

FSA can be applied at any level in the hierarchical system, following the principles of H2TS. It uses AOC, FRC, and effect metrics to provide a simplified approach to system analysis. The conservation equations are made dimensionless with reference values of state variables and processes that form the AOC. The resultant "process time" characterizes the change in a quantity of interest by a specific AOC, providing a metric of its partial effect on the state variable (FRC). Similarity criteria are derived by comparing individual process effect metrics and identifying distortions in crucial processes (**Muñoz-Cobo et al.** 2018).

A variation of FSA, known as Relative Scaling Analysis (RSA), was proposed for CANDU application (**Wan** 2007). More recently, FSA has been used for systems with interacting components during complex transient accident scenarios, as seen between IRIS and SPES3 (**Dzodzo et al.** 2019).

2.1.2.2. Dynamic System Scaling (DSS) method

The recently developed Dynamical System Scaling (DSS) approach evolves from H2TS and FSA methods, aiming to integrate the dynamic response of a system into the scaling framework. This method is based on the invariance principle of the process metric under affine coordinate transformation, enabling the quantification of time-dependent distortions (**Reyes et al.** 2015).

DSS has facilitated the first analysis of scaling distortions, leading to the identification of refined similarity criteria for design choices (**Yurko et al.** 2015). For fluctuating key parameters, such as gravity-driven draining systems, DSS introduces the identity transformation method to evaluate time-dependent scaling distortion (**Li et al.** 2017**;** 2018). It has also been utilized for scaling analysis in single-phase integral test facilities, deriving similarity laws at various levels (**Liu et al.** 2022).

A significant advantage of DSS is its ability to devise a sophisticated similarity method that uses dynamic response instead of pre-established reference values. Unlike traditional H2TS method, DSS views physical processes as geometric objects in a normalized coordinate system, permitting a quantitative comparison of time-dependent distortion between prototype and scaled model processes (**Frepoli et al.** 2015).

In thermal hydraulic experiments, similarity between a model and a prototype manifests in as overlapping or parallel phase curves in phase space throughout the transient period. Deviations in these phase curves allow quantification of scaling distortion, enabling detection of distortion at any point during the transient.

Table 2.1. – Comparison of parameters for H2TS, FSA and DSS scaling method

Parameter	**H2TS**	**FSA**	**DSS**
Reference time	t	t	t
Conserved quantity	Ψ	Ψ	$\Phi = \beta \Psi_0$
AOC	φ_i	φ_i	φ_i
Sum of AOC	$\sum_{i=1}^{n} \varphi_i$	$\varphi_e = \sum_{i=1}^{n} \varphi_i$	$\Psi_0 \omega = \sum_{i=1}^{n} \varphi_i$
Normalized AOC	$\varphi_i^+ = \frac{\varphi_i}{\varphi_{i,0}}$	$\varphi_i^* = \frac{\varphi_i}{\lvert\varphi_{e,0}\rvert}$	–
Normalized sum of AOC	$\frac{\varphi_{i,0}}{\Psi_0} \sum_{i=1}^{n} \varphi_i^+$	$\frac{\lvert\varphi_{e,0}\rvert}{\Psi_0} \sum_{i=1}^{n} \varphi_i^* = \frac{\lvert\varphi_{e,0}\rvert}{\Psi_0} \varphi_e^*$	ω
FRC of i-th AOC $\omega_{\mathbf{FRC,i,0}}$	$\frac{\varphi_{i,0}}{\Psi_0}$	$\frac{\varphi_{i,0}}{\Psi_0}$	–
Effective FRC $\omega_{\mathbf{FRC,e,0}}$	$\sum_{i=1}^{n} \frac{\varphi_{i,0}}{\Psi_0}$	$\frac{\varphi_{e,0}}{\Psi_0}$ or $\frac{\lvert\varphi_{e,0}\rvert}{\Psi_0}$	$\sim \frac{1}{\tau}$
$\mathrm{d}\Psi^+/\mathrm{dt}$	$\sum_{i=1}^{n} \omega_{FRC,i,0} \varphi_i^+$	$\lvert\omega_{FRC,e,0}\rvert \varphi_e^+$	ω
Normalized time	$t^+ = \omega_{FRC,max} t$	$\Omega_{FSA,e} = \lvert\omega_{FRC,e,0}\rvert t$	$\widetilde{t} = \frac{t}{\tau_s}$
Formalism	$\frac{\mathrm{d}\Psi^+}{\mathrm{d}t} =$ $\varphi_{i,max}^+ + \sum_{i=1}^{n} \frac{\omega_{FRC,i,0}}{\omega_{FRC,max}} \varphi_i^+$	$\frac{\mathrm{d}\Psi^+}{\mathrm{d}\Omega_{FSA,e}} = \varphi_e^+$	$\frac{\mathrm{d}\beta}{\mathrm{d}\widetilde{t}} = \tau_s \omega = \widetilde{\Omega}$
Distortion factor DF	$1 - \Pi_{i,R} = 1 - \frac{(\omega_{FRC,i})_R}{(\omega_{FRC,max})_R}$ $= 1 - \frac{(\omega_{FRC,i}/\omega_{FRC,max})_M}{(\omega_{FRC,i}/\omega_{FRC,max})_P}$	$1 - (\Omega_{FSA,e})_R =$ $1 - \frac{(\Omega_{FSA,e})_M}{(\Omega_{FSA,e})_P}$	$\eta_\chi(\widetilde{t}) =$ $\sqrt{1 + \widetilde{t}^2} \left(\widetilde{\Omega}_P - \frac{\widetilde{\Omega}_M}{\lambda_A}\right)$

2.1.2.3. H2TS, FSA and DSS comparison

Among H2TS, FSA, and DSS, two main differences should be highlighted:

- DSS implements the rules of geometric similarity to establish process similarity. Technically based on specific transformations, the DSS method can be transformed into five different scaling methods, including the widely used power-to-volume scaling. This unique property is not shared by H2TS or FSA.
- The scaling distortions in FSA and H2TS are static. The distortion at different times of a transient can only be approximated by computing the dimensionless parameters from data evaluated at various transient snapshots. Each snapshot would have a unique normalizing factor, such as the reference value for state of variable, and thus, it is not straightforward to compare different snapshots or to integrate the distortion over time. Conversely, DSS calculates the scaling distortion as a function of dimensionless process time. This allows us to compare the trajectories of the prototype and the process curve of the test facility for the entire transient as a time-dependent quantity.

Consolidating the previous sections on the description of the three methods (H2TS, FSA & DSS), we can identify the internal and complex connections among them in Table 2.1. Here, the superscript "$+$" is used for the H2TS quantity; "$*$" for FSA; and "$\sim$" for DSS to distinguish these methods. For the details of parameters and equations, Appendix C.1 would be helpful. Meanwhile, based on the equations from **Reyes et al. 2015**, an example of natural circulation can be studied between H2TS and DSS. Specifically, the advantages of DSS are demonstrated in Appendix C.2.1 through a comparison of dimensionless numbers and relationships. Most importantly, different metric used in the distortion definition allows one to qualitatively and quantitatively compare the discrepancy between scales.

2.1.2.4. Scaling Studies for Nuclear Applications

Nuclear thermal hydraulics, which concentrates on fluid behavior and heat transfer in nuclear reactors and associated systems, plays a crucial role in reactor safety, design optimization, and performance evaluation. Recently, significant advancements have been made in confident scaling for predicting nuclear thermal hydraulics, driven by advancements in computational capabilities, experimental methodologies, and theoretical understanding. This introduction will look into these recent developments, highlighting the challenges and opportunities of scaling for nuclear thermal hydraulics prediction.

Experimental Studies

For the experimental advances, the scaling methodology provides a quantitative understanding of potential behavior differences between a reduced-size experimental facility and a full-scale commercial plant during a specific transient. Scaling is vital in designing and operating smaller facilities to simulate large commercial plant behavior, thereby enhancing safety systems and anticipating accidental sequences. Researchers adopt various scaling analyses for experimental facility design, with this section focusing on the prevalent scaling problem and the methodologies that strive to identify resultant errors and uncertainties in experimental data or designs.

According to **Bestion, D'Auria et al. 2017**, achieving complete similitude, particularly in complex nuclear reactor systems and two-phase flows, is unfeasible. Thus, prioritizing the similarity of the most crucial processes between the prototype and experiment is vital. For a well-scaled test facility, the following specific objectives were met for each operational mode of interest:

- Identifying the thermal-hydraulic processes to be modeled;
- Determining the similarity criteria to be maintained across different scales;
- Establishing priorities for preserving similarity criteria;
- Setting specifications for the test facility design;
- Quantifying biases due to scaling distortions.

The thermal similarity between a scaled-down test facility and its original model is crucial. Therefore, a robust scaling methodology must be developed and employed to ensure the thermal transport similarity between the model facility and its original, such that the behaviors of natural circulation in the original can be replicated in the model. However, scaled test facilities are often designed with differing sizes and operating pressures compared to their originals. Despite the possibility of adjusting a system's size, the original behaviors of heat and fluid flow processes can't always be preserved due to distortions. This is particularly pertinent in nuclear safety research. For example, the most common scale ratios—1/2, 1/3, and 1/4 for height—employ the Ishii scaling method as shown in Table 2.2. This illustrates the theoretical relationships of the main parameters under the conditions of original pressure and fluid properties for the designs and research.

For the applications in Integral Test Facility (ITF), as listed in Table 2.3, there are three types: Reduced-Height Reduced-Pressure (RHRP), Full-Height Reduced-Pressure (FHRP), and Full-Height and Full-Pressure (FHFP). For example of different types, there are AMCE (**2017**), APEX (**1998**), ATLAS (**2008**), BETHSY (**2017**), LOBI/LOFT (**1987**), LSTF (**2018**), NIST (**2019**), PKL (**2014**), PUMA (**1998; 2008**) and etc. To ensure good scalability, the optimal height scale is chosen (≥ 1/3) of the size of the prototype (**Levy 1999**), and the pressure scale depends on the experimental objective.

Theoretical advances in DSS

DSS uses the system first and second derivatives, combining these with the H2TS and FSA methods. This new way of assessing the scaling issue is different from traditional methods, which has led to a lot of new research. **Reyes 2015** showed that DSS is good at identifying effect parameters when they compared equations of single natural circulation with H2TS and FSA methods. Later, **Frepoli et al. 2015** used DSS to combine LOFT and Semiscale Large Break Loss Of Coolant Accident (LBLOCA) data, showing it's helpful in analyzing scale distortions.

Table 2.2. – Basic ratios of reduced scale model for Ishii scaling method.

Height/vertical lengths	Vertical diameter	Time	Velocity	Power	Volume	Flow areas	Horizontal diameter
1:2	1:3.943	1:1.414	1:1.414	1:21.93	1:31.01	1:15.5	1:3.439
1:3	1:5.61	1:1.732	1:1.732	1:54.33	1:94.1	1:31.37	1:4.942
1:4	1:7.19	1:2	1:2	1:96	1:192	1:48	1:6.2

Table 2.3. – Some Integral Test Facility and their scaling methodologies

Name	Country	Power/MW	Pressure/MPa	Scaling method	Scale factor volume	Scale factor Height	Prototype/Power
AMCE	China/SNPTC	3	9.2	H2TS	1:94	1:3	CAP1400/AP1000
APEX	USA/OSU	1	2.55	H2TS	1:192	1:4	AP600/AP1000
ATLAS	Korea	-	17.5	Ishii	1:288	1:2	APR1400
BETHSY	France/CEA	2.86	15.5	P-V	1:100	1:1	Framatome PWR 2775
LOBI	EC-JRC/Ispra	5.28	15.7	P-V	1:700	1:1	KWU PWR 1300
LOFT	USA/INEL	50	2.4	P-V	1:60	1:2	Trojan PWR 3000
LSTF	Japon/JAERI	10	15.5	P-V	1:48	1:1	Westinghouse PWR 3423
MIST	USA	0.33	15.5	P-V	1:817	1:1	B&W 177-FA 2700
NIST	NuScale/USA	0.406	8.3	H2TS/DSS	1:227.5	1:3.3	NuScale SMR
PANDA	Switzerland/PSI	1.5	1	P-V	1:40	1:1	ESBWR SWR1000
PKL III	Germany/FRA	2.512	4.5	P-V	1:145	1:1	KWU PWR 3765
PUMA	USA	0.2	1.034	Ishii	1:580	1:4	GE-SBWR
SPES	Italy/SIET	6.49	15.5	P-V	1:427	1:1	Westinghouse PWR 2775

On the one hand, DSS has been helpful in relatively simple scaling scenarios. **Yurko et al.** 2015 showed that DSS could help identify design choices during a gas blowdown transient. In a similar way, **Li et al.** 2018 showed that DSS could effectively scale a gravity-driven draining process when used with identity transformation. On the other hand, DSS can also be used for more complex situations, like single-phase natural circulation. For instance, **Li et al.** 2018 used DSS and H2TS to analyze this circulation in a simple rectangular loop, finding main parameter ratios to guide reduced model design. DSS isn't just used for analyzing data, but also for combining data, comparing changes across different datasets. An example of this is a study by **Heagy et al.** 2019, which highlighted differences between facilities and also identified the applied model errors.

In another study, **Reyes** 2020 used DSS to explain the physical meaning of the temporal displacement rate in scaling bubble dynamics processes. Using DSS into data processing systems has also been successful. **Yoshiura et al.** 2021 programmed the DSS data processing algorithm into the RAVEN system, successfully processing data from a gravity-driven draining tank modeled in RELAP5-3D. Moreover, current research by **Duenas et al.** 2022 uses DSS to compare nuclear fuel gap conductance models.

Despite all these advancements, there's still a pending question: Can the five transformations of the DSS method be used for ITFs design? This issue is being looked at through the design and analysis of a simple prototype involving single-phase natural circulation loop (SPNCL), a common thing in nuclear reactors. The use of ideal scaled models, if possible, which meet similarity requirements and simplify structures, is seen as a possible way to validate the similarity design of the reduced-scale model (**Liu et al.** 2020).

2.1.3. Identification of Scaling Uncertainties

2.1.3.1. Scaling Process inside the BEPU Methodology

Uncertainties fall into three main categories: aleatory uncertainties, epistemic uncertainties, and numerical uncertainties (**Roy and Oberkampf** 2011). The BEPU approach primarily handles aleatory uncertainties. It begins with input uncertainty quantification, followed by uncertainty propagation calculations and sensitivity analyses.

Input uncertainty quantification is crucial before conducting uncertainty propagation calculations. Sources of input uncertainty include boundary/initial conditions (e.g., initial power, containment pressure), material properties (e.g., fuel thermal conductivity), and constitutive models (physical models, closure models, or code structures), among others. For example, the BEPU methodology application process entails the following steps (summarized in Figure 2.1).

For the regulatory purposes, two primary uncertainty analysis trends have emerged within the BEPU framework: 'input-driven' and 'output-driven' methodologies (**Pourgol-Mohammad** 2009). Key characteristics of the Uncertainty Quantification (UQ) method-

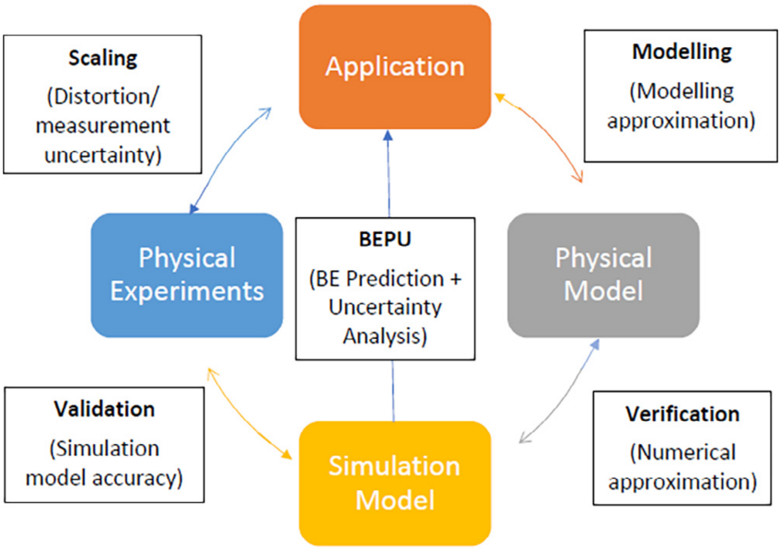

Figure 2.1. – Verification and validation process coupled with BEPU methodology (**Zhang** 2019).

ologies are enumerated in Table 2.4 (**Bestion et al.** 2016). Notably, the propagation process, or the convolution of uncertainties, can be performed in two primary ways as shown in Figure 2.2. In input-driven methods, the perturbations of uncertainty sources in inputs are propagated through code model inaccuracies, resulting in the range/distribution of the Figure of Merit (FoM). In output-driven methods, inaccuracies of calculations are characterized by comparing measured and calculated output in scaled-down facilities to obtain the uncertainty range in the actual nuclear facility by extrapolation.

Table 2.4. – Main characteristics of uncertainty quantification methodologies (**Bestion et al.** 2016).

Basic methodology	Extrapolation method	Propagation method	Combined propagation & extrapolation
Methods	UMAE-CIAU	MC or deterministic sampling/Meta models	CSAU, Use of meta models or not
SETs number	Must use many	Can use many	Can use many
IETs number	Must use many	No	Must use few
Reactor calculation number	1 (but low maturity)	>100/Cardinality number(meta-model)	Several (in between)

Uncertainty Propagation Based Approach: CSAU

The Code Scaling Applicability and Uncertainty (CSAU) methodology, as proposed by **Boyack** 1989 and widely applied in nuclear (**Muñoz-Cobo et al.** 2014**; Zhao and Mousseau** 2012), consists of three main components:

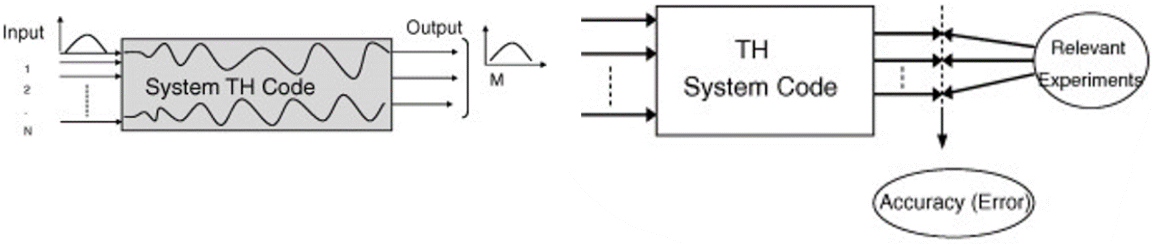

(a) Input-based UQ (b) Output-based UQ

Figure 2.2. – A schematic illustration of input/output-based uncertainty analysis methodologies (**Pourgol-Mohammad 2009**).

1. Requirements and Capabilities (Steps 1-6): During this stage, the scenario modelling needs are identified and matched with the capabilities of the code. This comparison helps to determine the suitability of the code for the specific scenario and points out any potential restrictions;
2. Assessment and Parameter Ranging (Steps 7-10): This part involves comparing code capabilities with experimental data to determine the code accuracy and ability to scale-up;
3. Sensitivity and Uncertainty Analysis (Steps 11-14): The final stage identifies the impact of individual factors on total uncertainty and how this uncertainty extends throughout the transient.

Step 10 is of particular significance as it evaluates scale-up capabilities to assess the scale effect. This applies to both experimental data and SETs, allowing for bias and error specification. For experiments, the scaling distortion and applicable data range should first be determined. Similarly, for the SETs, especially with the system code, it is crucial to evaluate whether the closure relations cover the reactor's range of interest (**Zuber et al. 1990**).

For a more explicit application **(Boyack et al. 1989)**, it's also the early work of scaling uncertainties quantification. The mean bias values R_m and their standard deviation S_R were curve fitted with respect to the geometric scaling group (L/D). For two-phase choking flow, the bias values constitute the systematic modelling errors for the postulated break location and used as the break flow multipliers in TRAC, which are required input parameters. The standard deviations $(S_R)_{2_{\phi}}$ account for all the uncertainties other than geometric scale. They are used to determine the range of R_m-uncertainty in the statistical analysis of Peak Clad temperature uncertainty.

$$(R_m)_{2-\phi} = 0.778 \exp\left(0.679\left(\frac{L}{D}\right)^{-0.25}\right);$$

$$(S_R)_{2-\phi} = 2.027 \exp\left(-2.16\left(\frac{L}{D}\right)^{0.25}\right)$$

Accuracy Extrapolation-Based Approach: UMAE-CIAU

Fully consistent with CSAU method, the Uncertainty Methodology based on Accuracy Extrapolation (UMAE) does not center on propagating individual parameter uncertainties derived from SETs **(D'Auria et al. 1995)**. Instead, it emphasizes extrapolating errors to full-scale NPP from an extensive database of integral experiments. This database includes similar and counterpart tests. Tests performed in differently scaled facilities are considered similar when the sequences of events and relevant thermal-hydraulic aspects align qualitatively; counterpart tests are similar experiments with Boundary and Initial Conditions (BICs) defined based on suitable scaling factors.

The UMAE methodology has been automated with the Code with the CIAU procedure (**D'Auria and Giannotti 2000**) for a specific transient of interest. CIAU accomplishes a requirement from an international devoted 'Specialists' conference (OECD/NEA – USNRC) held in Annapolis in 1996. This is the need for internal assessment of uncertainty, or the association between the code-models and the error in output. Specifically, this method employs fast Fourier transforms (FFTs) to analyze discrepancies between measurements and calculations (**D'Auria et al. 1997, Proek and Leskovar 2011**). This involves accuracy quantification in the frequency domain, defining the FoM for each calculation's accuracy. Most importantly, in this approach, scaling analysis holds a critical role in two aspects. First, during the code assessment process, where code development and enhancement are grounded in experimental data gathered from scaled test facilities. Second, in demonstrating the qualification of a nuclear power plant's nodalisation, a step is required to perform reliable nuclear power plant calculations.

More specifically, following the UMAE methodology, the solution to the scaling issue involves a four-step strategy:

- Code Qualification: Qualify the code against experimental data gathered from ITFs and SETs;
- Code Accuracy Verification: Demonstrate that the discrepancy between the measured and calculated trends only relies on the BIC values within the assigned variation ranges. Ensure that the scale of the concerned ITF does not affect it;
- Phenomena Prediction: Use the qualified code to predict the same relevant phenomena expected to be observed in a similar experiment or transient performed at a different scale;
- NPP Kv-scaled Calculation: Conduct nuclear power plant Kv-scaled calculations and reconcile any discrepancies between these calculations and measured trends in ITF. These discrepancies should only be accounted for by BIC values and hardware differences, i.e., distortions.

2.1.3.2. Quantification of Modelling Uncertainties under Scaling

Sources of Modelling Uncertainties

With the identified uncertainties for code prediction by **Bestion et al. 2016**, under the chronological order, the modelling uncertainties could be mainly composed of these uncertainties encountered or addressed during the process of setting up, running, and analyzing a CFD simulation. These uncertainties, along with user effects generated during the quantification process, are shown in Figure 2.3:

- **Input Uncertainty**: As the input parameters for the model need to be first defined, This includes uncertainties related to the initial and boundary conditions and physical properties of the materials.
- **Geometric Uncertainty**: Once the problem is defined, uncertainties here arise due to simplifications or approximations in the geometry of the computational model.
- **Physical Modelling Uncertainties**: After setting the problem and creating the geometry, uncertainties can arise due to the parameters of these physical models or from the physical processes that are not modeled.
- **Numerical Uncertainties**: Once the physical models are selected, uncertainties here include those from the selection of numerical models and from numerical solution errors.
- **Chaotic Behaviour Uncertainty**: They arise from the inherent unpredictability and sensitivity to initial conditions in turbulent flows.
- **Validation Uncertainty**: Finally, once the simulations are complete and the results are being analyzed, these uncertainties are associated with extrapolation beyond the validation range of the model.

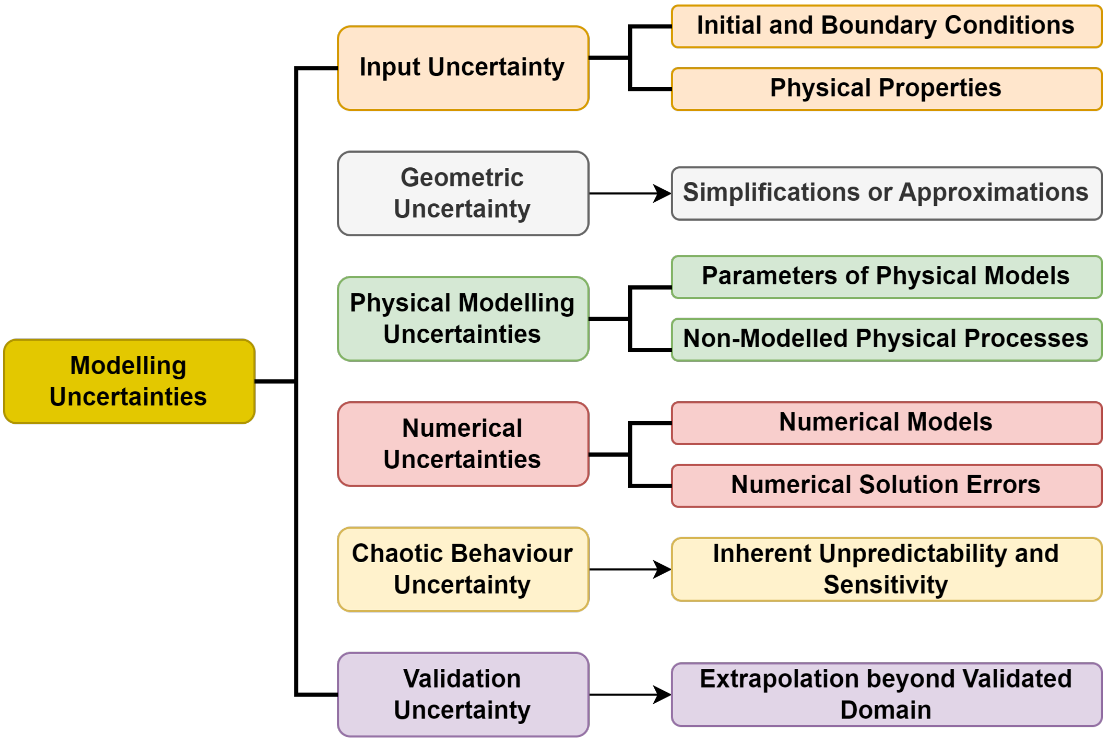

Figure 2.3. – Potential sources of modelling uncertainties for code prediction.

However, scaling uncertainty, sharing a similar nature with latest validation uncertainty, presents a significant challenge since the "real" quantity of interest at the reactor scale is unknown. Two strategies can be considered: the first relies only on code results to evaluate uncertainties, assuming that the variation between experimental and reactor scale code results reflects the "real" variation. Alternatively, conducting multiple experiments that vary scaling factors such as the Reynolds or Froude number can assist in defining a validation range for extrapolation or inclusion of the utilisation range. For a broader consideration, scaling uncertainty will be the next subject of discussion as the variation of modelling uncertainties under scale effect.

Modelling Uncertainties under Scale Effect

Shifting our focus to conceptual scaling uncertainty, we aim to define and construct this concept while setting aside the argument over whether scaling uncertainty should be nested within model uncertainty. Scaling uncertainties originate from the fact that experiments cannot feasibly reproduce the physics of safety transients without simplification (in terms of design and experimental conditions), while numerical tools cannot solve the exact equations. More specifically, **Bestion, D'Auria et al. 2017** present the origin of scaling uncertainty in the state-of-the-art report of OCED/NEA:

- Owing to the non-linearity and the broad spectrum of interacting scales in various reactor parts, not all similarities can be maintained in a scaled experiment;
- The conservation equations in reactor case calculation codes are space-time averaged and reliant on empirical correlations. This precludes them from being purely mechanistic and limits their upscaling ability. Moreover, a discretization scheme introduces error that may differ between the IETs and reactor case. Simulations may also exhibit compensating error effects that can hide model issues and may not behave conservatively during upscaling.

Thus, conceptual scaling uncertainty demands careful attention to both experimental data and prediction codes. For experimental data, such scaling uncertainty can be partly retraced by reviewing the applied scaling methodology from the design phase to the existing scaled facilities. For prediction codes, the scaling uncertainty might reemerge from the unexplored domain (dimension, physical property, input condition, model, etc.).

In order to treat both, based on the various available modelling scales from CFD local scale to sub-channel and system scale, **Bestion 2022** suggested the development of upscaling methods for modelling, and multiscale validation methods as depicted in Figure 2.4. In both scenarios, small-scale simulations supplement the experimental data for the development and validation of more macroscopic models, leveraging Separate SETs, Combined Effect Tests (CETs) and Integral Effect Tests (IETs). So that the numerical scale uncertainties can be identified and tackled more systematically.

Uncertainty Quantification for Code Qualification Including Scaling

Given the wide range of potential sources for scaling uncertainties, advanced quan-

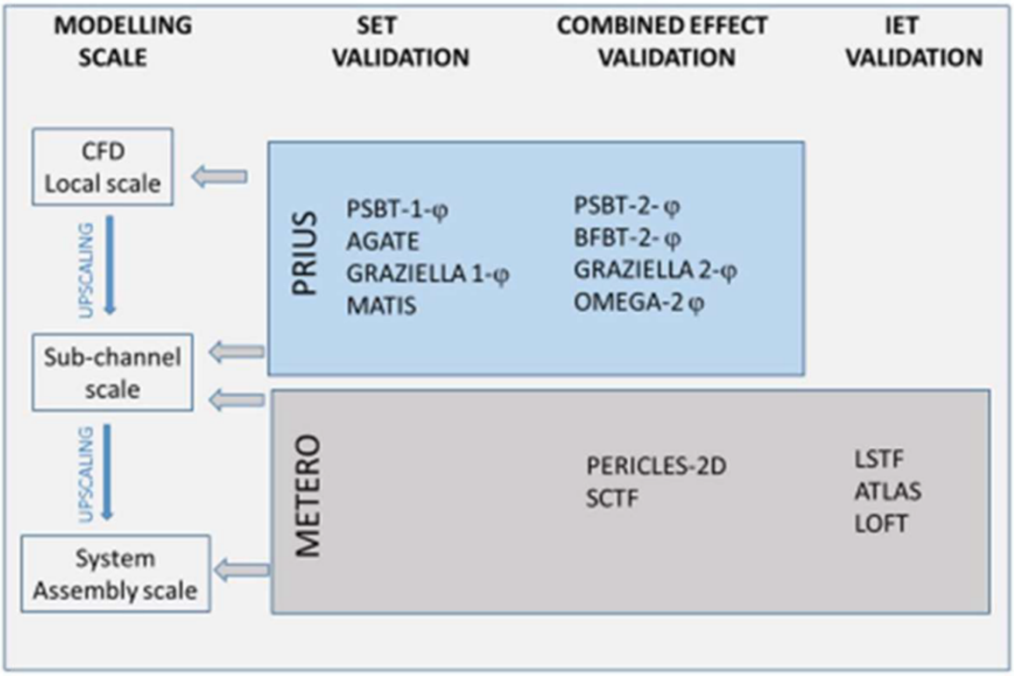

Figure 2.4. – The multiscale validation methods (**Bestion** 2022).

tification methods for scaling are needed. A better quantification of model uncertainties is proposed in the SAPIUM approach (**Baccou et al.** 2020). In this case, several steps of the BEPU may be revisited and updated including the Phenomenology Identification and Ranking Table (PIRT), the scaling analysis and the demonstration of code scalability. Like for system TH codes, model uncertainty quantification is also needed for application of the CFD tools (**Baccou et al.** 2022). For the scaling issues and predictive capability assessment, the author has commented that:

- Predictability in nuclear reactor uncertainty analyses heavily relies on accurate geometrical and thermal-hydraulic scaling due to the impact of scaling effects;
- Studies typically use small to medium-scale models, posing a challenge in upscaling to full-scale reactors, as findings from smaller scales may not fully apply to larger ones. Therefore, the identification and quantification of input uncertainties for large-scale applications is crucial;
- The consideration of scale-up effects is vital when creating input data sets and quantifying uncertain input parameters. In some cases, different correlations for the thermal-hydraulic code physical model are selected based on the field of application to account for scale differences;
- A key part of addressing scale-up effects in uncertainty analyses is the modification of ranges of physical model uncertainties, which necessitates the selection of appropriate experiments representing the application and the facility scale.

In cases where suitable experiments are unavailable, CFD simulations have emerged as an alternative for system code model evaluation. However, this approach requires a comprehensive VVUQ analysis of the CFD Simulation Model. For the development and application of model uncertainty quantification and calibration methods, **Baccou et al.** categorize various frameworks such as data assimilation, frequentist and Bayesian methods, and methods based on forward propagation and DoEs.

Specifically, forward uncertainty propagation of input uncertainties can be used when a physical parameter is independently known, or can be estimated, and was addressed in several previous NEA projects: the Uncertainty Methods Study (UMS) (**Glaeser et al. 2008**), Best-Estimate Methods Uncertainty and Sensitivity Evaluation (BEMUSE) (**de Crecy et al. 2008**), Post-BEMUSE Reflood Models Input Uncertainty Methods (PREMIUM) benchmark (**OECD/NEA 2017**) and currently Systematic Approach for Input Uncertainty quantification Methodology (SAPIUM) (**Baccou et al. 2020**). While the associated output UQ methods have now been widely used for industrial applications. This will also be explored and applied in section 4.1 and section 5.1.

Finally, the safe operation of nuclear reactors largely relies on precise extrapolation to full-scale applications. To ensure the reliability of the safety analysis in the face of uncertainty about scaling to full-scale nuclear power plant applications, safety margins are applied as a precautionary measure.

2.2. State-of-the-Art on Natural Circulation Loops (NCLs)

2.2.1. NCLs Physical Behaviors

Single-phase natural circulation loops (NCL) exhibit intriguing physical behaviors driven by buoyancy forces induced by temperature differences. These loops, without external pumping devices, rely on fluid dynamics and heat transfer phenomena. Key behaviors include the formation of stable convection currents, where heated fluid rises and cooler fluid descends, establishing a continuous circulation. Factors like loop geometry, fluid properties, and heat source characteristics impact flow patterns and heat transfer rates. Understanding these behaviors is vital for optimizing NCL systems in various applications, including nuclear reactors, geothermal energy, and thermal management. Further exploration of theoretical foundations, mathematical models, and experiments can enhance our understanding of NCLs leading to improvements in their design and implementation.

Single-phase natural circulation (NC) flow is governed by several parameters, grouped into three categories:

1. **Operating Conditions**: Under the operator's control, these parameters include heater power, system pressure, cooler secondary flow-rate, and its inlet temperature in a closed loop (**Vijayan et al. 2002**);
2. **Geometric Parameters**: Significant loop geometric factors including diameter and length of different pipe sections, heat source and heat sink length, orientation, and the elevation difference between sink and source. Also, local pressure

loss coefficients impact the steady-state flow-rate (**Vijayan et al.** 2019);

3. **Fluid Properties**: Properties such as density, dynamic viscosity, thermal expansion coefficient, specific heat and thermal conductivity affect the steady-state performance of single-phase natural circulation loops (**Çobanoglu and Karadeniz** 2020).

Various advanced reactor designs also examine different simulated coolants other than water. Molten salt and liquid metals, interesting to nuclear reactor systems, can have their natural circulation performance compared to water. Specifically, in SPNCL systems employing low Prandtl number fluids like sodium, several remarkable physical behaviors arise:

— **Enhanced Heat Transfer and Thermal Plumes**: Fluids like sodium, with low Prandtl numbers and high thermal conductivities, enhance heat transfer rates within SPNCLs, allowing for efficient thermal energy dissipation. While, thermal plumes are a key phenomenon in low Prandtl number flows like sodium. It means that the heat diffuses quickly compared to the velocity (momentum). This causes hot areas to generate buoyant forces, resulting in vertical fluid movement and creation of thermal plumes. An increase in Reynolds numbers (Re_t) suggests buoyancy adds to turbulence near the wall, an effect that diminishes with higher Prandtl numbers. This could be because buoyancy intensifies slow-speed vortices that are then confined by large-scale circulation caused by thermal plumes (**Guo and Prasser** 2021). In the PLANDTL-DHX test facility, thermal plume-induced mixing affects temperature profiles (**Nishimura et al.** 2000; **Gerschenfeld et al.** 2017);

— **Centrifugal Effects and Dean Vortices**: In the context of flow through elbows, centrifugal effects lead to the formation of secondary flow patterns, known as Dean vortices (**Röhrig et al.** 2015). These vortices, rotating in a plane perpendicular to the main flow direction, can significantly impact heat transfer and pressure drop characteristics downstream the elbow. Understanding and predicting these phenomena is crucial, particularly for complex systems with multiple bends and turns. Further research and reliable simulation tools are needed to predict these effects accurately in NCLs using low Prandtl number fluids like sodium;

— **Flow Stratification**: Fluids with low Prandtl numbers exhibit stronger buoyancy effects, leading to temperature and velocity stratification within the loop. This creates distinct layers with differing fluid properties. It's important to understand and characterize these stratified flows for optimal heat transfer and system performance. In the TALL-3D experiment, oscillations during transitions to natural convection were strongly affected by 3D phenomena occurring in the leg where stratification can block the flow (**Gerschenfeld et al.** 2017);

— **Nonlinear Flow Dynamics**: Sodium and other low Prandtl number fluids can exhibit complex and nonlinear flow dynamics. These dynamics, which can include flow reversals, oscillations, and instabilities, arise due to interactions among buoyancy forces, fluid viscosity, and heat transfer characteristics. Accurate analysis and modelling are necessary for stable and safe operation of SPNCL systems. For instance, numerical and experimental results for the EXOCET facility at CEA demonstrated the CATHARE code's ability to quantitatively predict flow reversals in natural circulation loops (**Vaux et Grosjean** 2022). However, with system codes, to study the time frequency of flow reversals or the geometry of the heated section remain challenging.

Understanding these physical behaviors forms the foundation for identifying and quantifying scaling effects. The study and understanding of low Prandtl number flow behaviors in SPNCL, especially with sodium, are crucial in designing and operating efficient and reliable systems. Accurate modelling and simulation of heat transfer rates, temperature distributions, and flow dynamics are key for optimizing system performance, identifying and quantifying scaling effects, and ensuring SPNCL's safety and longevity.

2.2.2. Experimental and Numerical studies

2.2.2.1. Natural Circulation Loop (NCL)

As we know, the stability is a key issue in operation of NCL for both single-phase and two-phase flows. For natural circulation in an inverted U-tube steam generator, flow reversal was found that the flow in the parallel U-tubes can be unstable (**De Santi et al.** 1986). As reported by **Vijayan** 2002, instabilities were observed only in the HHHC configuration, and all the other configurations experimented were found to be stable. The boundary of loop stability is strongly influenced by the choice of the constitutive law for the friction factor. Different sizes of HHHC loops have been established and studied using both experimental and simulation methods to reveal the dynamic mechanism of such phenomena.

With the advancement in computational power, DNS has become a feasible tool for certain applications. **Noorani et al.** 2013 performed DNS simulations of turbulent flow in curved pipes. The study predicted the dependence of turbulent pipe flow on curvature at two Reynolds numbers. It was shown that for the highest Re and curvature, the relaminarization (return to laminar flow (**Gomez et al.** 2021)) occurred near the inner wall. The study provided the full Reynolds-stress budget, which could be used to improve the predictions of eddy-viscosity models.

Due to the strong dependence of the flow field on operating conditions and intense interaction between buoyancy and frictional forces, NCLs are always susceptible to flow oscillations. Different modes of flow instability have been observed for almost all configurations, along with periodic flow reversals, flow bifurcation and even chaotic oscillations (**Basu et al.** 2014). The studies here highlight the changes in the mean flow due to centrifugal forces in the elbows, which directly affect the pressure loss. Notable work was carried out by Dean (**Dean and Hurst** 1959).

By employing 3D CFD simulation, **Kudariyawar et al.** 2016 investigated both the steady-state and transient-state characteristics of rectangular NCLs with different configurations, where the generation of unidirectional and bidirectional pulsing in

HHHC configuration at different powers was clarified with the temperature fields at different instants.

2.2.2.2. Natural Circulation System under Scaling

Research in recent decades extensively used natural circulation scaling modelling in nuclear power plant phenomena analysis and experimental facilities design. **Heisler** 1982 led the investigation into natural circulation phenomena for heat removal during the liquid metal fast neutron breeder reactor shutdown phase. The findings suggested the ideal fluid for experimental setups should mimic sodium and NaK, as the prototype fluid. Using water as the fluid was found unacceptable due to distortion.

Table 2.5. – Summary of literature review on NCL with scaling for experimental and numerical studies.

Reference	**Method**	**Objectives: Natural Circulation Loop**
Dean and Hurst 1959	Analysis & Exp	Centrifugal effects in elbows
Vijayan 2002	Exp & Simu	Instability influenced by friction term
Noorani et al. 2013	Simu DNS	Turbulent flow in curved pipes with relaminarization
Basu et al. 2014	Analysis & Simu 1-D codes	Instabilities: Flow reversal, bifurcation, chaotic oscillation
Kudariyawar et al. 2016	Simu 3D CFD	Bifurcation of HHHC at different power levels
Reference	**Method**	**Objectives: NCL under scaling**
Heisler 1982	Model analysis	Scaling of physical properties
Ishii et al. 1983	Model analysis	Geometry similarity for reduced-scale models using dimensionless equations
Schwartzbeck et al. 1989	Model analysis	Similarity requirements for different flows
D'Auria et al. 1991	Model analysis	Combining ITF and plant size data for NC
Vijayan and Austregesilo 1994	Exp & scaling analysis	Same height but different diameter with respect to certain correlations
Reyes 1994	NC scaling	Component and system level analysis: physical property leading to primary disparity in similarity; friction is manageable
Muñoz-Cobo et al. 2018	Top-down scaling	H2TS NC system phase
Liu et al. 2020	Model analysis	NC for liquid metal and molten salts

Ishii et al. 1983; 1984; 1998 provide benchmark work in natural circulation scaling modelling. Their model analysis is based on mass, overall momentum, energy, and solid energy balance equations for the single-phase fluid and two-phase mixture in the loop. By formulating dimensionless equations using steady-state parameters, they found that the modified Stanton number and Biot number influence the heating zone boundary layer temperature but do not significantly affect overall flow and energy distribution. Thus, not retaining these dimensionless numbers during slow transients causes no substantial distortions. Their method suggests that the experimental setup design doesn't require identical geometry and resistance across all sections; the entire loop needs to satisfy these parameters. The resistance number matching upper limit lies in the heat pipe section, so an area ratio is obtained for a given volume ratio through that section resistance match.

D'Auria et al. 1991 conducted modelling analysis of natural circulation phenomena at different stages in PWR systems. They extended the experimental data of ITFs combined with RELAP5 program calculations to real power plant phenomena. **vijayan and Austregesilo** 1994 carried out a scaling analysis of single-phase natural circulation and designed three model devices with the same height but different diameters. Both theoretical and experimental results suggested that for steady-state behavior, the model needs to maintain only the $Gr(D/L)$ number. For transient behavior, retention of the Gr number, the aspect ratio D/L, and the Stanton number is crucial.

Reyes 1994 made significant progress in natural circulation scaling. Component level conservation equations for both two-phase mixture and the solid domain were identified, forming a dimensionless number group. At the system level, the flow-rate of the natural circulation loop can be written with parameters from the reduced scale model using steady-state equations of momentum and energy conservation. The primary disparity in the similarity requirements for power, velocity, and residence time in natural circulation lies in the physical properties, leading to potential distortions. Reyes also noted that local resistance primarily provides the resistance in natural circulation. This can be managed with appropriate resistance parts and model structure design to achieve resistance similarity.

Muñoz-Cobo et al. 2018 utilized the top-down scaling step from the H2TS scaling methodology to establish a comparison between the LSTF facility and a-KWU type reactor in the ROSA 1.2 test. They paid particular attention to the momentum conservation equation during the natural circulation phase. This detailed examination allowed them to consider regions of the SPNCL as well as those with two-phase flow. Lastly, their scaling analysis demonstrated good scalability between the two facilities, as evidenced by the near-unit ratios of the non-dimensional π-monomial groups.

Natural circulation, a system-level phenomenon, can be affected by local phenomena. **Schwartzbeck et al.** 1989 discussed the similarity requirements of different flows in horizontal and vertical tubes, based on the Ishii similarity requirements. **Yu et al.** 2017 focused on the heat transfer modelling issue in single-phase natural circulation, deriving three modelling criteria for heat transfer similarity in heat exchangers. To achieve accurate heat transfer similarity, the pipe diameter should be proportionally reduced to its length.

Studies on natural circulation scaling modelling have been conducted for other types of reactors, including high temperature gas-cooled reactors. In these, the continuity equation includes a diffusion term, while the momentum equation is similar to those in light water reactors (**Reyes et al. 2010**). Research on natural circulation in liquid metal or molten salt results in similar criteria using dimensionless analysis of control equations (**Grewal and Gluekler 1982; Liu et al. 2020**).

In summary, as listed in Table 2.5, previous studies have conducted scaling analysis of natural circulation in single-phase water, two-phase water, liquid metal, and gas. These scaling analyses are based on the mass, momentum, and energy equations of natural circulation in a one-dimensional loop, with dimensionless analysis producing characteristic numbers. It's essential to identify characteristic numbers of locally important thermal hydraulic phenomena being modelled, such as flow regime, resistance, and heat transfer. The modelling process involves controlling both the model and the prototype by ensuring equality in their characteristic numbers.

2.2.3. High-Fidelity Simulation of NCLs

2.2.3.1. Numerical Simulations of Different Fidelity Level

By revising the ECCS licensing rules in 1989, **USNRC 1989** allowed the use of Best-Estimate (BES) thermal–hydraulics computer codes (such as CATHARE2, RELAP5, TRAC, and TRACE), with the requirement that uncertainty analysis accompany the results. Several methodologies, especially the ones shown in section 2.1.3.1, have been developed for the quantification of the uncertainties of such codes.

To relocate the position of BES among different fidelity levels over the years of development, a classification of modelling and simulation vocabulary and designations recently established by the OCDE/EGMPEBV is presented in Table 2.6 (**Le Pallec J. C. et al. under review**). High-fidelity levels implement microscopic models, whereas simulator levels use macroscopic models. The transition from the high-fidelity level to the simulator level involves identifying the most influential physical phenomena (PIRT analysis, sensitivity analysis) followed by simplification of these models (possibly through the use of surrogate models). The more comprehensive and expensive modelling levels, namely High Fidelity (HF) and Best-effort (BEF), can serve two purposes. First, they can be used to verify the accuracy of less detailed (macroscopic) levels. Second, they can aid in improving these less detailed levels by applying a process known as upscaling. To have a connection with currently recognized/agreed international documents, the terms - higher/lower fidelity simulations - will be used until the previous glossaries are commonly accepted.

These terms correspond to different levels of accuracy and complexity of simulation methods or models for nuclear applications. Hence, shown in Figure 2.5, the bias in modelling and the error in calculations tend to increase with lower fidelity simulations. For instance, higher-fidelity simulations using CFD code can capture complex phenomena such as turbulence, multiphase flows, conjugate heat transfers, etc. that are difficult or impossible to quantitatively evaluate with simpler methods. At the same time, we should distinguish the difference between a best-estimate simulation and method; the latter has been growing over years under the framework of BEPU.

Table 2.6. – Fidelity levels of numerical simulations (**CEA/IRESNE** 2022a).

Fidelity level	**Simulation**	**Modelling level for physical phenomena considered**
Simulator	Training simulators, real-time simulators, parametric studies, optimal solution finding	Simplified modelling using physical or surrogate models, ideal for fast computations
Best-Estimate (BES)	Routine/Industrial Calculations for day-to-day operations and process optimizations	Hierarchized modelling via PIRT analysis, balancing computational efficiency and accuracy
Best-Effort (BEF)	R&D calculations for deep understanding, bias quantification in BE	Equal-level modelling across all physics for comprehensive predictions
High-Fidelity (HF)	Reference calculations for in-depth analysis, future applications	Exhaustive modelling, capturing all phenomena with the highest level of detail for each physics

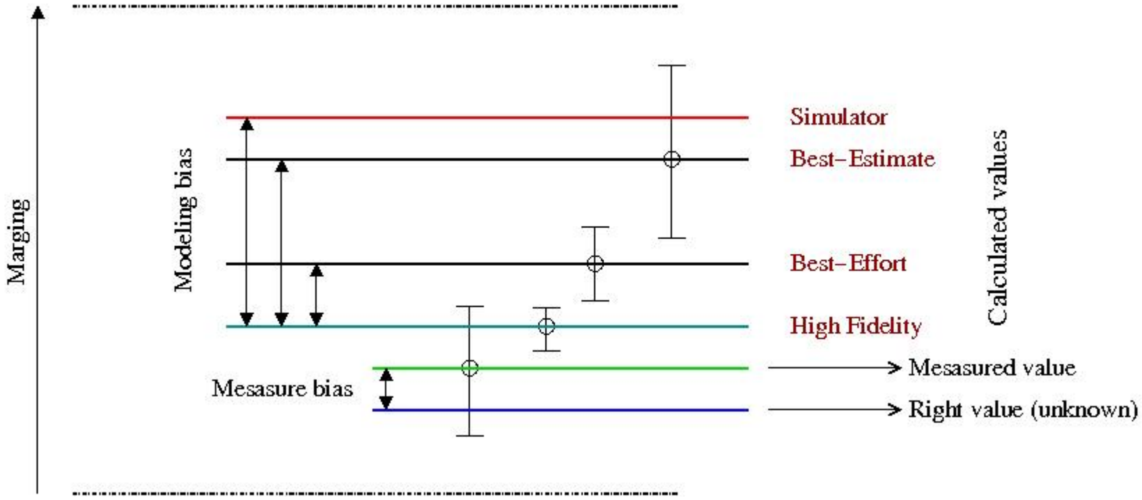

Figure 2.5. – Ranges of modelling bias and calculation errors for numerical simulations with different fidelity levels (**Le Pallec J. C. et al.** under review).

2.2.3.2. Scientific Computing Tools (SCTs) for VVUQ

In the context of Verification, Validation, and Uncertainty Quantification (VVUQ), the validation phase needs SET for individual phenomena and IET for combined phenomena. When experiments are not feasible, numerical benchmarking offers a viable alternative. This method is evident in code-to-code validation, where HF simulations are typically contrasted with a presumed lower-fidelity System Code.

The phenomenon of natural convection under investigation exhibits certain peripheral effects, including flow reversal, which may lead to overheating. Analysis on a downscaled model, initially established through scaling-down techniques, will be performed within the VVUQ framework. Prior to embarking on a scaled-down analysis, it's important to identify potential full-scale data. As an example, in Figure 2.6, invaluable data from the PHENIX tests (**Gauthe 2009**) can serve as a robust basis for the newly implemented MATHYS multiscale SCT (encompassing CATHARE, TrioMC, and TrioCFD). It's essential to bear in mind that CFD calls for particular considerations when it's employed in place of system codes. Examination reveals that while three-dimensional effects in the plena do not substantially alter the overall behavior of the primary circuits, local phenomena (such as the evolution of the IHX outlet jet) influence experimental measurements. These effects are precisely accounted for by the CFD portion of the coupled calculation (**Gerschenfeld et al. 2017**). Consequently, simulations on various scale levels using SCTs, which are capable of providing optimal solutions, must be scrutinized within the VVUQ framework. Following this, comparisons across different scale levels can be performed to quantify the scale effect using validated results.

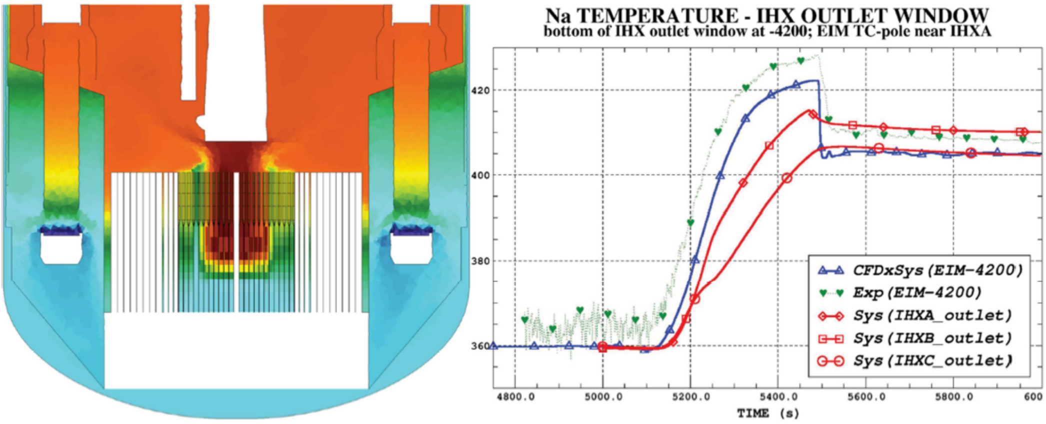

Figure 2.6. – Coupled models of the PHENIX reactor: (left) MATHYS model using CATHARE/TrioMC/TrioCFD; (right) for the natural convection test, comparison of simulation and experiments (**Gerschenfeld et al. 2017**).

To accurately simulate and forecast natural circulation in nuclear passive systems, sophisticated numerical models and computational tools are necessary. These tools can be grouped into three primary categories: system codes, sub-channel codes, and CFD codes.

- **System codes** like CATHARE2 (**Alpy et al. 2016**), RELAP5 (**Bovalini and D'Auria 1993**) and TRACE (**Julbe, Muñoz-Cobo et al. 2012**) provide a complete representation of the reactor coolant system, component by component, simulating its thermal-hydraulic behavior. However, due to their reliance on simplified models and assumptions and 0D-1D discretizations , they may have limitations in accurately predicting complex natural circulation phenomena;
- **Subchannel codes**, such as COBRA-TF (**Kelly et al. 1982**), FLICA4 (**Toumi et al. 2000**) and SUBCHANFLOW (**Imke et al. 2012**), are used for detailed analysis of flow and heat transfer in fuel assemblies or other reactor core components.

While more accurate than system codes, they still have limitations like the necessity for fine meshing and inability to capture certain complex phenomena like turbulence and three-dimensional flow patterns;

— **CFD codes**, including NEPTUNE_CFD (**Guelfi et al. 2007; Pérez Mañes et al. 2014**) , STAR-CCM+ (**Marfaing et al. 2018**) and TrioCFD (**Angeli et al. 2015**) offer a more accurate representation of fluid flow and heat transfer phenomena. Despite their advantages, applying CFD codes in nuclear passive systems has challenges such as high computational demands and the need for rigorous validation against experimental data.

System codes as SCT

System codes, as SCTs, are commonly employed to evaluate experimental data and aid in the application of scaling techniques. Transients are generally broken down into phases, and distortion is evaluated for each phase under assumed Boundary BICs. The primary goal is to establish whether the scaled-down facility, which complies with the basic principles of scaling laws, would demonstrate similar system behavior to a specific transient projected to occur in the prototype (**Reyes and Hochreiter 1998**). A preliminary confirmation that key processes are identified and addressed in the scaled-down facility within the reactor response range can be achieved by comparing code calculations between the scaled-down facility and the prototype. This comparison could also assist in pinpointing the sources of scaling distortion in the test facility and managing its effects.

However, as highlighted by **Levin and McPherson 1995**, scoping calculations are often performed with code models that haven't been validated for use with the prototype or test facility. This could lead to fundamental errors and cast doubt on the use of non-validated codes for identifying BICs for experiments designed to evaluate the codes. To avoid this issue, it's advised to employ codes in a restrained manner during both scaling and design stages, concentrating only on evaluating aspects of the design.

In terms of upscaling capabilities, the viewpoint of CATHARE peer experts is noteworthy. A report of **Bestion, D'Auria et al. 2017** suggests that such codes, once validated on certain scaled SETs and IETs, could predict phenomena of interest at the reactor scale under specific conditions. An optimal list of requirements for code upscaling is proposed:

1. Validate models for dominant phenomena of interest using IET;
2. Predict the scale effect (or its absence) for several IETs at different scales;
3. Validate important phenomena at local/component scales against several SETs at different scales to demonstrate good up-scaling capability of closure laws;
4. Ensure that the closure law validation range covers the full prototypical thermal-hydraulic range of interest as extensively as possible.

Given that scaled IETs inevitably contain some scale distortions, the code should also be capable of accurately predicting distorted phenomena. This necessitates validation in dedicated SETs for the phenomena in both distorted geometry (as distorted as in the IETs) and non-distorted geometry (to cover the reactor case). In addition, the code prediction uncertainty should include the uncertainty due to BICs, material properties, physical models, and numerical errors. It should also estimate the uncertainty resulting from non-modeled phenomena or code distortions due to limitations of the physical model. These last statements can be exemplified for CFD as follows:

1. Uncertainties related to the parameters of physical models, such as parameters of turbulence models and wall functions, are sources of uncertainties. Since these parameters were derived from basic flow configurations and may be used beyond their domain of applicability, the uncertainty related to this extrapolation should be considered;
2. Uncertainties related to non-modeled physical processes or intrinsic limitations of the models should also be addressed. For instance, any eddy viscosity model, like κ-ϵ or κ-ω, can't predict non-isotropic turbulence. Uncertainties stemming from these limitations must be accounted for when assessing the overall predictive capability of the code.

CFD codes as SCT

Over the years, the surge in computational power has significantly enhanced the precision of physical descriptions in numerical simulations, enabling the reduction of conservationism. This advancement has paved the way for the development of high-fidelity multi-scale codes. These innovative codes, which emerged over the past decade, are being utilized for new nuclear projects. By combining 1D and 3D thermal hydraulics, these codes provide the capability to perform localized analyses on critical reactor areas (**Bestion and de Crecy**2016). This trend has further extended into the multiphysics domain with the integration of other codes within coupled platforms for the development of a digital reactor (**Vaglio-Gaudard et al.** 2023). In fact, CFD has been increasingly advocated for use in nuclear reactor safety studies, subject to certain requirements (**Bestion et al.** 2016).

However, the application of these codes is not without challenges. Expert-authored Best Practice Guidelines were developed for single-phase flow (**mahaffy et al.** 2007). Subsequently, a more comprehensive guide was introduced to address remaining complexities (**Mahaffy et al.** 2015). The reduction of conservationism with these codes inherently comes with a higher computational cost, necessitating the extension of uncertainty analyses.

This extension of uncertainty analyses is crucial to complement BE approach within a nuclear reactor licensing framework. Due to the CFD nature, which is more complex than the one of 1D codes, a fresh assessment of uncertainties is required (**Bestion and de Crecy**2016). This assessment provides an unique opportunity to evaluate code accuracy at varying numerical scales by comparing BE system codes with CFDs.

2.2.3.3. CFD Modelling Approaches for NCLs

CFD simulations have gained popularity in the analysis and design of NCLs in nuclear passive systems due to their ability to provide detailed insights into complex fluid flow and heat transfer phenomena. However, as described in Section 2.2.1, SPNCLs with sodium flow exhibit many physical behaviors that are challenging or impossible to simulate with system codes. Consequently, the presence of different flow regimes, flow reversal and laminar-to-turbulent transition mechanisms, radial temperature distribution and other 3D phenomena deserve to be analyzed with more advanced approaches like CFD.

Such review of the CFD approaches used in NCL simulations reveals a significant confidence issue on RANS models, such as $k-\varepsilon$ and $k-\omega$ (**Launder et Spalding** 1974**; Menter** 1994). These models, while commonly used for their computational efficiency and ability to provide mean velocity and temperature values, may not correctly represent transient and complex flow dynamics of NCL due to their time-averaged nature. Furthermore, the use of these RANS models can result in a damping effect, thereby skewing assessments of both asymptotic stability and system dynamics. The assumptions in these models, such as isotropic turbulent viscosity, proportional turbulent momentum and energy transfer, and near-wall scaling laws, may not hold up in natural circulation, thereby limiting their precision. This limitation is particularly apparent when dealing with local mixing and stratification phenomena.

To mitigate these limitations, modified versions of these models have been proposed, integrating Low Reynolds Number Models (LRNM) for more accurate near-wall predictions (**Launder et Sharma** 1974). However, even these models can fall short in capturing complex fluid dynamics, especially in the context of streamline curvature impacts on turbulence. For more precise and comprehensive flow dynamics representation, Reynolds Stress Models (RSM) are suggested (**Shih et al.** 1993). These models, despite being computationally more expensive, provide a more detailed turbulence description, thereby enabling better capture of the effects of streamline curvature on turbulence and offering a more reliable solution for complex flow simulations .

After examining the capabilities and limitations of RANS models, including standard models and more sophisticated ones, advanced models like LES can offer more detailed three-dimensional flow predictions. These models, despite requiring more computational resources, could account for different flow regimes, effectively covering turbulent regions and becoming negligible during re-laminarizations. The LES model employs the Wall Adapting Linear Eddy-viscosity (WALE) Sub-Grid Scale (SGS) model, which has shown superior performance compared to the standard Smagorinsky model (**nicoud and Ducros** 1999). The WALE model can operate in alternating laminar and turbulent flow regimes without excessive damping of turbulent structures, making it well-suited for predicting NCL behavior.

However, for larger scales such as the ITFs, CFD simulation, even for RANS $k-\varepsilon$, remains challenging. For example, in a preliminary analysis to understand the characteristics of the PLANDTL-2, **Ono et al.** 2020 established an appropriate CFD model for the numerical simulation to reproduce the natural circulation in the decay heat removal system (DHRS) of a sodium-cooled fast reactor. Faced with this issue, CFD codes often need to be coupled with other codes to reduce computational costs and take advantage of the more mature system codes, such as the previously mentioned MATHYS (SCT of CEA) (**Nathalie et al.** 2021). It should be noted that, with the current

Table 2.7. – CFD simulations advances on rectangle NCLs

Reference	Approach	Problematics
Ambrosini et al. 2004	3D FLUENT	Validity of friction laws in the laminar-to-turbulent transitional regime. 3D effects such as secondary motion and asymmetry of profiles due to pressure drop at the bends.
Pilkhwal et al. 2007	3D RNG $k-\varepsilon$	Dynamic flow behavior and the effect of different heat and cooler arrangements. Investigate pulsating initiation.
Wang et al. 2013	3D LRNM	Effect of density variation due to temperature difference, and the impact of different heater input power at different inclinations
Krishnani et al. 2016	3D RNG $k-\varepsilon$	Validity of the Boussinesq approximation during non-linear stability analysis
Kudariyawar et al. 2016	3D std $k-\varepsilon$ & LRNM	Different flow behaviour in all four configurations and the "hot plug" theory
Pini et al. 2016	3D SST $k-\omega$	Time dependent and dynamic behaviour for a range of heating powers. Influence of fluid properties and pipe material on fluid flow dynamics
Luzzi et al. 2017	3D SST $k-\omega$	Comparisons between model and experiments for different cooler temperatures. Influence of the T-juction on flow
Borreani et al. 2017	3D RNG $k-\varepsilon$	Comparisons between model and experiments for different power levels. The influence of heat conduction across the pipe walls
Zhu et al. 2019	3D std $k-\varepsilon$	Reduce the flow oscillation. Influence of different rotation angles and enclosed flow areas.
Hashemi et al. 2019	2D/3D std $k-\varepsilon$ & LRNM	Comparisons of numerical models against 1D code. Influence of asymmetric heating and the effect of turbulence mixing.
Battistini et al. 2021	3D LES WALE	Reproduce stable and unstable transients of DYNASTY. stratification and counter-current flows occurring during flow reversal.
Katsamis 2022	2D/3D $k-\omega$ SST	Steady-state though some thermal transients and secondary motion in the cooler side for unsteadiness, laminar-to-turbulent transition and thermal stratification phenomena
Yan et al. 2023	3D std $k-\varepsilon$	Influences of different heating power inputs and the two configurations (spiral-shaped and C-shaped heat exchanger tubes) on heat transfer performance
Wilson et al. 2023	3D LES WALE & (U)RANS	Comparisons between four approaches: Launder-Sharma $k-\varepsilon$ (LRNM), $k-\omega$ SST, Elliptic-Blending RSM & LES WALE

computational power, CFD codes remain challenging to be applied to the transient analysis of a complete NCL. Therefore, multi-scale modeling is a current topic.

2.3. Summary

This literature review delves into the concept of scaling in the context of code qualification, starting with a discussion on similarity and scaling. It distinguishes between complete and incomplete similarities, and underlines the importance of identifying dimensionless numbers. The review provides a thorough examination of various scaling methodologies, including several quasi-static scaling methods and the dynamic DSS method. It also includes a comparison of these methods and their applications in the nuclear field. The intricacies of scaling uncertainties are examined, emphasizing the scaling process within the BEPU methodology and the identification of modelling uncertainties under scaling. The second section of the review explores NCLs, detailing their physical behaviors and related experimental and numerical studies. It focuses on high-fidelity NCL simulations across various fidelity levels using SCTs for VVUQ, and emphasizes the role of CFD modelling.

Apart from the deficiency of classic methodology, DSS offers the advantage of quantitatively (distortion metric) and synthetically (phase space) comparing different scaling solutions for given physics. More pragmatically within the framework of the thesis, heat transfer fluids from 4th generation nuclear reactors, such as molten salts and liquid metals, introduce shifts in local physical mechanisms that need to be considered for predictive NCL scaling. Especially, the different levels of turbulence modelling at core and boundary layer, with natural circulation profiles differing from those of a pressure-driven flow, require a higher fidelity simulation. Our approach to high-fidelity simulations serves a dual purpose - it not only provides an opportunity to enrich the validation boundary with reference data, but it also offers a means to effectively manage scaling: a deep understanding of these mechanisms supports critical analysis of their scale sensitivity and associated modelling risks.

In the case of a prototype, scaling techniques are employed and similarity criteria are conserved for various objectives, resulting in corresponding reduced-scale models. However, due to incomplete similarity, it becomes crucial to measure physical distortions across these scales. This measurement helps to identify the optimal scaled model with minimal distortion and also aids in the up-scaling process. Simultaneously and quite paradoxically, the assessment of physical distortion depends on modelling, which may introduce additional numerical distortions, combining both physical modelling and numerical solution errors. To address these distortions, the quality of code prediction must be evaluated or even improved, taking into account FoMs and uncertainties. Figure 2.7 illustrates this circular relationship, underscoring the need for further clarification to mitigate concerns related to up-scaling.

After the Verification and Validation (V&V) process, subsequent chapters will explore two crucial aspects of modelling evaluation: numerical solution uncertainties and physical modelling uncertainties. Once the simulation quality is quantified through

FoM and uncertainty, the study will partly address distortion measurement and variation in scaling uncertainty. In return, regardless of the coupling state of numerical and physical distortion, the prediction quality for code qualification will be evaluated again under potential scale effects. Finally, we will provide more details on this process in the concluding outlook through a flowchart.

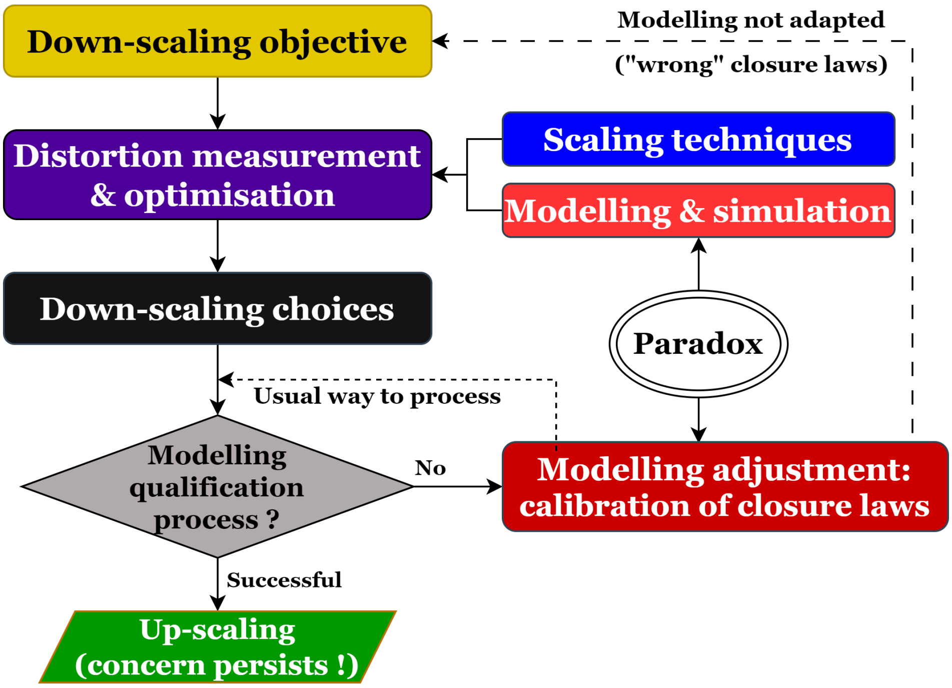

Figure 2.7. – Modelling & simulation under scaling with modelling qualification paradox.

3. Towards High-Fidelity Computations for Natural Circulation Loop

All models are wrong, but some are useful.

- George E. P. Box (1919–2013, Statistician)

Sommaire

3.1. Introductory Remarks

This chapter presents an in-depth investigation into advanced computational methods for Natural Circulation Loop (**NCL**) systems. We start by familiarizing ourselves with high-fidelity computational approaches, placing special emphasis on areas where scaling effects might manifest. This understanding indeed forms the foundation for quantifying scaling uncertainties in high-fidelity CFD simulations. It's crucial to recognize that high fidelity can enhance predictability in scaling scenarios, compared to traditional system code applications. Therefore, mastering the numerical intricacies that could be influenced by scaling in high-fidelity computations is essential to support this claim. This insight guides us towards accurate predictions and optimal NCL system functionality under scaling considerations.

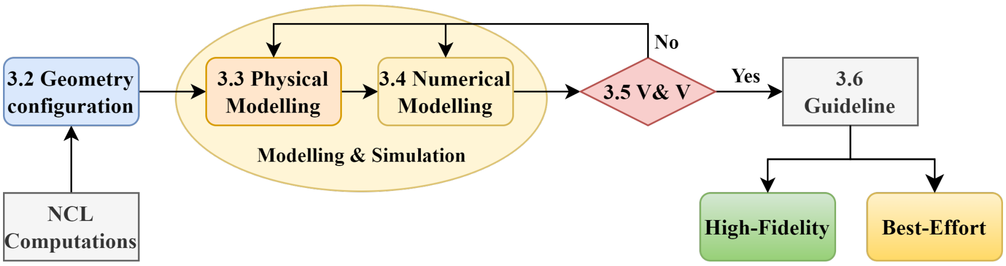

Figure 3.1. – Flowchart of Chapter 3 NCL computations.

Shown in the flowchat 3.1, the chapter is structured into six main sections to comprehensively understand high-fidelity computations and their scaling implications. Section 3.2, "Geometry Configuration," presents the physical structure of NCL systems, providing the specific loop and its geometric design under scaling consideration. Section 3.3, "Physical Modelling," discusses the translation of NCL physics into mathematical models, with particular emphasis on validating Boussinesq approximations under scaling concerns.

Section 3.4, "Numerical Modelling," explores numerical methods used in problem-solving for physical models, while Section 3.5, "Verifications & Validations (V&V)," ensures the accuracy and reliability of the numerical models. Finally, Section 3.6, "Practical Guideline of NCL Computations for Different Fidelity Levels," offers an overview of the practical application of these computations based on fidelity levels.

This chapter helps understanding the high fidelity computations for NCL systems, from their basic concept in geometry, through the detailed process of physical and numerical modelling, verification & validation, to their practical guideline.

3.2. Geometry configuration

3.2.1. Horizontal Heating Horizontal Cooling (HHHC) loop

Natural circulation for passive system is crucial for nuclear safety, reducing operator dependency, active systems costs and redundancies. However, possible cliff-edge effects (typically instability, such as some unstable or oscillating flow (**IAEA 2000**)) need to be identified and discarded so that a safe operating margin can be at least predicted and at best actually realized. Inline, the Horizontal Heater and Horizontal Cooler (HHHC) loop, chosen for this comprehensive exercise, is a configuration extensively studied in the nuclear domain (**Misale 2014**). This configuration is of academic interest because it presents challenges in numerical modelling and allows for the separation of certain numerical effects. The chosen NCL configuration of Figure 3.2(a) shares a peculiar feature with the classical Rayleigh–Bénard convection problem:

1. Below its **critical Rayleigh number** there is no flow.
2. Increasing the Rayleigh number over its critical value, a **flow ramp** can be initiated under the action of buoyancy forces and steady flows take place with either clockwise or counter clockwise directions. It is worth mentioning that flow onset is certainly an engineering target, it corresponds to a **(first) instability** boundary in the framework of dynamic system theory (**Strogatz 2019**), as the flow bifurcation shown in Figure 3.2(b) by our primary attempts. For the flow circulation to be initiated, the Reynolds number can increase from 0, and the computations will be challenged by numerical noise and turbulence modelling.
3. A **secondary instability** could emerge where either transition or turbulent flows develop. Several phenomena might be engaged: i) eddies at the exit of elbows due to the coupling of natural circulation and Dean vortices; ii) flow reversal due to increasing heater power for certain configurations, etc.

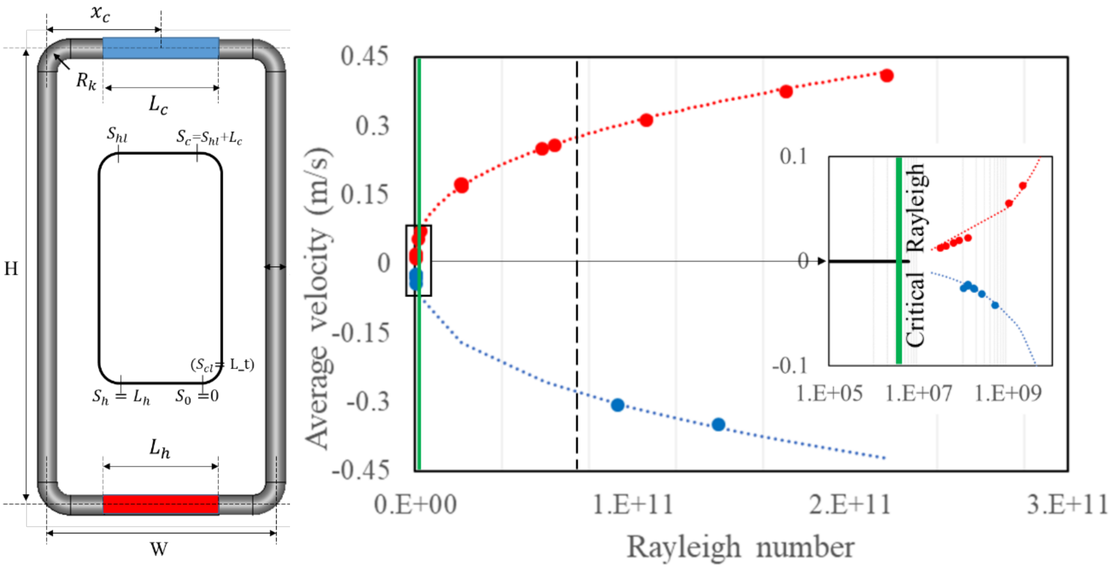

(a) HHHC loop

(b) Pitchfork bifurcation

Figure 3.2. – Pitchfork bifurcation by CFD simulation for HHHC NCL

As noted in literature section 2.2.1 about physical behaviors of NCL, Dean vortices possibly combined with thermal plumes (**Nishimura et al. 2000**), promote the local development of anisotropic turbulence. Thus, applying a turbulence model for such a problem (as will be actually required in a full scale model due to CPU limitations) raises the concerns regarding scaling.

3.2.2. Geometry Designs under Scaling Concerns

The design process for scaling a NCL demands a rigorous assessment of certain dimensionless ratios. As illustrated in Figure 3.2(a), even the most basic loop configuration involves several geometric parameters, as listed in Table 3.1, that can be gathered into various ratios, namely H/D, L_H/D and R_k/D. These ratios have a leading impact on the flow dynamics of the loop along with the imposed thermal loading, with consequential impacts on the mass flow-rate, heat transfer effectiveness, and stability of the NCL.

— The **H/D ratio**, represents the ratio of the loop height to the pipe diameter. It plays a significant influence on the buoyancy-driven flow within the loop.

— The **L_h/D ratio**, denotes the ratio of heating length to pipe diameter, it impacts the thermal loading to the loop. A loop with a higher L_h/D ratio allows the fluid to maintain prolonged contact with the exchanger surface, potentially enhancing the heat transfer.

— Finally, the **R_k/D ratio** sets the elbow curvature and its linked Dean vortices, which add to the loop's flow resistance. A smaller R_k/D ratio implies a steeper elbow turn, possibly leading to higher pressure losses and reduced natural circulation. Hence, a balance is needed: an elbow curve should not be too sharp, causing flow drop, nor too broad, raising the loop's size and cost.

Table 3.1. – Geometric specifications for a given HHHC loop

Geometry parameter	Specification
Diameter (mm)	$D/\frac{D}{2}/\frac{D}{4}$, $D = 46.4$
Height (m)	$H = 2.1$
Width (m)	$W = 1.14$
Elbow radius (m)	$R_k = 0.17$
Sink length (m)	$L_c = L_h = 0.8$
Total length (m)	$L_t = 6.188$

Maintaining similarity in these ratios between original and scaled designs helps replicate original behavior in terms of flow dynamics, heat transfer, and stability in the scaled model. However, adjustments might be needed to suit varying operating conditions and design constraints. Detailed analysis or simulations are crucial for accurate prediction under different conditions. In an industrial setting, NCL's geometric design might be more complex than the academic HHHC configuration. Variables like loop orientation and inclination, heat sink/source dimensions, etc., introduce additional scaling challenges both geometrically and computationally.

In order to observe such scaling, three dimensionless ratios have been selected for examining their respective physical impacts on the NCLs. We have categorized the scaled loops into three types, cf. Table 3.2. In the first category, designated $S_{1,i}$, the loops have varying ratios corresponding to different pipe diameters. For the second category, $S_{2,i}$, the ratios R_k/D and L_h/D are held constant. Lastly, the third category, $S_{3,i}$, is designed to study the curvature effect for the given geometry from $S_{2,2}$. Our focus in this study is primarily on the effects of scaling. Therefore, investigating geometries with consistent dimensionless ratios across varying pipe diameters is not prioritized. Additionally, the high computational cost of exploring such scenarios makes them less feasible for our current investigation. More details will be discussed in 3.5.2.

Table 3.2. – Dimensionless ratio for different HHHC loops.

Ratio	$s_{1,1}$	$s_{1,2}$	$s_{1,3}$	$s_{2,1}$	$s_{2,2}$	$s_{2,3}$
D (mm)	**46.4**	**23.2**	**11.6**	**50**	**25**	**12.5**
R_k/D	3.66	7.33	14.66	3	3	3
L_h/D	17.24	34.48	68.97	60	60	60
H/D	45.26	90.52	181.03	26	52	104
Ratio	$s_{3,1}$	$s_{3,2}$	$s_{3,3}$	$s_{3,4}$	$s_{3,5}$	$s_{3,6}$
D (mm)	**25**	**25**	**25**	**25**	**25**	**25**
R_k/D	3	4	5	6	7.2	10
L_h/D	60	60	60	60	60	60
H/D	52	52	52	52	52	52

3.3. Physical Modelling

3.3.1. TrioCFD inside CEA platform TRUST

We first present the tools that were used in this work to perform the CFD simulations. They were conducted using the CEA in-house platform TRUST [1] and TrioCFD [2]. Inheriting directly from Trio_U project (**Calvin et al. 2002**) of Nuclear Energy Department (DEN) from 1995 to 2015, TRUST is a HPC thermohydraulic engine for CFD, which was originally designed for conduction, incompressible single-phase flows, and Low Mach Number (LMN) flows with a robust weakly-compressible multi-species solver (**Nop et al. 2022**). TrioCFD, built on TRUST platform, is based on a kernel including mainly the equations, time schemes and numerical algorithms, representing 40 % of the software (**Tenchine et al. 2012**). Around the kernel are linked several modules

---

[1] https://cea-trust-platform.github.io/

[2] http://triocfd.cea.fr/

representing the space discretization methods or the physical models (**Angeli et al. 2015**). In this Figure 3.3, some available tools of TrioCFD based on TRUST are shown. While for more details about the platform, Appendix A.1 & A.2 would be helpful.

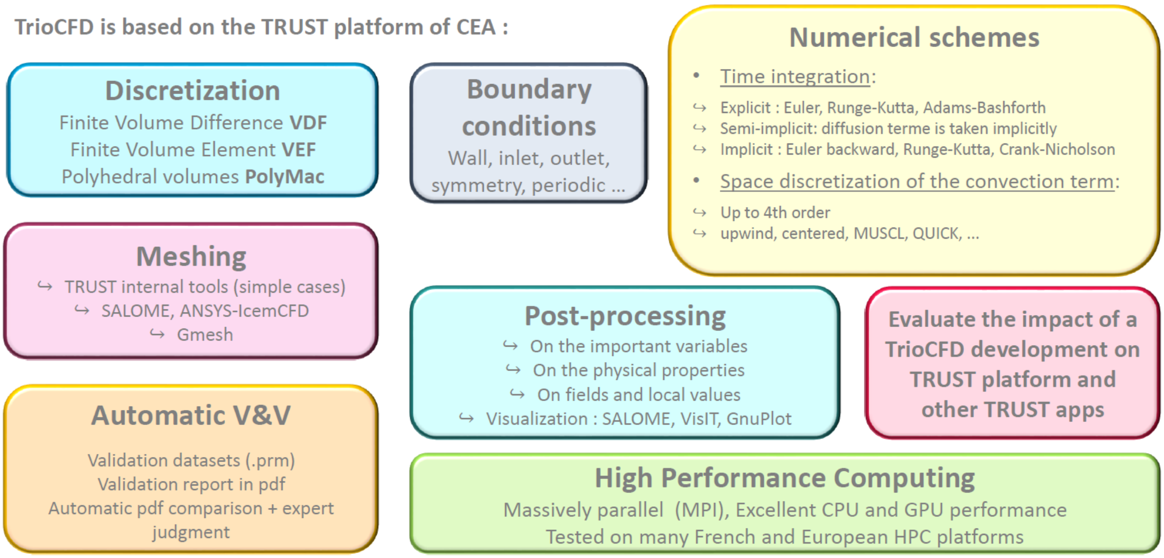

Figure 3.3. – Tools available for TrioCFD in the CEA in-house platform TRUST **Nop et al. 2022**.

3.3.2. Physical Properties

Investigating physical properties in NCLs using sodium coolant is crucial in nuclear engineering. Understanding these properties significantly impacts the operation and safety of nuclear reactors. Some key properties need to be considered: density, viscosity, thermal expansion coefficient, thermal conductivity, etc. The following Table 3.3 showcases the physical properties order of sodium coolant at 750K and 1 bar of our interests. As can be observed, liquid sodium possesses a high thermal conductivity and low viscosity, leading to a significantly low Prandtl number. This fluid characteristic means that heat diffuses faster than momentum, which increases the complexity of the simulations. These complexities touch various facets of simulation process, including numerical techniques, grid resolution, time steps, and the choice of turbulence models, among others.

It's noteworthy that during the scaling process, preservation of all physical properties and parameters is not always possible. **Rodio et al. 2017** highlighted the impact of uncertainties on boundary conditions and Equation of State (EoS) on the pressure and velocity of the mixture in the cavitation region. This brings into question the predictive accuracy for a given configuration, especially considering the variation ranges. Therefore, confirming the validation range of working scenarios is essential to reduce EoS parameter uncertainty, which could be part of numerical model uncertainty in scaling considerations. The following section, 3.3.3.3, further discusses this

Table 3.3. – Physical properties specifications of sodium flow at $750K$ and $1bar$

Physical properties	**Specification**
Density	$\rho_0 = 840\ kg/m^3$
Thermal expansion coefficient	$\beta_T = 2.77E^{-4}\ K^{-1}$
Dynamic viscosity	$\mu = 2.44E^{-4}\ kg/(m\cdot s)$
Specific heat	$C_p = 1268.5\ J/(kg\cdot K)$
Thermal conductivity	$\lambda = 65.38\ W/(m\cdot K)$
Prandtl number	$Pr = 0.00473$

issue, specifically addressing the Boussinesq approximations and associated scaling challenges.

3.3.3. Assumptions and Approximations

In CFD, assumptions and approximations simplify complex physical phenomena for computationally viable simulations. The physical model used depends on the specific scenario simulated. The progression from a fully compressible to a Low Mach Number model, and ultimately to an incompressible flow model with Boussinesq approximations, signifies increasingly simplified assumptions. However, Boussinesq approximation requires careful scrutiny as changing physical scenarios can introduce scaling issues. In this section, we'll select the suitable model for the given scenario and investigate Boussinesq approximation under scaling concerns.

3.3.3.1. Choosing the appropriate physical model

The choice of physical model in CFD is largely dictated by the characteristics of the specific scenario under consideration. As listed in Table 3.4, we outline below the key features of three progressively simplified models (**Rodio et al. 2019**):

- The **Compressible Model** accounts for full compressibility effects and all property dependencies on pressure and temperature. It makes use of the full Navier-Stokes (N-S) equations, which capture changes in density as a function of temperature, pressure, and flow speed. Density variations are taken to be both temperature and pressure-dependent.
- The **LMN model** is applicable for scenarios where the Mach number is less than 0.3 and pressure-induced density variations dominate over temperature-induced variations. This model handles pressure and temperature dependencies by making use of an EoS with an acoustic wave filter. It divides the pressure into a thermodynamic component, used in the energy equation, and a hydrodynamic component, used in the velocity equation.
- The **incompressible flow model with Boussinesq approximations** applies to

low-speed flows (Mach < 0.3) where compressibility effects can be neglected and density variations ($\Delta\rho/\rho_0$) are less than 0.1. The model assumes that the density and other properties are nearly constant, with the exception of the buoyancy term of the momentum equation, effectively decoupling the energy and momentum equations. Despite this simplification, the model still allows for the consideration of buoyancy-driven flows due to temperature differences.

The choice of an appropriate model should depend on the flow characteristics, such as the Mach number, the significance of pressure and temperature-dependent properties, and the role of buoyancy effects. Each model has its own strengths and limitations, and therefore, should be chosen judiciously based on the specific application. For instance, Table 3.4 lists actual applications in TrioCFD for a given natural circulation issue. It's worth noting that the other physical properties (such as dynamic viscosity, thermal conductivity etc.), discussed in the previous section 3.3.2 , are not dependent on local pressure but may be influenced by the local fluid temperature; i.e. $\rho = \rho(T)$ but $\rho \neq \rho(P)$. In the following study, we opt for the incompressible flow model with Boussinesq approximations, which may have either general or strict requirements. Both types of Boussinesq approximation will be investigated when the physical scenarios change for scaling consideration.

3.3.3.2. Incompressible flows with Boussinesq approximation

Under the Boussinesq approximation, the density of a fluid is considered mostly constant, except for variations due to temperature changes, expressed as

$$\rho(p, T) \approx \rho(T).$$

This approximation simplifies the momentum conservation equation and allows the energy equation to be decoupled from other equations, significantly reducing computational complexity. Separately, for low Mach number flows, the fluid can be assumed incompressible, leading to the divergence of the velocity field being zero, denoted as

$$\nabla \cdot \boldsymbol{u} = 0.$$

However, it introduces a challenge: it creates an interdependency between pressure and velocity that must be carefully managed to ensure mass remains constant. Managing this interdependency can be particularly complex when using certain computational methods like the finite volume method.

In spite of its simplifications , the incompressible flow assumption should be used judiciously. It can lead to significant errors if applied to scenarios where the flow undergoes substantial density changes, such as high-speed flows or flows involving significant temperature variations. Therefore, the validity of the incompressible flow assumption needs to be carefully evaluated for each specific application.

Table 3.4. – Comparison of different models for incompressible and dilatable flows.

	Compressible model	**Low Mach Number (LMN) model**	**Incompressible model with Boussinesq approximations**
Main physical assumptions	1) Full effects of compressibility 2) All properties are Pressure & Temperature (P&T) dependent	1) Compressibility effects 1.1) Mach < 0.3 1.2) $\frac{\partial\rho}{\partial P}\Delta P > \frac{\partial\rho}{\partial T}\Delta T$ dilated (EoS) * Density variations are temperature related and also pressure partially dependent.	1) Incompressibility 1.1) fluid mechanism: Mach < 0.3 1.2) no impact from thermodynamics P/T (EoS) 2) General Boussinesq $\Delta\rho/\rho_0$< 0.1 * Standard Boussinesq $\Delta x/x_0$< 0.1 (all properties)
Implemented equations	Use full Navier-Stokes equations, including changes in density due to temperature, pressure and flow velocity.	1) Treat 1.2) by EoS with acoustic wave filter $P(t,x) = P_{th}(t) + P_h(t,x)$ with $P_h(t,x)$ into velocity equation and $P_{th}(t)$ into energy (EoS) equation 2) Variations in density due to P& T	Buoyancy effects only in source term of QoM $\rho_0 g[1 - \beta_T(T - T_0)]$
TrioCFD application	-	*Quasi-compressible* model in TrioCFD with also temperature dependent μ, λ(T)	General Boussinesq $\Delta\rho/\rho_0$< 0.1 with μ, λ(T)
Problematics NC with ΔT<150K, P=1bar, u<3m/s	Indaptive for Ma <<1, complex to implement and require more computational resources.	Apply to certain components (such as expansion tank). If incompressible one fails with large pressure gradient compared to temperature, LMN can be useful but struggles with significant sound wave propagation.	Apply for pipe system with appropriate temperature differences and velocities. Other physical properties should be checked with strict Boussinesq approximations.

3.3.3.3. Boussinesq approximations under scaling concerns

Standard Boussinesq approximations for CFD

The Boussinesq approximation is a widely adopted simplification utilized primarily to model the impact of buoyancy in a fluid system. This approximation is built on certain strict conditions, once satisfied, which allow the representation of complex fluid behaviors in a relatively simplified manner. Nevertheless, when these conditions are not met, the alternative models or approximations should be considered. Meanwhile, the Boussinesq approximation makes the following key assumptions (**Gray and Giorgini 1976; Barletta 2022**):

- **Fluid density** is primarily influenced by local temperature changes, with pressure changes having negligible impact. Additionally, density is considered constant unless it contributes directly to buoyant forces.
- Apart from density changes due to temperature fluctuations, all **other fluid properties** are assumed to be constant.
- Difference between the local temperature and its reference value is minimal.
- Acceleration experienced by fluid elements within the flow domain, as well as the viscous stress, are both negligible.
- There is a very small difference between the local pressure gradient and the hydrostatic pressure gradient.
- Viscous dissipation, a measure of energy loss due to fluid friction, is assumed to be negligible.

Boussinesq approximations for liquid sodium flows

When applying the Boussinesq approximation, there is a tendency to directly use a density variation lower than 10%, which corresponds to the first condition. For water, this single assumption might be enough in terms of approximation. But what about liquid sodium? Which physical properties have limits? And where are these limits?

The current focus of study is the second circuit of the passive system in ASTRID (**CEA/DEN 2012**). The methodology in **Gray and Giorgini 1976** outlines three main steps, enabling us to explicitly detail Boussinesq approximations for various coolants and scenarios.

Step 1 : Linearized approximations of fluid properties
To solve our problem, we need relationships to determine fluid properties using two thermodynamic variables. Sometimes, these relationships aren't readily available, requiring handbook or EoS references. We use an analytical approach, approximating these functions with a linearized Taylor expansion, but we must validate this method afterwards.

We then present Table 3.5 which lists five physical properties derived from temperature and pressure variables. These form the basis of our further study, offering new variables for a more detailed analysis of Boussinesq approximations. Of particular note are two properties—dynamic viscosity and specific heat. As shown in Figure 3.4, these properties slightly deviate from linearity across the considered temperature range, suggesting their behavior may not strictly conform to a simple linear assumption. Further investigation is needed to confirm the importance of these properties for sodium flow in relation to approximations.

Table 3.5. – Linearized approximations of fluid properties

Physical properties	**T-dependent**	**P-dependent**
Thermal expansion/Compressibility	$\beta_T = -\frac{1}{\rho}\frac{\partial \rho}{\partial T}$	$\beta = -\frac{1}{\rho}\frac{\partial \rho}{\partial P}$
Dynamic viscosity rate	$a = -\frac{1}{\mu}\frac{\partial \mu}{\partial T}$	$b = -\frac{1}{\mu}\frac{\partial \mu}{\partial P}$
Specific heat rate	$c = -\frac{1}{c_p}\frac{\partial c_p}{\partial T}$	$d = -\frac{1}{c_p}\frac{\partial c_p}{\partial P}$
Thermal expansion rate	$e = -\frac{1}{\beta_T}\frac{\partial \beta_T}{\partial T}$	$f = -\frac{1}{\beta_T}\frac{\partial \beta_T}{\partial P}$
Thermal conductivity rate	$m = -\frac{1}{\lambda}\frac{\partial \lambda}{\partial T}$	$n = -\frac{1}{\lambda}\frac{\partial \lambda}{\partial P}$

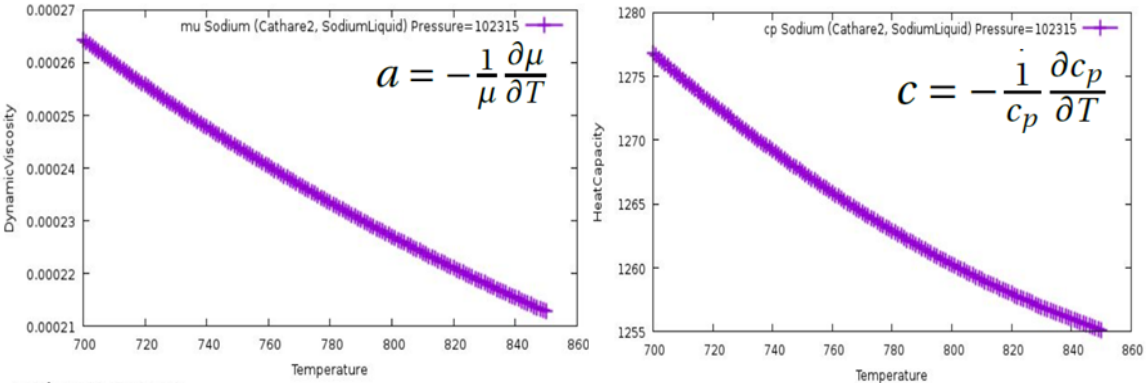

(a) Dynamic viscosity (T) (b) Specific heat (T)

Figure 3.4. – Physical properties variation over temperature at $1 bar$ (a) for dynamic viscosity μ; (b) for specific heat c_p

Step 2 : Calculate the coefficients of physical properties ratio

Using the recently derived properties, we will compare the flow of sodium with the typical water flow under analogous scenarios. Table 3.6 contains data from two sources: the properties of water are extracted from **Gray and Giorgini 1976**, while those of sodium are calculated from EoS using average temperature data from **Geffray et al. 2017**, under different pressure conditions. Notably, the most critical properties are highlighted: those dependent on temperature are in red, and those dependent on pressure are in green. Two key observations emerge from this analysis:

1. Beyond the general Boussinesq approximation where density variation is a key criterion, the standard approximation identifies other properties, more vital than density alone, for both water and sodium flow.

2. Different coolants possess distinct properties requiring individual verification. For instance, the thermal expansion coefficient rate for water and dynamic viscosity for sodium flow are crucial when considering temperature variance. On the other hand, for pressure variance, thermal conductivity for water and compressibility for sodium become pivotal.

Further differentiation of the importance of properties can be accomplished by comparing their rate magnitudes. For sodium flow, the order of importance for temperature variation is: **dynamic viscosity > thermal conductivity** > thermal expansion > density > heat capacity. In terms of pressure variation, the hierarchy is: **density > heat capacity** > thermal expansion.

Table 3.6. – Physical property rates for water and liquid sodium.

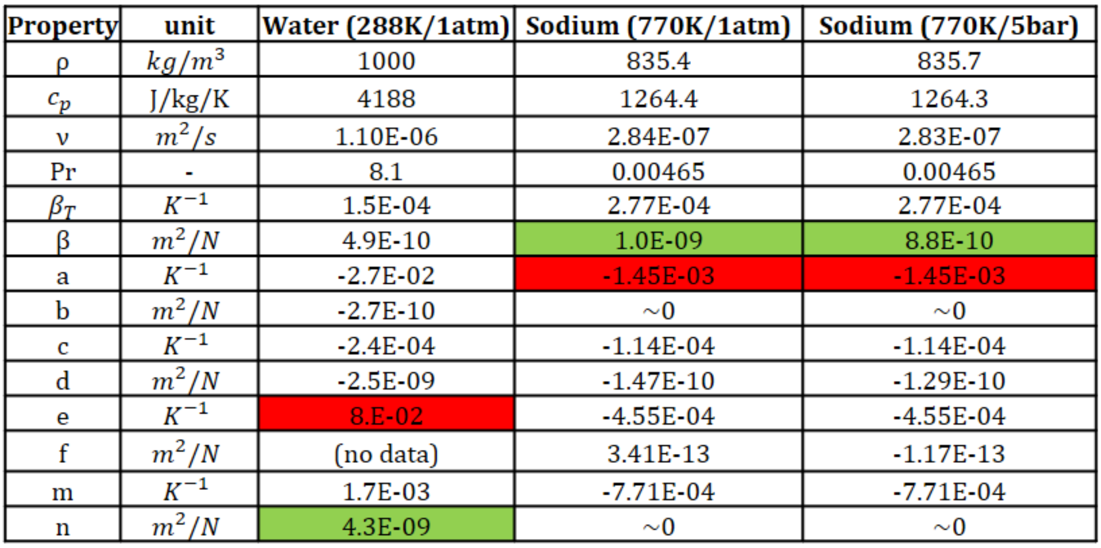

Property	unit	Water (288K/1atm)	Sodium (770K/1atm)	Sodium (770K/5bar)
ρ	kg/m^3	1000	835.4	835.7
c_p	J/kg/K	4188	1264.4	1264.3
ν	m^2/s	1.10E-06	2.84E-07	2.83E-07
Pr	-	8.1	0.00465	0.00465
β_T	K^{-1}	1.5E-04	2.77E-04	2.77E-04
β	m^2/N	4.9E-10	1.0E-09	8.8E-10
a	K^{-1}	-2.7E-02	-1.45E-03	-1.45E-03
b	m^2/N	-2.7E-10	~0	~0
c	K^{-1}	-2.4E-04	-1.14E-04	-1.14E-04
d	m^2/N	-2.5E-09	-1.47E-10	-1.29E-10
e	K^{-1}	8.E-02	-4.55E-04	-4.55E-04
f	m^2/N	(no data)	3.41E-13	-1.17E-13
m	K^{-1}	1.7E-03	-7.71E-04	-7.71E-04
n	m^2/N	4.3E-09	~0	~0

Fortunately, in the TrioCFD system, both dynamic viscosity and thermal conductivity can be computed as temperature functions rather than constants. This capability, despite being an extension to the Boussinesq approximations, not only circumvents the simple linear assumption made in the **step 1**, but also eliminates these properties from the top two threats. Consequently, this allows us to accommodate a larger temperature tolerance in TrioCFD computations regarding the extended Boussinesq approximation, as compared to the standard one.

Step 3: Plot the validity region of Boussinesq approximations
Considering the problem of natural convection in a horizontal fluid layer with a vertical thickness $L(cm)$, across which a temperature difference $\theta(K)$ is prescribed in **Gray and Giorgini** 1976. This scenario is often known as the Rayleigh-Bénard problem. The aforementioned ten properties are confined within their respective ϵ_i parameters. These parameters, alongside ϵ_{11}, represent the coupled effects of physical properties derived from the energy equation. To uphold the small variation approximation, all these ϵ_i values should be less than 10 %. We can consolidate these considerations

using coefficients from Table 3.6 and rewrite the constraints into Table 3.7. These restrictions can then be visually represented on a Cartesian coordinate system using $L-\theta$ in Figure 3.5.

Table 3.7. – Physical properties limitation for water and liquid sodium.

Property function	**Limitation line**	**Water (288K/1atm)**	**Sodium (770K/1atm)**	**Sodium (770K/5bar)**
Density (T)	$\varepsilon_1 = \beta_{T,0}\,\theta$	1.5E-4θ	2.77E-4θ	2.77E-4θ
Density (P)	$\varepsilon_2 = \beta_0 \rho_0 g L$	4.8E-6L	8.2E-6L	7.2E-6L
Viscosity (T)	$\varepsilon_3 = a_0\,\theta$	-2.7E-2θ	-1.45E-3θ	-1.45E-3θ
Viscosity (P)	$\varepsilon_4 = b_0 \rho_0 g L$	-2.7E-6L	~0	~0
Specific heat (T)	$\varepsilon_5 = c_0\,\theta$	-2.4E-4θ	-9.92E-5θ	-9.92E-5θ
Specific heat (P)	$\varepsilon_6 = d_0 \rho_0 g L$	-2.4E-5L	-1.2E-6L	-1.1E-6L
Th. Expansion (T)	$\varepsilon_7 = e_0\,\theta$	8E-2θ	-4.55E-4θ	-4.55E-4θ
Th. Expansion (P)	$\varepsilon_8 = f_0 \rho_0 g L$	(no data)	2.8E-9L	-9.5E-10L
Th. conductivity (T)	$\varepsilon_9 = m_0\,\theta$	1.7E-3θ	-7.71E-4θ	-7.71E-4θ
Th. conductivity (P)	$\varepsilon_{10} = n_0 \rho_0 g L$	4.2E-5L	~0	~0
Prandtl/Rayleigh	$\varepsilon_{11} = \beta_{T,0} g L / c_{p,0}$	3.5E-7L	2.15E-06L	2.15E-06L

Therefore, the most crucial properties will be identified by tracing the boundaries along the temperature and pressure axes. This will set up the valid regions for the Boussinesq approximation. As illustrated in Figure 3.5(a), general approximations are employed, indicating a permissible temperature difference of about 70K for sodium flow with an average temperature at 770K. However, as previously mentioned, the top two threats can be rendered temperature-dependent in TrioCFD. This alteration permits an expanded maximum temperature difference of up to 220K, useful in more practical scenarios (such as where the 2nd circuit temperature difference over the heat source in ASTRID is around 150K). As for pressure variance, sodium flow expresses less concern over the given range from 1 to 5 atm, where no major change is observed. Furthermore, the diagonal line, controlled by relation with ϵ_{11}, doesn't have direct impact on upper border of temperature.

In summary, the Boussinesq approximation is a vital simplification tool in fluid dynamics analysis. However, it brings potential scaling issues, particularly related to temperature differences, as per Figure 3.5. This problem is more pronounced with varying scales, where smaller models have a reduced acceptable temperature difference, and larger ones may require a temperature difference outside the valid region. Thus, it's essential to account for scale-specific temperature differences ensuring they lie within the Boussinesq approximation's valid regions. This attentiveness not only preserves the integrity of the scaling process but also guarantees the reliability of the subsequent CFD predictions.

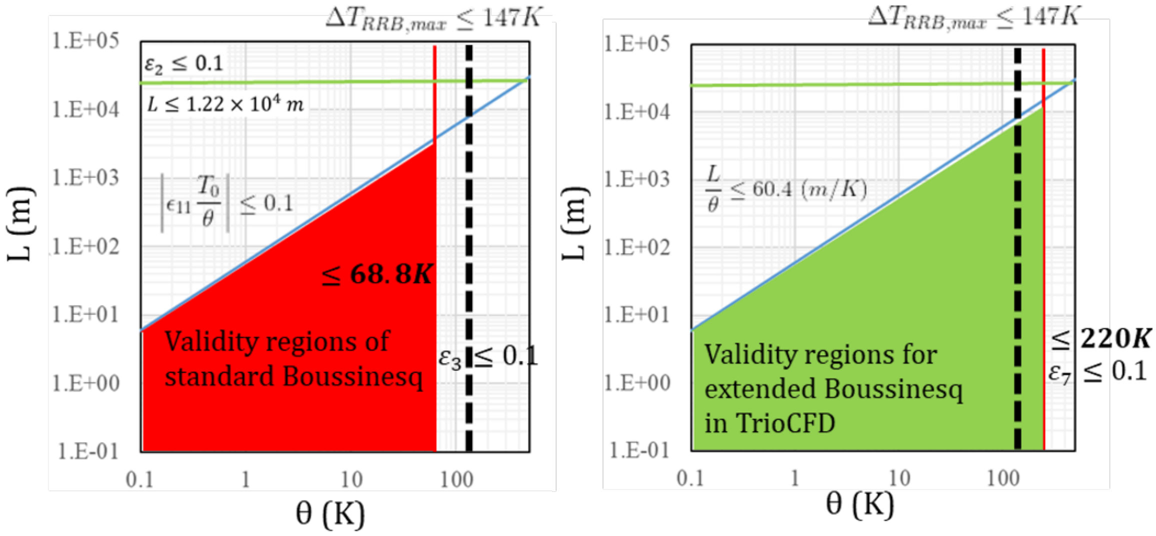

(a) Standard Boussinesq

(b) TrioCFD extensions

Figure 3.5. – Validity regions of the Boussinesq approximation in sodium flow ($T = 770K$, $P = 1bar$) (a) for standard Boussinesq approximation with ϵ_3 imposing from dynamic viscosity; (b) for extended Boussinesq in TrioCFD with temperature-dependant viscosity and conductivity while ϵ_7 imposing from thermal expansion

3.3.4. Governing Equations in CFD Code

To simulate the fluid dynamics and thermodynamics within a rectangular NCL (shown in Figure 3.2(a)), we employ the momentum equations along with the laws of mass and energy conservation. For accurate depiction of the system's behavior, these governing equations must be adapted and simplified for three-dimensional (3D) scenarios. Meanwhile, one-dimensional analysis for NCL can be referred to in Appendix B.1 for specific utility, particularly for the preparation of the scaling process where dimensionless analysis is required.

In CFD, the use of the Boussinesq approximation significantly simplifies the governing equations, rendering fluid velocity $\boldsymbol{u}$ and temperature T more amenable to computational analysis and resolution.

Mass Conservation (Continuity Equation)

For incompressible flows, the continuity equation simplifies to:

$$\nabla \cdot \boldsymbol{u} = 0$$

Momentum Conservation (N-S Equations)

For incompressible flows and assuming the fluid is Newtonian (the stress tensor is linearly related to the strain rate tensor), the N-S equations become:

$$\rho_0 \frac{\partial \boldsymbol{u}}{\partial t} + \rho_0 \boldsymbol{u} \cdot \boldsymbol{\nabla} \boldsymbol{u} = -\boldsymbol{\nabla} p + \boldsymbol{\nabla} \cdot \left[\mu (\boldsymbol{\nabla} \boldsymbol{u} + \boldsymbol{\nabla}^T \boldsymbol{u}) \right] + \boldsymbol{F}_v \tag{3.1}$$

Here, μ is the dynamic viscosity of the fluid (temperature dependent in TrioCFD shown in Table 3.4), and $\boldsymbol{F}_v$ is body force term. For incompressible flows, the effects of buoyancy are accounted for solely by gravitational forces. This simplification is known as the Boussinesq approximation. In this case, the force term is given by:

$$\boldsymbol{F} v = \rho_0 \boldsymbol{g} [1 - \beta_T (T - T_0)] \tag{3.2}$$

where β_T is the thermal expansion coefficient and T_0 is a reference temperature. In this relation, the negative sign indicates that if the temperature difference is positive $\Delta T = T - T_0 > 0$ (i.e., near the hot wall in natural convection), then the force is directed opposite to the gravity $\boldsymbol{g}$.

Energy Conservation

For incompressible flows where no phase changes occur and viscous heating is neglected, the energy conservation equation translates into a temperature equation:

$$\rho_0 c_p \left(\frac{\partial T}{\partial t} + \boldsymbol{u} \cdot \nabla T \right) = \nabla (\lambda \nabla T) + Q \tag{3.3}$$

Here, T is temperature, c_p is specific heat at constant pressure, λ is the thermal conductivity (temperature-dependent in TrioCFD), and Q denotes heat sources.

3.3.4.1. Large Eddy Simulation (LES)

LES is a mathematical model used in the field of fluid dynamics to model turbulent flows by filtering out the smallest turbulent structures (the eddies), and explicitly calculating the larger ones. The contributions from larger scales are isolated by introducing a spatially filtered average operator: $\overline{f} = \int_V G(x, x') f(x,t) dV$. Thus, any function in the flow field is decomposed as $f(x,t) = \overline{f}(x,t) + f'(x,t)$, where $f'(x,t)$ represents the subgrid-scale fluctuations.

The governing equations for momentum and energy conservation equations in LES are similar to the RANS equations, but instead of Reynolds stresses in the following, we have subgrid-scale (SGS) stresses. By filtering the equation 3.1, the momentum equation can be rewritten as:

$$\frac{\partial \overline{u_i}}{\partial t} + \frac{\partial \overline{u_i}\, \overline{u_j}}{\partial x_j} = -\frac{1}{\rho_0} \frac{\partial \overline{p}}{\partial x_i} + \frac{\partial}{\partial x_j} \left[\nu \left(\frac{\partial \overline{u_i}}{\partial x_j} + \frac{\partial \overline{u_j}}{\partial x_i} \right) \right] + \frac{\partial \tau_{ij}}{\partial x_j} + \frac{\boldsymbol{F}_v}{\rho_0} \tag{3.4}$$

and the filtered energy equation is given by:

$$\frac{\partial \overline{T}}{\partial t} + \overline{u_j} \frac{\partial \overline{T}}{\partial x_j} = \frac{\partial}{\partial x_i} \left(\frac{\nu}{Pr} \frac{\partial \overline{T}}{\partial x_i} \right) + \frac{\partial \vartheta_{ij}}{\partial x_j} + \frac{Q}{\rho_0 c_p} \tag{3.5}$$

where $\nu = \mu / \rho_0$ is the kinematic viscosity, $Pr = \mu c_p / \lambda$ is the Prandtl number.

The SGS stress tensor τ_{ij} is related to the SGS viscosity coefficient by the Boussinesq approximation:

$$\tau_{ij} \equiv \overline{u_i}\,\overline{u_j} - \overline{u_i u_j} = 2\nu_{sgs}\overline{S_{ij}} + \frac{1}{3}\tau_{kk}\delta_{ij} \tag{3.6}$$

where $S_{ij} = \frac{1}{2}\left(\frac{\partial \overline{u_i}}{\partial x_j} + \frac{\partial \overline{u_j}}{\partial x_i}\right)$ is the rate of strain tensor, and δ_{ij} is the Kronecker delta.

Likewise, the SGS stress tensor ϑ_{ij} in equation 3.5 is modeled by a simple gradient-diffusion hypothesis:

$$\vartheta_{ij} \equiv \overline{u_i}\,\overline{T} - \overline{u_i T} = \frac{\nu_{sgs}}{Pr_t}\frac{\partial \overline{T}}{\partial x_j} \tag{3.7}$$

where Pr_t is the turbulent Prandtl number for which the value 0.9 is commonly used for water, but not the case for low Prandtl number flow like sodium (see section 3.3.4.3).

In LES, the SGS stresses are modeled based on different approaches. Two common models are the Smagorinsky model and the Wall-Adapting Local Eddy-viscosity (WALE) model to deal with ν_{sgs}:

— For the **Smagorinsky model**, it is expressed as:

$$\nu_{sgs} = (C_s\Delta)^2\sqrt{2\overline{S_{ij}}\,\overline{S_{ij}}} \tag{3.8}$$

— For the **WALE model**, which accounts for the effects of both the strain and the rotation rate of the smallest eddies, the expression is:

$$\nu_{sgs} = (C_w\Delta)^2\frac{\left(\overline{S^d_{ij}}\,\overline{S^d_{ij}}\right)^{3/2}}{\left(\overline{S_{ij}}\,\overline{S_{ij}}\right)^{5/2} + \left(\overline{S^d_{ij}}\,\overline{S^d_{ij}}\right)^{5/4}} \tag{3.9}$$

where the tensor $\overline{S^d_{ij}}$ is defined as

$$\overline{S^d_{ij}} = \overline{S_{ik}}\,\overline{S_{kj}} + \overline{\Omega_{ik}}\,\overline{\Omega_{kj}} - \frac{1}{3}\left(S_{mn}S_{mn} - \overline{\Omega_{mn}}\,\overline{\Omega_{mn}}\right), \overline{\Omega_{ij}} = \frac{1}{2}\left(\frac{\partial \overline{u_i}}{\partial x_j} - \frac{\partial \overline{u_j}}{\partial x_i}\right)$$

and the values used for the constants C_s and C_w are respectively 0.18 and 0.5.

3.3.4.2. Reynolds-Averaged Navier-Stokes (RANS)

The fundamental idea behind RANS is to decompose the flow variables into mean and fluctuating parts, then to take the time average of the Navier-Stokes equations, resulting in additional terms known as the Reynolds stresses. When velocity and pressure are treated as random functions of space and time, their instantaneous values are decomposed as follows:

$$u(x,t) = \overline{U}(x) + \tilde{u}(x,t)$$

$$p(x,t) = \overline{P}(x) + \tilde{p}(x,t)$$

where the symbol $\overline{()}$ indicates the statistical averaging operator (or ensemble average), and the symbol $\tilde{()}$ represents the fluctuations (or deviations from these averages).

By Rewriting the equation 3.1, we have

$$\rho_0 \left(\frac{\partial \overline{U}}{\partial t} + \overline{U} \cdot \nabla \overline{U} \right) = \nabla \cdot \left(-\overline{P} I + 2\mu \overline{S} - \rho_0 \overline{\tilde{u}\tilde{u}} \right) + \boldsymbol{F}_v \tag{3.10}$$

The terms in equation can be broken down as follows:

- The left hand term represents the inertial forces. Here, ρ_0 is the constant density, $\overline{U}$ is the mean velocity, and the operator ∇ represents the gradient.
- The first right hand term is the divergence of the stress tensor. Here, $-\overline{P}I$ is the pressure term (I is the identity matrix), $2\mu\overline{S}$ is the viscous stress tensor with viscosity μ and rate of strain tensor $\overline{S}$, and $-\rho_0\overline{\tilde{u}\tilde{u}}$ is the Reynolds stress tensor, which represents the effect of the turbulent fluctuations on the mean flow. The system of equations is open due to the presence of correlations of fluctuating velocities $\overline{\tilde{u}\tilde{u}}$.
- More specifically, the rate of strain tensor $\overline{S}$ is defined as follows:

  $$\overline{S} = \frac{1}{2}\left(\nabla \overline{U} + \nabla^T \overline{U} \right)$$

  where $\nabla^T \overline{U}$ is the transpose of the velocity gradient tensor.
- The term $\boldsymbol{F}_v$ is a body force term, $\boldsymbol{F}_v$.

To solve these equations, the Reynolds stresses need to be modeled, which is usually achieved through turbulence models, such as the κ-ϵ or κ-ω models. Many models of the Reynolds stress tensor are possible, but only available currently in TrioCFD is κ-ϵ model for single phase flow, based on the Boussinesq assumption:

$$\overline{\tilde{u}\tilde{u}} = -2\nu_t \overline{S} + \frac{2}{3}\overline{\kappa} I \tag{3.11}$$

where $\kappa = \frac{1}{2}\overline{|\tilde{u}|}^2$ is the turbulent kinetic energy per unit mass and ν_t is the turbulent viscosity.

The κ-ϵ model allows to close the system of equations above by solving two additional equations, one for the turbulent kinetic energy κ, and the other one for the dissipation rate ϵ, as follows:

$$\frac{\partial \overline{\kappa}}{\partial t} + \overline{U_i}\frac{\partial \overline{\kappa}}{\partial x_i} = \frac{\partial}{\partial x_j}\left[(\nu + \nu_t/\sigma_\kappa)\frac{\partial \overline{\kappa}}{\partial x_j} \right] + P_\kappa - \overline{\epsilon} \tag{3.12}$$

$$\frac{\partial \overline{\epsilon}}{\partial t} + \overline{U_i}\frac{\partial \overline{\epsilon}}{\partial x_i} = \frac{\partial}{\partial x_j}\left[(\nu + \nu_t/\sigma_\epsilon)\frac{\partial \overline{\epsilon}}{\partial x_j} \right] + C_{1\epsilon}\frac{\overline{\epsilon}}{\overline{\kappa}}P_\kappa - C_{2\epsilon}\frac{\overline{\epsilon}^2}{\overline{\kappa}} \tag{3.13}$$

where

- ν is the molecular viscosity

— ν_t is the turbulent viscosity
— σ_κ andσ_ϵ are the turbulent Prandtl numbers for κ and ϵ, respectively with default values, 1 and 1.3.
— $C_{1\epsilon}$ and $C_{2\epsilon}$ are model constants, respectively with default values, 1.44 and 1.92.
— P_κ is the production of turbulence kinetic energy divised by density

$$P_\kappa = \tau_{ij}/\rho_0 \frac{\partial \overline{U_i}}{\partial x_j}$$

3.3.4.3. Heat transfer model

In CFD, the heat transfer model is often tightly connected with the hydraulic model through turbulence modelling. A key parameter in this coupling is the turbulent Prandtl number, denoted by Pr_t. This dimensionless number represents the ratio of momentum diffusivity (or kinematic viscosity, ν_t) to thermal diffusivity (α_t) in the turbulent flow. Furthermore, the Prandtl model inside the temperature field equation links viscosity and diffusivity:

$$\alpha_t = \frac{\nu_t}{Pr_t}$$

While the turbulent Prandtl number is close to unity for most fluids, this isn't universally the case. It has been found that a uniform profile of the turbulent Prandtl number is not suitable to describe the profile of turbulent heat flux and fails to accurately predict the profile of turbulent heat flux, especially in the near-wall region (**Duponcheel et al.** 2014). The value of the turbulent Prandtl number in the near-wall region is much larger than that in the channel center. Therefore, custom-defined values or functions can be assigned to Pr_t in TrioCFD, allowing for a more accurate portrayal of specific flows. This flexibility is especially beneficial in predicting near-wall thermal behavior for liquid metal flows, a significant area of interest in the nuclear R&D.

The turbulent Prandtl number (Pr_t) is a key player in the heat transfer model. While the formulations provided by **Kays** 1994 and **Weigand et al.** 1997 are widely acknowledged, a variable formulation for Pr_t in RANS simulations tends to show superior performance over a wide range of scenarios, as indicated by an a priori analysis of Direct Numerical Simulation (DNS) datasets. However, it's important to note that this variable formulation can generate high errors in unstable convective regimes (**Bhushan et al.** 2022).

During the transient phase of natural circulation, buoyancy increases can cause non-monotonic changes in mean velocity and temperature. This is evidenced by previous studies (**Zhao et al.** 2018), which reveal that quantities such as turbulent shear stress, turbulent fluctuations, skin-friction coefficient, and the Nusselt number initially decrease, then undergo an increase due to buoyancy-induced turbulence attenuation and subsequent recovery. Hence, it is necessary to monitor carefully for potential over-heating phases during start-up simulations.

In conclusion, the heat transfer model in CFD, underpinned by the turbulent

Prandtl number, is instrumental in precisely depicting and evaluating thermal behaviors across different fluid flows. This deepens the authenticity and trustworthiness of CFD simulations. Furthermore, understanding the intricate role of the turbulent Prandtl number within these models is not only critical to refining our current simulations but also opens an avenue for studying model uncertainty (see section 5.1). The impact of variations in the turbulent Prandtl number could provide valuable insights into improving the predictive capability of our CFD models.

3.3.5. Turbulence Modelling Approaches

Direct Numerical Simulation (DNS) solves the N-S equations without any turbulence model, meaning all spatial and temporal scales of turbulence are resolved. Consequently, the mesh in DNS must be sufficiently fine to capture vortices of sizes ranging from the smallest dissipation scale (Kolmogorov scale) to the length scale characteristic of the domain size. Turbulence theory indicates that the number of mesh points in 3D DNS is on the order of $O(Re^{9/4})$, where Re is the Reynolds number of the flow. As a result, the computational costs of DNS are challenging for high Reynolds numbers.

Unlike DNS, Large Eddy Simulation (LES) only resolves flow structures of large scales by filtering the N-S equations with a spatial filter, and the small unresolved scales are modeled using sub-grid scale models (**Bieder and Rodio** 2019**; Bieder et al.** 2019). The range of scales resolved in LES is much smaller than in DNS, significantly reducing computational costs. Many subgrid-scale models with various options are available. The WALE model (Wall-Adapting Local Eddy-viscosity) is the most commonly employed in TrioCFD, in order to correctly calculate near-wall flows in combination with wall functions (**Nicoud and Ducros** 1999).

Finally, Reynolds-Averaged Navier-Stokes (RANS) models consist of a set of averaged N-S equations, with turbulence models used to close the additional Reynolds stress tensor induced by fluctuations. RANS models only solve the mean flow at macroscopic scales, making it the most economical method for turbulence simulation. Two main RANS calculations are applied in this study (**Angeli and Peybernes** 2016):

- Standard linear $k-\epsilon$ model (Linear Eddy-Viscosity Model, LEVM) (**launder and Spalding** 1974);
- Non-Linear Eddy-Viscosity Model (NLEVM) (**Baglietto and Ninokata** 2005).

In essence, the choice of turbulence modelling - DNS, LES, or RANS - depends on the trade-off between computational cost and the degree of physical detail required in the simulation. Further details on the formulation of equations for LES and RANS are provided in Appendix A.2.

3.3.5.1. LES WALE model application

To explore wall-resolved LES behavior compared to DNS, we used a structured refinement for geometry $s_{2,2}$, with meshes ranging from coarse (M1) to refined (M3) as shown in Table 3.8. This improves grid resolution and better captures turbulent scales. As exemplified in Figure 3.6(b), refining the mesh in DNS enables us to better visualize the minutiae of the flow, the subtle swirls, and eddies. Our 2D simulation under $\Delta = 10K$ thus begins to mirror the actual flow more closely. However, it's vital to remember that computational limitations may prohibit the capture of the smallest details, even in the currently most refined DNS M2. On the flip side, mesh refinement in LES also captures turbulence more accurately, reducing assumptions about smaller-scale turbulence. Therefore, our LES results increasingly align with our DNS results, the benchmark 'true' solution.

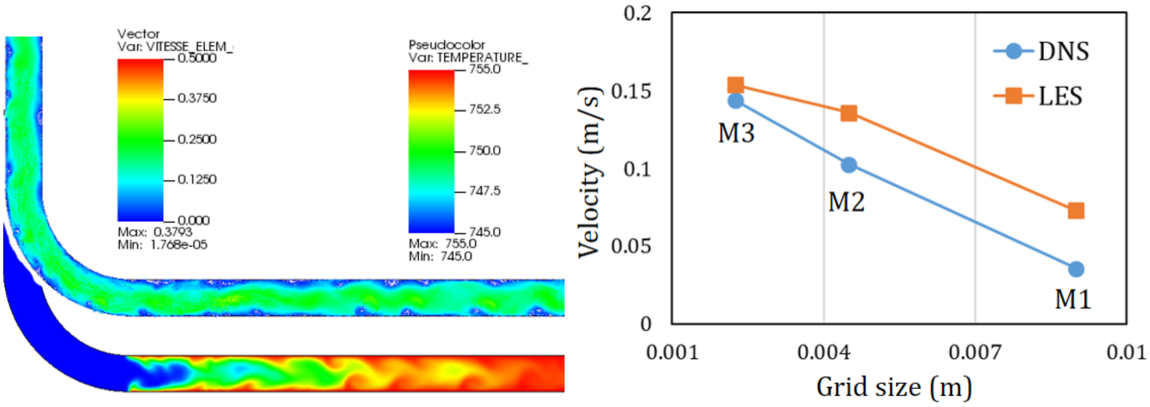

(a) LES M3

(b) LES & 'DNS'

Figure 3.6. – Velocity responses of LES and 'DNS' over refined meshes with geometric progression $s_{2,2}$ under $\Delta = 10K$ with (a) velocity vector & temperature field of LES M3; (b) velocity evolution for M1 to M3.

However, when interpreting this convergence, one must proceed with caution. The solution convergence between DNS and wall-resolved LES during mesh refinement does not necessarily align. The LES solution, inherently reliant on the SGS model to a degree, may not perfectly coincide with the DNS solution. This divergence is particularly pronounced in complex or transitional flows, as illustrated in Figure 3.6(a), where a strong local recirculation is observed at the elbow downstream, subsequently propagating along the pipeline.

Moreover, the temperature field and velocity vectors comparison for the 2D M2 mesh with 'DNS' and LES, as shown in Figure 3.7, demonstrates the advantage of LES. Particularly with three refined meshes, LES solutions tend to converge better than 'DNS'. Consequently, LES presents a strategic tool to economize CPU resources while achieving similar results in terms of high fidelity computation.

In summary, this progression of convergence between DNS and LES with mesh refinement serves as a useful tool for both validating LES models and investigating the impacts of grid resolution on simulation accuracy. By comparing the DNS and LES solutions at different stages of refinement, we can glean insights into the performance of the LES model, evaluate the appropriateness of our grid resolution, and gain a deeper understanding of the nature of turbulence.

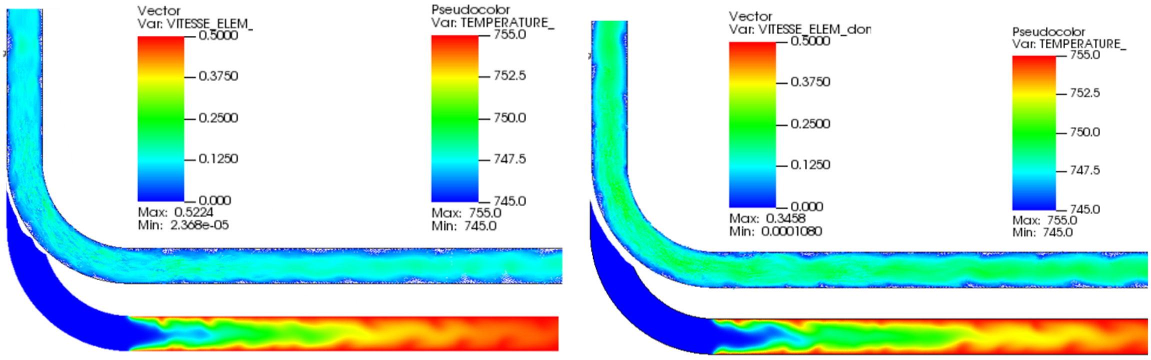

(a) 'DNS' M2

(b) LES M2

Figure 3.7. – Velocity vector & temperature field of Mesh 2 of geometry $s_{2,2}$ under $\Delta = 10K$ applying (a) 'DNS' and (b) LES.

3.3.5.2. RANS κ-ϵ models application

In the context of the two-equation κ-ϵ model, written in section 3.3.4.2, a dimensional analysis gives the turbulent viscosity as $\nu_t = C_\mu \frac{\kappa^2}{\epsilon}$. Two kinds of RANS κ-ϵ models implemented in TrioCFD are used in this work: the standard linear κ-ϵ model (LEVM) and a nonlinear one NLEVM proposed in **Baglietto et al. 2006**. The difference between the two κ-ϵ models lies in the modelling of the Reynolds stress tensors.

— For LEVM, the Reynolds stress tensors and the C_μ coefficient are given by:

$$\tau/\rho_0 = -\overline{\tilde{u}\tilde{u}} = \nu_t S_{ij} - \frac{2}{3}\kappa\delta_{ij},\ C_\mu = 0.09$$

— For NLEVM, quadratic terms are added in to Reynolds stress tensors with a modified C_μ detailed in **Baglietto et al. 2006**:

$$\begin{aligned}\tau/\rho_0 = -\overline{\tilde{u}\tilde{u}} = \nu_t S_{ij} - \frac{2}{3}\kappa\delta_{ij} + C_1\nu_t\frac{\kappa}{\epsilon}\left(S_{ik}S_{kj} - \frac{1}{3}\delta_{ij}S_{kl}S_{kl}\right)\\ + C_2\nu_t\frac{\kappa}{\epsilon}\left(\Omega_{ik}S_{kj} + \Omega_{jk}S_{ki}\right) + C_3\nu_t\frac{\kappa}{\epsilon}\left(\Omega_{ik}S_{jk} - \frac{1}{3}\delta_{ij}\Omega_{kl}\Omega_{kl}\right)\end{aligned}$$

$$\text{along with } C_\mu = \frac{2/3}{A + \frac{\kappa}{\epsilon}\sqrt{\frac{1}{2}S_{ij}S_{ij}}}$$

where $S_{ij} = \left(\frac{\partial U_i}{\partial x_j} + \frac{\partial U_j}{\partial x_i}\right)$ and $\Omega_{ij} = \left(\frac{\partial U_i}{\partial x_j} - \frac{\partial U_j}{\partial x_i}\right)$ with empirical coefficients C_i.

Figure 3.6(a) shows the NCL's pronounced local recirculation, challenging for models like LEVM that handle anisotropic turbulence poorly. As a linear model, LEVM provides only average details. However, NLEVM extends Reynolds stresses non-linearly, improving anisotropy handling, making it preferred for scenarios with significant recirculation, as in Figure 3.8. The models diverge more in their treatment of near-wall

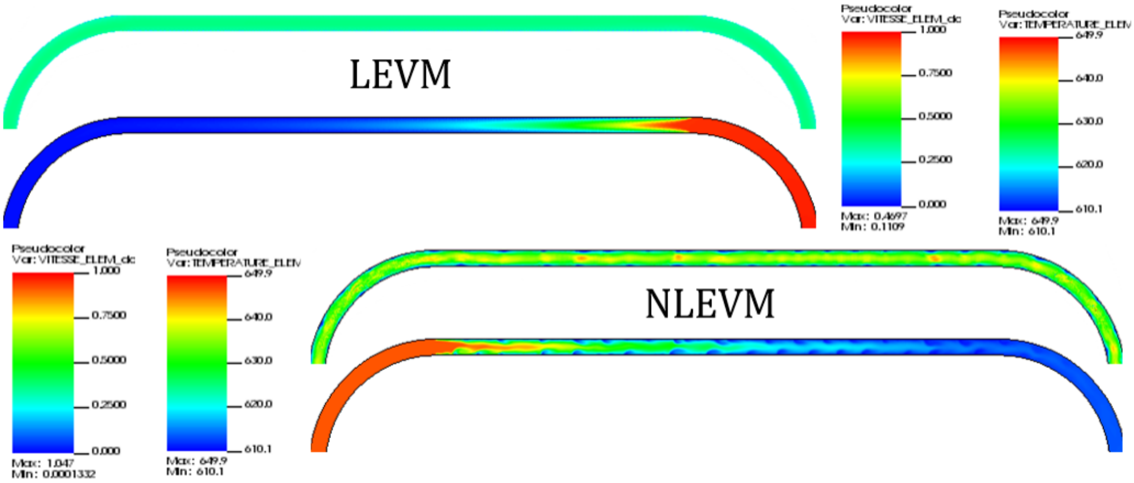

Figure 3.8. – Different (N)LEVM simulations of geometry $s_{1,2}$ under $\Delta = 40K$ for velocity (above) and temperature (below) field in 2D.

phenomena. LEVM uses a wall function that doesn't require a refined mesh (as modified M1 with y^+ in Section 3.3.6). Conversely, NLEVM uses an attenuating function near the wall requiring a refined mesh (as mesh M3 in Figure 3.6), offering more accurate near-wall turbulence resolution.

Despite this, it's worth noting that LEVM, by adjusting parameters in the wall function, can yield acceptable average flow-rate predictions using fewer CPU resources than NLEVM, offering a cost-effective solution for certain applications.

In conclusion, the choice between LEVM and NLEVM depends on the simulation's specific objectives. Different RANS methods can be employed to meet unique simulation goals and obtain desired QoIs. Therefore, model selection is not a one-size-fits-all decision, but should be tailored to each simulation task's particular needs and constraints.

3.3.6. Boundary Condition Modelling at Solid Walls

Refining near-wall mesh is key to prediction accuracy in complex industrial applications, but it can significantly increase computational time. Wall laws are often used to navigate this, enabling adequate wall distance (y^+) values and a proper transition to off-wall turbulent flow. For more on wall shear stress and wall function, refer to Appendix A.2.1.

TrioCFD offers robust methods with multiple options for effective wall law implementation. It integrates hydraulic and thermal formulas from Reichardt and Kader (**Angeli and Peybernes** 2016), compatible with both RANS and LES models. This combination provides a strong tool for managing computational challenges in complex industrial applications, balancing efficient resource use and prediction accuracy.

In hydraulic applications, the wall function for $U^+ = f(y^+)$ can be given as:

$$U^+ = \frac{1}{k}\ln\left(1 + ky^+\right) + A\left(1 - \exp\left(-\frac{y^+}{11}\right) - \frac{y^+}{11}\exp\left(-\frac{y^+}{3}\right)\right) \tag{3.14}$$

Similarly, in thermal applications, we have:

$$\begin{aligned} T^+ &= Pr\, y^+ \exp(-\Gamma) + \left[\frac{Pr_t}{k}\ln\left(1 + y^+\right) + \beta\right]\exp\left(-\frac{1}{\Gamma}\right), \\ \text{with } &\begin{cases} \beta &= \left(3.85Pr^{1/3} - 1.3\right)^2 + \frac{Pr_t}{k}\ln(Pr), \\ \Gamma &= \frac{0.01(y^+Pr)^4}{1+5y^+Pr^3}. \end{cases} \end{aligned} \tag{3.15}$$

where the Von Karman constant k is about 0.415 for flow driven by a pressure gradient. The turbulent Prandtl Pr_t is 0.9, which is typically applied for water, and the constant A is 7.44.

For pressure driven flow, with standard value of the Von Karman constant, Figure 3.9(a) provides a visual of the near-wall velocity profile for this wall function, covering three classic zones. Velocity profiles near the wall in CFD NCL simulations may not always follow the log-law, depending on flow conditions. The log-law is mostly valid for high Reynolds number flows with negligible buoyancy forces. Yet, for low Reynolds number or buoyancy-affected flows, secondary convection currents or density gradients can compromise its validity **Naveen et al.** 2014. Wall-attached structures and pressure fluctuations can also influence the near-wall velocity profile.

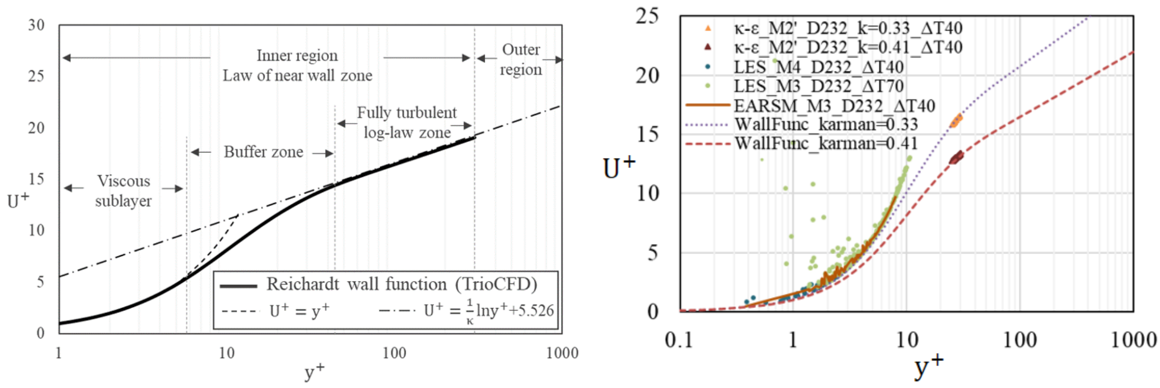

(a) Standard wall function in theory

(b) Different numerical models in TrioCFD

Figure 3.9. – Dimensionless velocity profile near wall for (a) standard wall function of hydraulic application; (b) different numerical models comparing to standard pressure-gradient flow in TrioCFD.

Past research recommends a Von Karman coefficient of 0.384 for zero-pressure-gradient boundary layers without heat transfer (**Osterlund and Sterlund** 2000**; Nagib and Chauhan** 2008). However, our study focuses on LES of non-pressure-gradient flows with heat transfer, examining the relationship between the dimensionless wall distance, y^+, and the dimensionless velocity, U^+, in the viscous sublayer. The Figure

3.9(b) shows findings from LES and RANS simulations:

- The LES shows generally higher U^+ values in the viscous sublayer than those seen in classic pressure-gradient-driven flows;
- Local recirculation near the wall leads to some scatter in the y^+ and U^+ data outside of the curve, reflecting changes in wall shear stress;
- Wall functions to model friction velocity near the wall have different values for the von Karman constant, k. When k is around 0.33, the average mass flow-rate can be accurately predicted from the reconstructed velocity profile.

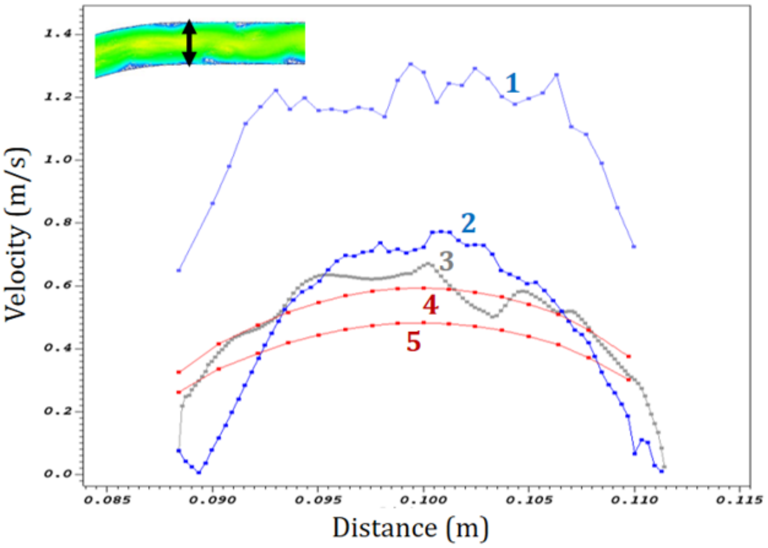

Figure 3.10. – Velocity profiles across the exit of elbow for (1) LES M2 with wall function; (2) LES M3 without wall function; (3) NLEVM (EARSM) M3 without wall function; (4) LEVM (κ-ϵ) M2 with wall function and modified k=0.33; (5) LEVM M2 with wall function and standard k=0.415.

Indeed, the velocity profile near the wall plays a critical role in shaping the global velocity field due to its effect on boundary layer development, wall shear stress, transition to turbulence, and turbulence production **Liang et al. 2022**. The Figure 3.10 illustrates the velocity profiles at the elbow exit as measured in both LES and RANS simulations, with and without the incorporation of wall functions. Please note that the velocity at the wall is zero, though it isn't depicted in the figure. From profiles 1 to 5, we can draw the following conclusions for our non-pressure-gradient flow with heat transfer in the NCL:

- The **Wall-modeled LES** tends to overestimate the velocity (see also Figure 3.6(b) with wall-resolved M2 solution). This discrepancy is due to the direct usage of the pressure-gradient sub-layer near the wall. On the other hand, the **wall-resolved LES**, which employs a refined mesh, generates a more accurate velocity profile.
- The **NLEVM**, also known as the Explicit Algebraic Reynolds Stress Model (EARSM), without a wall function yields predictions akin to those of the wall-resolved LES. This model capably captures the local recirculation near the wall.

— The **LEVM** which employs the standard κ-ϵ model and standard wall function, generates a substantially smoother velocity profile. While it fails to capture the complex physics, it compensates by allowing the average velocity to be attained through simple tuning of the wall function parameters.

In conclusion, wall functions play a critical role in accurately simulating flow characteristics, with the choice of the von Karman coefficient notably impacting the precision of the derived average velocity, especially in non-pressure-gradient flows with heat transfer. This study illustrates the unique strengths and weaknesses of both Linear and Non-Linear Eddy-Viscosity Models. While the former provides a decent approximation of average velocity with less computational demand, the latter more accurately represents local recirculation near the wall. However, wall-modeled LES fails to predict flow-rate well. Future research should delve deeper into model selection uncertainty, focusing on the choice of the von Karman coefficient (see section 5.1). This will further our understanding of model uncertainties, particularly in predicting flow-rate in complex fluid dynamics scenarios.

3.4. Numerical Modelling

3.4.1. Computational Domain and Mesh Generation

3.4.1.1. Physical and computational domains

The HHHC NCL system is divided into three specific physical regions: the heater, cooler, and adiabatic pipe domains, each having its unique influence on the mesh generation process:

— The **heater domain**, being the system's heat source, necessitates a finely detailed mesh to accurately model thermal gradients and buoyancy-driven flow.

— Similarly, the **cooler domain**, acting as the heat sink, requires detailed meshing for precise depiction of heat extraction and fluid property variations.

— The **adiabatic pipe domain**, despite having no heat transfer, needs localized refinement due to the crucial impact of geometric curvature on fluid dynamics.

Therefore, each of these physical domains plays a specific role in the overall system performance and must be carefully considered during the mesh generation process. The computational domain, a combination of these domains, highlights the complex interplay of thermal and fluid dynamics within the NCL.

3.4.1.2. Mesh generation by platform SALOME

An appropriate mesh is crucial for accurate CFD computations. Meshes were generated using the SALOME platform[3], discretizing the computational domain. Visual inspection initially assesses mesh refinement and uniformity. Greater refinement is needed in areas with expected flow recirculation, as depicted in Figure 3.11(b).

---

[3] https://www.salome-platform.org/

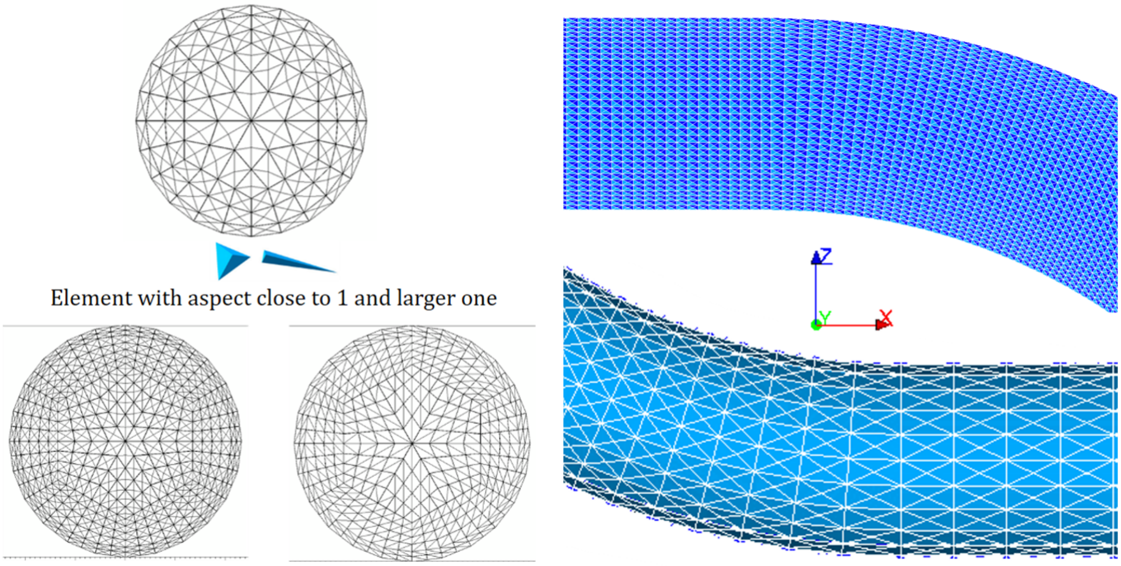

(a) Cross section

(b) Curved section

Figure 3.11. – Mesh generation by Salome for HHHC loop of geometry $s_{1,1}$ (a) in cross sections with different refinement; (b) in curved sections of Mesh1 in 2D and Mesh0 in 3D.

However, elongated cells can be used in regions with one-way velocity to save computational resources. In Figure 3.11(a), the cell aspect ratio, comparing the largest to smallest dimension in a mesh cell, is a practical evaluation metric. Higher aspect ratios may be acceptable if the flow aligns with the element's major dimension. Typically, the aspect ratio should be under 5, but can reach up to 30 in certain flow configurations. The cell shape also significantly affects numerical solution accuracy.

In grid refinement, without established order accuracy, three solutions with varying grid sizes are recommended by **Roache 2001**. In 3D non-structured meshes, the characteristic mesh size is estimated as $h = \left[\frac{V}{N}\right]^{1/3}$, where V represents total mesh volume and N the cell count. Isotropic refinement in Cartesian directions is usual, with structured refinement chosen at ratio 2. Table 3.8 provides a list of structured refined meshes for $s_{1,1}$ geometry (Table 3.2) in both 2D and 3D representations. Note that Mesh 2 is the upper limit in 3D due to its high computational demand.

In conclusion, this study emphasizes spatial convergence, numerical solution uncertainties identification, and quantification. Cell shapes critically influence simulation results, prompting preference for regular tetrahedra (3D) and triangles (2D) in future research. Given high computational demand, we will typically use 2D simulations, unless stated otherwise, in this thesis to develop an effective scaling methodology.

Table 3.8. – Mesh refinement in 2/3D for geometry $s_{1,1}$ of Table 3.2

Mesh	**Mesh 1**	**Mesh 2**	**Mesh 3**	**Mesh 4**
		3D mesh		
Tetrahedra	7.37E+06	5.90E+7	4.72E+08	**3.77E+9 !**
$h_{average}$	1.12E-03	5.60E-04	**X**	**X**
h_{min}	7.14E-04	3.57E-04	**X**	**X**
		2D mesh		
Triangle	2.25E+05	9.01E+05	3.60E+06	1.44E+07
$h_{average}$	1.13E-03	5.64E-04	2.82E-04	1.41E-04
h_{min}	6.95E-04	3.48E-04	1.74E-04	8.69E-05

3.4.1.3. Partition of computational domain

Parallel computation, vital for managing CPU capacity and time, partitions the domain into subdomains for manageable computation. TRUST/TrioCFD utilizes METIS [4] for mesh partitioning, creating ghost points for inter-partition communication. For instance, Figure 3.12(a) shows a mesh divided into 32 equally sized partitions along the centerline.

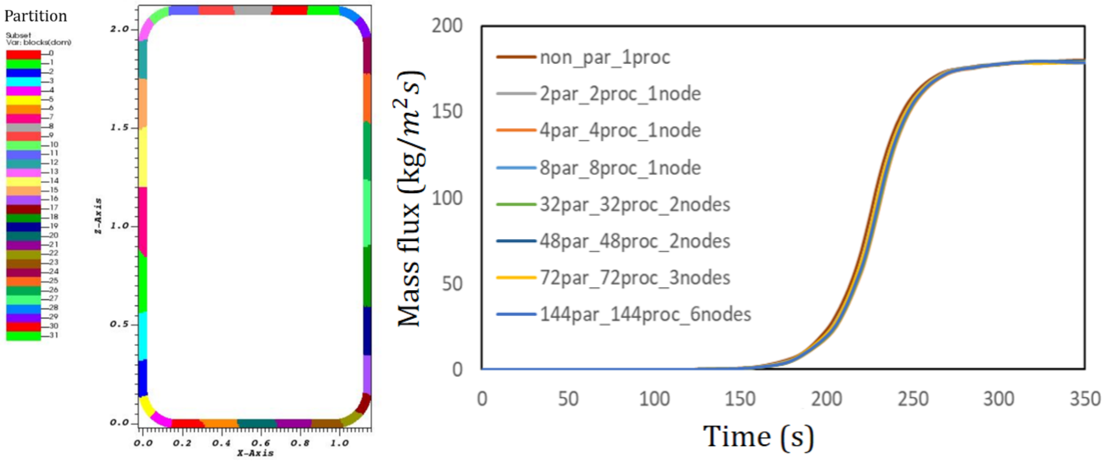

(a) Partitions

(b) Mass-flux for different partition

Figure 3.12. – Geometry $s_{1,1}$ with Mesh 2 (a) under 32 partitions by METIS library; and (b) partition number study in a cluster with different combination of processors and nodes.

With refined meshes, increased partitions could result in discontinuity and amplified communication surface. However, careful partitioning can form subdomains with minimal exchange surfaces, enhancing computations and lowering errors. Fig-

---

[4] https://github.com/KarypisLab/METIS

ure 3.12(b) shows minor partition exchange errors, indicating a consistent system behavior regardless of partition numbers, thus alleviating these concerns.

In conclusion, for a processor with 1.8GiB of memory utilizing the cluster (detailed in Table 6), it is recommended to maintain around 20K cells per partition to maintain the computational efficiency and processor performance, especially for meshes exceeding 2 million cells. For more details about processor performance study balancing the computation and communication overhead, please refer to Appendix A.4.

3.4.2. Numerical Methods

3.4.2.1. Temporal discretization

Temporal discretization plays a pivotal role in the numerical solution of fluid dynamics problems. It refers to the approximation of time-derivative terms in the governing equations, that convert the algebra-differential problem into an algebraic one at every step of the time serie. Different methods shown in Table 3.9 offer various advantages and challenges.

Temporal discretization schemes in TrioCFD

Temporal discretization methods can be broadly categorized into explicit and implicit methods:

- **Explicit methods**, such as the forward Euler method, are relatively simple and computationally efficient per time-step. However, they are conditionally stable and necessitate small time steps to ensure stability, especially for stiff problems commonly encountered in fluid dynamics.
- On the other hand, **implicit methods** remain stable regardless of the time step size. For turbulent flows, which often demand small time steps due to rapid variations in velocity and pressure, implicit methods can provide improved efficiency ($\min(x)/x$ with x=CPU*h). In TrioCFD, a multiplicative factor of time step can be eventually applied to speed up a calculation within the accuracy towards the stationary state in a time-marching procedure, provided that the stability is respected for such implicit method.
- The **semi-implicit (SIm) method** serves as a modification to the explicit method by solving the diffusion term implicitly. This approach boasts high accuracy but does not necessitate the solution of a linear system, thereby maintaining computational time between that of explicit and implicit methods.

Temporal discretization schemes versus flow characteristics

Advanced methods such as Runge-Kutta and Adams offer greater accuracy than the basic Euler method, as they consider not only the current state solution but also its higher-order derivatives or multiple past states. The choice of temporal discretization method, whether explicit or implicit, is determined by the specific characteristics of the flow:

- Explicit methods can be more efficient for steady flows or predictable conditions due to their computational simplicity. However, stability can be compromised unless the time step is small, leading to increased computational effort for

Table 3.9. – Classification of temporal discretization methods in TrioCFD

Method	**Scheme**	**Common order**	**Type**
Single-step	Euler Modified Euler Runge-Kutta	1st (can be) 2nd 2nd to 4th	Explicit/Implicit Semi-implicit Explicit/Semi-implicit
Multi-steps	Adams-Bashforth Adams-Moulton	2nd to 5th 2nd to 5th	Explicit/Semi-implicit Implicit

unsteady problems or ones with short timescales.

— In the case of incompressible flows, which can be either laminar or turbulent, the pressure evolves at an infinite speed, requiring implicit time integration methods. These methods are stable and can handle larger time steps, making them suitable for unsteady flows or ones with strong pressure-velocity coupling.

— Unpredictable flows, such as turbulence, usually require more sophisticated implicit methods due to their complex and nonlinear nature. In natural circulation systems, where buoyancy drives flow, stability is crucial, making implicit methods effective.

For natural circulation flows, the stiff nature of the equations, arising from the coupling of momentum and energy equations via the buoyancy term, favours implicit methods. Moreover, the turbulence kinetic energy budget may show either extra dissipation or production, depending on the scheme's stability. Methods like the Runge-Kutta algorithm, which damp the smallest scales, can introduce numerical dissipation proportional to the time step size (**Coleman** 1992).

Table 3.10. – Comparaison of time discretization methods for turbulent natural circulation flows

Scheme	**AM2/Implicit**	**RRK2/SIm**	**RK2/SIm**	**RK2/Explicit**
Time step size (s)	2.25E-03	1.58E-04	1.46E-04	1.82E-05
CPU time (CPU*h)	~ 2 000	~ 16 000	~ 16 500	~ 100 000
Efficiency	1	0.123	0.120	0.021
Average velocity (m/s)	0.154	0.152	0.159	x

Inline, Table 3.10 illustrates how implicit methods, like the 2nd order Adams-Moulton (AM2), have distinct benefits over other methods, such as the 2nd order semi-implicit (Rational) Runge-Kutta (R-RK2). For the reference calculation AM2, we set up a study spanning 100 seconds of physical time using the M3 mesh of the geometry $s_{2,2}$ as presented in Table 3.2. The time step size, chosen based on a solution convergence study (see the relevant section 3.5.1.3), is 2.25E-3. This study used 2K CPU hours, rendering it eight times faster than the semi-implicit method and almost 50 times faster than the purely explicit method, which wasn't even launched due to its inefficiency. Eventually, the output of simulation, the average velocity, shows only slight difference with large gap of efficiency.

In conclusion, the choice of the most suitable method relies on several factors, including the type of flow (laminar or turbulent), the stiffness of the problem (incompressible or compressible), and the available computational resources. For incompressible laminar flows, the semi-implicit method, which combines the advantages of both explicit and implicit methods, can be beneficial despite the CPU cost. However, for complex incompressible turbulent flows typically found in natural circulation systems, higher-order implicit methods often prove to be the most effective choice. These methods offer a favorable balance between accuracy and stability, making them particularly suitable for these applications.

3.4.2.2. Spatial discretization

In our simulations using TRUST platform, we employ a second-order centered scheme for handling the diffusion operator. As for the advection terms, various discretization schemes are available, each with its respective pros and cons listed in Table 3.11. The selection of an appropriate scheme depends on several critical factors:

- The complexity of the problem: **higher-order** schemes are preferred for turbulent flows, while lower-order ones can often adequately handle laminar flows.
- The **consistency with the order** of time discretization: it's essential to align the order of the general numerical scheme to prevent degradation caused by one of the schemes.

Table 3.11. – Classification of spatial discretization methods in advection term of TRUST/TrioCFD

Scheme	**Order**	**Advantage**	**Limitation**
Upwind	1st	Simple and stable, incorporates direction of flow	Diffusive, not accurate for problems with sharp gradients or discontinuities
MUSCL	2nd-3rd	High resolution, handles sharp gradients well	More complex to use, may produce spurious oscillations near discontinuities
Hybrid	Varies (1st or 2nd)	Switch between schemes to optimize accuracy and stability	Complexity of implementation, choice of switching criteria can impact performance
Center	2nd	Simple and high order accuracy for smooth solutions at low local Reynolds or Peclet numbers	Can cause numerical instability and spurious oscillations for advection-dominated problems, not well-suited to discontinuities

Considering the previous discussion for temporal discretization, we first applied a semi-implicit time integration method in a laminar flow regime. This required a hybrid scheme, essentially an adapted, stabilized centered scheme with upwind weight varying between 0 and 1. For turbulent flows with potential centrifugal effects, we used a 2nd-order Adams-Moulton (AM2) method and a 2nd-order centered differencing scheme to maintain accuracy, especially with strong velocity gradients along the loop.

In conclusion, the complexity of the flow regime and the necessary synchronization with the time discretization order drive the choice of spatial discretization scheme for the advection term in CFD simulations. Adaptability and careful selection are pivotal for obtaining accurate and reliable results.

3.5. Verification and Validations of NCL Simulations

Verification and Validation (V&V) activities are crucial in the field of CFD, ensuring numerical and physical accuracy. V&V methods offer a systematic way to ensure the quality of numerical simulations. Verification ensures the correct implementation and operation of a computational model. Conversely, validation evaluates the model's ability to accurately reproduce real-world phenomena or experimental data, such as natural circulation systems. These procedures are key in establishing trust in CFD simulations by showcasing the accuracy and reliability of the computational models used (**Roy and Oberkampf** 2011).

3.5.1. Verification of Simulation Solutions

Section 3.2 of the **ASN and IRSN** 2017 Guideline defines verification as a process to check whether equations are accurately solved numerically and from a data processing standpoint. Verification is about numerical methods, algorithms, their implementation, data flow diagrams, IT programme architecture and compliance with programming rules.

Practically, verification involves calculating test cases and comparing results to an analytical or reference solution (**Bestion et al.** 2016). However, a common belief is that accuracy verification for complex problems (like full N-S equations of fluid dynamics) is not feasible since exact solutions only exist for simple problems. This belief has led to disorganized code verification. Yet, systematic approaches like grid convergence tests are practical and efficient **(ASME** 2009**)**.

Section 2 of **ASME** 2009 VVUQ Standard mandates both code and solution verification, mathematical activities unconcerned with simulation model results' agreement with physical data. In general,

- Code verification checks code correctness and involves error evaluation for a known solution. The Method of Manufactured Solutions (MMS) generates exact analytical solutions needed for code accuracy verification if no known analytical solutions exist (**Roache** 2001). Alternatively, code-to-code comparisons can be made. Normally, this process should be ensured by code developers.
- Solution verification involves error estimation for the unknown exact solution. The most common method to obtain an error estimate is classical Richardson

Extrapolation (RE), and uncertainty quantification can be calculated by Roache's Grid Convergence Index (GCI) (**Roache** 2009).

In this section, we will follow the GCI method for **solution verification**, assuming a good code verification by TRUST/TrioCFD. Before quantifying numerical solution uncertainties, we must ensure that other errors are of lesser importance. This involves identifying, estimating, and comparing the errors.

3.5.1.1. Solution errors hierarchy

In CFD, ensuring the accuracy and reliability of computed solutions is paramount. The potential for solution errors, however, is a persistent concern that must be carefully managed. To better understand the sources of these inaccuracies, solution errors in CFD computations are typically divided into several categories, establishing a solution errors hierarchy.

Discretization Errors

Discretization errors arise when converting continuous mathematical models into a suitable discrete form for computation. Fluid dynamics problems are naturally continuous and described by differential equations. However, computational systems can only solve algebraic equations, necessitating a transformation of the original differential equations into a discrete representation. Discretization entails dividing the problem into manageable discrete components in both space and time. This computational process inherently introduces discretization errors, which significantly impact the overall accuracy of the computed solution.

Iteration Errors

Iteration errors, described in **Bestion et al.** 2016), are the second type of solution errors we encounter. They come into play when we solve the algebraic set of equations that represent our problem. We use certain methods, called numerical methods, to do this. Due to computational resource limitations, iterative solvers are a common type of numerical method employed.

Round-off Errors

The final category in the hierarchy of solution errors is round-off errors, which stem from the limited precision of computer arithmetic. Due to the finite number of digits that computers can handle, the precision of calculations is constrained. Although these errors are typically small, they can accumulate over time, especially in long or high-precision simulations, resulting in significant discrepancies in the final results.

To evaluate round-off errors, we can examine continuity errors in the time step. These errors indicate deviations from the conservation equation, where ideally the cumulative continuity errors for a flux field should be zero. In our simulations, we find that the cumulative continuity errors remain below 1^{E-16}, which is at the limit of double precision round-off error. This suggests that round-off errors may be negligible compared to other types of solution errors. Based on these findings, it is reasonable to minimize the focus on the impact of round-off errors in further studies.

In conclusion, it's particularly important to note that modelling error is a coupled error. The choice of model can influence the discretization process, and likewise, the chosen method of discretization can impact the fidelity of the model. By partially acknowledging and addressing the intertwined nature of **modelling errors**=**physical modelling errors** + **numerical solution errors** (**discretization**+**iteration**+**round-off errors**), also shown in Figure 2.3, we can more effectively enhance the accuracy and reliability of simulations.

3.5.1.2. Iteration errors

Iteration errors can vary based on the problem's complexity and the precision of the method used. Several factors can help manage and minimize these errors:

1. **Numerical methods/solvers selection**: The choice of solver can introduce iteration errors. For instance, iterative solvers like GMRES, BiCGSTAB, or conjugate gradients might not fully converge within a set iteration limit when used with implicit discretizations, leading to some degree of error. Similarly, multi-grid methods may fail to converge satisfactorily if the properties of the problem are not aligned with the multi-grid approach.
2. **Stopping criterion**: The iterative process should refine the solution until it closely approximates the exact solution, typically achieved using a predetermined threshold or maximum iteration number.
3. **Problem complexity**: More complex problems may require more sophisticated methods to minimize errors.
4. **Cost considerations**: While direct solvers can eliminate iterative errors, the time and storage resources they require might not be feasible for larger applications.

By carefully monitoring these factors, it is possible to effectively maintain an acceptable magnitude of iteration errors and ensure the balance of accuracy and CPU cost. For instance in Table 3.12, a comparison between computations involving 2.4 million (M3) and 7.2 million (M4) elements also demonstrates how iteration errors evolve with different iteration solvers in the face of varying algebraic system sizes.

The PETSc library[5] is used for the pressure matrix factorization, offering a choice between direct methods (like Cholesky factorization), and iterative methods like GCP, or multigrid solvers like HYPRE's BoomerAMG. The comparison shows that iterative methods can save memory at the cost of increased computation time. Multigrid methods balance between these extremes, making direct methods a good initial choice for the pressure solver.

For time discretization, we used an implicit scheme (2nd order of Adams-Moulton) in this LES study. We evaluated only iterative solvers due to the high cost of direct solvers. Tighter thresholds usually reduce computational efficiency without significantly affecting the output. Therefore, careful selection of numerical solver parameters can ensure acceptable iteration errors, but the trade-off between accuracy and computational cost is still crucial in CFD.

---

[5] https://petsc.org/release/

Table 3.12. – Iteration errors study for different numerical solvers & thresholds.

M3 with around 2.4E+6 elements & $dx_{\min}$= 1.6E-4 with 128 processors										
Pressure solver	Direct /Cholesky								Iterative /PCG	Iterative/ Multigrid
Implicit solver (time integration)	Direct /Cholesky	Iterative /GMRES			Iterative /IBICGSTAB	Iterative/Multigrid/Cli				
Threshold (max iter. numb.)	x	10^{-9} (5)	10^{-9} (10)	10^{-9} (15)	$--$ (10)	10^{-5} (130)	10^{-7} (130)	10^{-9} (130)	10^{-7} (130)	10^{-7} (130)
Efficiency	0.01	0.84	0.77	0.71	1	0.62	0.58	0.53	0.15	0.24
RAM(GiB)	123	49	49	49	52	60	60	60	29	33
Average massflux	x	129.2	128.9	128.8	128.3	129.2	129.3	128.5	129.0	129.3
M4 with around 7.2E+6 elements & $dx_{\min}$= 9.4E-5 m with 384 processors										
Normalized Eff.			0.70		1		0.81			
RAM(GiB)			261		271		299			

For the smaller grid number (M3), the Improved Stabilized Bi-Conjugate Gradient (IBICGSTAB) shows high efficiency for non-symmetric systems, with Generalized Minimal Residual (GMRES) following, and multigrid methods ranking third. However, for larger problems (greater mesh number in M4), the benefits of multigrid solvers become clear, while GMRES performance drops. Multigrid methods, including Algebraic Multigrid (AMG), have several advantages over Krylov subspace methods like GMRES or BiCGSTAB for large-scale problems, including optimal complexity, robustness, and grid-level scalability.

In summary, each of these sources of iteration errors requires thoughtful consideration and tailored strategies to minimize their impacts, thereby enhancing the reliability and accuracy of the CFD simulations. As illustrated in the Table 3.12, when parameters for diverse iterative solvers are selected wisely, the mass-flux results remain similar (less than 1% discrepancy). This difference should be compared with discretization error order, which will be explored in the following sections. Also, it's crucial to note that while maintaining a comparable level of iteration error, the computational cost emerges as a significant factor to consider. For problems of smaller scale, the IBICGSTAB solver may be employed, whereas for larger and more intricate problems during the scaling process, a multigrid solver proves to be more robust before grid-level scalability.

3.5.1.3. Discretization errors

In CFD simulations, iterative schemes are widely used to solve the complex, nonlinear matrix equations. Once iteration errors are minimized, focus shifts to discretization errors which become significant when simulations need precise resolution of critical flow structures, like turbulent mixing layers. These errors, however, carry inherent uncertainty due to our incomplete knowledge of their actual value, leading to epistemic uncertainties that can affect the accuracy and reliability of final results, particularly when working on a single grid.

To address this, we will investigate both temporal and spatial discretization errors, primarily using the GCI method to estimate the discretization error, particularly for non-linearity problems (**Bect et al. 2021**). This approach aids in understanding the origin, impact, and potential strategies for effectively managing these errors. The ultimate goal is not just to estimate these errors but to quantify the associated uncertainties.

Solution convergence for time discretization

In our study, due to simulation challenging with high Reynolds number, the turbulence model (LES WALE) is applied with an expected 2nd order of convergence (2nd Adams-Moulton and Center scheme for advection term), where different step sizes can be chosen as long as the accuracy is guaranteed.

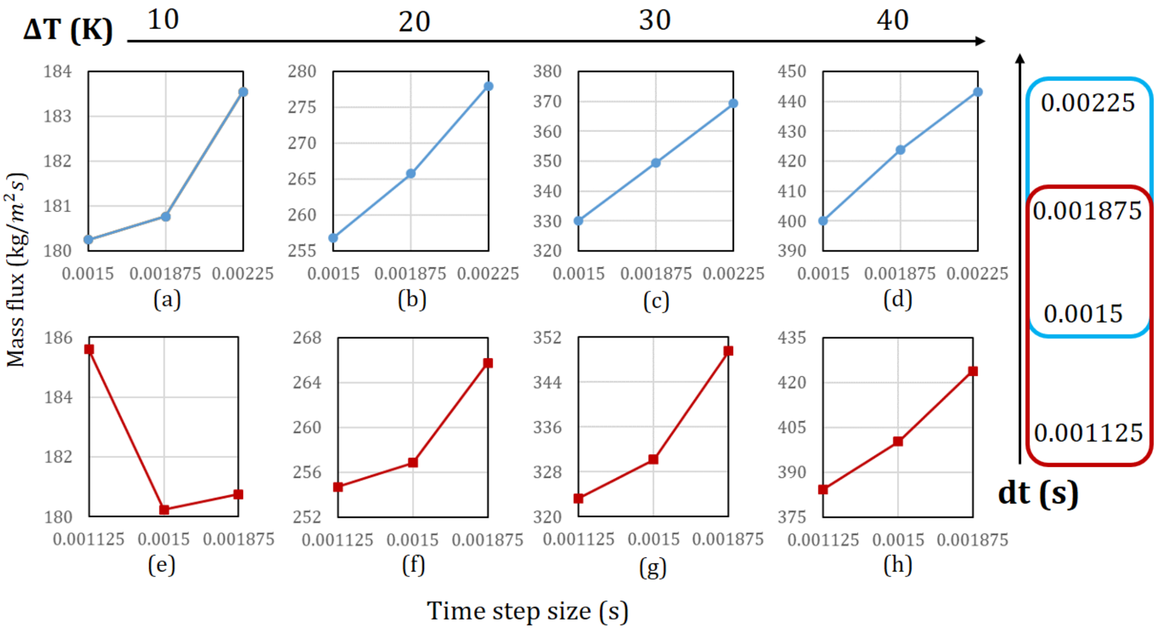

Figure 3.13. – Investigation of LES simulation solution convergence for geometry $s_{1,2}$ for time discretization with different temperature (from $10K$ to $40K$) and 2nd order Adams-Moulton time steps (from larger to smaller combination).

Therefore, we may wonder what is the solution convergence response between time dynamics (dt) and physical stiffness (ΔT) for given grid size? Figure 3.13 displays a study in the coordinate system between Reynolds number (related to ΔT) and time step size (dt). Solution convergence was observed for three grid points. Larger time step sizes reduce convergence capacity for larger Reynolds numbers, whereas smaller time step sizes improve convergence for larger ΔT. On the other hand, such combination is too small in Figure 3.13(e) with smaller Reynolds number where the time resolution is excessive and out of balance. Because excessively small time steps can lead to divergence if they attempt to resolve temporal scales that are smaller than the grid size can capture, especially when the Courant number becomes inappropriately low, signifying an over-resolution of the time scale compared to the spatial discretization.

In summary, with appropriate grid size, achieving an optimal balance between temporal resolution (time step size) and the intensity of physical phenomena (like buoyancy force) is key to perform efficient and accurate CFD simulations. It's about refining the time step size to adequately capture the dynamics of the flow, without overshooting and causing unnecessary computational expense.

Spatial discretization errors

The appropriate grid size in a simulation is a balance between **fidelity and computational cost**. As per ASME 2009, both the grid resolution for the convergence study and the minimal resolution for capturing the physics of the problem should be carefully determined. When flow physics exhibit specific length scales, the **coarsest grid used in the convergence study must adequately resolve these scales**. This is vital in LES, where the filter length relates to the grid resolution, affecting energy partitioning between resolved and unresolved scales. Without due care, the problem may vary for certain coarse-grid resolutions due to major shifts in the boundary between resolved and unresolved scales. The same holds true for DNS, resolving all pertinent flow scales up to viscous dissipation, even in the frequency domain.

The systematic grid convergence approach needs careful application. Temporal convergence on an inappropriate mesh can be disastrous, and maintaining the CFL condition of less than 1 in implicit time integration may be ill-advised. These challenges don't diminish the need to study this effect. Figure 3.14[6] presents three refined meshes (M1/M2/M3) for different time steps. Each mesh studies its coupling effect via the time step size (dt). Coarser meshes may not clearly exhibit time discretization convergence, but it is valid for M3, even with geometry changes (from $s_{1,2}$ to $s_{2,2}$).

A constant ratio (dt/dx) provides unique insights: low ratios can lead to non-convergence, while high ratios demonstrate significant coupling between the LES filter length and grid resolution, as evident in the overlap of M2 and M3. In industrial applications, a CFL number around 2 is preferred, since a CFL <1 is computationally intensive and not suitable for implicit methods. According to ASME 2009, when the spatial grid is refined in a convergence study, the size of dt likely decreases due to numerical stability. Thus, dt is implicitly considered in the convergence study. The grid convergence test, which accounts for both spatial and temporal grid convergence, is implemented explicitly. However, challenges may arise when the numerical methods have different accuracy orders in space and time or in different spatial directions.

---

[6] See Table 14 in Appendix D for the dataset

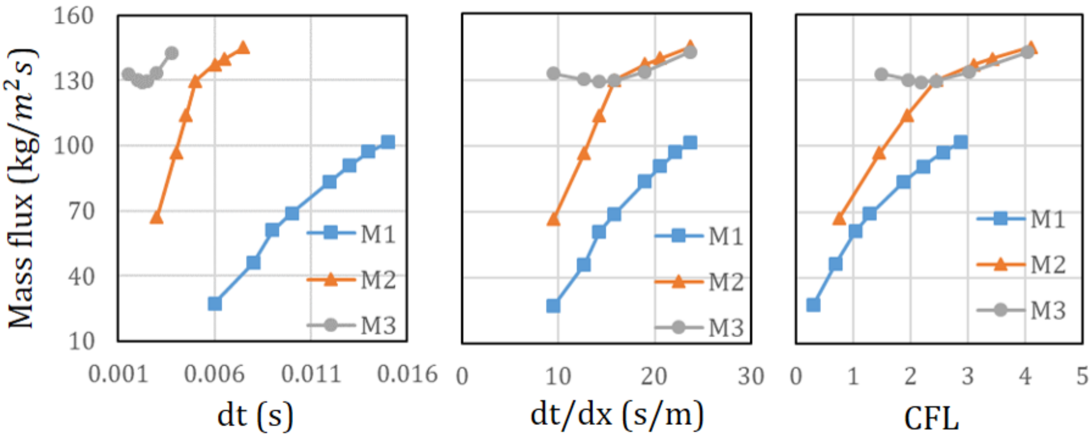

Figure 3.14. – Wall resolved LES simulation solution convergence of geometry $s_{2,2}$ under $\Delta = 10K$ for global discretization under (left) time step size dt, (middle) the ratio between time step and grid size dt/dx and (right) CFL number.

A systematic study of temporal discretization, available in Appendix A.1.2, further elaborates on this impact.

In conclusion, these observations provide valuable insights into how the interplay of time and space scale size for different axes of presentation. While no definitive answers are given, a compromise, between the mismatch of time-space scale size and the coupling effect of model-discretization, can be still given, so that three converged solutions can be given for further study. In the end, the exploration opens up avenues for further investigations and fine-tuning of these parameters for the discretization error estimation of grid-dependent model.

3.5.1.4. Numerical solution uncertainty quantification

Spatial and temporal discretization errors are the primary concerns in numerical solution errors, with iteration and round-off errors being of less significance. Two key strategies can be employed to estimate these discretization errors in CFD: a priori and a posteriori methods (**Jamelot** 2019):

- *A priori methods* predict error bounds before computation. Despite their theoretical appeal, they face challenges when dealing with nonlinearities and non-monotone nonlinear elliptic problems (**Abdulle and Vilmart** 2012).
- *A posteriori methods* estimate errors post computation and are now gaining prominence for their detailed error assessments.

In this work, we focus on the Grid Convergence Index (GCI) method for industrial applications. It uses either classical Richardson extrapolation (**Shyy et al.**2002) or recent least-squares extrapolation techniques (**Eça and Hoekstra** 2006) to estimate errors based on different grid sizes. The GCI method provides a 95% confidence interval for the solution by incorporating a safety factor (**Roache** 2016).

For the potential confusion of error/uncertainty, the pertinent definitions given by **IOS 1993** are as follows:

— error (of measurement): "result of a measurement minus a true value of the measurand"

— uncertainty (of measurement): "parameter, associated with the result of a measurement, that characterizes the dispersion of the values that could reasonably be attributed to the measurand"

The Grid Convergence Index (GCI) method as explained by ASME 2009 consists of these steps, along with the details of parameters shown in Table 3.13:

Table 3.13. – Estimation of numerical solution errors and uncertainties through GCI method based on Richardson extrapolation

Numerical solution errors	Grid sizes $\boldsymbol{h_i}$	$h_1 > h_2 > h3$
	Computed solutions $\boldsymbol{f_i}$	$f_1; f_2; f_3$
	Ratio $\boldsymbol{r}$	$r = h_2/h_3(> 1.3)$
	Apparent convergence order $\boldsymbol{p}$	$p = ln\left(\frac{f_1-f_2}{f_3-f_2}\right)/ln(r)$
	Extrapolated solution $\boldsymbol{f_{ext}}$	$f_{ext} = f_3 + \frac{f_3-f_2}{r^p-1}$
	Normalised relative error $\boldsymbol{e_n}$	$e_n = \left\lvert\frac{f_3-f_2}{f_3}\right\rvert$
	Estimated extrapolation error $\boldsymbol{e_{ext}}$	$e_{ext} = \left\lvert\frac{f_{ext}-f_3}{f_{ext}}\right\rvert$
Conversion	Safety factors $\boldsymbol{F_s}$	3 (or 1.25)
Numerical solution uncertainties	Grid Convergence Index $\boldsymbol{GCI}$	$GCI = F_s \cdot \frac{e_n}{r^p-1}$
	Uncertainty band $\boldsymbol{U_{GCI}}$	$U_{GCI} = GCI * f_3$
	Penalised uncertainty band $\boldsymbol{U_{num}}$	$U_{num} = U_{GCI}/k,\ k = 1.1 - 1.15$
	Confidence Interval $\boldsymbol{CI_{GCI}}$	$CI_{GCI} = [f_3 - U_{num}; f_3 + U_{num}]$

Procedure of numerical solution uncertainty quantification

1. Define a **representative mesh size**, $\boldsymbol{h} = (V/N)^{1/3}$, for unstructured meshes where V is total volume and N is cell count.
2. Opt for a **twofold refinement** with an integer scaling ratio greater than 1.3, according to **Dowding 2016**, and consider the reference solution as a benchmark. Uniformly apply grid refinement across all Cartesian directions. $\boldsymbol{h_3}$ denotes the finest grid size.
3. If both ratios are equal, calculate the **apparent order** $\boldsymbol{p}$ analytically from discrete solutions on the successively refined grids, along with the **extrapolated solution value**, **normalized relative error**, and **estimated extrapolation error**.
4. Determine the $\boldsymbol{U_{95\%}}$ **uncertainty range** in GCI by multiplying the **numerical solution errors** by a safety factor, $\boldsymbol{F_s}$.

5. The **safety factor**, informed by empirical studies, varies with the quality of available solutions: 1.25 for smooth grid convergence with plentiful solutions, and 3.0 for erratic grid convergence with sparse solutions.
6. Harmonize GCI's 95% confidence interval with international standard measures by converting $\boldsymbol{U_{GCI}}$ to $\boldsymbol{U_{num}}$ using a new penalizing factor $\boldsymbol{k}$ as per **ASME 2009**.
7. Center the confidence interval, $\boldsymbol{CI_{GCI}}$, on the finest solution for the highest fidelity.

Application of GCI method for TrioCFD simulation

To implement the GCI method, we need a set of converging solutions with progressively refined meshes. While turbulence models ideally require 3D grids due to their intrinsic eddy structure, we use the $s_{1,1}$ geometry for 3D calculations to balance accuracy and computational resources. Given the computational constraints of mesh M2, we use a significantly coarser mesh M0 for grid convergence study. Despite satisfactory flow structure representation, particularly the centrifugal effect at the elbow exit as shown in Figure 3.15[7], there is no observable convergence due to insufficient discretization. Consequently, we shifted to a 2D approach to focus on scaling methodology development, which readily allows for M3 and even M4 meshes as shown in Figure 3.14.

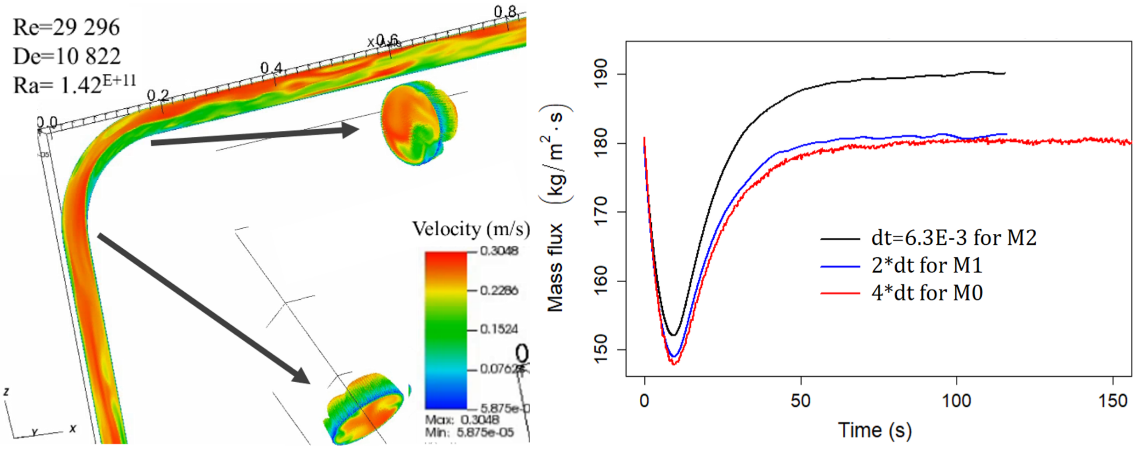

(a) Dean vortices mixed with turbulence (b) 3D time evolution for 3 successively refined meshes

Figure 3.15. – 3D fluid flow and convergence study for geometry $s_{1,1}$ under $\Delta = 10K$.

As a result, instead of Dean vortices[8] combined with turbulence in 3D, local recirculation is produced and propagated within the 2D configuration in the Figure 3.6(a), introducing a similar numerical challenge. As demonstrated in the previous section, a compromise has been made between time and space discretization, resulting in a time dynamics ratio dt/dx of 15 and a CFL number around 2 for M3 mesh.

---

[7] for more snapshots of the flow dynamics in Figure 33

[8] also shown in Figure 32

The results of the GCI calculations and the corresponding visual demonstrations can be found in Figure 3.16. The computed errors is transformed into numerical solution uncertainties, which is centered on the solution f_3, computed with the finest mesh, Mesh M3. The extrapolated solution, as the grid size approaches zero, is indicated and covered inside the range of confidence interval.

$\mathbf{f_i}$	**r**	**p**	$\mathbf{f_{ext}}$
61.2;114.1;129.2	2	1.81	135.2

$\mathbf{e_n}$	**GCI**	$\mathbf{U_{num}}$	$\mathbf{CI_{GCI}}$
0.117	0.0583	16.43	[112.76; 145.63]

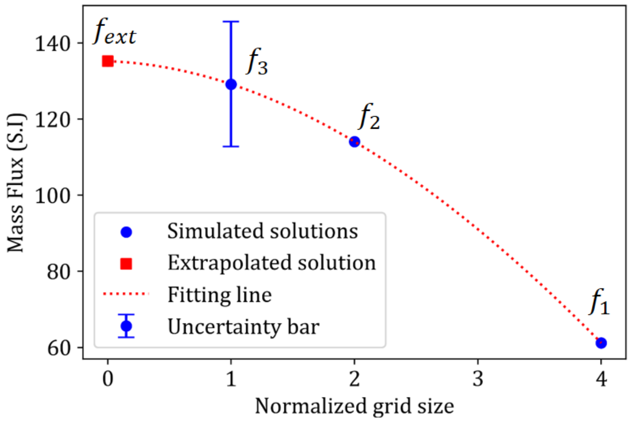

Figure 3.16. – Illustration of numerical solution uncertainties through GCI method in 2D for geometry $s_{2,2}$ under $\Delta = 10K$ along with data.

3.5.2. Validation of CFD Results

Following the section 3.3 of **ASN and IRSN 2017** Guideline, the validation process is ideally a two-step procedure carried out to minimize error compensations:

- **Separate effects validation**: This aims to validate the physical models of scientific computing tools under conditions that isolate major physical phenomena as much as possible.
- **Integral validation**: This stage checks the tool's ability to accurately simulate all physical phenomena and their interactions.

For practical numerical validation, **ASME 2009** outlines the steps in Section 7.3: (1) estimate uncertainty in experimental data; (2) estimate uncertainty for the numerical error in a simulation (solution verification as described in section 3.5); (3) estimate uncertainty in the simulation due to input parameter uncertainty; (4) evaluate the validation uncertainty; (5) Interpret the validation comparison.

Due to the lack of specific experimental data for our NCL with sodium coolant, we employ bibliographical results from **Vijayan et al. 2019** for validation. Our procedure focuses on two parts: physical confirmation on separate geometry effects and on integral effects from industrial correlations:

- Bibliographical results confirm ("validate") the **separate geometry effects** due to the absence of experimental data. This allows comparison of our CFD results with established trends.

— Empirical correlations from industrial research are used to validate our CFD solutions, serving as a robust reference for validation, especially in dimensionless analysis.

To ensure consistency in the validation process, uniform choices such as physical models, spatial mesh, temporal discretization, numerical schemes, and calculation options must be maintained across all validation cases. This ensures the credibility and accuracy of our CFD results.

3.5.2.1. Physical confirmation for separate geometry effects

Effect of loop elevation

A small increase in elevation leads to an increase in the buoyancy force, consequently augmenting the flow-rate. For instance, consider geometry $s_{1,2}$ with an elevation of 2.1 m, compared to $s_{2,2}$ with an elevation of only 1.3 m. The former demonstrates a larger flow-rate (around 180 to 130) under the same sink and source temperature difference, as shown in the respective Figure 5 and Figure 3.14.

Interestingly, there seems to be a compensatory region between the dominant buoyancy and friction zones where the natural circulation flow remains relatively unaltered despite changes in elevation. According to **Vijayan et al. 2019**, this occurs between 20 m and 30 m. Additionally, this critical elevation appears to be related with the heater power, and may also vary with the loop diameter and local loss coefficient.

Effect of loop pipe diameter

The pipe diameter plays a significant role in the functioning of a NCL. A larger diameter typically leads to an increased flow-rate, predominantly owing to a reduction in local pressure loss — the energy loss primarily associated with friction, but also factors like pressure gradients and specific pipe characteristics. Therefore the flow-rate increases with an increase in pipe diameter, which is consistent with the relation derived in Equation 0.30 in Appendix B.1:

$$\dot{m} = \left(\frac{2\rho^2 \beta_T g H Q_h}{C_p R}\right)^{1/3}$$

where Q_h is imposed heating power and flow resistence $R = (\frac{f L_t}{D} + K)/A^2$. Therefore, for a given input power Q_h, a larger loop diameter effectively reduces the resistance R (not considering friction factor f and other resistance impact K), thus enhancing the flow-rate. For different type of heat source, the supplementary study is shown in Appendix B.4.2.

Effect of heating transfer length

We define a heat transfer efficiency as the ratio of the temperature difference between the hot and cold leg to the heat source and sink, $\Delta T_{h,ss}/\Delta T_{hc}$. It's well known that a sufficiently large ratio of heating length to diameter (L_h/D) ensures full flow development (since the heat exchange mechanism differs between the thermal entrance zone and the fully developed zone). As illustrated in Figure 3.17(a), an increase in this ratio indeed enhances heat transfer efficiency. Moreover, similar to the effect of elevation, the impact of heating length is also associated with the diameter in Figure 3.17(b). Smaller pipe diameters can improve efficiency but at the expense of reduced flow-rate. Therefore, a balance must be struck between the pipe diameter and heating length to optimize heat transfer efficiency and flow-rate.

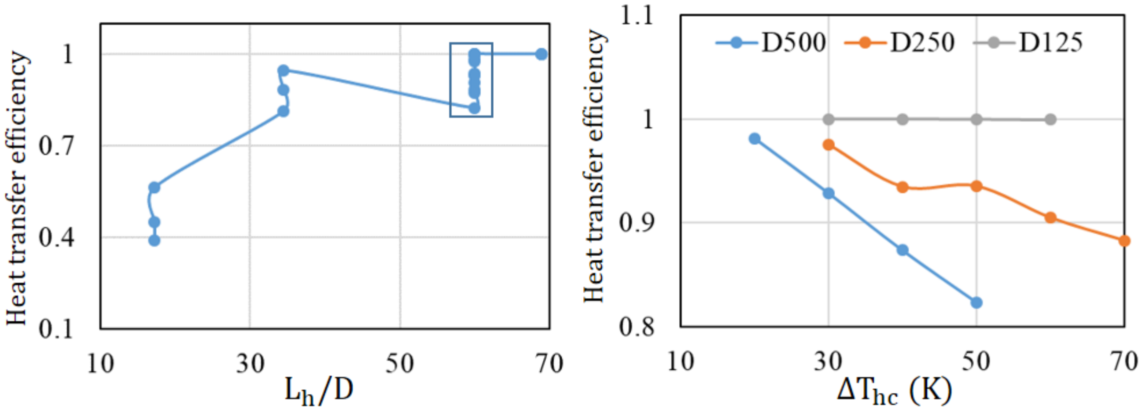

(a) Heating length impact

(b) Pipe diameters and power impact

Figure 3.17. – Heat transfer efficiency for (a) different ratios between heating length and pipe diameters, and locally (b) different sink/source temperature for $L_h/D = 60$ using three different pipe diameters.

Effect of curvature ratio

In the momentum equation for a NCL, as highlighted in Momentum equation 0.5, the total pressure loss comprises three main components: wall frictional effect, local pressure loss due to curvature effect, and additional pressure loss attributed to other influences (such as the inherent effect of turbulent flow regime). This relationship is detailed in the Appendix B.4.3 and is expressed as:

$$l_{eff} = 1 + \frac{L_{cp}}{L_t}\left(\frac{f_{cp}}{f} - 1\right) + l_{extra} \tag{3.16}$$

Where L_{eff} is normalized effective length of total pressure loss, L_{cp} is actual length of curved sections, L_t is the total length of loop, f_{cp} is friction factor due to curvature effect and lastly l_{extra} normalized length due to other physical effects. While, loss coefficients for standard and nuclear power plant-specific flow obstructions are often dictated by the Reynolds number. For turbulent flows, these coefficients stabilize beyond a certain Reynolds number (**Spedding et al. 2004**).

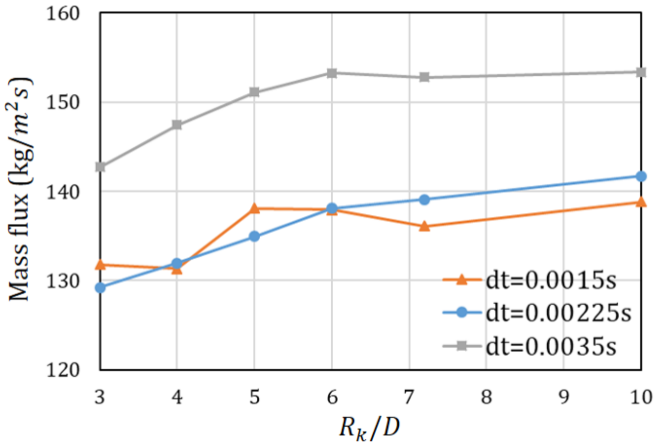

Figure 3.18. – Effect of curvature ratio for 6 different curvatures under different time dynamics using M3 of geometry $s_{3,i\in[1;6]}$ with ΔT=10K.

We examined curvature effects on flow-rates over time, holding other ratios constant. As we transition from elbow to curved pipe configurations ($R_k/D < 10$ to $R_k/D > 10$), turbulence increases, leading to enhanced flow-rates in Figure 3.18. Despite fluctuations possibly due to pressure loss from local recirculation, smoother curvature consistently results in higher flow-rates.

3.5.2.2. Physical confirmation for industrial correlations

While confirmation of geometry effects is important, industrial applications often favor physical correlations using dimensionless numbers for scalable configurations. Our initial step involved correlating modified Grashof Gr_m and Reynolds numbers Re_{ss} with dimensionless geometry factors N_G (Figure 3.19). This method enhances system understanding, aiding both research and practical uses. A dimensionless correlation for the steady-state mass flow-rate is provided in Appendix B.3 (**Vijayan et al. 2002**).

$$Re_{ss} = \left(\frac{2}{p}\frac{Gr_m}{N_G}\right)^{\frac{1}{3-b}} = C\left(\frac{Gr_m}{N_G}\right)^r, \text{with } C = \left(\frac{2}{p}\right)^r, r = \frac{1}{3-b} \tag{3.17}$$

where $Gr_m = \rho_0^2\beta_T g D^3 \Delta T_r/\mu^2$ with $\Delta T_r = Q_h H/(A_r C_p \mu)$ and $N_G = L_e/D$. It should be noted that ΔT_r is not necessarily equivalent to **source/sink temperature difference ΔT_{hc}** nor **hot/cold leg temperature difference at steady state $\Delta T_{h,ss}$**.

The dimensionless steady-state flow-rate data is compared with data from various flow regimes in the literature. The values of p and b for different flow regimes are listed in the Figure 3.19 [9] along with corresponding C and r values.

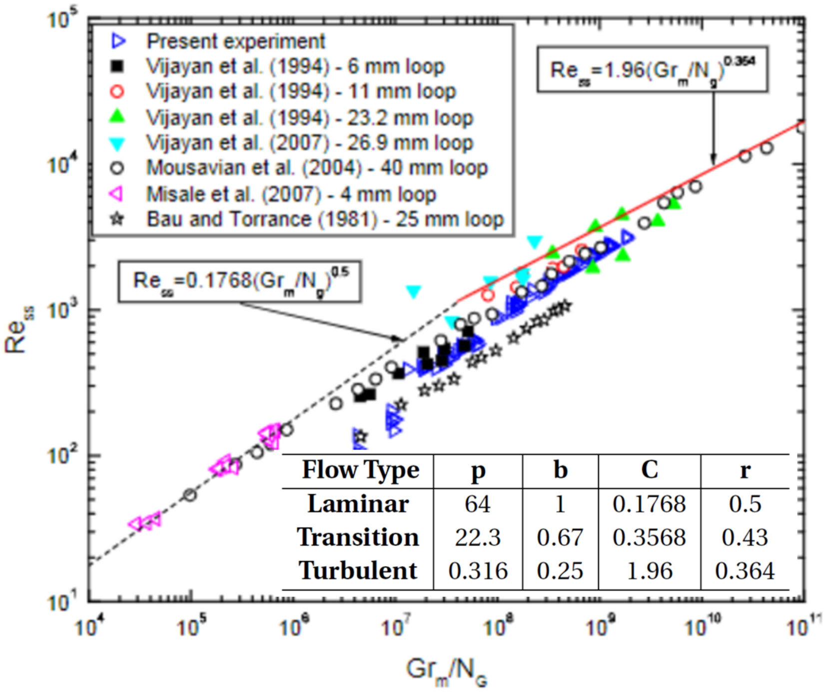

Flow Type	p	b	C	r
Laminar	64	1	0.1768	0.5
Transition	22.3	0.67	0.3568	0.43
Turbulent	0.316	0.25	1.96	0.364

Figure 3.19. – Correlation for NCL systems for different regimes (**Vijayan et al. 2008**).

As indicated in Table 3.14, the difference between $\boldsymbol{\Delta T_{hc}}$ and $\boldsymbol{\Delta T_{h,ss}}$ for $s_{1,3}$ is notably small due to its larger heating length ratio. Alternatively, Figure 3.20 can be considered, where Gr'_m uses the temperature difference directly from the source/sink. Conversely, Gr_m factors in the actual temperature difference, and the correlation performs better for turbulent flows, closely aligning with the empirical value of 0.364, as highlighted in red. However, for laminar flows, denoted in blue, the results are consistent because the heat transfer is highly efficient due to the low flow-rate.

In a specific rectangular loop, pressure loss rises due to both pipe friction and elbow curvature, represented by N_G. To consider the curvature effect, we use an effective length L_{eff} instead of total length L_t. We simplify this by using empirical curvature correlations, and more details of pressure drops at geometric discontinuities in steady state conditions can be found in Appendix B.4.3.

Correlations using effective length must account for both general straight pipe friction, curved pipe friction and even other physical effects like turbulence. This can be achieved by using the effective length in previous equation 3.16. In the thesis, the following empirical correlations **Crawford et al. 2007** have been applied to calculate the total equivalent length of pressure loss $(L_e/D)_{total} = (L_e/D)_{elbow} + (L_e/D)_{cp}$ due to only curvature effect from both elbow and curved pipe:

---

[9] Loop data from **Vijayan et al. 1994**, **2007**; **Mousavian et al. 2004**; **Misale et al. 2007**; **Bau and Torrance 1981**

Table 3.14. – Modified Grashoff values under different scenario

Parameter	ΔT_{hc}	$\Delta T_{h,ss}$	**Velocity**	$Gr_m(\Delta T_{h,ss})$	**Reynolds**
$s_{1,1}$	10	5.65	0.277	1.52E+11	3.70E+04
	20	9.02	0.379	3.32E+11	5.06E+04
	30	11.70	0.453	5.15E+11	6.06E+04
$s_{1,2}$	20	18.93	0.308	3.53E+10	2.06E+04
	30	26.53	0.400	6.43E+10	2.67E+04
	40	32.55	0.480	9.48E+10	3.21E+04
$s_{1,3}$	20	20	0.213	1.62E+09	7.13E+03
	30	30	0.275	3.13E+09	9.20E+03
	40	39.996	0.329	4.99E+09	1.10E+04

— For the curved pipe, an equivalent length can be written:

$$(L_e/D)_{cp} = 2.4792 f_{cp} Re^{0.25}/k \tag{3.18}$$

where k is curvature ratio found in Dean number $De = Re\sqrt{k} = Re\sqrt{D/2R_k}$ and f_{cp} can be calculated by different correlations in Table 10.

— For the pressure drop in an elbow bend, either these two can be used

$$(L_e/D)_{elbow} = 1.25 k^{1.5} Re^{0.35} \tag{3.19}$$

As shown in Figure 3.21 (a), an increase in the Reynolds number leads to a significant pressure loss, thereby inflating the dimensionless ratio N_G. This, in turn, results in a reduction in the x-axis value, making the correlation steeper. Using actual CFD data to calculate the pressure loss converted into a dimensionless ratio, we can plot the new correlation as shown in Figure 3.21 (b). Notable observations from the figure are:

— Laminar flows demonstrate substantial improvement, aligning with the empirical value of 0.5 for the exponent of the correlation.

— Turbulent flows don't exhibit significant changes due to the impact of other physical phenomena, specifically the presence of local circulation in the loop.

However, the correlation only provides steady-state information and does not capture the stability process, particularly the transition during the establishment of natural circulation. This limitation also applies to other proposed correlations, such as the thermal correlation utilizing Stanton number. To obtain a more comprehensive validation or confirmation, further dynamic analysis is needed, which requires benchmark simulations or experimental data.

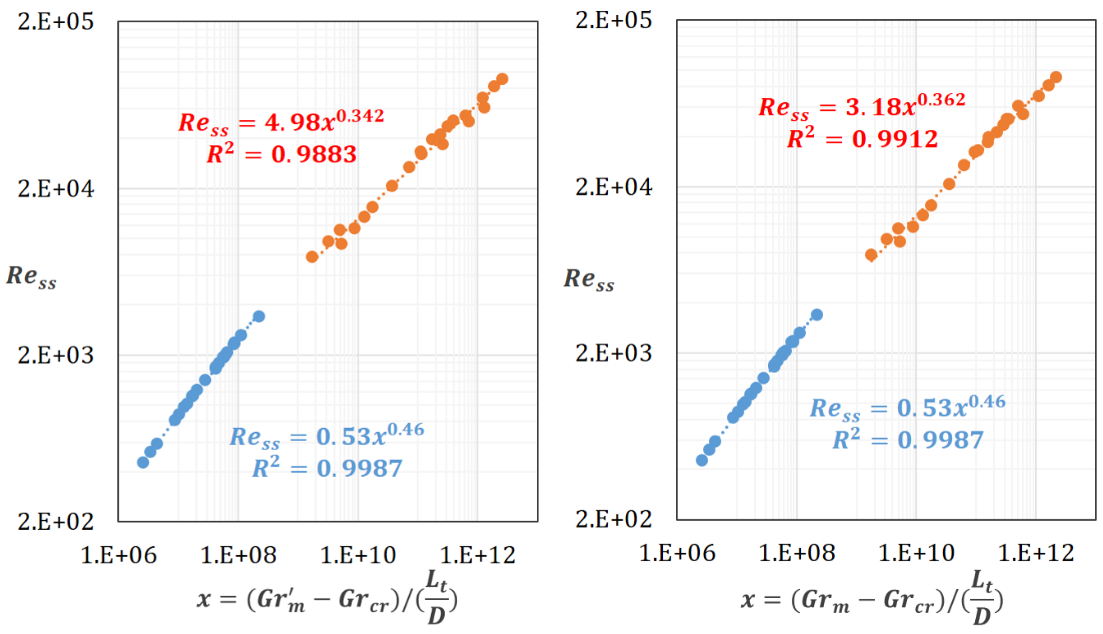

Figure 3.20. – Physical correlations with different heating length ratios for the modified Grashof number using: (left) ΔT_{hc}, and (right) $\Delta T_{h,ss}$.

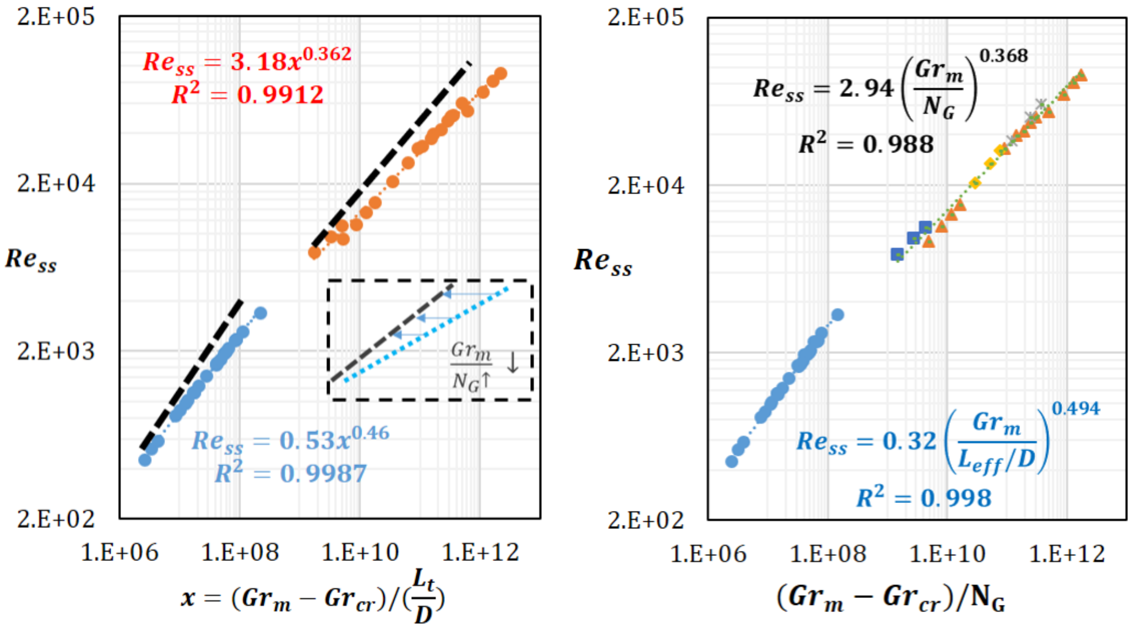

(a) Present CFD computations

(b) Literature corrections

Figure 3.21. – Physical correlations for different geometry factors by: (a) present CFD computations; (b) our CFD results using literature correlations.

3.6. Practical Guideline of NCL Computations for Different Fidelity Level

This chapter offers an in-depth exploration of the complexities involved in NCL simulations. It commences with an examination of the chosen geometry configurations, particularly the HHHC loop, and then delves into the scaling concerns associated with geometric designs. The discussion progresses to physical and numerical modelling, which are outlined in the order presented in Table 3.15, using the TrioCFD within the CEA platform TRUST. The chapter concludes with an emphasis on modelling evaluation, including Verification and Validation (V&V), as well as Uncertainty Quantification (UQ). These elements together constitute the guideline for NCL computations. This guideline also encompasses the investigation of the scaling effect on modelling uncertainties under different levels of fidelity.

As emphasized in Section 2.2.3.1, the adoption of different fidelity levels in simulations is essential to balance computational efficiency with precision based on distinct objectives. For general tasks like average mass flow assessment, Best-Effort (BEF) simulations are usually enough. They provide an optimal balance of accuracy and computational resource usage. However, for intricate details, such as dynamics or exact field distribution, are needed, High-Fidelity (HF) simulations are a must. Despite being more computationally intensive, these simulations offer detailed insights into complex phenomena, making them indispensable for in-depth analysis and future applications. Especially, The approach to HF simulations offers twofold benefits. They enrich the validation range with reference data and effectively manage scaling in NCL computations. While, the approach BEF can effectively help us investigate the larger scale problems.

Transitioning from the HF to BEF level is not a straightforward task. It involves a careful identification and simplification of the most influential physical phenomena within the NCL. This critical step ensures the verification of the less detailed models' accuracy while enhancing them through an upscaling process. The provided Table 3.15 further elaborates on these fidelity levels, offering comprehensive guidelines for NCL computations at both HF and BEF levels. It covers various aspects of modelling, verification, validation, uncertainty, and scaling for both types of simulations. By following these guidelines, researchers and engineers can effectively manage NCL computations in various settings, ensuring the ideal balance between computational resource usage and precision.

Table 3.15. – Practical guidelines of NCL computations for different fidelity levels.

Modelling/Simulation/Qualification Process			**High-Fidelity**	**Best-Effort**
Physical phenomena	PIRT		NCLs Physical Behaviors (§2.2.1)	
Physical modelling	Selection of SCT		TRUST/TrioCFD (§2.2.3.2)	
	Physical properties		§3.3.2	
	Assumptions & Approximations		Compressibility/Boussinesq approx. (§3.3.3)	
	Governing Equations (§3.3.4)		§3.3.4	
	Turbulence closure laws		LES WALE (§3.3.5.1)	RANS LEVM (§3.3.5.2)
	Solid walls treatment (§3.3.6)		Wall resolved	Wall modelled
	Heat transfer model		§3.3.4.3	
Numerical modelling	Domain/Mesh/Partition		§3.4.1	
	Numerical Methods	Discretization techniques	Finite Volume Elements (VEF) (§A.1.1)	
		Temporal discretization (§3.4.2.1)	Implicit (≥ 2nd)	Euler implicit
		Spatial discretization (§3.4.2.2)	Center/Hybrid	Upwind
		Iterative solvers	§3.5.1.2	
Verification	Code Verification		ASME 2009 Standard or TrioCFD log	
	Solution Verifications	Solution errors hierarchy	§3.5.1.1	
		Iteration errors	§3.5.1.2	
		Discretization errors	§3.5.1.3	
Validation	Experimental data or Reference calculation		§2.2.2	
	Separate effects validation/confirmation		§3.5.2.1	
	Integral validation/confirmation		§3.5.2.2	
Uncertainty	Numerical solution uncertainties		§3.5.1.4	
	Numerical model uncertainties		§5.2.1	
Scaling	Numerical modelling uncertainties under Scaling		§4.2.3.3 / §5.5 and Outlooks	

4. Scaling Analysis of Numerical Solution Uncertainty

失之毫厘，差之千里。

- 《左传》

A millimeter miss is as good as a thousand miles.

- "Zuo Tradition" (4th century BC)

Sommaire

4.1. Introductory Remarks

Thermal-hydraulic system predictions in nuclear power plants, using CFD simulations, require uncertainty quantification of the computed results. This UQ should provide a certain degree of confidence and coverage. Multiple sources of uncertainty must be evaluated, including model parameters, numerical uncertainties, experimental data, boundary and initial conditions (BICs), geometric uncertainties (**ASME 2009**). The NEA benchmark has outlined the key uncertainties to be quantified in Figure 4.1 for practical nuclear applications (**Fokken et al. 2017**), where the mesh and time scheme etc. stand out and belong to numerical uncertainties shown in Figure 2.3.

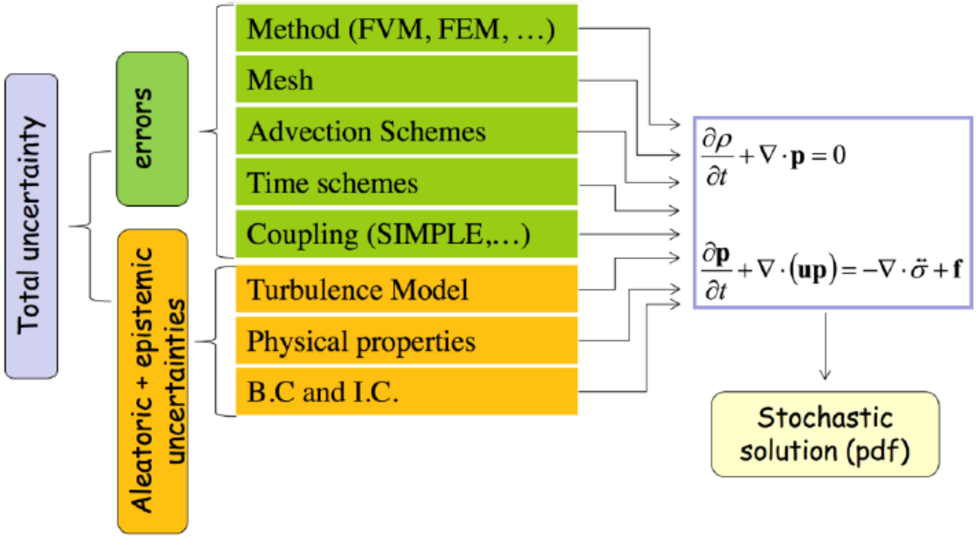

Figure 4.1. – Sources of errors and uncertainties in CFD identified from NEA benchmark (**Fokken et al. 2017**).

In this chapter, we explore the evolution of numerical solution uncertainties for distortion effect for NCL. The investigation of NCL onset is particularly significant as we rely on DNS with low Reynolds numbers, allowing us to explore the behavior of the system in a controlled-distortion set-up (physical distortion accommodated). This provides us with a unique opportunity to deeply investigate the numerical solution uncertainties and gain valuable insights. Moreover, we recognize the importance of investigating the establishment of NCL in regions of turbulence, focusing on both steady-state flow-rate and half-time. This flow regime and their parameters are particularly relevant as they frequently occur in real-world applications. Through analysis of the scaling uncertainty in this phase, we are able to better understand dynamic FoMs as well as the solution uncertainties inherent in grid-dependent models.

Through this chapter, our aim is to offer a comprehensive understanding of the scenarios studied and to explore the scaling behavior of numerical solution uncertainties in NCL, which forms an important part of modelling uncertainties. By examining both the onset and establishment phases, we contribute to identify, quantify, if possible, correlate the scaling effect under different distortion accommodation.

4.2. Scale Effect of Numerical Solution Uncertainties for NCL Onset

4.2.1. FoM: Critical Rayleigh Number

As outlined in section 3.2.1, the HHHC loop, similar to the Rayleigh-Bénard convection problem, exhibits a threshold, the onset of convection, above which natural circulation gradually develops in a random flow direction, due to a pitchfork bifurcation. This configuration exhibits three critical characteristics: first, no flow occurs below a certain critical Rayleigh number; second, upon exceeding this critical value, a flow ramp emerges, culminating in asymptotic flow states in either direction; and third, under specific conditions, secondary instabilities can manifest, such as vortex formation downstream of bends, flow reversal and oscillations.

For the investigation of scaling numerical solution uncertainties, the critical Rayleigh number is selected as a relevant FoM for the following reasons:

1. **Representative of NCL onset**: the critical Rayleigh number quantitatively defines the onset of flow under various flow resistances for natural circulation.
2. **Accessible by CFD**: this delicate phenomenon is challenging, if not impossible, to investigate using system codes. CFD demonstrates its advantage in revealing the threshold provided one uses specialized methods or pays the price of high space and time resolutions with classical ones.
3. **Free of model uncertainty**: with classical CFD tools, the estimation of such a critical value can be extrapolated from above the threshold in the laminar flow regime where DNS are affordable. Therefore, under scaling investigation the

numerical uncertainties can be examined with minimal impact from the use of numerical models, such turbulence models in this context.

As we know, Rayleigh number Ra can be expressed by $Gr \times Pr$. Therefore, the modified Rayleigh number can also be written for NCL with previously mentioned modified Grashof and Prandtl number in Equation 3.17. For more details of the relation between the parameters, please refer to Appendix B.3.2.

4.2.2. Propagation of Solution Uncertainties by Monte Carlo Sampling

Once the numerical choices have been clarified, allowing for the provision of high-fidelity data for both laminar and turbulent flow regimes (utilizing DNS and LES respectively) with their associated numerical uncertainties, the critical Rayleigh number Ra_c (considered herein as FoM) can be computed. A Monte Carlo sampling extrapolation is employed for FoM calculations, which can be summarised in the following steps:

1. **Quantification of numerical solution uncertainties** U_{num} for given scenario by GCI method, detailed in section 3.5.1.4;
2. **Normal distribution of velocity** → probabilistic distribution for $u^{1/r}$, where r is the exponent determined in the correlation displayed in Figure 4.2(a) and as found in Equation 3.17;
3. **Linear Regression** of three databases ($Ra\&u^{1/r}$) by **Monte Carlo sampling** ($Ra \propto u^{1/r}$), with Ra value computed using heating power;
4. At a chosen threshold u, where mass flow becomes less significant due to an exhaustive onset time, determine the **intercepts**, which are $\boldsymbol{Ra_c}$ and its associated probabilistic distribution;
5. **Quantify the confidence interval** of the mode value of Ra_c through statistical methods.

As depicted in Figure 4.2, the unsteady zone, where turbulent flow can be identified, exhibits considerable differences when contrasted with the laminar regime (for which DNS proves to be the better option). Furthermore, the laminar regime is first traversed by the flow beyond the onset of natural circulation. To accurately forecast the critical Rayleigh number, one extrapolates the computed flow-rate within the laminar regime (with less perturbation by the elbows). For this purpose, the heating strategy, which involves imposing a heating power, reveals straightforward details due to small temperature alterations over the horizontal heater. The sole disadvantage is a longer transient time caused by a lower heat exchange coefficient on the heater accompanied by a minimal flow-rate, as also observed in **Misale 2014** with extended oscillations for the HHHC loop.

Thus, with a fixed cooler temperature of 620K, several heating powers were applied to achieve the steady-state solution via a semi-implicit time integration method for

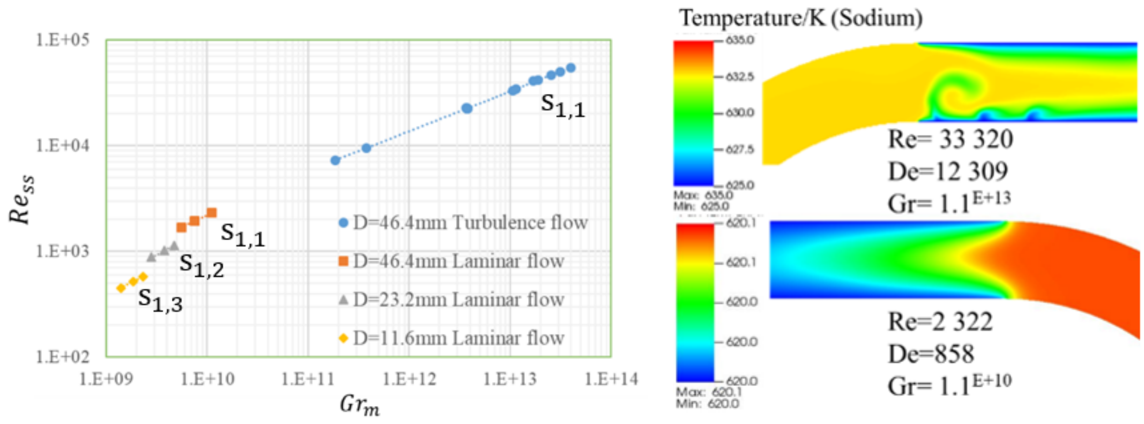

(a) Correlations for different flow regimes (b) Samples of thermal fields

Figure 4.2. – Flow regimes (a) correlations with different diameters for given powers; and (b) temperature fields of geometry $s_{1,3}$ for different flow regime.

the DNS approach. Figures 4.3, 4.4 and 4.5 present the results of the aforementioned procedures for an NCL of geometry $s_{1,3}$. More specifically, solution uncertainties can be calculated using the GCI method (see section 3.5.1.4), where a normal distribution within the range $(-2\sigma, 2\sigma)$ is assigned to the velocity $\mathcal{N}(u_{\text{finest}}, (U_{\text{num}}/2)^2)$. Then, three uncertainty bands with given standard deviations are sampled and propagated to obtain the extrapolated value of the critical Rayleigh number. The referred processes are accomplished using the Monte Carlo random method, enabling the possible distribution of FoM to be obtained.

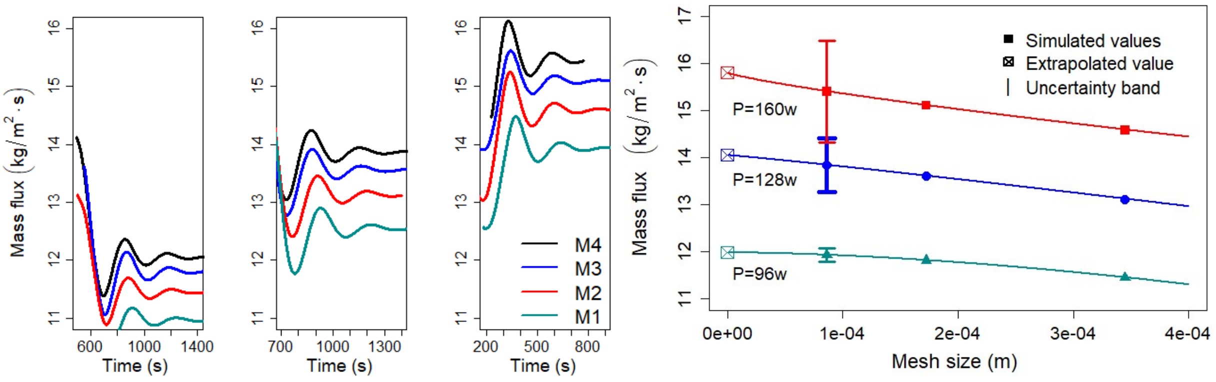

(a) Mass-flux data (b) UQ solution by GCI method

Figure 4.3. – Solution convergence and uncertainty quantification of geometry $s_{1,3}$ with (a) mass-flux for different heating power 96/128/160 W; and (b) numerical solution uncertainties quantification by GCI method.

For such a geometry, the possible critical Rayleigh number Ra_c distribution is displayed in Figure 4.5, where 95% of data with positive values lie in the range

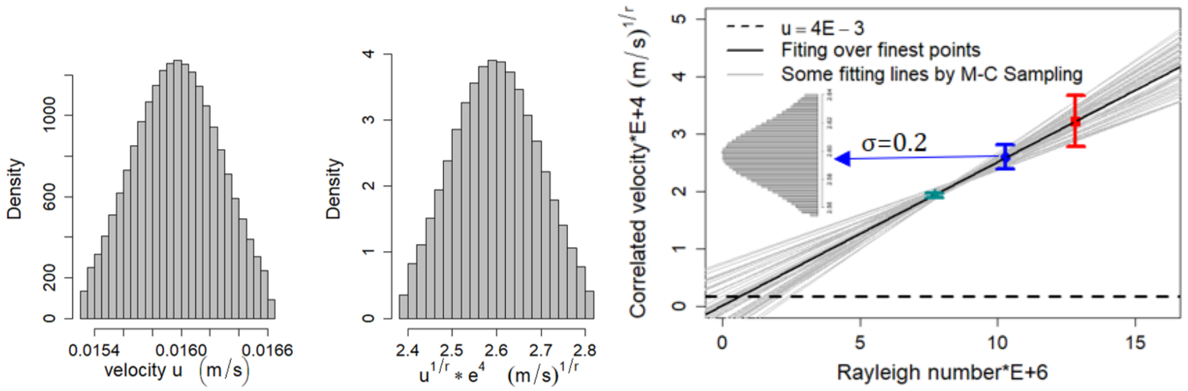

(a) Normal distribution at 128 W (b) Propagation by MC sampling

Figure 4.4. – Ra_c extrapolation for geometry $s_{1,3}$ with: (a) normal distribution over input quantity to be propagated at 128 W; (b) propagation of GCI solution uncertainties by Monte Carlo sampling.

$[6.82 \times 10^4, 2.56 \times 10^6]$. Due to wide range of critical values, an additional analysis for probabilistic fitting has been conducted using the ***Fitter*** tool in Python. So that the most probable value (mode) of the Ra_c distribution can be determined with a 95% confidence interval, using Maximum Likelihood Estimators. The mode value 8.78×10^5 can be estimated directly with the chosen beta distribution using the ***Bootstrap*** tool in the R language.

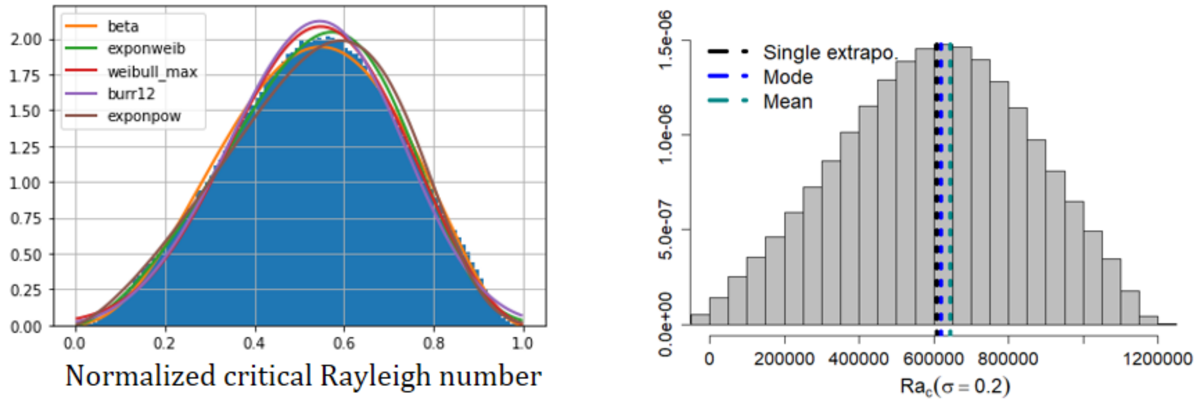

Figure 4.5. – Probabilistic fitting for Ra_c for geometry $s_{1,3}$ by: (left) ***Fitter*** in Python and (right) ***Bootstrap*** in R language.

Conversely, a value of 6.1×10^5 for Ra_c is derived from a single extrapolation of the results on the finest mesh M4, as represented by the black line. The disparity in Ra_c values between single extrapolation and mode value from Ra_c distribution illustrates a statistical bias favoring uncertainty propagation, highlighting the importance of further statistical refinements, such as the standard deviation of the input distribution.

Therefore, in Figure 4.6, we can observe a significant user effect on the uncertainty range of FoM, simply by changing the standard deviation. Here, in order not to include the negative value for 95% data of critical value, the standard deviation of 0.2 has been chosen for both Ra_c value and its mode value under scaling comparison.

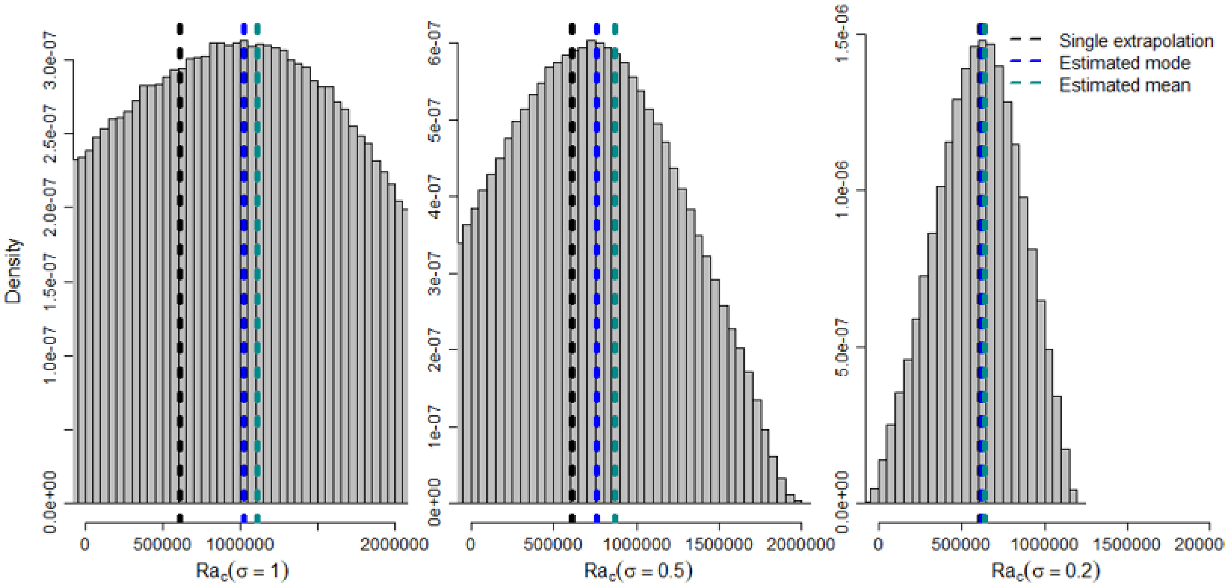

Figure 4.6. – Impact of standard deviation of input solution uncertainties on the Ra_c distribution output.

4.2.3. Scaling Uncertainty Investigation for NCL Onset

As outlined in section 2.1.1, researchers often investigate kinematic similarity (invariance of speed ratios) and dynamic similarity (invariance of force ratios). Here, we attempt to reveal the scaling effect of numerical solution uncertainties under different types of similarity.

4.2.3.1. Kinematic similarity

To investigate the impact of scaling under varying geometrical ratios, three distinct geometries denoted as $s_{1,j\in[1,3]}$ are employed (see Table 3.2 for details of geometry). In adherence to the principle of kinematic similarity, which necessitates a consistent velocity profile, lower heating powers are applied to configurations with larger pipe diameters. The Rayleigh number (Ra), which is the Grashof number (Gr) multiplied by the Prandtl number (Pr), can also be scaled using the dimensionless geometry factor $\frac{L_t}{D}$, given that Pr is approximately constant and independent of domain geometry.

The obtained results align with the physical correlations discussed in Section 3.5.2.2. As shown in Figure 4.7, the correlations for all three pipe diameters largely conform to empirical trends. In the laminar flow regime, the power factors approximate a value of

$\frac{1}{2}$, consistent with the classical Hagen-Poiseuille law. This is observed in both cases under investigation. Additionally, incorporating the geometry factor improves the leading coefficient in the correlation, thus enabling alignment across all examined geometries.

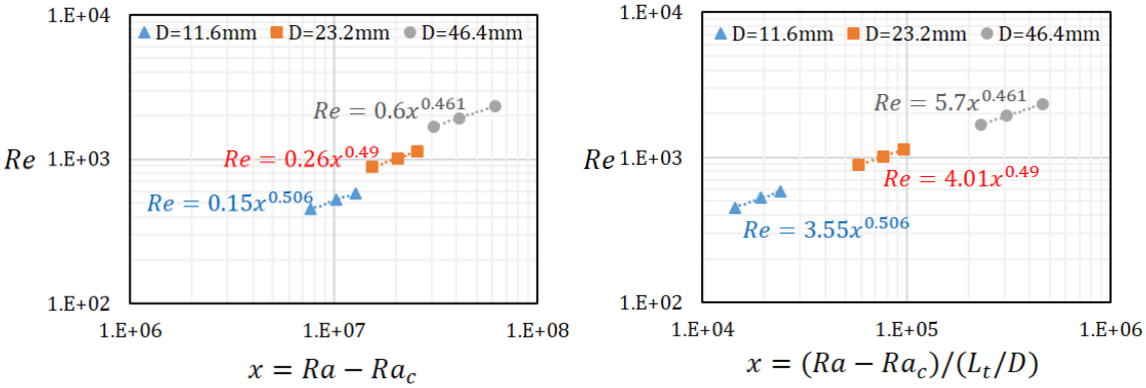

Figure 4.7. – Steady-state Reynolds number vs Rayleigh numbers for kinematic similarity with: (left) classical Rayleigh number and (right) scaled Rayleigh number, using M3 meshes.

4.2.3.2. Dynamic similarity

In order to preserve a dynamic similarity, the same Reynolds number must be maintained across differing geometries (see Table 3.2 for details). However, due to computational expenses, we fix the geometry $s_{1,1}$, which has the largest diameter (D=46.4mm). As depicted in Figure 4.8, the physical correlations run parallel to each other, showcasing similar power factors. On introducing the geometry factors, as anticipated, all correlations overlap, despite slight discrepancies. Thus, the dynamic similarity provides a more straightforward demonstration of differences under scale changes (overlapping correlations) than its kinematic counterpart.

Nonetheless, sole coefficients are insufficiently persuasive and informative for a quantitative comparison of scale effects. Consequently, we have also investigated the uncertainty related to the critical Rayleigh number for this scale changes.

4.2.3.3. Solution uncertainties for different similarities criteria

The procedures outlined in the previous section 4.2.2 have been implemented to compute the Ra_c for different similarity types: yellow for kinematic and orange for dynamic. Intriguingly, in the kinematic similarity case, Table 4.1 reveals a decline in the convergence capability (p_{GCI}) as the diameter size increases. Importantly, this led to a very poor convergence for geometry $s_{1,1}$ (D=46.4 mm), making it impossible to extend the uncertainty analysis to this case.

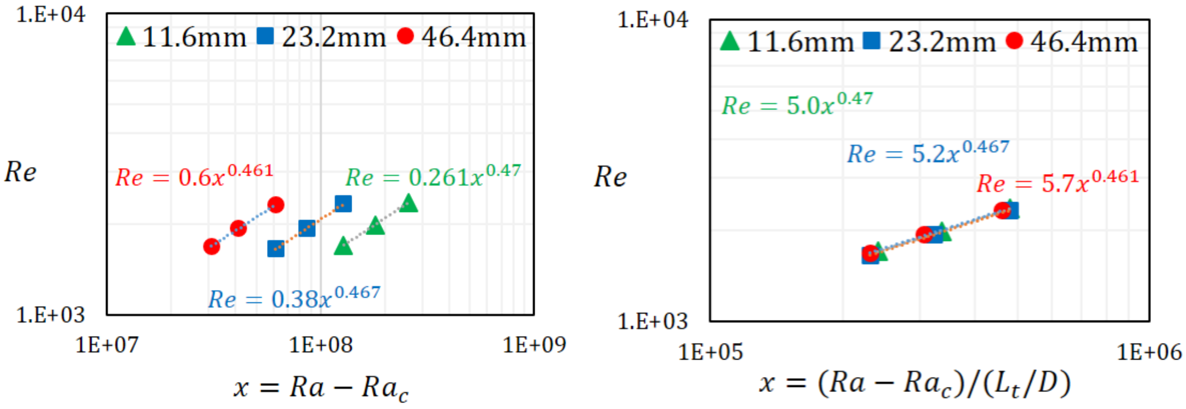

Figure 4.8. – Steady-state Reynolds number vs Rayleigh numbers for dynamic similarity with: (left) classical Rayleigh number and (right) scaled Rayleigh number, using M3 meshes.

Regardless of the method applied—single extrapolation or uncertainty propagation—it is clear from Table 4.1 that Ra_c exhibits different values and ranges for different pipe diameters. This scaling effect was anticipated due to the data disparity observed in the left figures of Figures 4.7 and 4.8. As a result, a new dimensionless number for flow threshold—scale invariant—can be derived as $Ra_c * (L_t/D)$, facilitating the estimation of Ra_c values from one scale to another. This provides a practical guideline for scaling.

Focusing again on the pink rows, the single extrapolation approach seems to be successful, while the statistical approach appears less reliable (see the last two rows of Table 4.1). Except for the shifted most likely extrapolated point, the estimated critical value requires reassessment. When the statistical nature is retained, non-physical solutions need to be excluded from the probabilistic distribution, indicating the necessity for further refinement to boost confidence. A preliminary study on standard deviation in Figure 4.6 has justified this requirement.

As indicated by the green rows, considering the broad range encompassing 95% of the Ra_c data distribution, we assess the bandwidth of the numerical solution uncertainties. This analysis is based on both Monte Carlo extrapolation and statistical estimation methods. The main results are the following:

- Regardless of the similarity type chosen between the scales, a change in the uncertainty bandwidth (see "bandwidth of mode" line) with scale is observed. The decline of p_{GCI} with scale broadens the numerical solution uncertainty bands for MC sampling. This, in turn, leads to an expansion of the uncertainty bandwidth for the output values Ra_c through uncertainty propagation.
- Indeed p_{GCI}, characterizing the convergence capability of the simulated solutions, decreases not only with an increase in diameter (column 1 & 2), but also with an increase in Reynolds number for a specific pipe diameter (column 1 & 3). Therefore, the extrapolation of Ra_c is essentially executed using data originating

from different balances of physical effects, treated as physical distortions. Both Figure 4.7 and 4.8 prove this point: as the pipe diameter increases, the progressively rising De value pushes the correlation exponent away from the laminar flow value, $\frac{1}{2}$, indicating an increasing influence of flow anisotropy inside and right at the outlet of elbows. This subsequently leads to an enhanced impact of flow distortion between the scales.

— When examining kinematic similarity (highlighted in yellow), it's essential to consider the combined influence of the numerical solution (as reflected by p_{GCI}) and physical effects (resulting from variations in Re and De numbers). We might question whether these physical effects can be mitigated in dynamic similarity where the same Reynolds numbers are maintained. As indicated in the orange section, when bandwidths between two scales are re-scaled using a dimensionless geometry factor, the newly defined bandwidths for scaling are achieved and equal. Therefore, since similar Reynolds numbers yield comparable numerical solutions (p_{GCI}), the scaling effect doesn't manifest for this specific numerical solution uncertainties related to the NCL onset threshold within the laminar zone.

Table 4.1. – Critical Rayleigh number and uncertainty with various pipe diameters under different similarities

Geometry	$s_{1,3}$	$s_{1,2}$	$s_{1,3}$
Diameter (mm)	**11.6**	**23.2**	**11.6**
Heating power (W)	96/128/160	48/64/80	320/464/624
Velocity (mm/s)	13.7/15.9/17.8	13.5/15.5/17.3	24.9/29.8/34.4
Reynolds number	446/513/570	884/1017/1135	817/976/1126
Dean number	83/97/107	231/266/297	151/180/208
Single extrapolation from finest solutions (M4)			
Ra	$7.70^{E+6}/1.03^{E+7}/1.28^{E+7}$	$1.54^{E+7}/2.05^{E+7}/2.57^{E+7}$	$2.57^{E+7}/3.72^{E+7}/5^{E+7}$
$\boldsymbol{Ra_c}$	2.69^{E+6}	5.48^{E+6}	2.63^{E+6}
$\boldsymbol{Ra_c \cdot (L_t/D)}$	1.43^{E+9}	1.46^{E+9}	1.40^{E+9}
MC extrapolation from GCI (M2/M3/M4)			
$\boldsymbol{p_{gci}}$	0.58/0.55/0.503	0.37/0.35/0.31	0.37/0.32/0.25
$\boldsymbol{Ra_c}$ **(95 % data)**	$[2.17^{E+6}, 3.06^{E+6}]$	$[2.79^{E+6}, 7.43^{E+6}]$	$[2.93^{E+4}, 7.24^{E+6}]$
Mode (95 % C.I.)	$[2.664^{E+6}, 5.6945^{E+6}]$	$[5.692^{E+6}, 5.695^{E+6}]$	$[3.497^{E+6}, 3.502^{E+6}]$
Bandwidth of mode	4.85^{E+2}	2.44^{E+3}	5.01^{E+3}
Bandwidth /$\boldsymbol{(L_t/D)}$	0.91	9.14	9.4
Estimated $\boldsymbol{Ra_c}$ **(boot)**	2.66^{E+6}	5.69^{E+6}	3.50^{E+6}
Estimated $\boldsymbol{Ra_c \cdot (L_t/D)}$	1.42^{E+9}	1.52^{E+9}	1.87^{E+9}

In summary, using dynamic similarity enables a more direct comparison of scaling effects from numerical solution uncertainties. This is evidenced not only by the overlap of physical correlations in Figure 4.8, but also by the comparable bandwidth scaled using the geometry factor (last green row in Table 4.1). Conversely, kinematic similarity is overshadowed by physical effects (different Reynolds numbers), thus making the scaling effect on numerical solution uncertainties less recognizable. Therefore, our delicate threshold analysis indicates that, particularly within the laminar flow zone with low Dean numbers, the influence of scaling on numerical solution uncertainties is predictable and can be associated with a scaling law for bandwidth with a geometry factor. This implies that the selected numerical methods and parameters maintain a high degree of scalability and reliability within this specific context. In addition, for a better understanding of why Ra_c and its extrapolated bandwidth behave differently with the geometry factor, a more straightforward demonstration is shown in Figure 19 of Appendix B.3.2.

4.3. Scale Effect of Numerical Solution Uncertainties for NCL Establishment

4.3.1. FoMs: Steady-state Flow-rate and its Half-time

Further to the threshold investigation discussed just before, the actual NCL in operation is more likely to be turbulent, as shown in the Figure 3.19. It's worth mentioning that, as explained in section 3.5.1.3, the ASME Standards insist on accurate grid resolution to capture physical phenomena precisely. In methods such as LES and DNS, grid resolution significantly impacts the energy distribution and flow-scale resolution, which could potentially alter the problem definition. In other words, the numerical error, to some extent, overlaps with the modelling errors with scale-dependent models. Consequently, investigating the scaling effect of numerical solution uncertainties hold great interest but also presents considerable challenges.

Regarding natural circulation, the power-cooling mismatch primarily refers to a situation where the system generated heat isn't adequately balanced by its cooling capabilities. In transient conditions or due to fluctuations in operational parameters, this mismatch can potentially lead to overheating or undercooling issues, unless properly managed. Studying the flow-rate and half-time of natural circulation establishment provides vital insights for system safety and optimization, particularly in cooling or heat transfer applications. During onset phase, the half-time period needed for a system to reach half of its steady-state value is indicative of its rapid response, while the flow rate at the asymptotic state allows characterizing system steady behavior. Thus, monitoring both FoMs is relevant in design phase as indicators of the safe, efficient, and reliable operation of natural circulation systems.

After choosing the FoMs to investigate in turbulent flow, the problem for scale effect study must be selected. In the nuclear piping (**Mohanty et al. 2012**), high-cycle fatigue due to flow-induced vibration and low-cycle thermal fatigue are potential causes of long-term operational aging. **IAEA 2011** recommends to establish an evaluation method for fatigue crack growth for elbows and tees of pipe joints. Hence, the curvature ratio will be the object of study, hopefully revealing the scaling effect for numerical solution uncertainties.

4.3.2. Scaling Uncertainty Investigation for NCL Establishment

Since the FoMs include both flow-rate and half-time, the same procedures detailed in section 3.5.1.4 can be applied. Firstly, for given temperature difference of heat source/sink, the natural circulation establishment is expected for different curvature ratios. As demonstrated in Figure 4.9 [1], three meshes under structured refinement are utilized to compute the flow transient from ΔT=40K to 10K starting at 50s using wall-resolved LES WALE model.

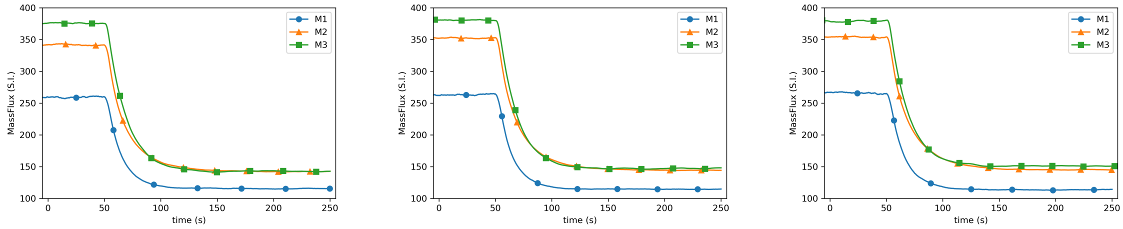

(a) $R_k/D=3$ (b) $R_k/D=4$ (c) $R_k/D=5$

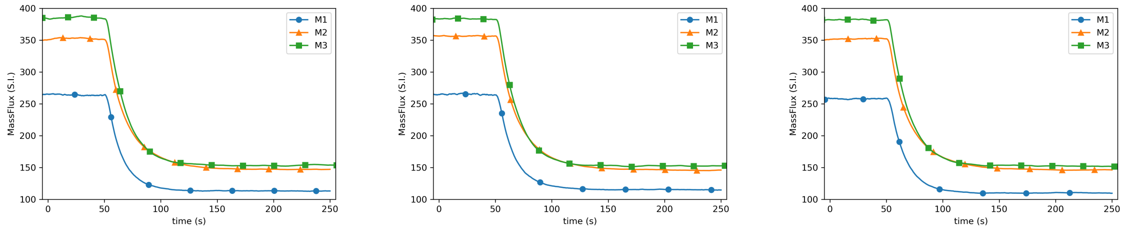

(d) $R_k/D=6$ (e) $R_k/D=7.2$ (f) $R_k/D=10$

Figure 4.9. – NCL establishment from ΔT=40K to 10K for different curvature ratios (geometry $s_{3,i\in[1;6]}$) with mesh refinement.

Visually, the solutions at two different imposed temperatures have both converged for given meshes (M2 & M3). The GCI method allows us to determine the numerical solution uncertainties on the finest solution (M3). However, as shown in Figure 3.18 before, the flow under different curvature ratios is highly sensitive to time setting-up flow. Thus, in Figure 4.10 [2], two strategies for time step sizes, dt/dx and CFL, as explained in Figure 3.14, are applied. The results from both cases will be used for reproducibility tests to more accurately reveal the scaling effect.

---

[1] dataset can be found in Table 17 of Appendix D

[2] dataset can be found in Table 18 & 21 of Appendix D

In Figure 4.10, several insights can be observed from these reproducibility tests:

— Generally, when CFL < 5, both the flow-rate and its solution uncertainty bands decrease in conjunction with an increasing curvature ratio ($D/2R_k$). This can be briefly stated as follows: with the increase in flow resistance due to sharp changes in the elbow, the flow-rate decreases; whereas, with a decrease in the Reynolds number, the numerical solution becomes less challenging, resulting in a smaller uncertainty band;

— Interestingly, for each physical scale (given temperature difference), a larger CFL number reveals smaller uncertainty bands. It can be observed in Figure 3.14, where M2 and M3 tend to overlap for larger CFL number due to implicit effect of temporal discretization. It should be noted that the CFL must be maintained within a reasonable range to avoid overly small (incompatible with the spatial scale) or overly large (incompatible with the physical scale) time steps;

— The fluctuation between two extremes could be attributed to the transition from a curved pipe to an elbow (with an increasing curvature ratio) or simply to the variation in grid quality for each geometry (as observed in Table 17 with slight differences in grid size).

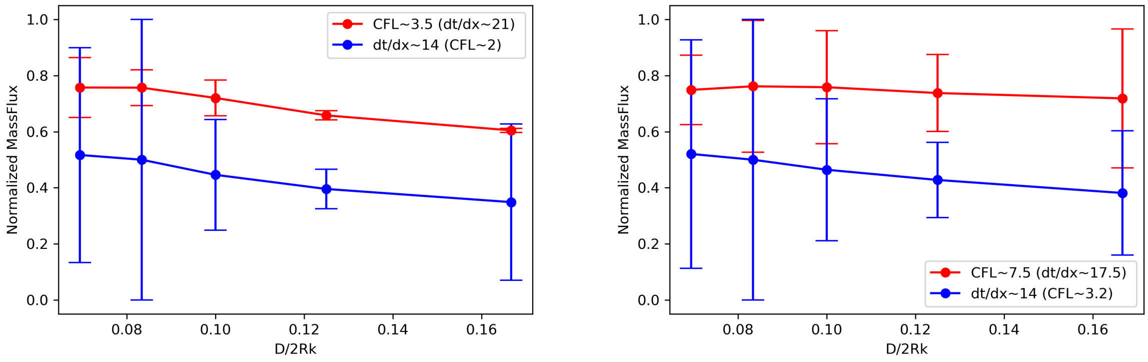

(a) ΔT=10K

(b) ΔT=40K

Figure 4.10. – Numerical solution uncertainties for mass-flux normalized by all data of different curvatures (geometry $s_{3,i\in[1;6]}$) under (a) ΔT=10K and (b)ΔT=40K with different time dynamics.

For a more comprehensive understanding of the flow-rate and its uncertainty during NCL establishment, three geometries with similar grid quality and consistent curvature ratios have been extracted from the previous figure. Thus, the following observations can be reaffirmed in Figure 4.11:

1. A larger temperature difference results in an increased Reynolds number, thereby challenging the current grid scale compared to the physical scale. This leads to the observed degradation of all solution uncertainty bands due to physical stiffness;

2. For a larger curvature ratio, both the flow-rate and its associated uncertainty bands decrease locally. This is attributed to a decreased Reynolds number resulting from the presence of a larger pressure loss in elbows.

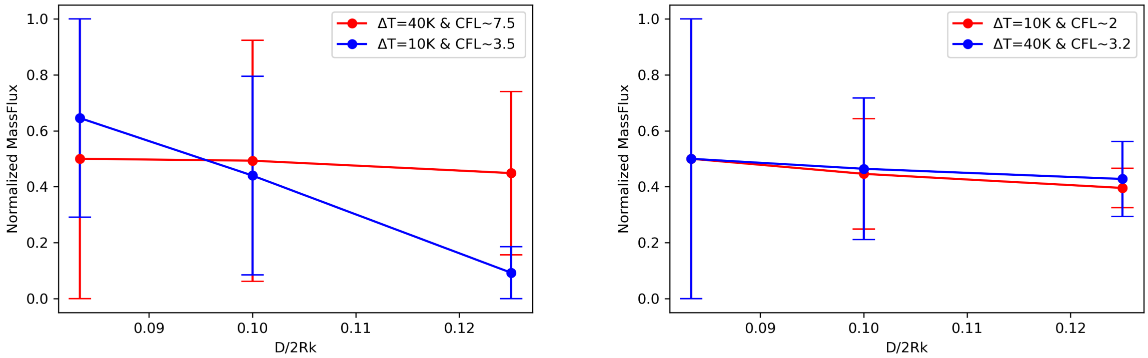

(a) $\Delta T = 40K \rightarrow 10K$

(b) $\Delta T = 10K \rightarrow 40K$

Figure 4.11. – Scaling effect of numerical solution uncertainties of mass-flux normalized by each dataset for curvatures under NCL flow establishment.

With respect to half-time, solution convergence can only be achieved by preserving the same CFL for all meshes through careful tuning of time-step sizes. As observed in Figure 4.12[3]:

- The relatively simple flow resistance from four solely smooth elbows results in a slight difference in half-time, as shown in Figure 4.12(a). This half-time supposes to quantify the challenges during NCL establishment from one asymptotic state to another, alternatively, NCL activation (if starting from a stagnant state);
- With the high sensitivity of half-time, a slow decrease is still identifiable with increasing curvature ratios (despite the normalized process by large variation). This is due to the abrupt changes at the elbow intensifying pressure losses. Such unsteady or chaotic behavior accelerates the activation of natural circulation, thus leading to a shorter establishment time. The trend is qualitatively towards an increase in thermal fatigue, while the range is clearly too low for any concern;
- Similar to the nature of half-time itself, the uncertainty bands generally increase with the curvature ratios due to the numerical solution challenges in the presence of more anisotropic turbulence. As a result, a degradation in the numerical solution uncertainties is observed with increasing curvature ratios.

In summary, the study finds that the establishment of NCL is influenced by the curvature ratio, affecting metrics like flow-rate and half-time along with their uncertainties. Reproducibility tests demonstrated that consistency in CFL across meshes is crucial for half-time solution convergence. Anisotropic turbulence challenges degrade numerical uncertainties, especially as curvature ratios rise. Flow-rate uncertainty

---

[3] dataset can be found in Table 19 of Appendix D

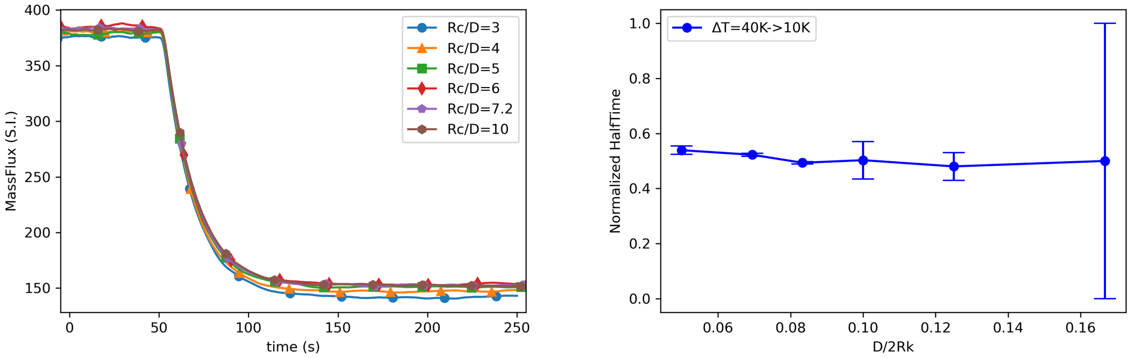

(a) M3 mesh

(b) Half-time

Figure 4.12. – Numerical solution uncertainties for normalized half-time of flow establishment from ΔT=40K to 10K for different curvature ratios (geometry $s_{3,i\in[1;6]}$) (a) at finest mesh M3 and (b) at half-time.

diminishes with lower Reynolds numbers, whereas half-time uncertainty correlates directly with curvature ratios. In other words, the variation in uncertainty range for a given scale effect can be of opposite sign depending on the FOM considered, as highlighted in our specific study. Given limited data, the general uncertainty is particularly fragile, requiring further exploration.

4.4. Summary

As explained in Figure 2.3, numerical solution uncertainties are crucial components of numerical uncertainties we explore in this chapter. We focus on two main aspects:

1. **Numerical solution uncertainty quantification for simulation evaluation:** The uncertainty quantification is rooted in the GCI method for specific refined meshes. The FoMs, along with the uncertainty bandwidths, are established to enable partial evaluation of the simulation quality via solution convergence (model uncertainty will be covered in the next chapter). Regardless of the presence or absence of a turbulence model, both DNS and LES remain grid-dependent throughout the computations. The pivotal distinction resides in the handling of the NCL physical phenomena.
    a) For DNS, a low Reynolds number flow is addressed, wherein the curvature effect is relatively suppressed (small Dean number). Consequently, numerical solution uncertainties can be deduced for given flow-rates with a selected time scheme.
    b) For LES, flow with a higher Reynolds number is studied. In this case, the sub-grid model must anticipate the phenomena evoked by both natural circulation and elbows. Numerical solution uncertainties can be computed

as well, but it's subject to the influences of the turbulence model and time discretization.

2. **Scaling distortion measurement for code qualification:** Following the modelling evaluation by the calculated FoM and the quantified uncertainties for each scale, the scaling effect can be studied for the chosen problematics:
   a) For flows with a low Reynolds number, the critical Rayleigh number, acting as a pivotal indicator of NCL onset threshold, is examined across its uncertainty bandwidth. Diameter variation is adopted to observe the impact of similarity criteria:
      i. *Dynamic similarity:* With accommodated physical distortion, the uncertainty bandwidth is scaled by a numerical effect, which can be quantified as p_{gci} due to solution convergence capability. Thus, the numerical solution uncertainties vary proportionally with scale and can be reunified by a geometry factor related to scaled parameters (L_t/D).
      ii. *Kinematic similarity:* the scaling effect is overshadowed by the coupled effect of distortion. With the coupling of numerical and physical distortions, the uncertainty bandwidth doesn't follow to a specific scaling law and requires further investigation.
   b) For transitional or turbulent regimes involved once the transient is onset, the flow-rate stands as a pivotal Quantity of Interest (QoI). Its half-time offers insights into the NCL establishment capability. This scenario shows again the difficulty to correlate numerical uncertainties with physical distortion. Contrary to the flow with a low Reynolds number, the numerical solution uncertainties can't be straightforwardly scaled with a geometric factor due to the intertwined impacts of numerical and physical distortion. Given the significance of the elbow effect in this context, the scaling examination will bifurcate into two scales of interest (Reynolds and Dean dimensions) for FoMs and their uncertainties:
      i. *FoMs:* Varied time discretization strategies were employed for reproducibility evaluations.
         — The flow-rate decreases with a greater geometric curvature ratio (increasing $D/2R_k$) due to a more pronounced centrifugal influence.
         — Conversely, for close Reynolds number values, an escalating Dean number ($Re*(D/2R_k)^{1/2}$) accelerates the NCL establishment, resulting in a reduced half-time.
      ii. *Uncertainty bandwidth:* This responds distinctly to the varying Reynolds and Dean scales.
         — The flow-rate's uncertainty bandwidth magnifies with increasing Reynolds scales, implying that a smoother curvature scenario exhibits both a larger Reynolds number and a broader uncertainty bandwidth.

- Analogously, the uncertainty bandwidth of the half-time swells with Dean scales, suggesting that a scenario with rougher curvature presents both a larger Dean number and an expanded uncertainty bandwidth.

In summary, while the scaling effect does impact numerical solution uncertainties, its relationship can only be meaningfully defined in the simplest cases. When distortions are coupled—both numerical and physical—modelling evaluation and distortion measurements become interdependent. Therefore, when considering the scaling methodology for CFD (a flowchart outlining the principles will be provided in the outlook), it's important to assess the strength of this interdependence. This assessment will help decide whether a complete reassessment of solution uncertainties at the reactor scale is worthwhile. Although this is clearly the best option, it is very time and cost-consuming computationally. Alternatively, numerical best practices learned at a smaller scale could be applied instead. Given the limited data and complexity of the topic, further investigation is necessary. While some preliminary insights into variations in scaling uncertainty have been provided, more in-depth horizontal comparisons focusing on physical modelling uncertainties under scaling effects are forthcoming.

5. Scaling Analysis of Physical Modelling Uncertainty

书山有路勤为径，学海无涯苦作舟。

- 韩愈

The mountain of knowledge has its trails, and diligence paves your way; Learning is an endless ocean, with persistence serving as your boat.

- HAN Yu (768-824, Poet)

Sommaire

5.1. Introductory Remarks

As shown in both Figure 2.3 and 4.1, turbulence models fall under the category of physical models and are responsible for physical modelling uncertainties. In highly turbulent flows, uncertainties in physical properties can propagate through hydrodynamic equations in unpredictable and challenging ways. These uncertainties, along with uncertain model parameters (e.g., RANS and LES) and boundary conditions, can lead to significant discrepancies between simulation and experimental results. Merely improving discretization schemes, mesh quality, or linear solvers may not always achieve better agreement between them. Moreover, the scaling effect on the model uncertainty remains challenging due to model validation range under scale changes. To address this, accepting that certain boundary conditions and model parameters follow a stochastic process allows us to quantify the uncertainty introduced by these random variables in numerical simulations (**Bestion et al. 2016**).

To quantify uncertainty in CFD simulations, there are two options: intrusive and non-intrusive methods (**Xiu and Karniadakis 2003**). Both methods introduce uncertainties through selected input parameters represented by probability density functions (PDFs), although their propagation through the CFD code differs. Due to the closed nature of commercial CFD packages, modifying them for intrusive techniques is not feasible. As a result, non-intrusive methods have become the preferred option for many scientists and engineers. Some commonly used methods for model uncertainty quantification for nuclear applications include: Monte Carlo simulations (**de Crécy et al.** 2008; **Munoz-Cobo et al.** 2014), Polynomial Chaos Expansion (PCE) (**Badillo et al.** 2014; **Rodio et al.** 2017), Bayesian Inference method (**Phillips et al.** 2021; **Marrel et al.** 2022), Multi-fidelity method (**Forrester et al.** 2007) etc. Among all the UQ methods applied, the PCE method demonstrates advantages and popularity, as shown in the NEA benchmark in the Table 5.1. One advantage of PCE over other methods for UQ in CFD is its efficient capture of the effect of uncertainties in the input parameters. PCE represents the response using a combination of polynomials for the PDF of the uncertain parameters. This facilitates accurate estimation of statistical moments, comprehensive sensitivity analysis using Sobol's indices, all without the computational burden associated with extensive sampling techniques like Monte Carlo.

Table 5.1. – CFD prediction and uncertainty quantification for NEA benchmark: GEMIX mixing layer test (**Fokken et al.** 2017).

User	**UQ method**	**CFD Code**	**Runs**	**Turbulence model**	**Wall treatment**	**Mesh size**
01	PERCEIVE (Propagation + Extrapolation)	Code_Saturne	6	EBRSM and κ-ω	Wall-resolved	652320
02	Anchored-ANOVA + POD-Kriging	P2REMICS	2	κ-ω SST	Wall-resolved	712704
03	EDF WAVE Method	ANSYS CFX	36	standard κ-ϵ	scalable wall-func.	813276
04	Distinction between Categorical & Continuous Variables	TrioCFD	220	standard κ-ϵ	standard wall func.	59850
07	PCE	CUPID	103	standard κ-ϵ	standard wall func.	156260
09	ASME V&V 20-2009	ANSYS Fluent	24	low Re of κ-ϵ	damping func.	62418
10	Monte Carlo	ANSYS Fluent	144	standard κ-ϵ	scalable wall func.	3696000
11	Deterministic Sampling	ANSYS CFX	4	Zonal LES (beta)	Wall-resolved	3596992
15	PCE	ANSYS CFX	16	κ-ω SST	Scalable wall func.	300000
16	Unscented Transform Deterministic Sampling	OpenFOAM	8	κ-ϵ	Standard wall func.	675168
18	PCE	Code_Saturne	22	LES (Smagorinsky)	Wall resolved	20644596
19	Root Sum Square of individual Uncertainties + GCI	STAR-CCM+ 1	15	Elliptic Blending κ-ϵ	standard wall func.	1637784
20	Monte Carlo	Star-CCM+	640	κ-ω	y+ wall treatment	5753458

In this chapter, our focus will be on the evolution of physical modelling uncertainties by PCE meta-modelling. We begin by identifying the crucial input parameters for the applied models. Next, we conduct an analysis by meta-modelling the wall-resolved LEVM model. This analysis involves utilizing a qualified surrogate model for quantile computation, sensitivity analysis, and calibration against reference solutions. Once the procedures for physical modelling uncertainty quantification are specified, we apply the analysis to the wall-resolved LES model. The analysis is conducted for varying FoMs, including time averaging, Power Spectral Density (PSD), and Dynamic Time Warping (DTW), to assess and evaluate the CFD solutions with rich information. Finally, we investigate and discuss the scaling effect on the uncertainties.

5.2. Meta-Modelling for Turbulence Models

5.2.1. CEA Uncertainty Platform Uranie

Uranie [1] is an in-house software framework developed by CEA, dedicated to uncertainty quantification, sensitivity analysis, calibration, surrogate model generation, optimizations, and more. For more details about Uranie, please refer to Appendix A.3. Here, our focus is on the meta-model, as depicted in Figure 5.1, which represents the process within the "Modeler" module of Uranie. These surrogate models require a set of elements, which can be a Design-of-Experiments (DoE) specifically created for analysis or a collection of independent measurements or calculations. This set of elements serves as input to create the model, which can be exported in various formats for reuse within Uranie or other software codes.

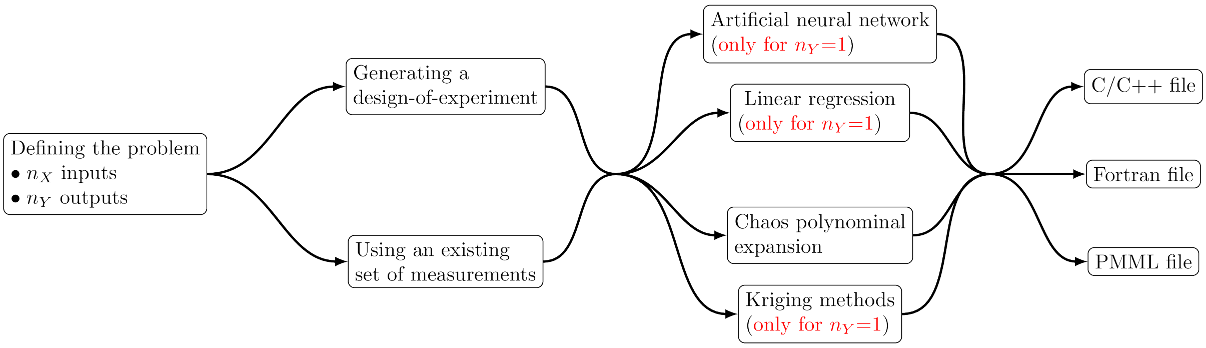

Figure 5.1. – Simplified decomposition of the surrogate model creation process into a four-important-step recipe in Uranie.

The fundamental concept behind PCE is that any square-integrable function can be expressed as a sum of terms. Each term is a product of PCE coefficients and orthogonal polynomial basis functions. The expression can be written as follows:

$$f(\boldsymbol{x}) = \sum_{\boldsymbol{\alpha}} f_{\boldsymbol{\alpha}} \Psi_{\boldsymbol{\alpha}}(\boldsymbol{x})$$

Here, $f_{\boldsymbol{\alpha}}$ represents the PCE coefficients, and $\Psi_{\boldsymbol{\alpha}}$ denotes the orthogonal polynomial basis. The index α corresponds to a multi-index, whose dimension is equal to the dimension of vector $\boldsymbol{x}$, and the L1 norm of α represents the resulting polynomial degree.

The Nisp library, short for Non-Intrusive Spectral Projection, offers functionality accessible through a dedicated wrapper within the Uranie platform. The analysis steps using the Nisp methodology are shown in Figure 5.2, and the steps are described and will be followed in the next section of LEVM meta-modelling application:

1. **Specification of uncertain parameters:** Define the uncertain parameters (ξ) contributing to overall uncertainty;

---

[1] https://sourceforge.net/projects/Uranie/

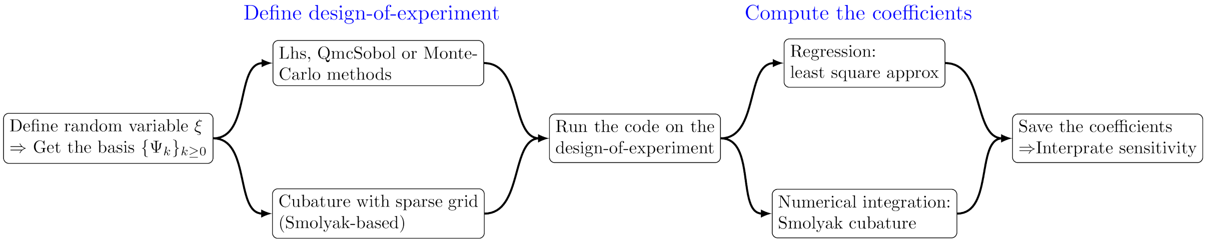

Figure 5.2. – Simplified decomposition of the surrogate model creation process into a four-important-step flowchart in Uranie (**CEA** 2022b).

2. **Build stochastic variables:** Construct stochastic variables (ξ_i) associated with the uncertain parameters;
3. **Build a DoE:** Generate a DoE to efficiently sample the input space;
4. **Build a polynomial chaos:** Construct a polynomial chaos expansion using regression or integration methods;
5. **Uncertainty and sensitivity analysis:** Perform uncertainty and sensitivity analysis using the constructed polynomial chaos expansion, enabling the assessment of the impact of uncertain parameters on the model output.

These steps outline the workflow of Nisp methodology, which leverages PCE for uncertainty quantification and sensitivity analysis. It's important to note that PCE serves only as a propagation method rather than a complete UQ methodology.

5.2.2. Parameters of Turbulence Models for Meta-Modelling

Before building stochastic variables and DoE for PCE, it's important to understand the two types of uncertainty it addresses: epistemic and aleatoric. According to **Najm** 2009, epistemic uncertainty arises from a lack of knowledge about a quantity with a constant true value, while aleatoric uncertainty is due to random variability. In frequentist perspective, only aleatoric uncertainty variables can have a PDF based on observed variability. However, in the Bayesian framework, probability represents the degree of belief in a proposition and allows assigning a PDF to variables with epistemic uncertainty given sufficient information. Thus, epistemic uncertainties from incomplete physical models can be handled by constructing PDFs based on expert judgment and available quantitative information (**Bestion et al.** 2016).

5.2.2.1. Step 1 : Specification of uncertain parameters

Regarding the conditions for DoE, classic DoE assumes independence among model parameters. However, if the model parameters are not independent, a dependent DoE should be employed. For our studies:

- In URANS-LEVM simulations, the von Karman coefficient (Vk) remains unaffected by the imposed turbulent Prandtl number (prdt). The determination of

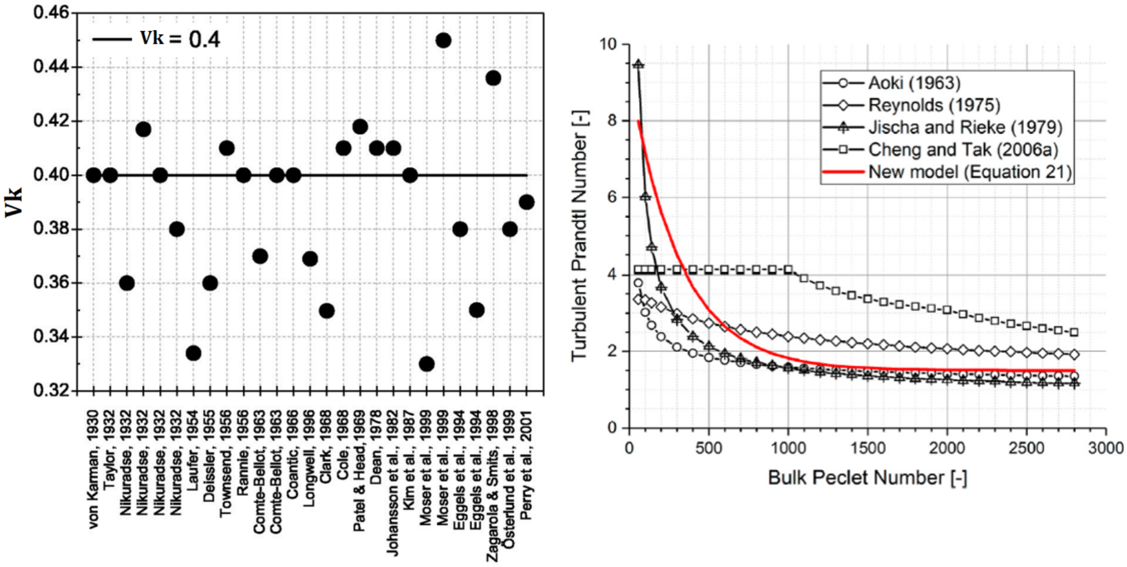

(a) Von Karman coefficient Vk

(b) Turbulent Prandtl number prdt

Figure 5.3. – Literature study of input parameters of LEVM on (a) Von Karman coefficient in wall function (**Zanoun et al. 2003**) and (b) Turbulent Prandtl number with molecular Prandtl Pr=0.01 (**Huang et al. 2022**).

the von Karman constant relies on experimental data and theoretical considerations of the velocity profile in the logarithmic region of the boundary layer. However, it is important to acknowledge that the turbulent Prandtl number can still influence the outcomes of URANS simulations, especially in cases involving heat transfer and buoyancy-driven flows, thereby affecting the overall flow behavior;

- In LES with WALE model, the choice of SGS coefficient, often denoted Cw, is generally considered independent of the imposed turbulent Prandtl number prdt. The turbulent Prandtl number typically affects heat transfer calculations but is not usually a factor in determining Cw, which is more closely tied to the flow characteristics and turbulence model.

5.2.2.2. Step 2: Build stochastic variables

Studies have indicated that the Vk constant can vary based on the Reynolds number or the (kinematic) viscosity, leading to proposed modified values for specific cases (**Smart 2022**). For standard pressure-driven flows, values around 0.41 are commonly used in Figure 5.3(a). In the case of high Reynolds number zero pressure gradient turbulent boundary layers in incompressible flow without heat transfer, a constant Vk value of 0.38 has been identified (**Osterlund and Sterlund 2000**). However, for zero pressure gradient boundary layers encountered in natural flows, such as heat exchangers driven by natural convection, the coefficient is smaller than the established value of 0.38 (**Nagib and Chauhan 2008**). Therefore, an initial uniform distribution of the Vk constant ranging from 0.3 to 0.45 is applied before the calibration process with reference. Regarding the SGS coefficient, the default value in the code is 0.5, but a variation of 40% is considered with a uniform distribution to study the sub-grid model.

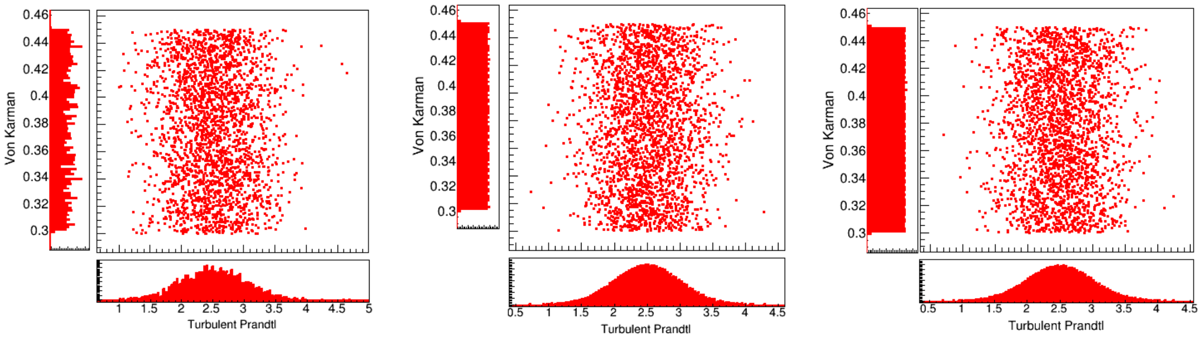

(a) SRS (b) LHS (c) Sobol

Figure 5.4. – Comparison of Design of Experiments (DoEs) by different sampling techniques: (a) Simple Random Sampling (SRS); (b) Latin Hypercube Sampling (LHS) and (c) Sobol Sampling.

For the turbulent Prandtl number, the standard default value for water is generally set at 0.9. However, research suggests considerable variations, particularly in low Prandtl number flows (Pr=0.01) as indicated in Figure 5.3(b). For instance, **Bremhorst and Krebs 1992** reported a range of turbulent Prandtl numbers (prdt) between 1.2 and 2.7 for liquid sodium at low Reynolds numbers. More recently, **Taler 2016** indicated a prdt range of 1.4-2.1 for liquid sodium flows at higher Reynolds numbers, ranging from 40,000 to 120,000. Given these variations, an averaged value of 2.5 for the turbulent Prandtl number is derived from the correlations presented in Figure 5.3(b). This value serves as an initial estimate and follows a Gaussian distribution for use in forthcoming studies. To ascertain the most reliable input parameters, various sampling techniques were evaluated, as shown in Figure 5.4. Ultimately, Latin Hypercube Sampling (LHS) was chosen for future research due to its inherent advantages.

5.3. URANS - Wall-Modeled LEVM Meta-Modelling & Analysis

5.3.1. Meta-model for Flow-rate Prediction by PCE

5.3.1.1. Step 3: Build a DoE

For the LEVM model, the LHS technique has been employed to generate a DoE composed of Von Karman coefficient and turbulent Prandtl, which is utilized to compute the output result (Mass-flux) shown in the Figure 5.5. Different sampling techniques can be applied for specific requirement of DOE. Prior to conducting the formal sensitivity study, a strong correlation between the Von Karman coefficient from the wall function and the FoM mass-flux has been observed.

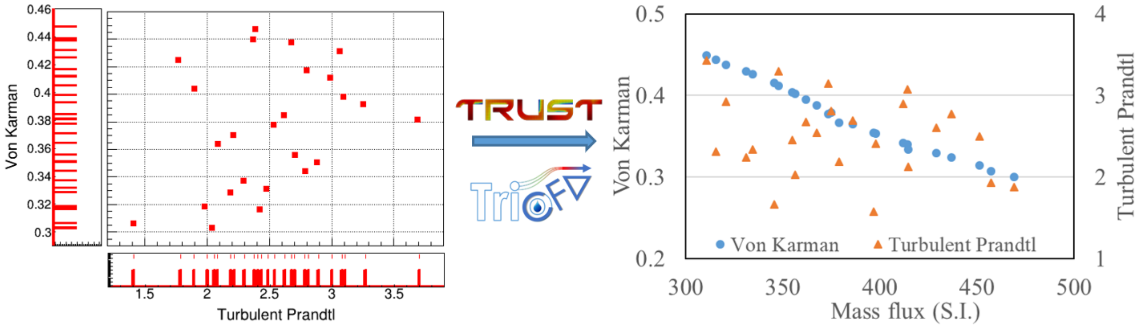

Figure 5.5. – TrioCFD computations based on given DoE by Uranie samping for LEVM.

5.3.1.2. Step 4 : Build a polynomial chaos expansion metamodel

Following the remark about square-integrable functions, both inputs can be decomposed on a specific orthogonal polynomial-basis, so that the PCE coefficients can multiply the Legendre ($\mathscr{L}$) and Hermite ($\mathscr{H}$) polynomials, for the uniform and normal laws, respectively. In this study, the Uranie platform has employed the Ordinary Least Squares Regression (OLS) method as a PCE-regression approach to calculate the coefficients for forming the polynomials. A total of 25 training data points were used to generate a 4th order polynomial. Figure 5.6(a) presents the detailed coefficients with their respective ranking orders. The blue cell corresponds to the mean value of FoM prediction from the meta-model.

However, the inclusion of less significant coefficients may affect the robustness and accuracy of the model. To address this, the adoption of a sparse regression technique like Least Angle Regression (LARS) can offer enhanced effectiveness. Figure 5.6(b) [2] shows a validation case that highlights the advantages of such a sparse technique. For more details of polynomials construction and advanced techniques, please refer to Appendix A.3.3.

During the generation of each meta-model, it is essential to validate the quality of the model predictions. This validation process involves assessing not only the R^2 value, which indicates the model explanatory power, but also the Q^2 value (Leave-One-Out). While the meta-model typically demonstrates a satisfactory R^2 value by fitting a sufficient amount of data, achieving a consistently high Q^2 value (at least 0.8) is not always guaranteed. Detailed insights into the quality of the meta-model can be obtained from the provided Table 5.2, emphasizing the importance of evaluating its performance based on both the R^2 and Q^2 values. If available, the inclusion of validation error, which utilizes separate data from the training ones, would be

---

[2] LEVM dataset for Uranie and UQLab in Table 22

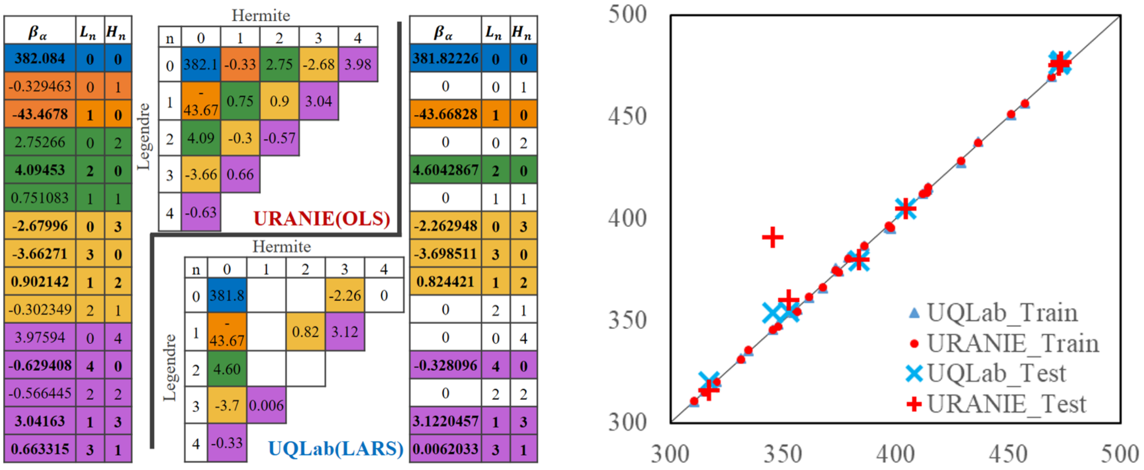

β_α	L_n	H_n
382.084	**0**	**0**
-0.329463	0	1
-43.4678	**1**	**0**
2.75266	0	2
4.09453	**2**	**0**
0.751083	1	1
-2.67996	**0**	**3**
-3.66271	**3**	**0**
0.902142	**1**	**2**
-0.302349	2	1
3.97594	0	4
-0.629408	**4**	**0**
-0.566445	2	2
3.04163	**1**	**3**
0.663315	**3**	**1**

Hermite

n	0	1	2	3	4
0	382.1	-0.33	2.75	-2.68	3.98
1	-43.67	0.75	0.9	3.04	
2	4.09	-0.3	-0.57		
3	-3.66	0.66			
4	-0.63				

Legendre

URANIE(OLS)

Hermite

n	0	1	2	3	4
0	381.8			-2.26	0
1	-43.67		0.82	3.12	
2	4.60				
3	-3.7	0.006			
4	-0.33				

Legendre

UQLab(LARS)

β_α	L_n	H_n
381.82226	**0**	**0**
0	0	1
-43.66828	**1**	**0**
0	0	2
4.6042867	**2**	**0**
0	1	1
-2.262948	**0**	**3**
-3.698511	**3**	**0**
0.824421	**1**	**2**
0	2	1
0	0	4
-0.328096	**4**	**0**
0	2	2
3.1220457	**1**	**3**
0.0062033	**3**	**1**

(a) PCE coefficients

(b) Model validation

Figure 5.6. – Construction and validation of meta-model by PCE: (a) OLS regression method in Uranie and (b) LARS sparse regression method in UQLab.

beneficial. Here, the results obtained from Uranie demonstrate relatively accurate predictions, which have also been cross-validated using the UQLab platform[3].

Table 5.2. – Validation of meta-model by PCE (sparse) regression method in Uranie and UQLab.

Platform	**Mean**	**Std Dev.**	**Order**	**Coeff.**	**$1-R^2$**	**Q^2**	**Valid. Err**
Uranie	382.084	44.297	4	15	4.05E-04	0.9406	9.3E-02
UQLab	381.822	44.243	4	9	6.09E-04	0.9987	5.6E-03

5.3.2. Quantile Computation & Sensibility Analysis

5.3.2.1. Step 5: Uncertainty and sensitivity analysis

When the polynomial coefficients are known, it is straightforward to evaluate the meta-model on new samples of the input random vector. In this step, we initiate the quantile computation for the validated meta-model to assess the uncertainty band. This computation can be performed using either direct computation or the more advanced Wilks method (**Wilks 1941**). The latter is an empirical estimation, based on order statistic which allows to get an estimation on the requested quantile, with a given confidence level β, independently of the nature of the law, and most of the time, requesting less estimations than a classical estimation. The figure illustrates the 95% prediction interval for the meta-model prediction, considering the uniform

---

[3] https://www.uqlab.com/

distribution Vk and the Gaussian distribution prdt. The lower and upper bounds of the uncertainty band are determined to be 310.6 and 467.6, respectively.

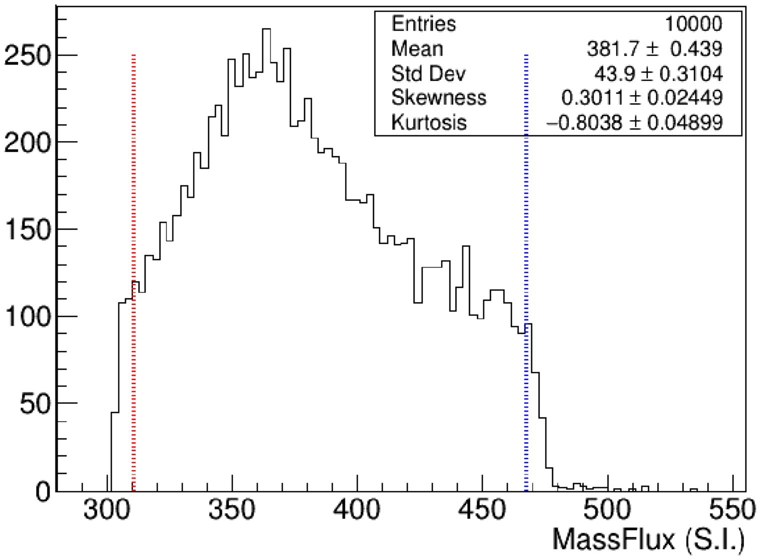

Figure 5.7. – Quantile computation of mass-flux based on validated meta-model for LEVM inside the histogram distribution.

Another important property of PCE is that the coefficients encode important information about the Analysis of Variance (ANOVA) decomposition of the surrogate model, which can be exploited to effectively calculate global sensitivity indices at very limited costs. Performing such sensitivity analysis after UQ is crucial to gain insights into the influence of input parameters on the model output and to understand their relative importance. The first-order sensitivity index measures the contribution of a single input parameter to the overall output uncertainty. On the other hand, the total-order sensitivity index captures the combined effect of a parameter and its interactions with other parameters. By utilizing PCE coefficients and Sobol indices, we can gain a deeper understanding of the model behavior, identify critical parameters, and prioritize efforts for uncertainty reduction and model improvement.

As shown in the Figure 5.8, for input Vk, a first-order Sobol index of 97.6% indicates that the Von Karman coefficient directly accounts for 97.6% of the output variance. The total-order Sobol index of 98.9% suggests that Vk, when considering its interactions with the turbulent Prandtl number, accounts for 98.9% of the output variance. The small difference of 1.3% indicates that these interactions have minimal impact on the output. Meanwhile, as shown in the Table 5.3, the **Martinez 2011** algorithm in Uranie is recommended, as it provides an estimation of the 95% confidence interval for each determined coefficient.

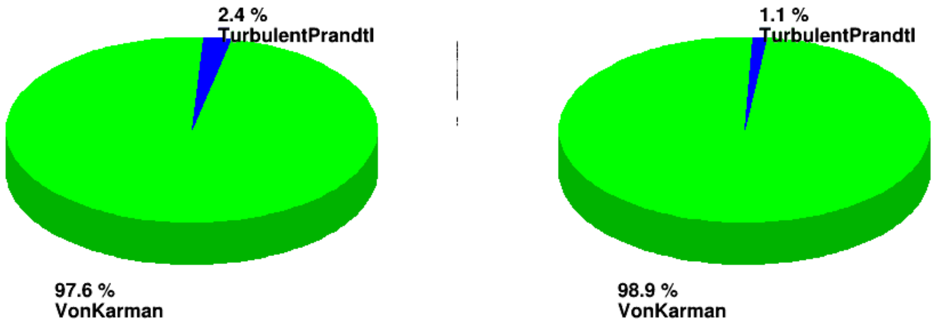

Figure 5.8. – Sensitivity analysis of input parameters on mass-flux for LEVM for: (left) first order and (right) total order of Sobol's indices.

Table 5.3. – Sensitivity analysis of input parameters on mass-flux for LEVM with confidence interval on Sobol's indices by **Martinez** 2011.

Parameter	**Order**	**Sobol**	**C.I. Lower**	**C.I. Upper**
VKarman	First	0.974	0.972	0.975
VKarman	Total	0.974	0.951	0.996
Prdt	First	0.0241	0.0015	0.0467
Prdt	Total	0.0211	0.0201	0.0220

5.3.3. Calibration with High-Fidelity Solutions

Within VVUQ framework, the calibration procedure of a model, also called sometimes "Inverse problem" (**Tarantola** 2005) or "data assimilation" (**Asch et al.** 2016) depending on the hypotheses and the context, is an important step of uncertainty quantification. Other than validation (**Trucano et al.** 2006), this step is the process of aligning code calculations with benchmarks by adjusting implemented parameters. The central question is: What parameter values minimize the difference between a set of observations and predictions under chosen statistical hypotheses?

Defining a calibration analysis entails several crucial steps: (1) specifying the reference observation set; (2) identifying the model that is supposed to accurately represent reality; (3) defining the parameters to be analyzed; (4) selecting the method for parameter calibration; and (5) choosing the distance function to measure the discrepancy between the observations and the model's predictions.

In this section, the Approximate Bayesian Computation (ABC) method has been used, which performs Bayesian inference without the need to explicitly evaluate the model likelihood function (**Wilkinson** 2013). As shown in the Figure 5.9, two different LES references have been chosen: the M3 solution training dataset and a single M4 solution using average input values. This method enables the calibration of values closest to the observed ones through a generated meta-model.

By using various reference results in Table 5.4, which account for acknowledged numerical solution errors, the standard κ-ϵ model can calibrate the Vk coefficient to approach the expected mass flow-rate. This is why we observe that for larger flow-

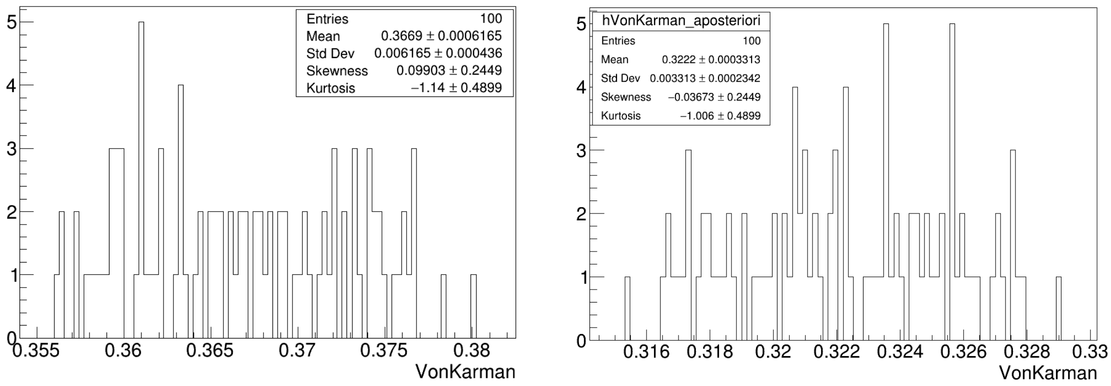

(a) Calibrate with LES-M3 solutions

(b) Calibrate with LES-M4 solution

Figure 5.9. – Calibration of Von Karman coefficient in wall functions of LEVM with LES solutions on: (a) M3 and (b) M4 meshes.

rates, the Vk coefficient is smaller, serving to create a steeper logarithmic slope for velocity near the wall. This step is crucial for multi-fidelity method where lower fidelity simulations (e.g. Best-Effort) require such calibration from High-fidelity ones.

Table 5.4. – Calibration of input parameters of LEVM (URANS) with LES solutions on M3 and M4 meshes.

Calibration reference	**Parameter**	**Mean value**	**Std deviation**
M3	Von Karman	0.367	0.0062
	Turbulent Prandtl	1.476	0.172
M4	Von Karman	0.322	0.0033
	Turbulent Prandtl	1.476	0.172

5.4. LES - Wall-Resolved WALE Meta-Modelling & Analysis

From the previous section, we discussed a comprehensive process of applying the Nisp methodology of PCE to generate a qualified meta-model by verifying different errors, computing the quantile using the Wilks method, conducting sensitivity analysis to identify the inputs impact, and finally, if needed, performing calibration for multi-fidelity methods.

In this section, the LES WALE model is employed to generate such a surrogate model for better predicting various FoMs considered. Due to the rich information from the High-Fidelity simulations, we won't only calculate the mean value using the classic Time Averaging (TA) technique, but also extract and study the frequency, magnitude, and even time series comparison. Therefore, we begin with FoMs using:

- The TA technique to obtain the mass-flux and temperature difference over the heater ($\Delta T_{h,ss}$);
- The Power Spectral Density (PSD) technique to quantify the maximum frequency of dissipated energy (EpsFreMax), and the mean value of power density of temperature near wall (TmpPDMean);
- Finally, Dynamic Time Warping to calculate the similarity cost between two time series of velocity near the wall at the downstream (CostVit).

Due to the poor predictive quality of certain FoMs, as shown in the red rows in Table 5.5[4], only the accepted ones are detailed in the following sections.

Table 5.5. – Meta-model of LES model for FoMs based on different techniques.

Methods	**FoMs**	Q^2	**Wilks_Quantile**	**SA_Sobol**	**Cali_ABC**
TA	MassFlux	0.957	Y	Y	Y
	Tmp_Diff	0.930	Y	Y	N
PSD	eps_FreqMax	0.841	Y	Y	N
	Tmp_PDMax	0.269	N	N	N
	Tmp_PDMean	0.791	Y	Y	N
DTW	CostTmp	0.234	N	N	N
	CostVit	0.742	Y	Y	N

5.4.1. Time-averaged Figures-of-Merit (FoMs)

As shown in the Figure 5.10, both FoMs are quantified using the Wilks method with double 95%. The mass flow-rate has a smaller uncertainty range than the LEVM in the Figure 5.7. The distribution of temperature difference exhibits both significant skewness (3rd central moment) and kurtosis (4rd central moment), hence, the concentrated values lean more towards the left side.

With this meta-model, the output trend for each input parameter can be displayed within a given input range. The Figure 5.11(a) illustrates a direct correlation between mass flow-rate and the SGS coefficient Cw. Increasing Cw results in larger values of turbulent viscosity, leading to stronger damping of turbulent fluctuations. This implies that the model predicts a more damped turbulent flow, with less energy in high-frequency turbulent fluctuations. This trend aligns with a more laminar flow that exhibits less small-scale turbulence.

In general, a higher value of Prdt signifies that the turbulent diffusivity of momentum and heat exceeds the molecular diffusivity, meaning that turbulent fluctuations of velocity and temperature are more effective in flow mixing and momentum and heat transfer. In certain instances, as shown in the Figure 5.11(b), increasing Prdt could also lead to a decrease in the level of dissipation, especially in flows where other mechanisms, such as buoyancy or stratification, inhibit turbulent mixing. In these cases, increasing Prdt can enhance mixing and escalate the level of turbulence in the flow, leading to a reduction in the level of dissipation.

---

[4] dataset for LES with different FoMs in Table 23 & 24

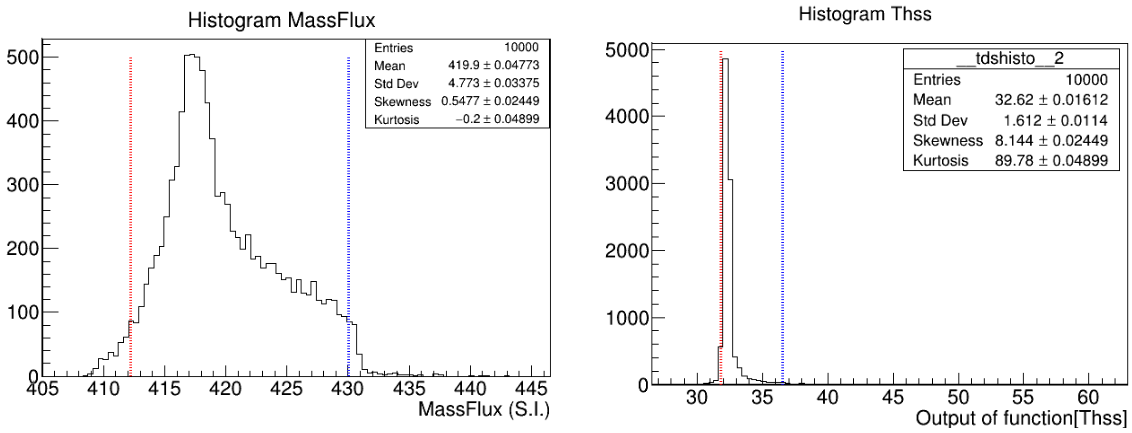

(a) Mass flow-rate

(b) Temperature difference $\Delta T_{h,ss}$

Figure 5.10. – Quantile computations of (a) mass flow-rate and (b) temperature difference $\Delta T_{h,ss}$ based on validated meta-model for LES-WALE model.

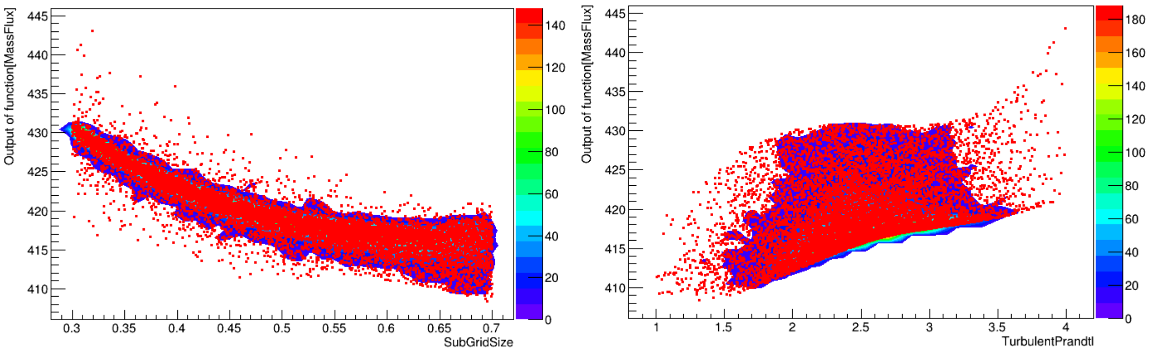

(a) SGS coefficient versus mass flow-rate

(b) Turbulent Prandtl number versus mass flow-rate

Figure 5.11. – Prediction based on LES-WALE meta-model with 10000 sampling to display the prediction domain.

For the SGS coefficient, the first-order Sobol index of 81.5% means it directly accounts for 81.5% of the output variance. A total-order index of 77.5% implies that, considering both its direct impact and interactions with the Turbulent Prandtl, it contributes to 77.5% of the variance. The decrease from first-order to total-order suggests that there's some interaction with the SGS coefficient. The degree of interaction may require further analysis, but this gives a starting point. From here, some practical skills for generating a high-quality meta-model are as follows:

- Ensure that the Time Averaged of FoMs is evaluated over a long enough time horizon to characterize the average value. Otherwise, the coefficient of determination (Q^2) of the model may not be high enough due to incomplete information, leading to poor predictions;
- If the averaging time is fixed, consider increasing the number of Design of Experiment (DoE) samples to capture more detailed information and better understand the underlying trends.

Therefore, a comprehensive and adequate DoE, along with a well-characterized output, are fundamental for effective meta-model predictions.

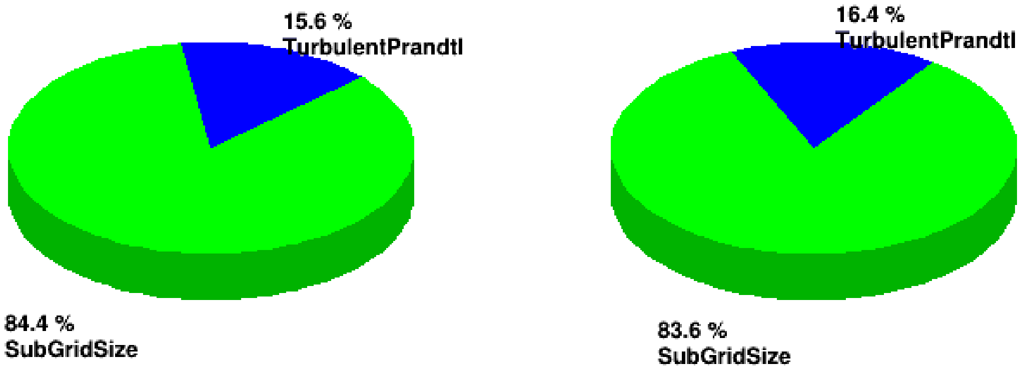

Figure 5.12. – Sensitivity analysis of input parameters on mass flow-rate for LES-WALE for: (left) first order and (right) total order of Sobol's indices.

5.4.2. FoMs based on Power Spectral Density (PSD)

In a NCL, flow dynamics are primarily driven by buoyancy caused by density differences from temperature gradients. Various elements, including loop geometry (centrifugal effect due to curved section) and fluid properties (low prandtl number flows), can significantly influence these dynamics. PSD analysis, and specifically the -5/3 power-law slope in the inertial subrange, plays a pivotal role in turbulence studies. This slope reflects the energy cascade process in turbulent flows and is characteristic of isotropic 3D turbulence as per Kolmogorov's theory (**Liao et al.** 2015).

However, this -5/3 power-law slope isn't universal. Specifically, in non-isotropic turbulence or in 2D flows, the inertial subrange slope can differ. For instance, a 2D flow can exhibit a -3 slope in the spectrum (**Bertocchi et al.** 2019). Therefore, the

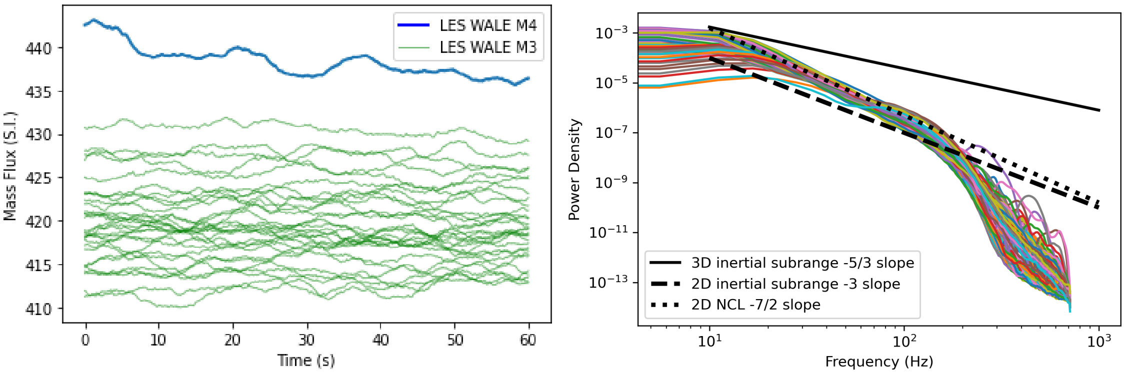

(a) Mass flow-rate with different meshes

(b) Power spectrum of M4 computations

Figure 5.13. – Power spectral density of mass flow-rate for LES WALE computations with M3 and M4 meshes.

precise nature of the turbulence, including its isotropy and dimensionality, must be considered when interpreting PSD results. As shown in the Figure 5.13, the fluctuating velocity profiles reveal turbulence information. The power density for the velocity at the elbow downstream has been computed with the M4 mesh. Due to the nature of the Natural Circulation Loop (NCL), neither -5/3 nor -3 slopes correspond to our observations. Interestingly, a steeper slope of approximately -7/2 is found.

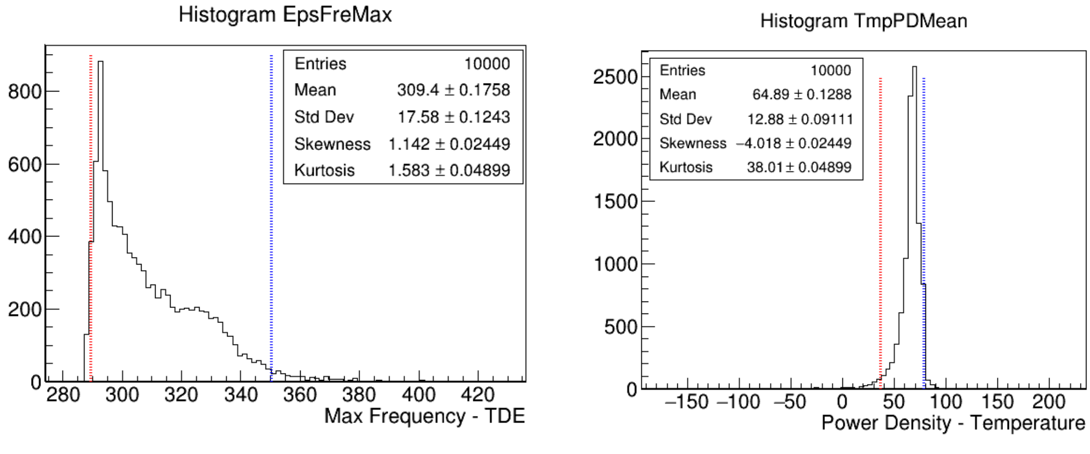

(a) Maximum frequency of dissipated energy

(b) Mean value of power density

Figure 5.14. – Quantile computation of: (a) maximum frequency of dissipated energy (EpsFreMax) and (b) mean value of power density of temperature difference $\Delta T_{h,ss}$ (TmpPDMean) based on validated meta-model for LES-WALE model.

As shown in Figure 5.14, PSD analysis applied to the dissipated energy from fluctuating velocities enables the detection of the maximum frequency. This information provides valuable insight into potential issues related to stress fatigue. Similarly, in Figure 5.10(b), the PSD of the temperature reveals a substantial kurtosis value. This result indicates the primary magnitude of temperature fluctuations downstream of the elbow. Through such techniques, we can better monitor and mitigate stress and thermal fatigue issues, particularly in critical components like elbows.

5.4.3. FoMs based on Dynamic Time Warping (DTW)

The LEVM cannot accurately capture the details of eddies, which are crucial in NCL near the wall. Consequently, the PCE predictions on the wall function (related to Von Karman coefficient) and the turbulent energy equation (related to turbulent Prandtl number) tend to be ’steady’. To effectively capture such dynamic evolution and meta-model time-dependent outputs in LES, a variety of methods could be employed (**Mai et al. 2016**). Alternatively, a less expensive approach could involve pre-processing the QoIs by DTW, which quantifies the time-dependent outputs and also links with the reference. Implementing warping costs can avoid the need for time-dependent PCE and instead utilize classic PCE with a dynamic metric.

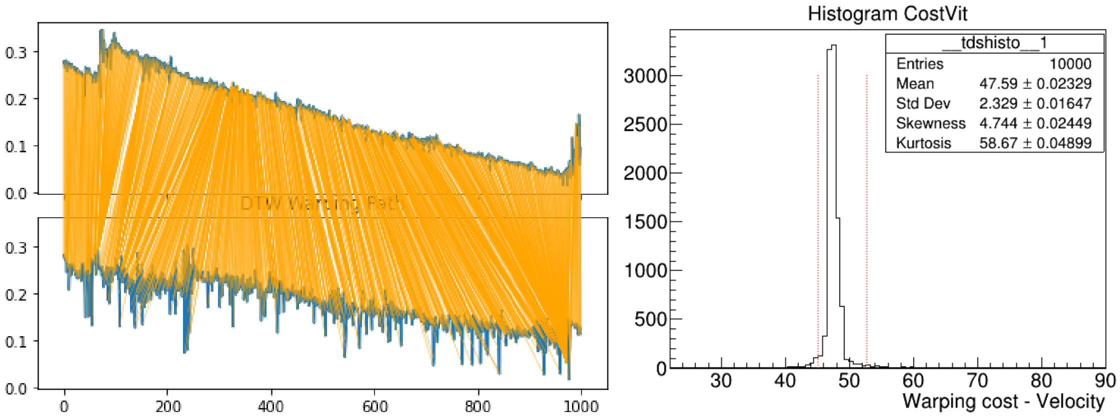

(a) Similarity match between M3 and M4 meshes

(b) Warping cost of velocity

Figure 5.15. – Quantile computation for meta-model of LES WALE with DTW-based FoM: warping cost of velocity at the downstream near wall.

For DTW, it exhibits resilience to time shifts and distortions between two time series. This is particularly useful in situations where system responses may occur at different time scales due to factors such as thermal inertia, coolant circulation rates, or control actions. By capturing these temporal deviations, DTW provides a more accurate and insightful comparison of system behaviors, enabling the early detection of anomalies or system changes. Moreover, this tool can be employed to identify and quantify scaling distortions between FoMs with different scales.

As depicted in Figure 5.15, the normalized velocity profile is computed to determine the warping cost, which quantifies the similarity between two time series. This cost is then predicted by the generated metamodel. Through this technique, differences in time series or scaling distortions can be calculated using conventional PCE.

5.5. Scale Effect of Physical Modelling Uncertainties

To parallel the previous chapter's exploration of numerical solution uncertainties under scale changes, we'll tackle the same issue on curvature. We aim to see how turbulence closure laws react to varying physical scales: buoyancy (Re/Ra-based) and centrifugal effect (De-based). Buoyancy term relates to changes in temperature or power, directly affecting Reynolds or Rayleigh numbers' magnitudes. Conversely, centrifugal effect, driven by curvature ratio changes, results in varied physical scales in the curved area, characterized by the Dean number. In the end, we try to reveal the scaling effect on physical modelling uncertainties for such high-fidelity simulations.

5.5.1. Model Uncertainty Quantification under Scale Changes

Similar to Figure 4.9, as the imposed temperature changes from 10K to 40K, the NCL exhibits different responses under varying curvature ratios. Visually in Figure 5.16[5], it appears that the flow becomes more fluctuated and dispersed as the temperature difference increases. We have selected the largest and smallest curvature ratios to illustrate the temperature profile downstream of the elbow/curved pipe in the Figure 5.17. For the smallest value of 0.05, the curved pipe exhibits a longer thermal mixing length with more developed turbulence, which occurs in the heat exchange section. Meanwhile, smoother curve pipe shows larger Reynolds number, but much smaller Dean number over the one with value of 0.167.

The same five steps as in previous sections are used to quantify physical modelling uncertainties for each case by PCE meta-modelling, with wall-resolved LES results shown in Figure 5.18[6]. The following reproductivity tests are performed to confirm these results:

— For the 40K to 10K case, surprisingly, the uncertainty bands are bigger for smaller Reynolds numbers (10K indicated in blue). This is due to the differences in the numerical solution to which the turbulence model is applied for given grid size. One might expect the model prediction to improve as the (buoyancy) physical scale moderates. However, this physical scale is dependent on the corresponding (temporal) discretizations. In this case, the CFL condition has a larger value for the 40K case, which may result in insufficient time dynamics. Consequently, the expected stiff physics is not manifested, leading to a smaller uncertainty band. Further investigation is necessary to determine the appropriate CFL zone in

---

[5] dataset for transition from 10K to 40K in Table 26 with the case from 40K to 10K in Table 25

[6] dataset of model uncertainties for different scale changes in Table 27

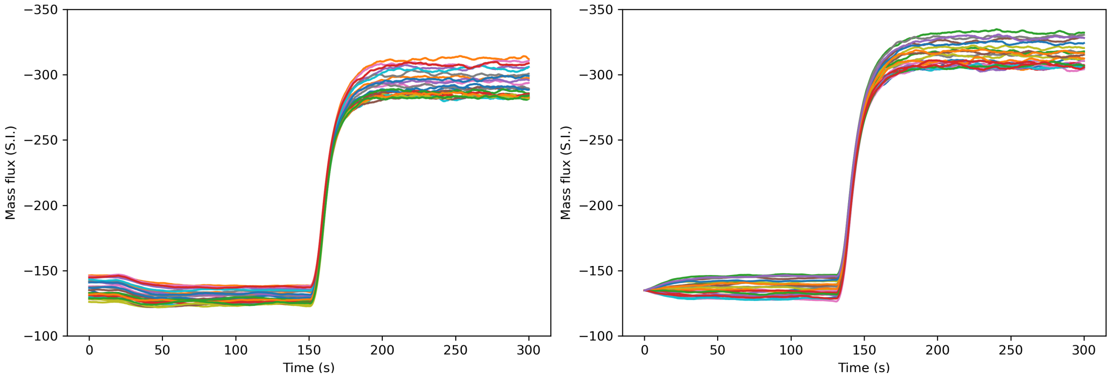

(a) $D/2R_k$=0.167 (b) $D/2R_k$=0.1

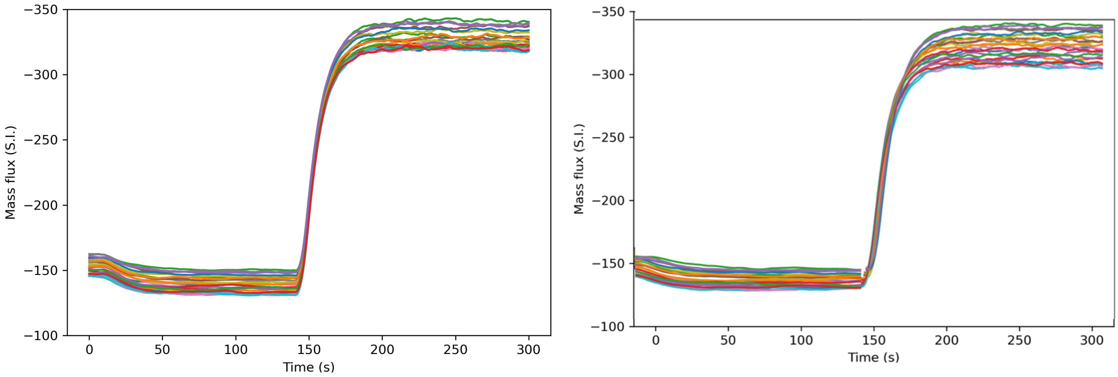

(c) $D/2R_k$=0.069 (d) $D/2R_k$=0.05

Figure 5.16. – Mass flow-rate of NCL establishment from 10K to 40K for different curvature ratios with M3 mesh of geometry $s_{3,i}$.

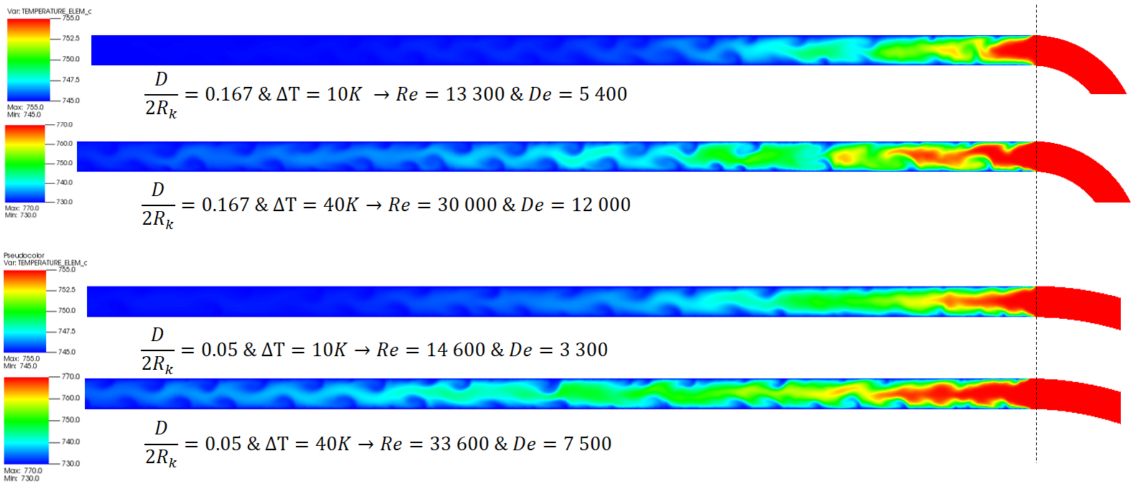

Figure 5.17. – Temperature profiles of NCL establishment from 10K to 40K at the downstream of curved section with different curvature ratios.

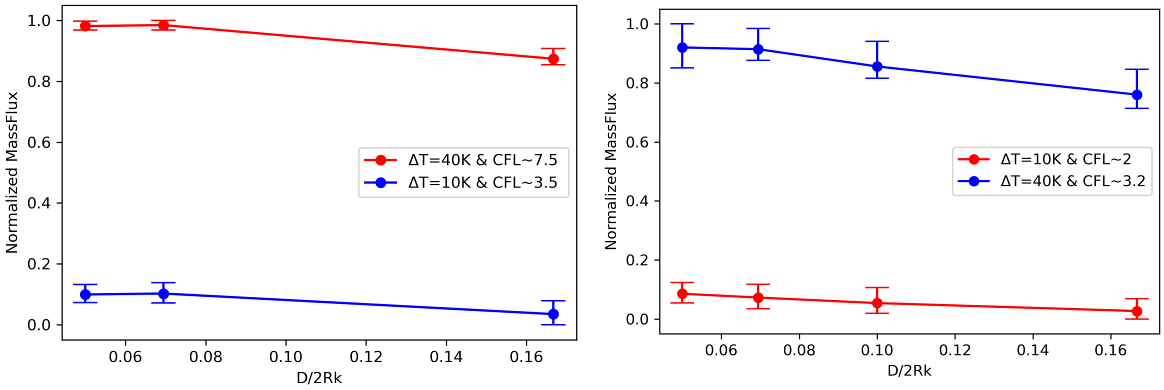

(a) $\Delta T = 40K \rightarrow 10K$

(b) $\Delta T = 10K \rightarrow 40K$

Figure 5.18. – Scaling effect of numerical model uncertainties of normalized mass flow-rate for different curvature ratios under NCL flow establishment.

which the numerical solution errors has less impact (specifically temporal one under given grid resolution);

- For the 10K to 40K case, smaller time steps are used, indicating smaller CFL zones for both case. As expected, the uncertainty bands grow as the physical scale stiffens. Notably, the CFL for the 40K case is reduced to half, falling into the same range of 1 to 5 with case with 10K;
- Similar studies are conducted for halftime investigations in Figure 5.19. For scenarios with larger CFL zones (7.5->3.5), the uncertainty bands appear to be generally larger. But for each case of itself, the changes remain small.

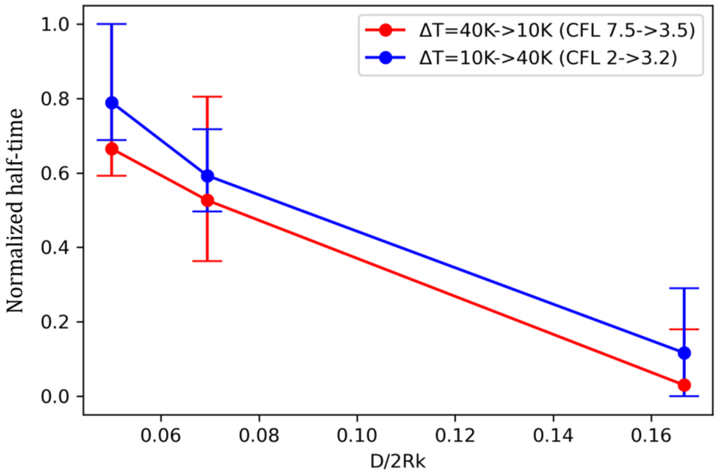

Figure 5.19. – Quantile computation of NCL establishment half-time based on validated meta-model for LES-WALE model.

The observed changes related to (buoyancy) physical scale suggest that, with a comparable level of numerical solution errors, the physical modelling uncertainties generally increase with stiffer physics. This effect is especially noticeable for the LES WALE model, where the filtered method becomes increasingly uncertain when more eddies need to be modeled than resolved. For a more comprehensive understanding of the scaling effect associated with geometric similarity, the case transitioning from 10K to 40K, maintaining a CFL range under 5, is then utilized for (centrifugal) physical scale.

5.5.2. Scaling Analysis for Physical Modelling Uncertainties

In the previous chapter on numerical solution uncertainties, we established that the physical modelling uncertainty bands under scale change can be implicitly linked to the converged order p_{gci} for different grid resolutions. However, the changes in physical modelling uncertainty bands for various curvature ratios appear to be less pronounced. This can be attributed to the relatively strong scalability of the turbulence closure law under similar discretization approaches, including spatial and temporal resolutions. For the second physical scale related to centrifugal effect, there are slight variations in the uncertainty bands as turbulence develops more or less for Dean based scales. To quantify the resolved capacity of the LES filtered model, the resolved eddy ratio can be calculated. An example demonstrating this is shown in Figure 5.20, where the stiffest elbow exhibits a slight increase in the most degraded zone (0.0216% of total cells having less than 20% of eddies resolved).

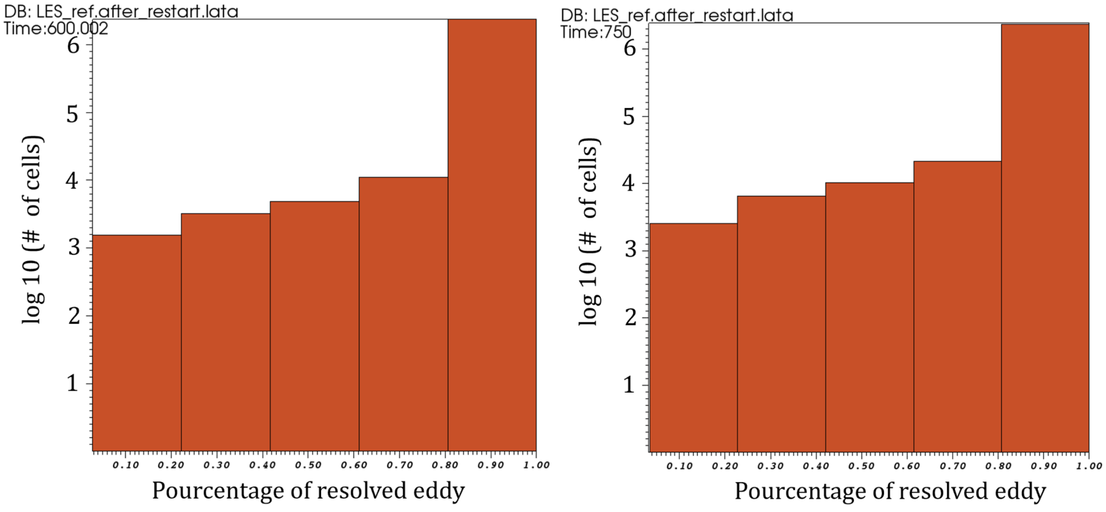

(a) $\Delta T = 10K$

(b) $\Delta T = 40K$

Figure 5.20. – Percentage of cells with given resolved eddy ratio for LES WALE computations during NCL establishment from 10K to 40K in geometry $s_{3,1}$ with $D/2R_k = 0.167$.

To obtain a more quantitative perspective on the resolved eddy ratio, the Table 5.6 presents both scale changes for both buoyancy and centrifugal effects. Once again, as the Re/Ra based physical scale increases from 10K to 40K, the ratio for at least 80% resolved eddies declines from 99.04% to 98.48 % due to increased buoyancy. In terms of Dean based scale, as the curvature ratio increases, the ratio (with at least 80% resolved) decreases for both the 10K and 40K cases. We can now plot the uncertainty band versus the resolved ratio as shown in the Figure 5.21. Broadly, as the centrifugal scale stiffens, the resolved ratio decreases and the uncertainty bands increase differently for each scale. Nevertheless, due to the non-linearity of the NCL physics, more scenarios are required to confirm these tendencies.

Unlike LES simulations, RANS simulations do not have an equivalent ratio for evaluating simulation quality because they model all turbulent scales instead of resolving them. However, the quality of a given RANS simulation can still be assessed using metrics such as Reynolds stress residuals, turbulent kinetic energy (TKE), y+ value, dissipation rate, etc. These evaluated quantities can then be associated with physical modelling uncertainties to better understand the underlying physics and quantify the evolution trend across different simulation levels.

Table 5.6. – Resolved eddy ratio for LES WALE computations during NCL establishment from 10K to 40K for different curvature ratios.

Curvature	**$\Delta T(K)$**	**Resolved eddy ratio (%)**				
$D/2R_k$	**$10K \rightarrow 40K$**	**[0-20)**	**[20-40)**	**[40-60)**	**[60-80)**	**[80-100]**
0.05	10	0.0189	0.0663	0.0616	0.152	99.70
	40	0.0237	0.0379	0.0568	0.166	99.72
0.069	10	0.0297	0.0890	0.0890	0.124	99.67
	40	0.0148	0.0890	0.0940	0.252	99.55
0.1	10	0.0104	0.0729	0.172	0.385	99.36
	40	0.0052	0.0365	0.146	0.401	99.41
0.167	10	0.0108	0.0808	0.210	0.657	99.04
	40	0.0216	0.1724	0.334	0.997	98.48

As discussed by Bestion et al. 2016, the scalability of PCE in CFD simulations is generally not a concern. However, the level of uncertainty introduced by uncertain BICs, turbulence closure laws, and numerical solution errors can vary significantly across different scales. Unlike turbulence closure laws, which are formulated based on physical arguments at smaller scales, numerical solution errors are often the main source of discrepancies between CFD simulations and experimental results.

It is worth noting that turbulence model coefficients and wall functions are generally assumed to be independent of the system's size. However, our studies on NCL have revealed a dependence of the turbulence model on the physical scales, which can effectively vary with different system sizes. Despite this dependence, the model uncertainties observed in our investigation are relatively less pronounced compared to the numerical solution uncertainties. This can be attributed to the grid-dependent nature of the turbulence models, which aligns with the previous discussions.

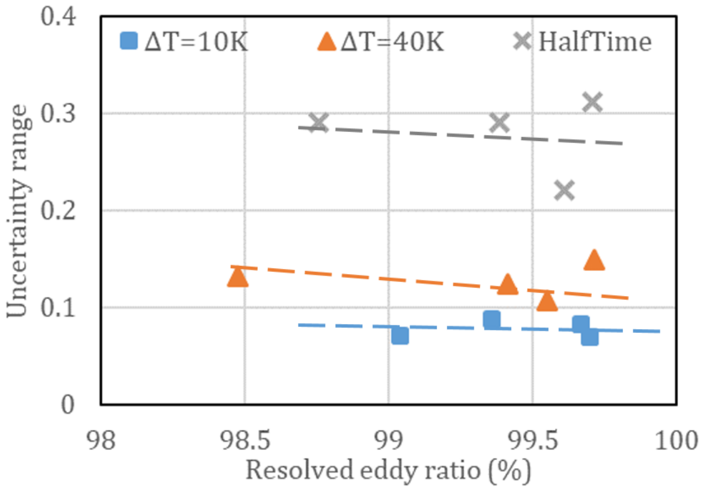

Figure 5.21. – LES filtered model uncertainties versus resolved eddy ratio under curvature effect (four different curvature ratio in Table 5.6) for geometric similarity with the ratio with more than 80% eddies resolved.

5.6. Summary

Before beginning the summary, we recognize that the numerical and physical modelling uncertainties are often intertwined, similar to distortion effects. To identify the the uncertainties evolution of each type under the distortion effect. we show the difficulty of correlating the numerical uncertainties with scale effect. Here, the physical modelling uncertainties related to physical models applied are evaluated under different distortion accommodations. While a comprehensive analysis of global modeling uncertainties, which encompasses various types of uncertainties, may seem more logical, our current independent investigation will provide us with a clearer understanding of the scale effect on each uncertainty, despite the coupled effects.

Among all the UQ methods for parameters of physical models, PCE stands out not only because it offers a reasonable computational cost but also because it has inherent coefficients for sensitivity analysis. Therefore, for the time-frozen PCE method, TrioCFD turbulence models have been investigated with respect to the chosen parameters across several studies: uncertainty bandwidth, sensitivity orders, and calibration of input parameters. For a meta-model with two input parameters, the flowchart of this process is illustrated in Figure 5.22, with detailed steps provided at the end of section 5.2.1. Crucially, the generated meta-model must be validated to ensure accurate predictions and effective utilisation.

For the DoE obtained by sampling, the FoMs are derived from the modelling and simulation using TrioCFD. As a component of modelling evaluation, uncertainty quantification via meta-modelling enables us to determine the uncertainty bandwidth. Finally, the scaling effects can be analyzed based on these results for distortion measurement.

1. **For the FoMs**, depending on the fidelity of simulations, various field information

can be utilized and reprocessed to determine FoMs:

   a) Flow-rate through time-averaging. As mentioned in the previous chapter, it increases for a smoother curvature ratio.
   b) Half-time consistently decreases with an increasing Dean number, given a similar magnitude of Reynolds number.
   c) Additionally, we can delve deeper into CFD data which might not be achievable in real experiments. For instance, quantities based on frequency/power density can be derived using PSD. And warping cost, as the indicator of similarity between two time series, can be determined using DTW.

2. **For the uncertainty bandwidth**, with high-fidelity (HF) simulation by the LES WALE model, the general prediction quality is relatively consistent across different scales (change of curvature ratio). We especially focus on the change of physical scales: the one of Reynolds and Rayleigh due to changes in imposed temperatures, and the other one of Dean number scale due to variations in curvature ratio.

   a) Given an appropriate range of CFL numbers (indicating comparable resolution efforts), scales with larger Reynolds numbers exhibit a slightly broader bandwidth for flow-rate.
   b) For a comparable Reynolds number, an increasing Dean number doesn't lead to significant variations in bandwidth, largely because of the high quality of the resolved eddy ratio shown in Table 5.6. Concurrently, a slight degradation can be observed in this Table for rougher curvature ratios (Dean scale). However, for half-time, the bandwidth variation remains less pronounced.

In conclusion, the previous chapter highlighted that numerical solution uncertainties experience significant variations when faced with different discretization efforts. Here, a relatively similar bandwidth of physical modelling uncertainties indicate that for HF simulations, the turbulence model has fewer concerns about scaling issues due to its superior simulation quality. Ensuring good control over discretization efforts for trustworthy physical modelling provides reference data through HF simulations.

It's undeniable that best-effort (BEF) simulations, like the URANS method previously used, are intended for reactor or component level applications. On the other hand, performing HF simulations provides not only a benchmark for calibrating BEF simulations but also serves a vital role in distortion measurement, serving as a reference to be paralleled or overlapped with. Importantly, we've noted that its physical modelling exhibits fewer scaling distortions, a characteristic that might not hold true for BEF simulations. This is especially the case when considering the unique characteristics of velocity and temperature profiles in the boundary layers of liquid sodium under NC, compared to standard models derived from forced convection scenarios. Pursuing research on BEF simulation for scaling investigation seems to be the logical short-term continuation of the research that has been conducted.

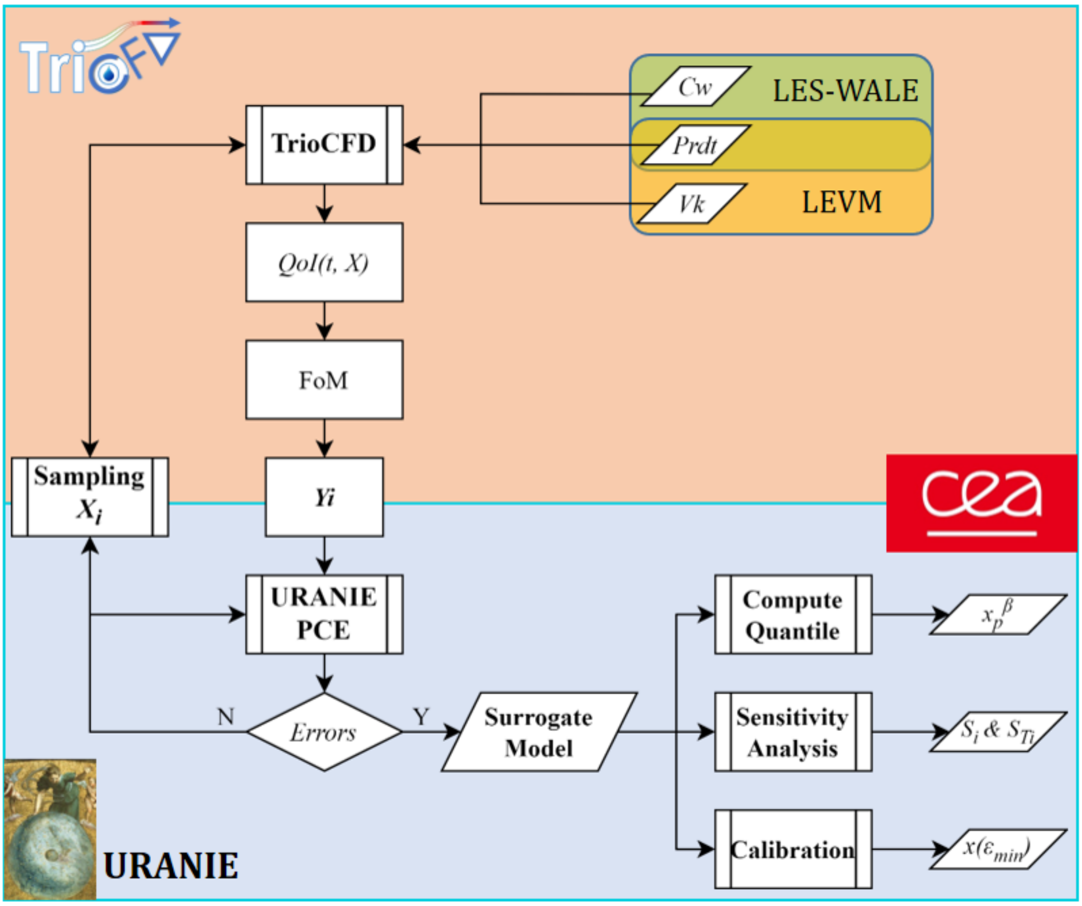

Figure 5.22. – Flowchart of uncertainty quantification and other analysis for turbulence models via URANIE platform.

6. Conclusions and Outlooks

We do not learn from experience… we learn from reflecting on experience.

- John Dewey (1859–1952)

The conclusions provide an integrated synthesis of our work's key findings, rather than simple superposition. For more detailed insights specific to each chapter, readers are invited to consult the chapter summaries (see §2.3, §3.6, §4.4 and §5.6).

Highlights of thesis work outlines - outcomes with ASN's request for scaling

In line with the first stage of ASN's request for SCT qualification, a comparison of physical phenomena between scales is carried-out thanks to high-fidelity (HF) simulations: they opportunely provide insights sometimes unattainable by other means. Accordingly, §3.6 provides practical guidelines for NCL simulations at different fidelity levels, enabling the evaluation of differences between scales for principal physical phenomena and influential parameters. These simulation approaches can be further ranked for use within a down-scaling process, with the discrepancy in predictions being dependent on the considered FoM. For example, the LES WALE model (HF) captures differing intensities of local recirculation downstream of the elbow for given curvature ratios (geometrical difference – scale effect), whereas the lower fidelity model, such as LEVM (Best-Effort BEF), fails to reconstruct the exact flow field. Moreover, HF simulations are also essential for accurately reconstructing the specific behavior of NCL sodium flow heat transfer on the boundary layer.

In line with the second stage of ASN's request, since any scaling process of a complex system would likely lead to an incomplete similitude (geometrical and physical differences have been intentionally introduced in this thesis work), the up-scaling capacities of applied models are assessed for different scales. Importantly, considering the differences between the validation and utilisation ranges, the evaluation involves not only the adjustment of applied models between the calculated and reference values but also the uncertainty management for the scaling process. Despite the lower fidelity of BEF simulations, owing to CPU costs, this remains the only feasible approach for large-scale scenarios. Thus, in Chapter 5, with the flow-rate under investigation, the LEVM model can be calibrated with reference data from the LES WALE model for the adjustment of model parameters. For uncertainty management, both §3.5.1.4 and §5.5 outline the detailed process of modelling uncertainty quantification. Noticeably, 5.5 addresses scaling effects using the HF approach, but the investigation principles are also relevant for further application of the BEF approach. On this issue, our view is that adjusting the uncertainties of the BE approach parameters to cover scale effects should have limited utility. Instead, the trend of the deviation should be monitored to demonstrate that it is controllable and correlatable. If fails, either the BE approach, the scale-down configurations, or both should be changed.

To conclude on the ASN's request, the modelling choices in safety studies (physical models, spatial mesh, temporal discretization, numerical schemes, convergence criteria, calculation options, etc.) should be ensured for the utilisation range and reevaluated for validity after the scaling process. In this way, the SCT qualification can be affirmed within this range, considering computed FoMs and uncertainties. As a tentative answer to the request of the ASN regarding scaling-transposition issues, a comprehensive roadmap for addressing the MUSQ will be provided in the outlooks, as for sure, requiring further refinements.

Framework of current research works for scaling analysis of NCL

In Figure 6.1, the left side shows a brief flowchart of scaling analysis through CFD simulations, in particular with a view to determining the optimised scaled model. Initially, for a given prototype, the down-scaling process is applied to obtain the scaled models ($s_{i,j,k}$) for specified objectives, ensuring that similarities are -at best- preserved (incomplete similitudes are most of the time unavoidable). In the absence of experimental data, the modelling approach employs CFD simulations of various fidelity levels. By initiating this numerical toolbox, denoted as "MUQCFD" (which constitutes a main outcome of this work), we can determine the FoMs and some of modelling uncertainties for the different scales under investigation. At this point, these quantities needs to be further analyzed to assess the up-scaling capacity of applied models (for simulations of different fidelity approach). Finally, scaling distortions are quantified and evaluated with the aim of either selecting the optimal scaled model or refining the previous process to better manage such distortions. It should be noted that the choice of BEF capacity will play a key role in this process, as it influences the acceptability of scale distortions, in particular on the qualification under reactor scale.

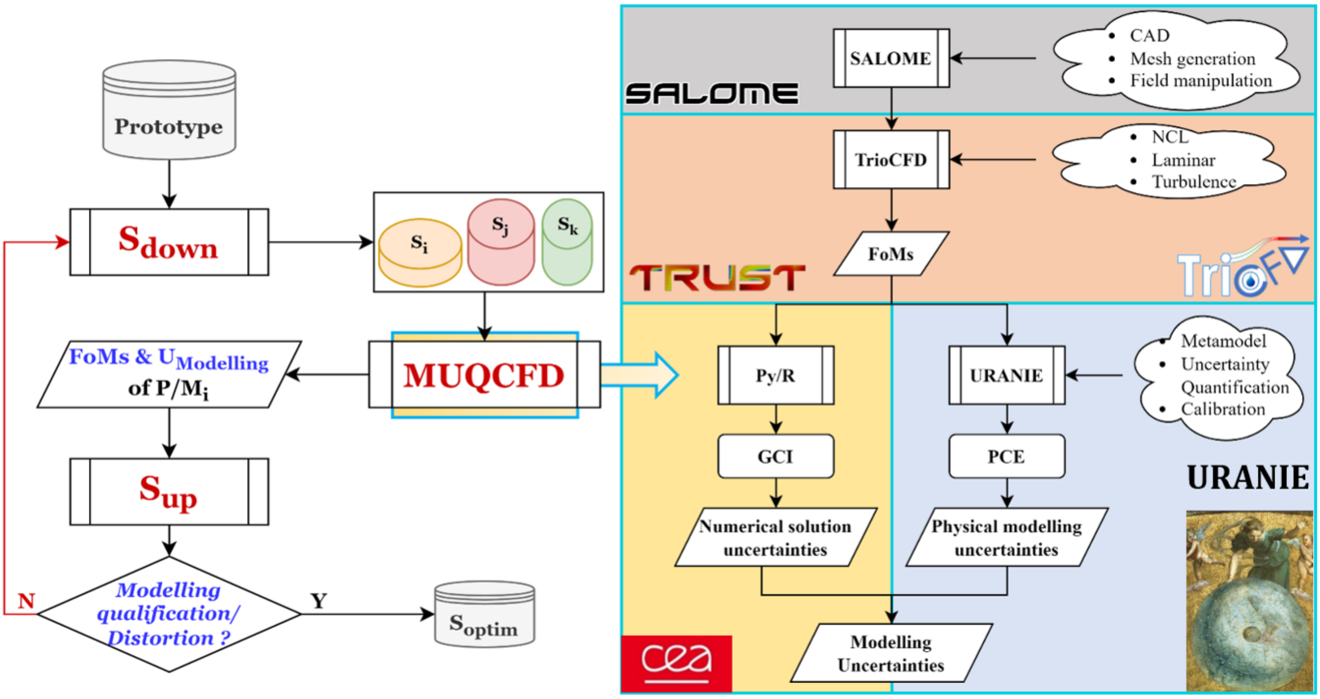

Figure 6.1. – Brief flowchart of scaling analysis through modelling.

As previously explained, this outlines the global concept of scaling analysis. To implement it as a practical methodology, we outline several explicit steps, supported by the results obtained for the case of NCL sodium flow:

- **Step1: Fix the problematics and SCTs**
  For a passive system with NCL, the primary objective is to conserve the fluid flow of sodium coolant and thermal energy transport through different scales.

Therefore, depending on the physical complexity, different fidelity levels should be chosen among the approaches that are available in a given SCT. In our case, HF and BEF simulations are adopted by using TRUST/TrioCFD.

— **Step2: Choose the Scales of Interest (SoIs)**
For a NCL with sodium flow, buoyancy and friction forces are two main phenomena to scale. For the bouyancy effect, the scale change through heating and cooling temperature difference can be considered; for the friction effect, the scale change through bends curvature can be adopted, hence through geometric difference. So that SoIs are chosen for further scaling effect investigation: respectively, Reynolds/Rayleigh-based scale and Dean-based scale.

— **Step3: Scaling identification and ranking for modelling**
When using TrioCFD for NCL modelling, the specified process of simulation reveals several concerns against the scaling issue. Shown in Table 3.15, the assumptions, such as Boussinesq approximation, are limited by the temperature range, related to the Rayleigh-based scale. And further, the process of physical and numerical modelling are all scale-related. Here, we mainly investigated the scaling effects on discretizations (spatial & temporal) and turbulent closure laws.

— **Step4: FoMs computations and uncertainty quantification**
Selecting the QoIs or FoMs to be computed, different techniques of data processing can be applied to process the CFD output fields. For example, the time averaging for flow-rate over the established state, the frequency analysis by PSD method etc. The details of computation and quantification of both discretization and closure laws are shown on the right part of Figure 6.1 as "MUQCFD" (Modelling Uncertainties Quantification for CFD). Here, numerical solution uncertainties are calculated based on GCI method, while physical modelling ones are computed through PCE meta-modelling method by URANIE (cross-validated with UQLab). The simulations with different fidelity approaches are elaborated to obtain the calculated and reference data for further comparison.

— **Step5: Scaling analysis through distortion metric**
The obtained FoMs and uncertainties are compared across the chosen scales. With the MUQCFD module, the primary focus of the research is to utilize HF simulations more effectively as alternative guidelines for relevant experiments. Within the framework of classic approaches to complex reactor issues, as shown in flowchart 1.3, the study plans to explore how HF and best-effort (BEF) simulations can be integrated to address scaling challenges related to modelling uncertainties. The objective of the up-scaling process is to confirm that we can adequately address scaling uncertainties, allowing the utilisation range to be defended before the validity range established. Besides, the distortion metric allows us to select the optimal scaled model for the scaling design through this modeling process before the actual experimental approach. In this study, only the HF simulations are initially conducted to confirm the high quality of the reference data and identify the scaling effects for modelling process. These simulations are then supposed to be compared with calculated data from BEF simulations in terms of simulation quality and distortion measurement.

Feedback from scaling analysis of HF simulations for NCL

Consistently with ASN requirements, modelling choices in safety studies must be examined for scaling, regarding model adjustments and uncertainty management. The Table 6.1 summarizes results from previous chapters on assumptions (§3.3.3.3), numerical uncertainties (§4.4), and physical modelling (§5.6).

The **Boussinesq approximation** can be treated as an adopted physical model as far as the validity region (ΔT_x) aligns with the scope of utilisation (ΔT). This validity region has been comprehensively established through physical analysis in §3.3.3.3. In TrioCFD applications, some physical properties can be temperature-dependent, contrary to the strict Boussinesq's assumptions with constant values. Thanks to these temperature-dependent properties (viscosity and thermal conductivity), the validity regions for the applicable temperature range are significantly extended. However, this could still pose challenges to some components of a given transient, such as the expansion tank. Therefore, it is recommended to check this point, following the steps provided in the section. To assist with this, the validity-domain map displayed in Figure 3.5 could serve as a valuable guideline.

As important parts of modelling uncertainties, **numerical uncertainties** are verified through the numerical schemes and meshes, with spatial discretization being crucial in CFD simulations compared to system codes. In Computational Fluid Dynamics, challenges can vary substantially depending on the Reynolds numbers involved:

- At low Reynolds numbers, with the Dean effect neglected, the study traces scaling effects using an applied geometry factor (L_t/D) for both FoMs and uncertainties.
- At high Reynolds numbers, where the Dean scale also plays a role, uncertainties do not scale straightforwardly with parameters, but the trend is interpretable through underlying physics.

Accordingly, it was concluded that the strength and correlatability of interdependencies should be evaluated for CFD scaling methodology. This assessment will help decide between two options: either performing a complete reassessment of resolution uncertainty at the reactor scale, which is optimal but computationally expensive, or applying numerical best practices learned at smaller scales instead.

Similarly, for **physical modelling**, metamodels replace turbulence models with suitable discretization efforts, enabling the calculation of model uncertainty at a manageable CPU cost. The results indicate that the LES WALE model, as a high-fidelity simulation, exhibits predictive accuracy and excellent scalability. With a high value of the resolved eddy ratio, both SoIs show similar FoMs, and their uncertainties have less pronounced variation. These simulations serve as valuable reference data and methodology for subsequent BEF studies: a methodological guideline is that the target should be to monitor the trend of the BEF uncertainty deviation with some key physical distortions to show that it is controllable-correlatable.

Ultimately, the **modeling uncertainties** shown in Figure 2.3, which are currently being investigated in this work, consist of numerical (solution) uncertainties and physical modeling uncertainties. The coupling of both could be further examined using the GCI method and re-evaluated for scaling effects.

Table 6.1. – Summary of scaling analysis for modelling choices.

Scales of Interest	**Reynolds/Rayleigh-based Scale**	**Dean-based Scale**
Assumptions - Boussinesq approximation (§3.3.3.3)		
Standard Boussinesq	$\Delta T \leqslant \Delta T_x$ with x all concerned physical properties, such as density, viscosity. However certain temperature-dependant $x(T)$ in TrioCFD can extend the available validation range	Less concern for geometrical difference
Numerical (solution) uncertainties - Spatial discretization (§4.4)		
Low Reynolds	Scaled by geometry factor under dynamic similarity (similar Re number across the scales)	Dean effect can be neglected despite the change in curvature
High Reynolds	Flow-rate and its uncertainty increase with increasing Re number	Half-time decreases with increasing De number; opposite variation for the uncertainty
Physical modelling - Turbulence model by HF simulations LES WALE (§5.6)		
Low Reynolds	Not concerned	Not concerned
High Reynolds	Similar flow-rate, but slightly broader uncertainty bandwidth with increasing Re number	Similar flow-rate with high quality simulations evaluated by solved eddy ratio, but slight degradation with increasing De number. For the half-time, the trend remains less pronounced.

Outlooks

This research has identified several potential pathways for further investigations and improvements to the scaling methodology. Here are some suggested directions:

For NCL Simulations:

1. Using the TRUST/TrioCFD tools, further research can delve into the application of NLEVM (wall-resolved URANS), comparing its accuracy and efficiency against the LES WALE model (HF). For LEVM (URANS with wall laws), three-dimensional simulations could be explored for safety cases to capture the 3D effects, in contrast to current PhD works that rely on 2D simulations.
2. When there's a large temperature variance that poses challenges for the Boussinesq approximation, the LMN (Low Mach Number) model might be tested, especially for specific components like the expansion tank.
3. Given the limited experimental data available, cross-validation is recommended. Other tools, like Code_Saturne and Neptune, might be beneficial, particularly for 3D cases using similar models.

For Uncertainty Management:

1. Beyond the two types of uncertainties currently considered, it would be worth to quantify the additional uncertainties identified in Figure 2.3 to complete the roadmap for addressing scaling issues in modelling.
2. For better quantification of numerical solution uncertainties, least-squares extrapolation could be an alternative to the traditional Richardson extrapolation. This is particularly true when multiple solutions are generated without clear convergence due to specific coupling effects.
3. To improve the performance of lower-quality meta-models, expanding the DoE size is suggested. Enhancing the current DoE by adding points in areas where the model lacks accuracy, like through adaptive sampling, could be beneficial.
4. Automation of the MUQCFD process is feasible through Python and C++, as both the GCI and URANIE meta-model components are compatible. TrioCFD validation file module, written in C++, further enables operational automation. However, standalone coupling in URANIE with external codes may require algorithmic optimization for parallel computing with TrioCFD.

For Scaling Analysis - Methodology:

Before HF simulations (even for single phase) become standard for industrial use, BE simulations serve for larger-scale applications. Building on the lessons learnt from the PhD work, the general MUSQ methodology shown in Figure 6.2 is proposed, with regards to ASN's request. The left-side of methodology addresses the down-scaling process and the associated validation. A standard process begins with the down-scaling using PIRT and the advanced methodology Dynamical System Scaling (DSS) identified in the literature review.

Specifically, within the validation range and before up-scaling step (the latter being sketched on the right-side of Figure 6.2), BE modelling predictability will be challenged by facing a set of scale effects. The effective use of BE simulations across different scales should lead to an analysis of the impact of physical distortions on computed FoMs and uncertainties. In that aim:

— HF simulations could be useful to provide reference data (in addition to experiments) but also to identify key mechanisms that could be strongly scale-dependant and possibly of fragile representation by the BE approach;

— accordingly, the DSS technique could be instrumental in designing some distorted configurations-experiments (with distortions to be strongly consistent with the incomplete similitude connected to the down-scaling process).

Regarding the numerical resolution, best practise will be established in the validation perimeter (as the PhD work was exemplary) and the numerical uncertainty dependence with the scale effects (following grid and time-step refinements typically) will be balanced.

To address both points (numerical resolution and physical modelling uncertainties), the MUQCFD process could be applied: as such, several techniques employed in this work for HF simulations can also be reused for BE, to quantify the numerical uncertainties (via GCI method) and physical modelling uncertainties (via meta-modelling).

Regarding the up-scaling process, numerical and physical distortions can be addressed separately, consistently with the requirements in ASN's Guide 28, for up-scaling of applied models: the non-correlability of the BE modelling with some key physical distortions should lead either to some adjustments of the BE approach choice (of which, switching from LEVM to NLEVM could be typical), either to add (with cost and time-line consequences for an industrial project) some new down-scaled configurations (in order to get additional data and / or to reduce physical distortions, by so improving the up-scaling correlability for the BE approach), or both. One should importantly note that, as far as the BE approach was used along the down-scaling process, if it comes out that its predictability with some key distortions is actually poor (typically, non-correlatable), it is wise to redo the down-scaling process itself[1]. Finally, depending on the conclusions from the down-scaling study about numerical resolution, a complete reassessment of solution uncertainties at the reactor scale may be decided or the lesson learnt during validation considered instead applicable at reactor scale so that solution uncertainties remain of much lower concern than physical distortions.

As a next exploratory step, this methodology could be evaluated by applying it to a reactor-sized passive system, such as the RRB of the ASTRID reactor project or to any smarter choice connected to the current R&D for AMRs - SMRs designs.

---

[1] this has to do with the paradox underlined in the introduction section

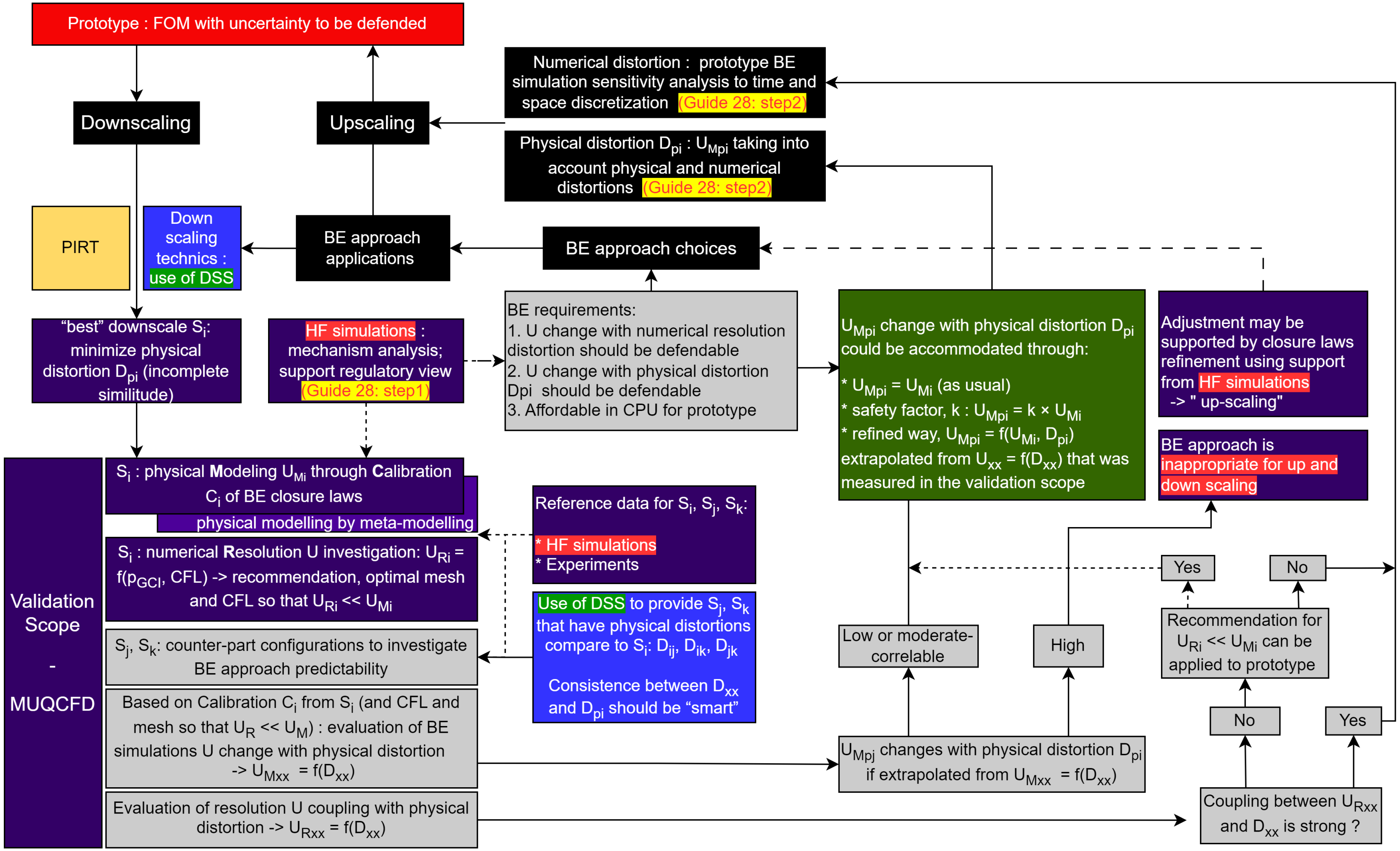

Figure 6.2. – Flowchart of general MUSQ methodology.

7. Appendix

If I have seen further it is by standing on the shoulders of Giants.

- Sir Isaac Newton (1642–1727)

A. CEA in-house Scientific Computation Tools (SCTs)

A.1. TRUST Platform

TRUST[1] is an open-source HPC-based thermal-hydraulic CFD simulation platform developed at CEA (Department of Energy). It was originally designed for incompressible single-phase and Low Mach Number flows, but now also allows simulating real compressible multi-phase flows. TRUST is also being progressively ported to support GPU acceleration (NVidia/AMD). This software is OpenSource (BSD license). TRUST has a very good scalability allowing simulations of more than 2 billion elements on 50 000 processors. TRUST is used as the basis for many specialised applications in the nuclear and new energy fields. To locate the placement of TRUST platform under development strategy for the thermal hydraulics codes, the Figure 1 would be helpful.

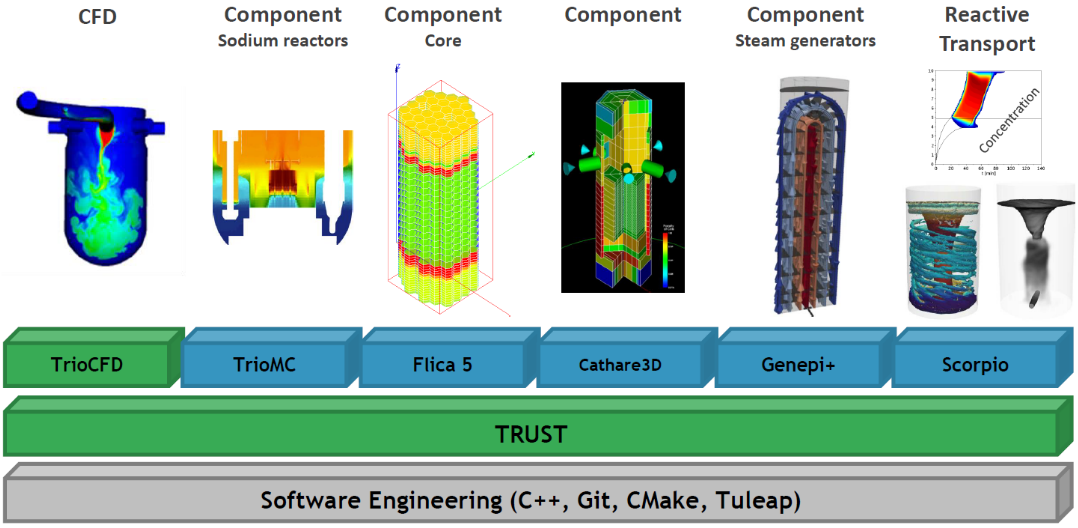

Figure 1. – TRUST platform under development strategy for the thermal hydraulics codes **Nop et al.** 2022.

A.1.1. Discretization of governing equations

The fluid mechanics equations are addressed using staggered finite-volume techniques as implemented in TrioCFD. They accommodate either fully parallelepiped or fully tetrahedral meshes, which can be structured or unstructured. The discretization techniques used for these mesh types are known as finite volume differences (VDF) for parallelepipeds and finite volume elements (VEF) for tetrahedra. By merging finite difference and finite element methods with the finite volume approach, these methods efficiently handle incompressible Navier-Stokes problems up to moderate

---

[1] https://github.com/cea-trust-platform

and high convection dominated flows. In this setup, the variables for velocity and temperature are located at the cell faces, and the corresponding finite elements in VEF are nonconforming P1. Pressure is located at the gravity center in VDF and is additionally located at nodes (P1-bubble) in VEF. In 3D scenarios, pressure unknowns can optionally be added at edges in specific cases, such as thermal stratification or natural convection (**Angeli et al. 2015**).

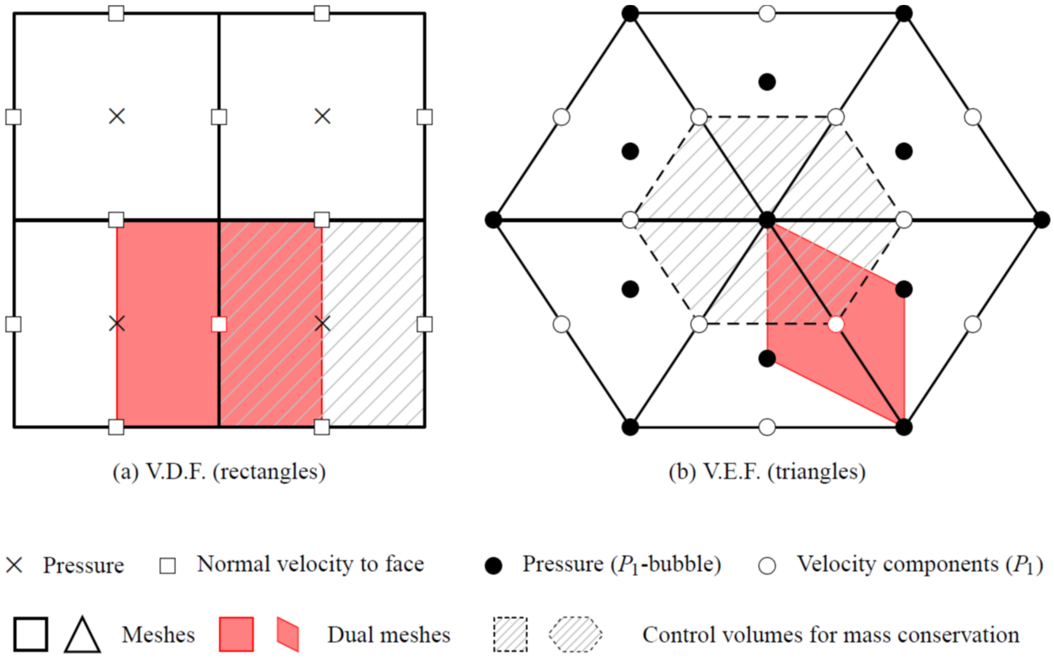
(a) V.D.F. (rectangles)

(b) V.E.F. (triangles)

Figure 2. – Schematic 2D representation of discretization methods in TrioCFD with respective positioning of degrees of freedom and control volumes (**Angeli et al. 2015**).

A dual mesh mesh is constructed such that the degrees of freedom are located at the center of dual elements in Figure 2. The equations are integrated over these new control volumes. The VDF resolution hinges on finite difference approximations of fluxes, while the VEF resolution relies on a variational approximation using P1 basis functions. Consequently, the number of control volumes equals the number of faces in the mesh, approximately twice the number of cells. Hence, for an equal number of elements, the VDF discretization is computationally more efficient than VEF, owing to fewer control volumes and a better-conditioned pressure matrix.

The staggered arrangement of velocity and pressure eliminates spurious pressure modes, often referred to as "checkerboard patterns", as opposed to a collocated arrangement. The computation of velocity and pressure fields are decoupled through a projection method, wherein an intermediate velocity is calculated, and mass conservation is then adjusted by solving a Poisson equation for pressure on every control volume. Due to the presence of curved section, only tetrahedra and triangle shown in Figure 3.11 are available by using VEF for discretization of governing equations.

A.1.2. Time discretization errors

In our study, the semi-implicit time scheme (rather time-consuming) is used to compute laminar flow with a DNS approach. For the low Reynolds range of transition flow, NLEVM approach could be useful with either semi-implicit or implicit time scheme. Finally, due to simulation challenging with high Reynolds number, the turbulence model (WALE - a sub-grid model of LES) is applied with implicit time step, where different step sizes can be chosen as long as the accuracy is guaranteed.

Although intuition tells us the above-mentioned rule, in practical terms, such as in industry, a more economical approach is often favored. Therefore, two scenario shown in Table 1 for time discretization are studied for given geometries with $\Delta T = 10K$ similar to previous simulation in Figure 3.6(a).

Table 1. – Specifications of study cases for time discretization error

Case	1	2
Geometry	$s_{1,1}$	$s_{1,2}$
Mesh	M 2	M 3
Time integration	1st order implicit Euler	2nd Adams-Moulton
Advection	Upwind	Center
Expected convergence order	1	2

Case1: Applications with 1st order truncation error

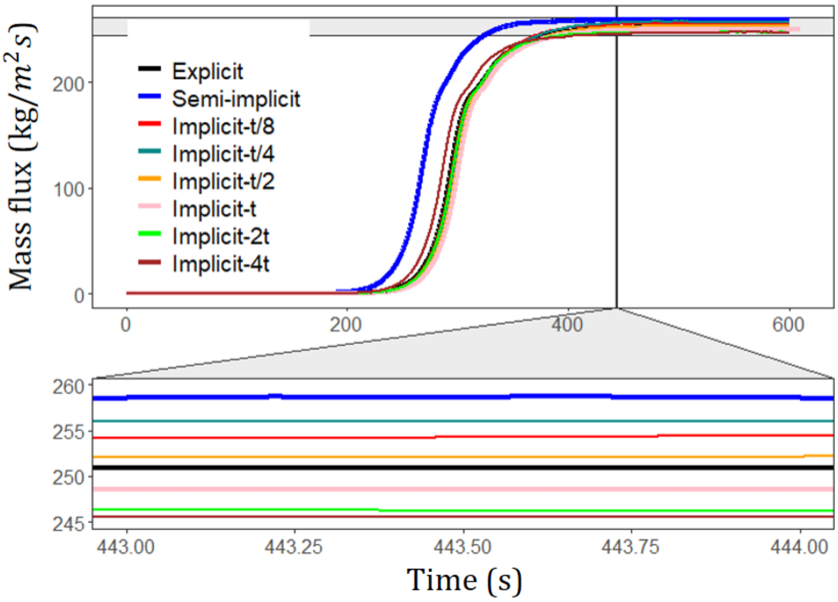

Figure 3. – Asymptotic mass flux rate versus time-step size for different time scheme and for geometry $s_{1,1}$ under $\Delta T = 10K$.

The 2D approach with an M2 grid is presented in the Figure 3, which depicts the flow response under different time schemes, transitioning from the initial meta-stable state to the flow onset and ultimately reaching the asymptotic "steady" state. The flow responses are encapsulated in the mass flux at the steady state and the activation time (the time taken to reach half of the steady flow rate). These responses reveal the effects of several key errors: iterative convergence error, temporal and spatial discretization error. Further analysis suggests the following:

- For **larger time steps** ($2\Delta t$ & $4\Delta t$), a substantial iterative convergence error occurs when solving the algebraic systems as the maximum number of iterations per time step is reached before a specific iterative tolerance is met. This precludes the study of discretization errors.
- When the time step size is reduced, the time discretization error decreases in accordance with a convergence order associated with the chosen method. The mass flux increases and converges towards the semi-implicit method, then decreases with the **smallest time step** ($\Delta t/8$, still larger than the semi-implicit time step) due to the accumulation of iterative errors.
- The **explicit approach**, which requires the smallest time step to satisfy the Courant–Friedrichs–Lewy (CFL) criteria, exhibits a significant discrepancy compared to the semi-implicit and $\Delta t/4$ implicit cases.
- Additionally, the **activation time** is influenced by numerical noise (as discussed in a previous section). Compared to the implicit method, the semi-implicit method initiates significantly earlier, which can be attributed to its less diffusive numerical scheme, resulting in less smoothing of the numerical noise.
- Finally, within the asymptotic zone for time discretization, the **iterative error** (which should be proportional to the iterative residuals of the implicit solver according to **Oberkampf and Roy 2010**) decreases over the time step size as shown in the Figure 4.

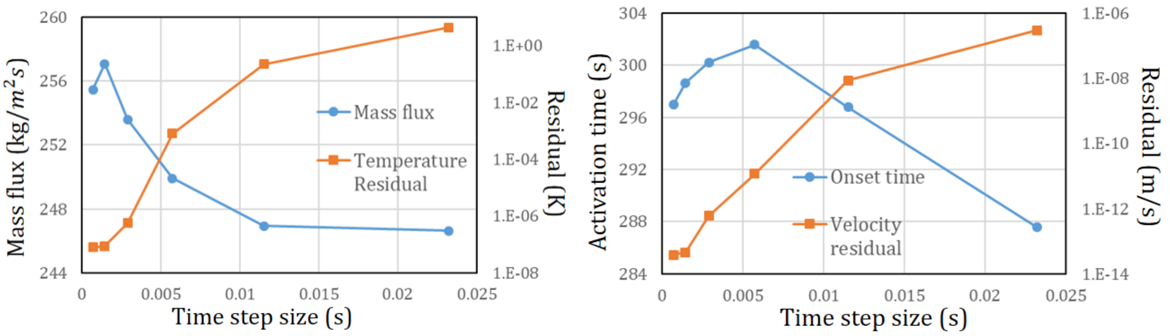

(a) Mass flux V.S. Residuals

(b) Onset time V.S. Residuals

Figure 4. – Mass flux and onset time response for backward Euler method of geometry $s_{1,1}$ under $\Delta T = 10K$.

Based on this analysis, it can be inferred that the explicit approach performs poorly due to the high stiffness of the flow (see linear approximation and potential iterative error accumulation). Conversely, the implicit and semi-implicit approaches yield consistent results. The semi-implicit method could be utilized as it lessens the impact of iterative errors compared to the fully implicit choice, while maintaining a reasonable CPU cost. For the implicit method, iterative error should be minimized before the space discretization error, thereby avoiding both a too small time step (leading to accumulative iterative error) and a too large time step (potentially distorting the physical characteristics).

Despite the analysis above, as a reminder, we do not observe solution convergence for this case of time discretization. We may question whether the discretization order is inadequate, or perhaps the mesh is not suitable for this type of time discretization study. Let's examine case 2, where all the aforementioned concerns are addressed.

Case2: Applications with 2nd order truncation error

In the current case under the same $\Delta T = 10K$, a general second-order discretization scheme is employed in Figure 5. As the time step is progressively refined, the solution initially converges, capturing a greater detail of the flow temporal dynamics. However, upon further reduction of the time step size, the solution unexpectedly diverges. This divergence occurrence may due to numerical errors amplified at excessively small time steps or discrepancies between the temporal and spatial scales being resolved.

On the other hand, for the previous case utilizing first-order time discretization, the non-convergence could be due to the inherent diffusive nature of the first-order scheme which can excessively damp the flow features and thus compromise the accuracy of the solution. Therefore, reducing the time step doesn't lead to noticeable convergence, as the solution is already limited by the low-order nature of the discretization scheme.

It's noteworthy that while LES models are designed to adapt to the grid size, exhibiting some inherent capacity to adjust to different time step sizes, excessively small time steps can still lead to divergence if they attempt to resolve temporal scales that are smaller than the spatial scales that the mesh can capture. For example, in the same Figure 5, for a strong buoyancy force under $\Delta T = 40K$, a finer spatial scale resolution is required. In such a scenario, using the same time step and spatial scale size may not ensure accurate prediction, resulting in different convergence capabilities.

Therefore, we may wonder how to improve the solution convergence while not paying price for more refined mesh. As illustrated in the Figure 6, we conducted a systematic study regarding the relationship between Reynolds number (larger ΔT) and time step size (dt). We observe the solution convergence by given three grid points. Clearly, for the combination of larger time step sizes, the convergence capacity starts to diminish over larger Reynolds number. When the smaller time step is introduced, the improvement of temporal dynamic resolution results in the better solution convergence for larger ΔT. On the other hand, such combination is too small in Figure 6(e) with smaller Reynolds number where the time resolution is excessive and out of balance.

In summary, with appropriate grid size, achieving an optimal balance between temporal resolution (time step size) and the intensity of physical phenomena (like

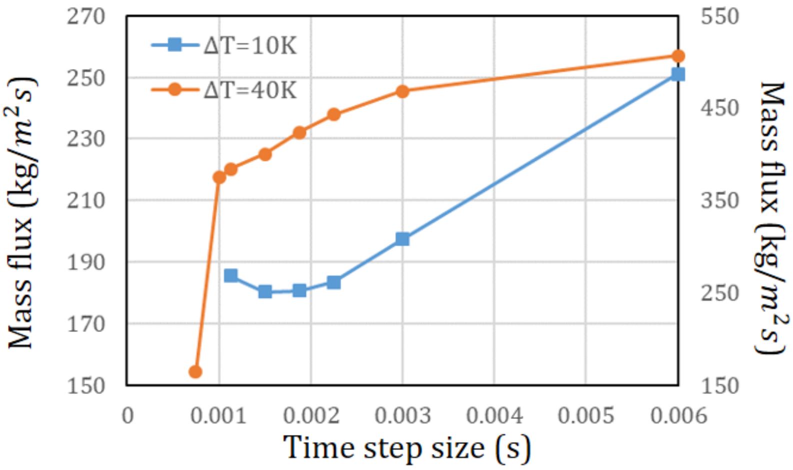

Figure 5. – Asymptotic mass-flux rate versus time-step size for 2nd order Adams-Moulton method for geometry $s_{1,2}$ under $\Delta T = 10K$ & $40K$.

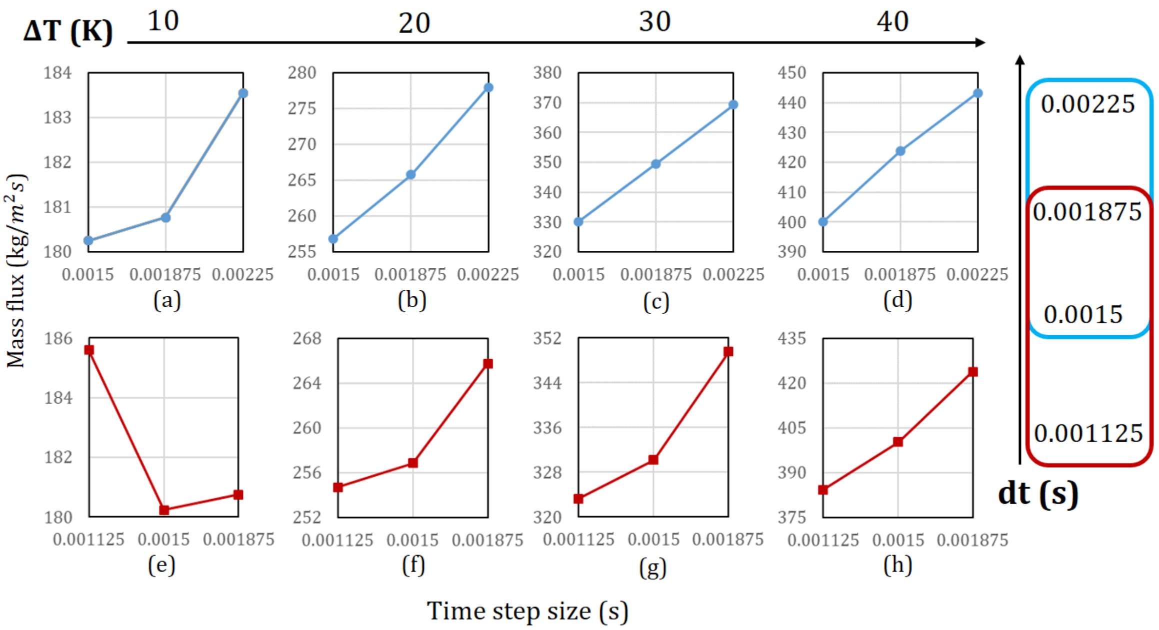

Figure 6. – Investigation of solution convergence for geometry $s_{1,2}$ for time discretization with different temperature (from $10K$ to $40K$) and 2nd order Adams-Moulton time steps (from larger to smaller combination).

buoyancy force) is key to efficient and accurate CFD simulations. It's about refining the time step size to adequately capture the dynamics of the flow, without overshooting and causing unnecessary computational expense.

A.2. TrioCFD code

TrioCFD [2] is a generic CFD tool, developed at the Nuclear Energy Department (DEN) from 1995 to 2015 under the name Trio_U. With the transition to open source in 2015, Trio_U was separated, with the computational/digital platform TRUST and the application for local-scale flow simulation taking on the name TrioCFD. The code is dedicated to simulating unsteady, incompressible, or weakly compressible (low-Mach) flows for nuclear applications (reactor thermohydraulics) but not limited to them (turbulent single-phase flows on complex geometries). An explicit interface tracking module (Front Tracking, FT) also enables the simulation of local-scale two-phase flows. The highly modular architecture of the software, based on object-oriented design, has been utilized to develop new applications within the TRUST platform, such as PAREX+, GENEPI+, or FLICA5. For the tools available for TrioCFD, the Figure 7 would be helpful.

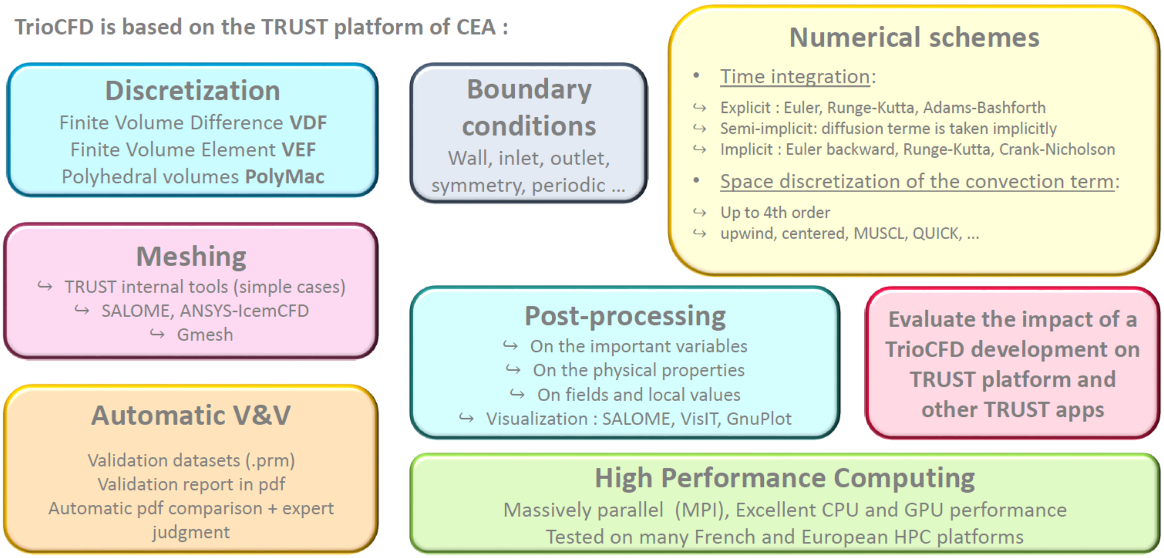

Figure 7. – Tools available for TrioCFD in the TRUST platform **Nop et al. 2022**.

A.2.1. Wall shear stress related to wall function

Wall shear stress, denoted by τ_w, significantly influences heat transfer, flow separation, and drag characteristics. This stress arises from the viscous friction experienced by a fluid flowing over a solid surface and primarily depends on the velocity gradient at the wall.

---

[2] https://sourceforge.net/projects/triocfd/

In CFD, a common practice is to employ a linear approximation within the grid cell adjacent to the wall. This approximation can lead to discrepancies between the calculated and actual wall shear stress, resulting from the variable velocity gradients in the flow. The relationships can be represented as:

$$\tau_{w,actual} = -\rho\nu \frac{\partial U}{\partial y}_{y=0} \quad \text{and} \quad \tau_{w,CFD} = -\rho\nu_w \frac{U_w}{y_w} \tag{0.1}$$

Here, ν_w represents the effective wall viscosity, and U_w and y_w represent the velocity and the distance of the first cell from the wall in CFD, respectively. The assumption is made that the normalized velocity U^+ is a function of the dimensionless distance from the wall y^+, represented by $U^+ = f(y^+)$, where y^+ is defined as :

$$y^+ = \frac{u_\tau y}{\nu} \tag{0.2}$$

where u_τ denotes the friction velocity. We can write the relation of mentioned velocities with τ_w represented also as $-\rho u_\tau^2$.

$$U^+ = \frac{U}{u_\tau} = \frac{U \cdot u_\tau}{u_\tau^2} = -\frac{\rho U \cdot u_\tau}{\tau_w} \Rightarrow \tau_w = -\frac{\rho U \cdot u_\tau}{f(y^+)} \tag{0.3}$$

Finally, we can gather the relations in Equation 0.1, 0.2 and 0.3 to bridge the relation between the effective wall viscosity and molecular one through wall function.

$$\tau_w = -\frac{\rho U \cdot u_\tau}{f(y^+)} \Rightarrow \nu_w = \frac{y_w u_\tau}{f(y^+)} = \nu \cdot \frac{y^+}{f(y^+)} \tag{0.4}$$

By modifying the effective wall viscosity, ν_w, we can bridge the gap between the actual and calculated wall shear stress, providing a more accurate representation of the flow dynamics near the wall in CFD simulations. Explicitly, tuning this wall function appropriately, the effective wall viscosity can be rendered equivalent to the product of molecular viscosity(ν), wall distance (y^+), and a function $f(y^+)$, which serves as a correction factor accounting for the non-linearity of the velocity profile near the wall.

In summary, the function $f(y^+)$ can be selected from a range of available wall functions, each with its unique strengths and limitations. The choice of the wall function should be driven by the specific requirements of the simulation and the nature of the flow. Consequently, it provides a degree of flexibility and control in addressing the discrepancy in wall shear stress prediction, offering a path to enhanced accuracy in CFD simulations.

A.3. URANIE platform

URANIE[3] is a software framework dedicated to uncertainty quantification, sensitivity analysis, calibration, and the generation of surrogate models, optimizations, and more. This framework is written in C++ and heavily relies on the ROOT software framework[4], developed at CERN since the late nineties. ROOT is designed to handle large amounts of data and provide various services. URANIE, built on top of ROOT, offers additional methods, including:

- Generation of design-of-experiments
- Generation and training of surrogate models
- Sensitivity analysis methods
- Visualization tools dedicated to uncertainty
- Parametric optimization methods (mono and multi-criteria, with or without constraints)
- Calibration methods with or without uncertainties, including Bayesian estimations with a priori knowledge

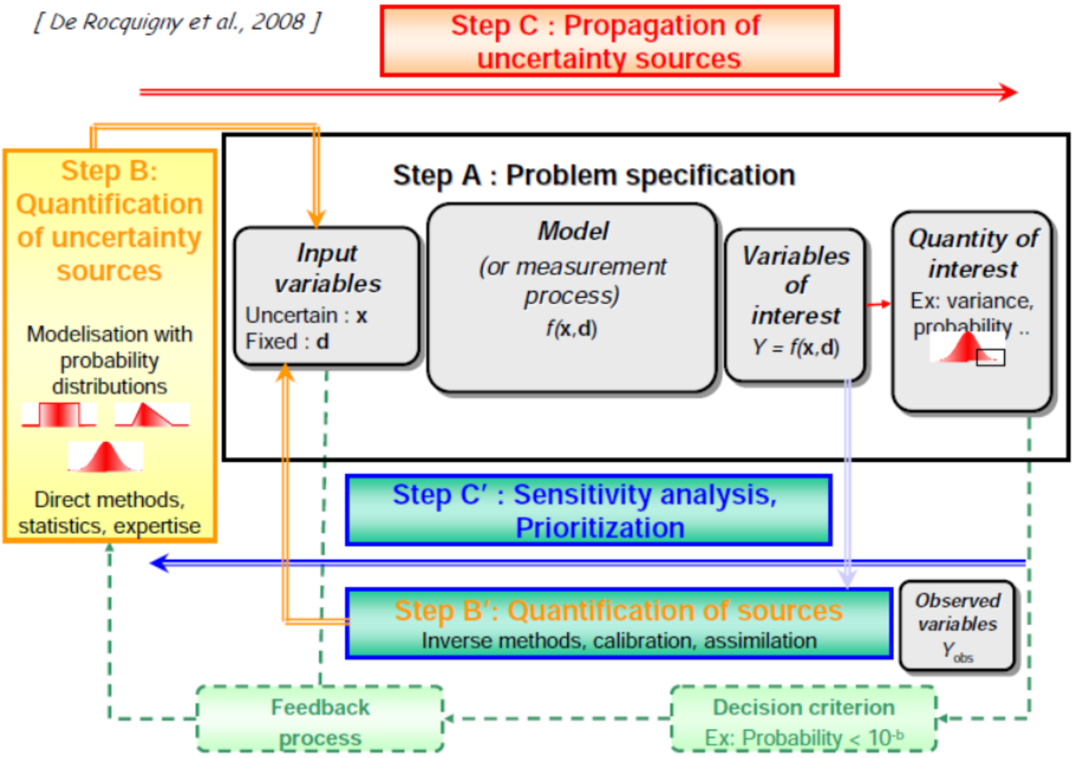

Figure 8. – Sketch of the various kinds of analysis that can be done in a VVUQ analysis (**de Rocquigny** 2012).

URANIE provides different interfaces to address various problems. The native C++

---

[3] https://sourceforge.net/projects/Uranie/

[4] https://root.cern/

interface, inherited from ROOT, allows the creation of scripts for conducting studies. The Python interface, suitable for users more familiar with the Python language, facilitates integration with the Salome framework. The XML interface is used to interface certain elements of uncertainty propagation or sensitivity analysis within more integrated software, reducing the user's effort. In day-to-day usage, C++ and Python scripts remain the primary means of conducting verification, validation, and uncertainty quantification (VVUQ) analysis.

The Figure 8 shown below represents different kinds of analysis using URANIE.

- **Problem Specification (A):** Input variable definition of the problem under consideration along with the outputs, called variable of interest (VoI) and their quantity of interest (QoI). All these are linked through the provided model (function, code, surrogate model, etc.).
- **Quantification of Uncertainty Sources (B):** Probability laws are assigned to the input variables, and their parameters are fixed (mean, standard deviation, etc.). Various kinds of correlation can also be introduced to complete the system description.
- **Propagation of Uncertainty Sources (C):** From steps A and B, the uncertainties on input variables are propagated to the quantity of interest, for instance, through a Monte Carlo approach or design-of-experiments techniques.
- **Quantification of Sources (B'):** Utilizing information available from step A and a given dataset, it is possible, under certain assumptions, to calibrate the physical models using random variables. This process aims to extract as much information as possible from the data and prior knowledge.
- **Sensitivity Analysis (C'):** Based on the inputs from steps A and B, sensitivity analysis allows for the prioritization of input variables according to their impact on a given quantity of interest. Some methods provide quantitative estimations, such as the fraction of the standard deviation of the output under consideration, as shown in the figure below.

A.3.1. URANIE modules

The URANIE platform consists of various modules, as demonstrated in Figure 9, each serving a specific function:

- **DataServer module:** The core module of URANIE, it encompasses the TDataServer object which contains essential information about problem variables, such as names, units, probability laws, and data files. It facilitates basic statistical operations.
- **Sampler module:** This module utilizes the attributes of TDataServer (random variables) to create different designs-of-experiments. It offers a wide range of design options, some of which are designed to be called by more complex methods.
- **Launcher module:** The Launcher module applies an analytic function or an external simulation code to the content of a TDataServer. The content can be derived from a design-of-experiments generated using a TSampler object or

loaded from external sources (e.g., ASCII files, SQL databases).

- **Modeler module:** The Modeler module allows the construction of surrogate models that establish a relationship between input factors and output responses. It supports various modeling techniques such as polynomial models and neural networks.
- **Sensitivity module:** This module enables sensitivity analysis of output responses with respect to input factors. It introduces the fundamental concepts of sensitivity analysis and provides methods for analyzing the impact of input factors on output responses.
- **Optimizer and Reoptimizer modules:** The Optimizer and Reoptimizer modules are dedicated to optimization and model calibration. Model calibration involves adjusting the "degrees of freedom" of a model to achieve the best fit with experimental data. The optimization techniques support single-criterion and multi-criteria optimization with or without constraints.
- **Relauncher module:** The Relauncher module provides a technical architecture for parametric studies within the URANIE platform. It enables secure utilization of multiple processors and threads in a straightforward manner.
- **Calibration module:** The Calibration module is specifically designed for obtaining accurate estimations of model parameters. It employs various techniques, each making specific assumptions about the model, but all methods require data for calibration.

Before delving into the internal organization of the platform, it is important to consider the dependencies of URANIE. These dependencies are categorized as compulsory and optional. The compulsory dependencies are essential for the platform, while the optional dependencies are depicted as blue boxes.

A.3.2. Surrogate models

The Modeler module discusses the generation of surrogate models which aim to provide a simpler, and hence faster, model in order to emulate the specified output of a more complex model (and generally time and memory consuming) as a function of its inputs and parameters. As shown in Figure 10, all these surrogate models require a set of elements, which can either be a design-of-experiments specifically created for the analysis or a collection of independent measurements or calculations. This set of elements serves as input to create the model, which can then be exported in different formats for reuse within URANIE or any other software code.

The fundamental concept behind polynomial chaos expansion (referred to as PCE) is that any square-integrable function can be represented as a sum of terms. Each term is a product of PC coefficients and orthogonal polynomial basis functions. The expression can be written as follows:

$$f(\boldsymbol{x}) = \sum_{\boldsymbol{\alpha}} f_{\boldsymbol{\alpha}} \Psi_{\boldsymbol{\alpha}}(\boldsymbol{x})$$

where $f_{\boldsymbol{\alpha}}$ are the PCE coefficients, $\Psi_{\boldsymbol{\alpha}}$ is the orthogonal polynomial-basis. The

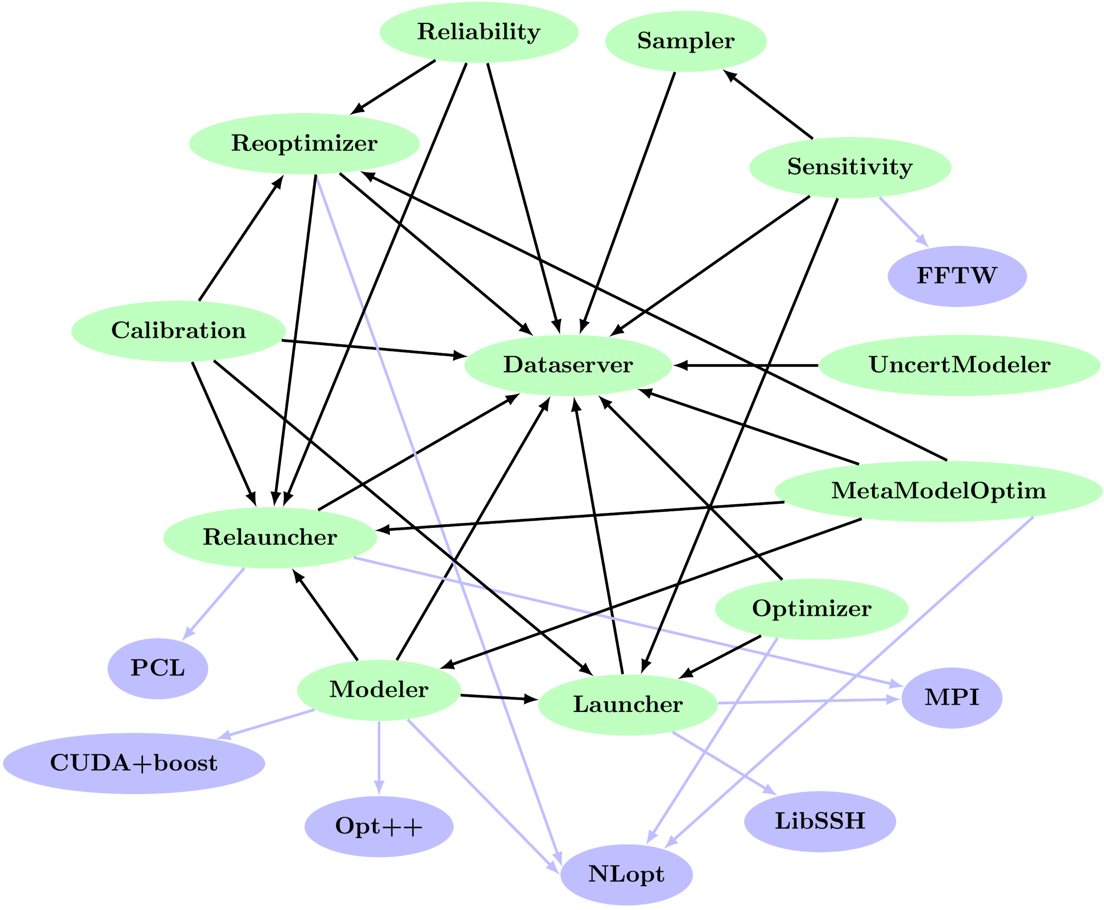

Figure 9. – Organisation of the URANIE-modules (green boxes) in terms of inter-dependencies, along with the external dependencies (blue boxes).

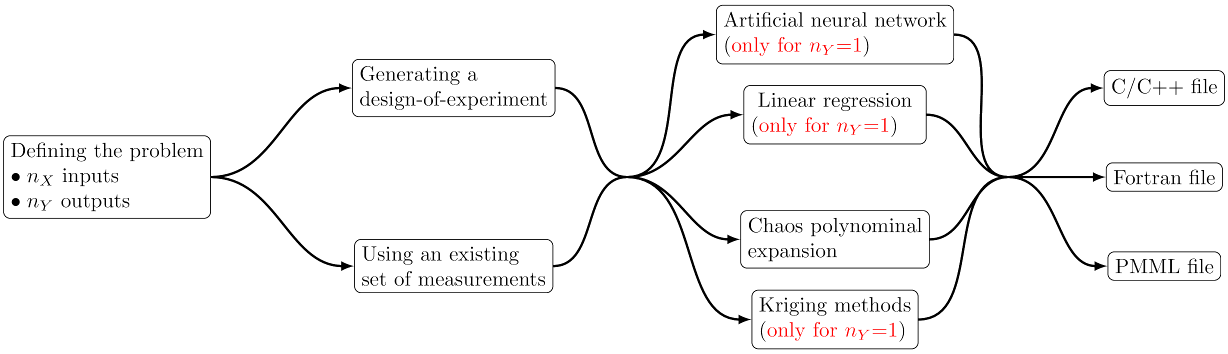

Figure 10. – Simplified decomposition of the surrogate model creation process into a four important-step recipe in URANIE.

index over which the sum is done, α, corresponds to a multi-index whose dimension is equal to the dimension of vector x and whose L1 norm is the degree of the resulting polynomial. Originally written to deal with normal law, for which the orthogonal basis is Hermite polynomials, this decomposition is now generalised to few other distributions, using other polynomial orthogonal basis (the list of those available in URANIE is shown in Table 2).

Table 2. – List of best adapted polynomial-basis to develop the corresponding stochastic law in URANIE.

Distribution\Polynomial type	Legendre	Hermite	Laguerre	Jacobi
Uniform	X			
LogUniform	X			
Normal		X		
LogNormal		X		
Exponential			X	
Beta				X

The Nisp library, which stands for Non-Intrusive Spectral Projection, provides functionality that can be accessed from the URANIE platform through a dedicated wrapper. The main features of the Nisp wrapper are outlined below.

The Nisp library utilizes spectral methods based on polynomial chaos to create surrogate models and enable the propagation of uncertainties in numerical models. The steps involved in this type of analysis, using the Nisp methodology, are schematically represented in Figure 11 and are described as follows:

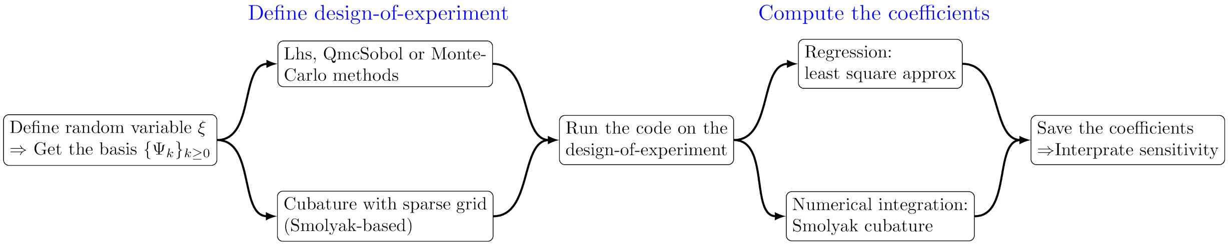

Figure 11. – Schematic view of the PCE-Nisp methodology in URANIE.

- **Specification of uncertain parameters:** Define the uncertain parameters (ξ) that contribute to the overall uncertainty.
- **Building stochastic variables:** Construct stochastic variables (ξ_i) associated with the uncertain parameters.
- **Building a design-of-experiments:** Generate a design-of-experiments to sample the input space efficiently.
- **Building a polynomial chaos:** Construct a polynomial chaos expansion using either regression or integration methods.

- **Uncertainty and sensitivity analysis:** Perform uncertainty and sensitivity analysis using the constructed polynomial chaos expansion, enabling the assessment of the impact of uncertain parameters on the model's output.

These steps outline the workflow of Nisp methodology, which leverages polynomial chaos for uncertainty quantification and sensitivity analysis.

For the better understanding of different method for PCE, the Table 3 regroups the advantages and disadvantages of integration and (sparse) regression methods.

Table 3. – Comparison of Polynomial Chaos Expansion methods

Method	Advantages	Disadvantages
Projection/Integration	Accuracy	Complexity
	Convergence	Sensitivity
	Flexibility	Curse of dimensionality
Regression	Scalability	Approximation error
	Flexibility	Overfitting
	Robustness	Convergence
Sparse Regression	Sparsity	Algorithm complexity
	Computational efficiency	Selection of tuning parameters
	Robustness	Sensitivity to noise

A.3.3. PCE for turbulence models

We'll discuss here a simple example of polynomial chaos development and its implications. In the case where a system is depending on two random variables, X_U and X_N, that follow respectively a uniform and normal (Gaussian) distribution, giving rise to a single output Y. Following the remark about square-integrable functions, both inputs can be decomposed on a specific orthogonal polynomial-basis, such as $X_U = \sum_\alpha f_\alpha^U \mathscr{L}_\alpha$ and $X_N = \sum_\alpha f_\alpha^N \mathscr{H}_\alpha$, where f_α^U and f_α^N are the PCE coefficients that respectively multiply the Legendre ($\mathscr{L}$) and Hermite ($\mathscr{H}$) polynomials, for the uniform and normal law and where α is the multi-index (here of dimension 1) over which the sum is done.

It is now possible to write the output, Y, as a function of these polynomials. For the i-th simulation, we have the chaos polynomial function:

$$Y^i = \sum_{|\alpha|_1 \leq n_X} \beta_\alpha \Psi_\alpha (X_U^i, X_N^i)$$

where α is the multi-index of dimension 2 over which the sum is performed. The Ψ polynomials are built by tensor products of the inputs basis following the previously defined degree. In the specific case of the simple example discussed here, this leads to a decomposition of the output that can be written as polynomial chaos decomposition:

$$\begin{aligned}
Y^i = &\beta_{0,0} \quad (|\alpha|_1 = 0)\\
&+ \beta_{1,0}\mathscr{L}_1(X_U^i) + \beta_{0,1}\mathscr{H}_1(X_N^i) \quad (|\alpha|_1 = 1)\\
&+ \beta_{1,1}\mathscr{L}_1(X_U^i)\mathscr{H}_1(X_N^i) + \beta_{2,0}\mathscr{L}_2(X_U^i) + \beta_{0,2}\mathscr{H}_2(X_U^i) \quad (|\alpha|_1 = 2)\\
&+ \beta_{2,1}\mathscr{L}_2(X_U^i)\mathscr{H}_1(X_N^i) + \beta_{1,2}\mathscr{L}_1(X_U^i)\mathscr{H}_2(X_N^i) + \beta_{3,0}\mathscr{L}_3(X_U^i) + \beta_{0,3}\mathscr{H}_3(X_U^i) \quad (|\alpha|_1 = 3)\\
&+ \dots
\end{aligned}$$

As the example of LEVM shown in Figure 5.6, the PCE coefficient for 4th order can be replaced in the written equation. From this development, it becomes clear that a threshold must be chosen on the order of the polynomials used, as the number of coefficient is growing quickly, following this rule $N_{coef} = \frac{(n_X+p)!}{n_X!p!}$, where p is the cut-off chosen on the polynomial degree. In this example, if we choose to use $p = 4$, this leads to only 15 coefficients to be measured shown in Figure 12.

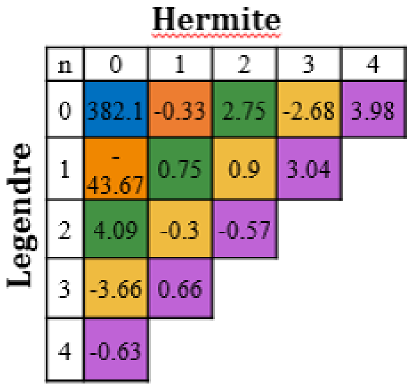

n	0	1	2	3	4
0	382.1	-0.33	2.75	-2.68	3.98
1	- 43.67	0.75	0.9	3.04	
2	4.09	-0.3	-0.57		
3	-3.66	0.66			
4	-0.63				

Figure 12. – PCE coefficient for LEVM meta-model for polynomial construction.

These coefficients are characterising the surrogate model and can be used, when the inputs are independent, to estimate the corresponding Sobol's coefficients. For the uniform and normal example, the first order coefficients are respectively given by

$$S_1^U = \frac{\beta_{1,0}^2 + \beta_{2,0}^2}{Var(Y)} \text{ and } S_1^N = \frac{\beta_{0,1}^2 + \beta_{0,2}^2}{Var(Y)}$$

whereas the total order coefficients are respectively given by

$$S_T^U = \frac{\beta_{1,0}^2 + \beta_{2,0}^2 + \beta_{1,1}^2}{Var(Y)} \text{ and } S_T^N = \frac{\beta_{0,1}^2 + \beta_{0,2}^2 + \beta_{1,1}^2}{Var(Y)}$$

The complete variance of the output, can also be written as

$$Var(Y) = \sum_{|\alpha|_1 \leq 2} \beta_\alpha^2$$

For the quantile computaton, the Wilks quantile computation is an empirical estimation, based on order statistic which allows to get an estimation on the requested quantile, with a given confidence level β, independently of the nature of the law, and most of the time, requesting fewer estimations than a classical estimation. Going back to the empirical way: it consists, for a 95% quantile, in running 100 computations, ordering the obtained values and taking the one at either the 95-th or 96-th position. Wilks computation on the other hand request not only a probability value but also a confidence level. The quantile x_p^β represents the x_p quantile given the p probability but this time, the value is provided with a β % confidence level, meaning that β % of the obtained value is larger than the theoretical quantile. This is a way to be conservative and to be able to quantify how conservative one wants to be. To do this, the size of the sample must follow a necessary condition:

$$n > \frac{ln(1-\beta)}{ln\ p}$$

Table 4. – Size of the sample for wilks computation for given probability and confident level.

β/p	**0.995**	**0.975**	**0.95**
0.99	919	182	90
0.95	598	119	59

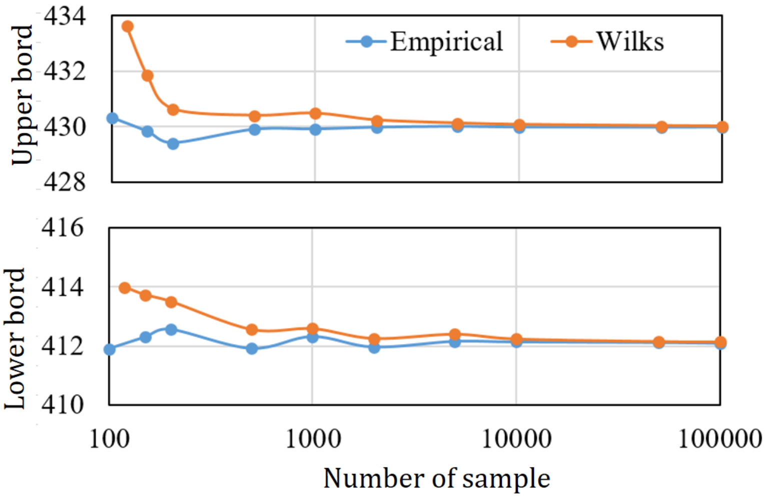

Figure 13. – Convergence of quantiles computation for different sample size in wilks method with double 95%.

An example of minimum sample size for given propabiblity and confident level for Wilks method is given in Table 4. While for the actual application under 95% probability with 95% confident level, we can observe the convergence between two quantile computation methods over sample size in Table 13. For this rather simple case, the difference between them is not evident.

For Sparse regression method in UQLab[5], a complementary strategy to favour sparsity in high dimension consists in directly modifying the least-square minimization problem by adding a penalty term. Several algorithms exist that solve the penalized minimization problem, including Least Absolute Shrinkage and Selection Operator (LASSO), Least Angle Regression (LAR), Orthogonal Matching Pursuit (OMP), Subspace pursuit (SP) and Bayesian Compressive Sensing (BCS).

The Table 5 shows the advantages of sparse regression method having higher Leave-One-Out quality Q^2 for the surrogate model and smaller validation error, even for such simple case with only two inputs. While in this study, the classic regression method exisiting in both URANIE and UQLab will be applied for code-to-code cross-validation.

Table 5. – Comparison of PCE methods in URANIE and UQLab

Regression	**Mean**	Q^2	**Validation Err**
Least-Squares Regression			
URANIE	382.08	0.9406	6.08E-03
UQLab	382.08	0.9406	4.91E-03
Sparse Regression in UQLab			
LARS	381.82	0.9987	3.04E-03
OMP	381.79	0.9987	2.80E-03
SP	381.87	0.9985	2.26E-03
BCS	381.85	0.9987	2.13E-03

A.4. HPC Computations

The HPC systems are designed to handle large scale, computationally intensive tasks efficiently and are optimized at every level for these tasks. The local workstation, while capable, is a general-purpose machine and might not be as finely tuned for these specific types of tasks. As we can observe from Figure 6 where 40 processors are used under different environments and show different response mainly due to:

1. Advanced CPU architecture: AMD EPYC CPUs may provide enhanced per-core performance and superior inter-core communication, exhibiting approximately half the average communication time typically observed.
2. Enhanced Memory Bandwidth: HPC systems typically feature multiple memory channels, offering superior bandwidth, a critical aspect for CFD simulations. As observed, the HPC case boasts a network bandwidth over 15 times greater than the workstation.

---

[5] https://www.uqlab.com/

3. Faster and larger storage systems: HPC systems frequently employ high-speed storage solutions such as NVMe drives or distributed parallel file systems, here allocating twice the amount of RAM compared to workstation.
4. Superior networking: HPC systems can often exhibit lower latency. As demonstrated, they offer nearly seven times higher bandwidth interconnectivity, facilitating improved inter-node communication.
5. Cooling and Power Delivery: HPC clusters have optimized cooling systems and power delivery, allowing higher sustained clock speeds.
6. System optimizations: HPC systems have OS tuning, HPC-specific libraries, and better job scheduling for efficient resource utilization.
7. Software optimization: TrioCFD may be better optimized to work on HPC clusters.

Table 6. – Computation efficiency between a workstation and different HPC cluster using 40 processors.

Location	**WorkStation**	**HPC(TGCC/Topaze/Milan)**		**HPC(TGCC/Topaze/A100)**
Processor	Intel(R) Xeon(R) Silver 4114 CPU @ 2.20GHz	AMD EPYC CPU @2.45GHz		Nvidia Ampere GPU
Processor number	40	128		128
Memory Size/GiB	128	256		512
OS	Debian 9.13 amd64	Red Hat		Red Hat
Version	TRUST-1.9.1(int32)	TRUST-1.9.1(int64)	TrioCFD-1.9.1-gpu(int32)	TrioCFD-1.9.1-gpu(int32)
Computer time (s)	64898.1	37192	27391	27604
Timesteps	44445	44444	44445	44445
Secondes / pas de temps	1.46019	0.83683	0.61629	0.62108
solveurs Ax=B	1.13923(78%)	0.640107(76%)	0.49033(79%)	0.47166(75%)
assemblage matrice_implicite	0.08523	0.05036	0.04098	0.03867
convection	0.03155	0.00919	0.00821	0.00823
diffusion	0.01537	0.03141	0.03263	0.03118
RAM (MB)	9534	12937	11904	17598
Communications avg	8.20%	3.40%	6.5	4.20%
Network latency (s)	3.30E-05	3.81E-06	3.74E-06	4.97E-06
Network bandwidth max (MB/s)	26.89	296.724	148.665	427.085
Average waiting time	6.71%	3.17%	5.85%	4.00%
Average velocity (m/s)	-0.11074	-0.11097	-0.11095	-0.11094

When performing CFD simulations, the precision of floating-point values frequently plays a critical role. These values are generally expressed in programming languages as either 'float' or 'double', corresponding to 32-bit and 64-bit representations, respectively. As evidenced in both Table 6 and Table 7, simulations using the int64 data type invariably require more computational time to complete identical calculations compared to those using int32. Interestingly, this increase in computational time does not correspond to a significant deviation in the prediction of average velocity, suggesting that round-off errors hold less relevance in our simulation context.

The central focus of these two figures is also to elucidate the impact of employing CPU and GPU versions of TrioCFD on computational efficiency. It is clear that when a single node with 128 processors is utilized for the actual simulation, the performance of both versions appears to be similar in every terms. Figure 14 presents the speed-up coefficient for the initial time step. Up to approximately 5,000 cores, an ideal speed-up is maintained. This corresponds to around 20,000 tetrahedral cells or 23,600 pressure points per core. As the number of elements per core decreases, the communication between the processor cores significantly increases, resulting in a considerable decrease in parallel performance. It's important to note that the cost associated with pressure resolution accounts for 60 % to 80 % of the total cost for one time iteration. This substantial proportion underscores the importance of optimizing this aspect of the computation to enhance overall performance (**Angeli et al.** 2015).

Table 7. – Computation efficiency for different TrioCFD version between CPU/GPU in different HPC cluster using 128 processors.

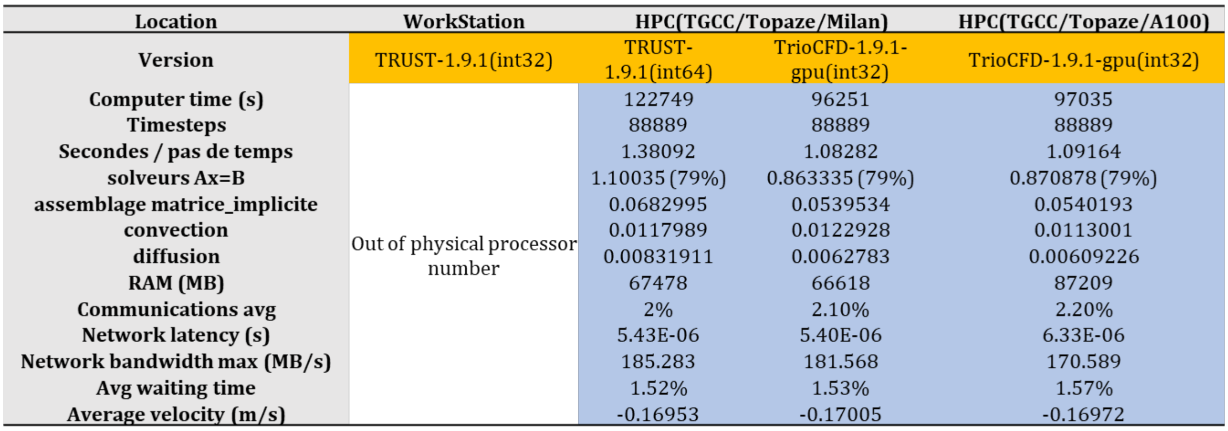

Location	**WorkStation**	**HPC(TGCC/Topaze/Milan)**		**HPC(TGCC/Topaze/A100)**
Version	TRUST-1.9.1(int32)	TRUST-1.9.1(int64)	TrioCFD-1.9.1-gpu(int32)	TrioCFD-1.9.1-gpu(int32)
Computer time (s)	Out of physical processor number	122749	96251	97035
Timesteps		88889	88889	88889
Secondes / pas de temps		1.38092	1.08282	1.09164
solveurs Ax=B		1.10035 (79%)	0.863335 (79%)	0.870878 (79%)
assemblage matrice_implicite		0.0682995	0.0539534	0.0540193
convection		0.0117989	0.0122928	0.0113001
diffusion		0.00831911	0.0062783	0.00609226
RAM (MB)		67478	66618	87209
Communications avg		2%	2.10%	2.20%
Network latency (s)		5.43E-06	5.40E-06	6.33E-06
Network bandwidth max (MB/s)		185.283	181.568	170.589
Avg waiting time		1.52%	1.53%	1.57%
Average velocity (m/s)		-0.16953	-0.17005	-0.16972

One may naturally inquire about the optimal number of partitions for a given mesh. Generally, using more partitions should, in theory, expedite computational time. However, the efficiency based on partition number is more complex and illustrated in the Figure 15. Specifically, the figure 15(a) illustrates the effect of the partition number on processor efficiency. The grey area, representing about 20K cells per partition, shows that increasing the partition number reduces the degrees of freedom (DoF) per partition. While this results in more communication between partitions, the gain in resolution efficiency per processor decreases.

On the other hand, the blue area, representing roughly 40K cells per partition, reveals a larger matrix to solve. This scenario leads to a decline in pressure resolution due to the increased size. Interestingly, the red area, corresponding to around 30K cells, presents exhaustive pressure resolution with direct/segregated solvers. This might be attributed to problems with L3 Cache, but these issues do not manifest with iterative and multigrid solvers for pressure after verifying the solver outputs. Moreover, in CFD applications, the choice of GPU over CPU can greatly influence computational efficiency. With their parallel processing capabilities, tasks like solving large linear systems of equations are typically time-consuming. While CPUs are versatile, they might not offer the same level of parallelism for such specific tasks, making GPUs a favorable choice for intensive computations.

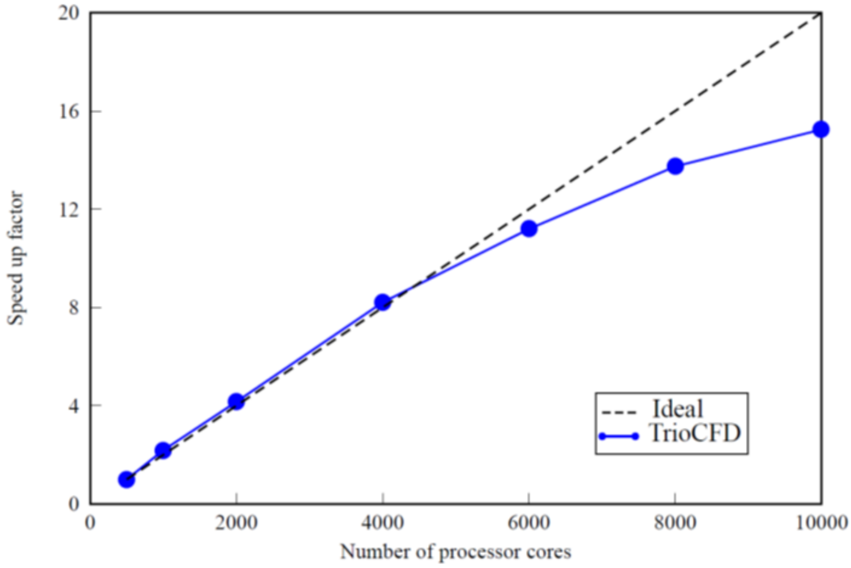

Figure 14. – Measured speed up factor in VEF when increasing the number of processor cores (**Angeli et al. 2015**).

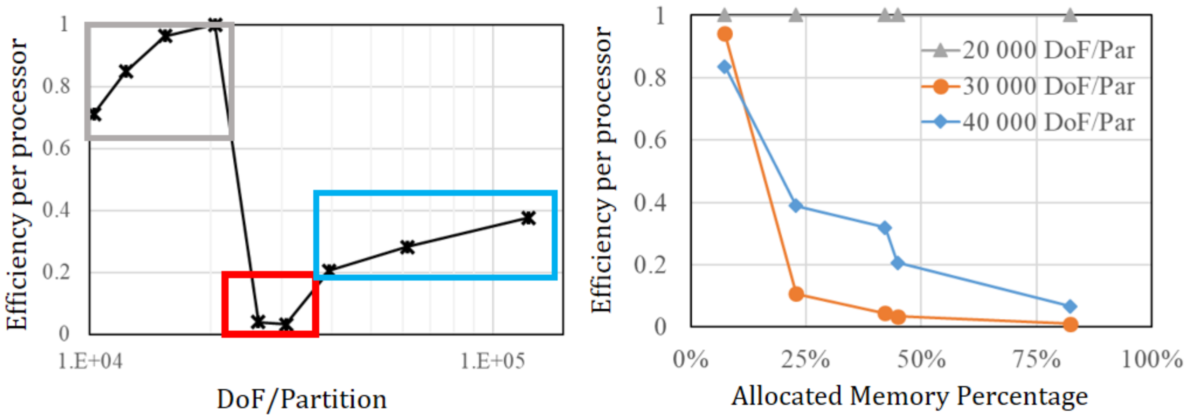

(a) Partitions

(b) Massflux for different partition

Figure 15. – (a) Partition distribution by METIS library; (b) Partition number study in a cluster with different combination of processors and nodes.

B. Dimensionless Analysis of Natural Circulation Loop

B.1. Steady-State Behavior of Single-Phase Systems

To develop the flow equations for the HHHC loop, we initially consider a simple uniform diameter rectangular loop with four curved pipelines/bends (denoted as R_k). The heater is either supplied with a uniform heat flux or, like the cooler, maintains a fixed temperature, while the pipelines are considered adiabatic. The conservation equations for mass, momentum, and energy are provided below, following certain simplifications. This section explains the derivation principles employed by **Vijayan, A. K. Nayak, and Kumar** 2019, providing a deeper understanding of these concepts.

Conservation of Mass (Continuity Equation)

Within the context of the HHHC loop, the continuity equation manifests as the incompressible flow equation, derived with the approximation that the fluid density remains constant. This results in the equation $\nabla \cdot \boldsymbol{u} = 0$, where $\boldsymbol{u}$ is the velocity field of the fluid, which can be further written as:

$$\frac{\partial u}{\partial s} = 0,$$

where s coordinate along the centerline of loop.

Conservation of Momentum

The Navier-Stokes equations are derived from the coupled momentum and mass conservation equations in fluid dynamics. However, when considering the HHHC loop, these equations can be tailored to fit the specific conditions and requirements of the system. By achieving a delicate balance between frictional forces and buoyancy forces within the loop, the resulting momentum equations can be simplified and formulated as follows:

$$f L_t \rho_0 \frac{\mathrm{d}u}{\mathrm{d}t} + \left(\frac{f L_t}{D} + K\right) \frac{\rho_0 u^2}{2} - \rho_0 \beta_T g \oint T \,\mathrm{d}z = 0 \tag{0.5}$$

where L_t denotes the total loop length and ρ_0 is the reference density. The second term is indicative of the frictional force and other pressure loss, which counterbalances the buoyancy force articulated by the third term, driven by a differential in temperature. It's noteworthy that the integral of temperature over the total length, $\oint T ds$, can be closely approximated by the integral over the vertical displacement, $\oint T dz$, due to our specific focus on the buoyancy effects within the vertical segments of the loop.

Conservation of Energy

The energy equation is crucial for understanding the thermal behavior of the fluid in the loop, particularly in capturing heat transfer effects at the interfaces of the heater and cooler. It is worth noting that in this context, the conductive heat flux is negligible compared to the convective heat flux. This holds true well beyond a certain threshold, but it is no longer valid either below or just above that threshold. Considering these conditions, the energy equation can be simplified and represented as follows, assuming the heater imparts a uniform heat flux or maintains a constant temperature, while the cooler retains a fixed temperature:

$$\frac{\mathrm{d}T}{\mathrm{d}t}+u\frac{\partial T}{\partial s}=\begin{cases}\frac{4U_h(T_h-T)}{\rho_0 C_p D}=\frac{4q_h}{\rho_0 C_p D},\ s\in[0,s_h]\\ 0,\ s\in(s_h,s_{hl})\cup(s_c,l_t)\\ \frac{-4U_c(T_c-T)}{\rho_0 C_p D},\ s\in[s_{hl},s_c]\end{cases}\tag{0.6}$$

where $s\in[0,s_h]$ is the heater section, $s\in(s_h,s_{hl})\cup(s_c,l_t)$ is the adiabatic pipeline and $s\in[s_{hl},s_c]$ is the cooler section. In order to easier compare with industrial case, the above equations are rewritten in terms of mass flow rate (or in mass flux to generalize 2D/3D case).

$$\frac{\partial\dot{m}}{\partial s}=0\tag{0.7}$$

$$\frac{L_t}{A}\frac{\mathrm{d}\dot{m}}{\mathrm{d}t}+\left(\frac{fL_t}{D}+K\right)\frac{\dot{m}^2}{2\rho_0 A^2}-\rho_0\beta_T g\oint T\,dz=0\tag{0.8}$$

$$\frac{\mathrm{d}T}{\mathrm{d}t}+\frac{\dot{m}}{\rho_0 A}\frac{\partial T}{\partial s}=\begin{cases}\frac{4U_h(T_h-T)}{\rho_0 C_p D}=\frac{4q_h}{\rho_0 C_p D},\ s\in[0,s_h]\\ 0,\ s\in(s_h,s_{hl})\cup(s_c,L_t)\\ \frac{-4U_c(T_c-T)}{\rho_0 C_p D},\ s\in[s_{hl},s_c]\end{cases}\tag{0.9}$$

Even though the transient state is interesting where multi numerical errors impact together on activation time and slope, the steady state is firstly investigated. Therefore, based on eqaution (0.7) (0.8) and (0.9), the flow equations can be derived:

$$R\frac{\dot{m}^2}{2\rho_0}=\rho_0\beta_T g\oint T\,dz=\rho_0\beta_T gH\Delta T_h,\ \text{with}\ R=\left(\frac{fL_t}{D}+K\right)/A^2\tag{0.10}$$

$$\frac{\dot{m}}{\rho_0 A}\frac{\partial T}{\partial s}=\begin{cases}\frac{4U_h(T_h-T)}{\rho_0 C_p D}=\frac{4q_h}{\rho_0 C_p D},\ s\in[0,s_h]\\ 0,\ s\in(s_h,s_{hl})\cup(s_c,l_t)\\ \frac{-4U_c(T_c-T)}{\rho_0 C_p D},\ s\in[s_{hl},s_c]\end{cases}\tag{0.11}$$

Heater with fixed heating temperature T_h

As seen in the heater description in equation (0.11), for the fixed heating temperature, the derivation will be same with cooler one.

$$\frac{\mathrm{d}T}{\mathrm{d}s} = \frac{4U_h(T_h - T)}{C_p D}\frac{A}{\dot{m}} \tag{0.12}$$

$$\frac{\mathrm{d}T}{\mathrm{d}s} + PT = PT_h, \text{ with } P = \frac{4U_h A}{C_p D\dot{m}} \tag{0.13}$$

$$\Rightarrow Te^{Ps} = \int PT_h e^{Ps}\mathrm{d}s + cste \tag{0.14}$$

with initial condition over inlet and outlet of heater $s = 0, T = T_{s_0} = T_{cl}$ and heat transfer coefficient $U_h(s)$ as variant over the heated/cooled wall.

$$cste = T_{s_0}e^{Ps_0} = T_{s_0}, \text{ with } s_0 = 0$$

$$\boxed{T(s) = T_h - (T_h - T_{s_0})e^{-Ps}} \text{ for heater with fixed } T_h \tag{0.15}$$

Cooler with fixed cooling temperature T_c

Same derivation applied on cooler with fixed cooling temperature T_c and initial conditions at inlet of cooler $s = s_{hl}, T = T_{hl}$ where T_{hl} is the temperature of hotleg and outlet temperature of heater if the flow mixing is well achieved in vertical pipeline.

$$cste = T_{s_{hl}}e^{Ps_{hl}}, \; with \; s_i = s_{hl}$$

$$\boxed{T(s) = T_c - (T_{s_{hl}} - T_c)e^{-P(s-s_{hl})}} \text{ for cooler with fixed } T_c \tag{0.16}$$

Pipelines with hotleg and coldleg temperature T_{hl} and T_{cl}

For adiabatic pipelines, the temperature should theoretically be homogeneous; however, in reality, it depends on factors such as the heat transfer efficiency of the heater/cooler and the rate of flow mixing progress, among others. To determine the theoretical buoyancy force generated by the temperature difference, $\Delta T_h = T_{hl} - T_{cl}$, we can derive this relationship from Equations (0.15) and (0.16) at the outlet of both.

$$T_{hl} = T_h - (T_h - T_{cl})e^{-P(s_h - 0)} = T_h - (T_h - T_{cl})e^{-P\Delta s}, \; with \; \Delta s = s_h \tag{0.17}$$

$$T_{cl} = T_c + (T_{hl} - T_c)e^{-P(s_c - s_{hl})} = T_c + (T_{hl} - T_c)e^{-P\Delta s}, \; with \; \Delta s = s_c - s_{hl} \tag{0.18}$$

Here, the length of heater and cooler is equal to Δs. Then, we can obtain the hotleg and coldleg temperature by solving the joint equation (0.17) and (0.18).

$$T_{cl} = \frac{1-e^{-P\Delta s}}{e^{P\Delta s}-e^{-P\Delta s}}(e^{P\Delta s}T_c + T_h) \tag{0.19}$$

$$T_{hl} = \frac{1-e^{-P\Delta s}}{e^{P\Delta s}-e^{-P\Delta s}}(e^{P\Delta s}T_h + T_c) \tag{0.20}$$

and naturally, we have:

$$\Delta T_h = T_{hl} - T_{cl} = \frac{e^{P\Delta s}+e^{-P\Delta s}}{e^{P\Delta s}-e^{-P\Delta s}}(T_h - T_c) - \frac{2(T_h-T_c)}{e^{P\Delta s}-e^{-P\Delta s}} \tag{0.21}$$

$$or\ \Delta T_h = (cothP\Delta s - cschP\Delta s)(T_h - T_c) = (cothP\Delta s - cschP\Delta s)\Delta T_{hc} \tag{0.22}$$

Where $coth$ denotes the hyperbolic cotangent and $csch$ represents the hyperbolic cosecant, with $P = \frac{4U_hA}{C_pD\dot{m}}$. To better understand, the variation of temperature difference over the heater and the imposed temperature over $P\Delta s$ is depicted in Fig. 16. When heat transfer is more efficient, the value of $x = P\Delta s$ is larger, and the normalized temperature approaches 1. However, theoretically, the two temperature differences will never be equal. To describe the asymptotic evolution of x and y, the first-order derivative is calculated for small x values (which are also frequently encountered in real situations). A constant a_T has been employed to approximate $cothP\Delta s - cschP\Delta s$ as $a_T * P\Delta s$. As a result, we obtain approximations of normalized temperature:

$$\frac{\Delta T_{h,ss}}{\Delta T_{hc}} = cothP\Delta s - cschP\Delta s = \begin{cases} a_T * P\Delta s,\ for\ P\Delta s \in (0,6) \\ 1,\ for\ P\Delta s \in (6,+\infty) \end{cases} \tag{0.23}$$

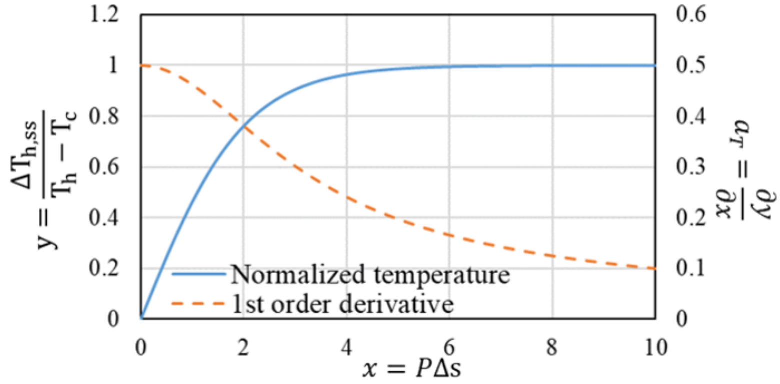

Figure 16. – Theorectical normalized temperature in natural circulation loop

Mass flow rate at steady state $\dot{m}_{ss} = \dot{m}$ with heating temperature T_h

From Equation (0.10) and (0.22), we obtain

$$\dot{m} = \left(2\rho^2\beta_T g H \Delta T_h / R\right)^{1/2} \tag{0.24}$$

$$\frac{\dot{m}^2}{coth\frac{B}{\dot{m}} - csch\frac{B}{\dot{m}}} = \frac{2\rho^2\beta_T g H \Delta T_{hc}}{R} \tag{0.25}$$

where $P\Delta s = \frac{4U_h A\Delta s}{C_p D} / \dot{m} = B/\dot{m}$. Since the expression of $\dot{m}_{ss}$ in (0.25) requires numerical method such as iteration or approximate estimation. For the approximation in (0.23), the clearest case is when $P\Delta s$ is larger enough, so that we have

$$\text{Equation}(0.25) \Rightarrow \frac{\dot{m}^2}{\approx 1} = \frac{2\rho^2\beta_T g H \Delta T_{hc}}{R} = \frac{2\rho^2\beta_T g H \Delta T_{h,ss}}{R} = \frac{2\rho^2\beta_T g H}{R}\frac{Q_h}{\dot{m}C_p}$$

$$\Rightarrow \boxed{\dot{m} = \left(\frac{2\rho^2\beta_T g H Q_h}{C_p R}\right)^{1/3}} \tag{0.26}$$

Another case is $\Delta T_{h,ss} \neq T_h - T_c$, we have $coth\frac{B}{\dot{m}} - csch\frac{B}{\dot{m}} \sim a_T * \frac{B}{\dot{m}}$

$$\text{Equation}(0.25) \Rightarrow \frac{\dot{m}^2}{a_T * \frac{B}{\dot{m}}} = \frac{\dot{m}^3}{a_T * B} = \frac{2\rho^2\beta_T g H \Delta T_{hc}}{R}$$

$$\Rightarrow \boxed{\dot{m} = \left(\frac{2\rho^2\beta_T g H}{RC_p} a_T \Delta T_{hc} \frac{4U_h A\Delta s}{D}\right)^{1/3}} \tag{0.27}$$

Mass flow rate at steady state with heated power Q_h

As seen in the heater description in equation (0.11), for the fixed heated power.

$$Q_h = q_h A_w = q_h \pi D_h L_h = \frac{q_h}{D_h}\pi D_h^2 \Delta s = \frac{q_h}{D_h}\pi \frac{4A_h}{\pi}\Delta s = \frac{4q_h A\Delta s}{D} (= q_h A_w)$$

where A_w is wet area of heater and A_h is flow section of loop through heater. To reapear the heating power in (0.27). We start the conservation of equations for imposed temperature and power.

$$Q_h = C_p \dot{m} \Delta T_{h,ss} = U_{eq} \Delta T_{hc} A_w$$

$$U_{eq} = \frac{\Delta T_{h,ss}}{\Delta T_{hc}} \frac{C_p \rho u A}{A_w} = \frac{\Delta T_{h,ss}}{\Delta T_{hc}} \frac{C_p \rho u D}{4L_h}$$

$$\Rightarrow \frac{B}{\dot{m}} = \frac{4U_h A\Delta s}{C_p D\dot{m}} = U_h\frac{4L_h}{C_p\rho u D} = \frac{U_h}{U_{eq}}\frac{\Delta T_{h,ss}}{\Delta T_{hc}} = \frac{U_h}{U_{eq}}a_T\frac{B}{\dot{m}} \Rightarrow \boxed{\frac{U_{eq}}{U_h} = a_T} \tag{0.28}$$

To be noticed, the equivalent heat transfer coefficient for imposed temperature is always small than the effective heat transfer coefficient over the heater. Therefore, we can regroup two different heat sources by equation conservation.

$$Q_h = \frac{4q_h A\Delta s}{D} = a_T\Delta T_{hc}\frac{4U_h A\Delta s}{D},\ with\ q_h = U_{eq}\Delta T_{hc} = U_h\Delta T_{h,ss} = a_T U_h\Delta T_{hc} \tag{0.29}$$

Here, we can review the (0.27) by considering the (0.29)

$$\boxed{\dot{m} = \left(\frac{2\rho^2\beta_T gH}{RC_p}a_T\Delta T_{hc}\frac{4U_h A\Delta s}{D}\right)^{1/3} = \left(\frac{2\rho^2\beta_T gHQ_h}{C_p R}\right)^{1/3}} \tag{0.30}$$

$$\text{with} \begin{cases} Q_h = \frac{4q_h A\Delta s}{D} \\ q_h = U_h\Delta T_{h,ss} = a_T U_h\Delta T_{hc} \\ R = (\frac{L_t}{D} + K)/A^2 \end{cases}$$

Here, we find out that equation (0.26) and (0.30) are equivalent for different heat transfer efficiency; which can all related to imposed power Q_h. Then, since $\Delta T_{h,ss} = Q_h/(\dot{m}C_p)$, we can rewrite (0.22) with Q_h.

$$\boxed{\Delta T_{h,ss} = \left(\frac{RQ_h^2}{2\rho^2\beta_T gHC_p^2}\right)^{1/3}} \tag{0.31}$$

In summarizing the aforementioned equations, we observe that at steady state, $\dot{m} \propto Q_h^{1/3}$ and $\Delta T_h \propto Q_h^{2/3}$. During calculation preparation, these correlations can be utilized to predict an approximate mass flow rate, enabling the design of an efficient synthesized noise for start-up acceleration. Notably, during experiments, the mass flow rate in natural circulation is often too small to measure accurately, making the heated temperature difference between the hot leg and cold leg a more reliable indicator of flow characteristics. Ultimately, the proposed derivations for two distinct heat sources can prove valuable in unifying various experimental and simulation scenarios.

B.2. Generalization of Dimensionless Flow Equations

It is important to note that utilizing the aforementioned dimensional flow equations can make comparing the performance of various natural circulation loops challenging. For instance, a loop with a smaller height may exhibit a larger flow rate if its resistance is minimal. Consequently, the development of a dimensionless equation for the steady-state flow rate in single-phase natural circulation loops is advantageous for advancing the scaling methodology.

Dimensionless momentum equation

From (0.8), we replace extra flow resistance either from bent or other physical phenomena K by effective length L_{eff} with $\frac{fL_t}{D}+K=\frac{f}{D}L_{eff}$.

$$\frac{L_t}{A}\frac{\mathrm{d}\dot{m}}{\mathrm{d}t}+\frac{f}{D}L_{eff}\frac{\dot{m}^2}{2\rho_0 A^2}-\rho_0\beta_T g\oint T dz=0 \tag{0.32}$$

with the empirical correlation for friction factor $f=p/Re_b$ and $Re=\dot{m}D/(\mu A)$ for different flow regimes. For the expression of L_{eff}, more details can be found in section B.4.3, where several correlations and properties of equivalent bend length are given.

$$l_{eff}=1+\frac{L_{cp}}{L_t}\left(\frac{f_{cp}}{f}-1\right)+l_{extra}$$

$$\frac{L_t}{A}\frac{\mathrm{d}\dot{m}}{\mathrm{d}t}+\frac{p\mu^b\dot{m}^{2-b}}{2\rho}\frac{L_{eff}}{D^{1+b}A^{2-b}}=\rho_0\beta_T g\oint T dz \tag{0.33}$$

For such uniform diameter loop, the following substitutions are applied to make the momentum equation (0.33) and the energy equation (0.11) dimensionless.

$$\dot{m}^+=\frac{\dot{m}}{\dot{m}_{ss}};\ t^+=\frac{t\dot{m}_{ss}}{\rho_0 V};\theta=\frac{T-T_c}{\Delta T_{h,ss}} \tag{0.34}$$

$$S=\frac{s}{H};\ Z=\frac{z}{H};\ l_i=\frac{L_i}{L_t};\ d_i=\frac{D_i}{D_r}\ a_i=\frac{A_i}{A_r} \tag{0.35}$$

$$with\, D_r=\sum_i^t D_iL_i/L_t;\ A_r=\sum_i^t A_iL_i/L_t$$

We start with first term from left hand side of (0.33) in general way with $L_t/A=\sum_i^t L_i/A_i=\sum_i^t l_iL_t/a_iA_r=\gamma L_t/A_r$,

$$\sum_i^t\frac{L_i}{A_i}\frac{\mathrm{d}\dot{m}}{\mathrm{d}t}=\sum_i^t\frac{l_iL_t}{a_iA_r}\frac{\mathrm{d}\dot{m}}{\mathrm{d}t}=\sum_i^t\frac{l_iL_t}{a_iA_r}\frac{\mathrm{d}\dot{m}^+\dot{m}_{ss}}{\mathrm{d}t^+\frac{\rho V}{\dot{m}_{ss}}}=\gamma\frac{\mathrm{d}\dot{m}^+}{\mathrm{d}t^+}\frac{\dot{m}_{ss}^2L_t}{V\rho_0A_r}=\gamma\frac{\mathrm{d}\dot{m}^+}{\mathrm{d}t^+}\frac{\dot{m}_{ss}^2}{\rho A_r^2} \tag{0.36}$$

To keep the transient term dimensionless, we divise (0.33) by $\frac{\dot{m}_{ss}^2}{\rho_0A_r^2}$,

$$\gamma\frac{\mathrm{d}\dot{m}^+}{\mathrm{d}t^+}+\frac{p\mu^b\dot{m}^{2-b}}{2\rho_0}\frac{L_{eff}}{D_r^{1+b}A_r^{2-b}}\frac{\rho_0A_r^2}{\dot{m}_{ss}^2}=\rho_0\beta_T g\oint T dz\frac{\rho_0A_r^2}{\dot{m}_{ss}^2} \tag{0.37}$$

Since mass flow rate as average quantity over the whole loop, we continue with second term of dimensionless equation (0.37) with the reference geometry size such as D_r

and A_r

$$\frac{p\mu^b \dot{m}^{2-b}}{2\rho}\frac{L_{eff}}{D_r^{1+b}A_r^{2-b}}\frac{\rho_0 A_r^2}{\dot{m}_{ss}^2} = \frac{p\frac{\mu^b}{\mu^b}\frac{L_T}{D_r}\frac{A_r^2}{D_r^b A_r^{2-b}}\frac{l_{eff}}{d_i^{1+b}a_i^{2-b}}{\dot{m}^{+}}^{2-b}}{2\frac{\dot{m}_{ss}^{b-2}}{\mu^b}\dot{m}_{ss}^2} = \frac{p\frac{L_T}{D_r}\frac{l_{eff}}{d_i^{1+b}a_i^{2-b}}{\dot{m}^{+}}^{2-b}}{2\frac{D_r^b\dot{m}_{ss}^b}{\mu^b A_r^b}} \tag{0.38}$$

$$\Rightarrow \frac{pN_G {\dot{m}^{+}}^{2-b}}{2Re_{ss}^b},\ with \begin{cases} N_G = \frac{L_T}{D_r}\frac{l_{eff}}{d_i^{1+b}a_i^{2-b}} \\ Re_{ss} = \frac{D_r\dot{m}_{ss}}{\mu A_r} \end{cases} \tag{0.39}$$

At last, we continue on right hand side of equation (0.37) with $\oint T dz = \oint \theta \Delta T_{h,ss}\mathrm{d}z = H\Delta T_{h,ss}\oint \theta \mathrm{d}Z$.

$$\rho_0\beta_T g\frac{\oint T dz}{\oint \theta \mathrm{d}Z}\frac{\rho_0 A_r^2}{\dot{m}_{ss}^2} = \rho_0\beta_T g H\Delta T_{h,ss}\frac{\rho A_r^2}{\dot{m}_{ss}^2} = \frac{\rho_0^2\beta_T g H A_r^2}{\dot{m}_{ss}^2}\frac{Q_h}{C_p\dot{m}_{ss}} \tag{0.40}$$

$$\Rightarrow \frac{\rho_0^2\beta_T g A_r^2}{\dot{m}_{ss}^3}\frac{Q_h H}{C_p} = \frac{\rho_0^2\beta_T g D_r^3/\mu^2}{\frac{\dot{m}_{ss}^3 D_r^3}{\mu^3 A_r^3}}\frac{Q_h H}{A_r C_p \mu} \tag{0.41}$$

The Grashof number is defined as the ratio of buoyancy force to viscous force $\rho_0^2\beta_T g L^3\Delta T/\mu^2$.

$$\rho_0\beta_T g\oint T dz\frac{\rho_0 A_r^2}{\dot{m}_{ss}^2} = \frac{Gr_m}{Re_{ss}^3}\oint \theta \mathrm{d}Z, \text{with} \begin{cases} Gr_m = \rho_0^2\beta_T g D^3\Delta T_r/\mu^2 \\ \Delta T_r = Q_h H/(A_r C_p\mu) \\ Re_{ss} = D_r\dot{m}_{ss}/(\mu A_r) \end{cases} \tag{0.42}$$

Note that ΔT_r is not always equal to ΔT_{hc} or $\Delta T_{h,ss}$. If ΔT_r corresponds to the former, then the classical Grashoff formula for pipes applies. We can examine the Grm formula to compare it with the classical formula.

$$Gr_m = \frac{\rho_0^2\beta_T g D^3}{\mu^2}\Delta T_r = \frac{\rho_0^2\beta_T g D^3}{\mu^2}\frac{Q_h H}{A_r C_p\mu} = \frac{\rho_0^2\beta_T g D^3}{\mu^2}\frac{H}{A_r C_p\mu}C_p\rho_0 u A_r\Delta T_{h,ss}$$

$$\Rightarrow Gr_m = \frac{\beta_T g D^3 H}{\nu^3}\cdot u\cdot\Delta T_{h,ss} = \frac{\beta_T g D^3}{\nu^2}(\frac{H\cdot u}{\nu})\cdot\Delta T_{h,ss} = \frac{\beta_T g D^3}{\nu^2}Re_H\cdot\Delta T_{h,ss} \tag{0.43}$$

To avoid confusion between the two temperature differences, we can use $\Delta T_r = Re_H\cdot\Delta T_{h,ss}$ with $Re_H = H\cdot u/\nu$. At last, we organise the two dimensionless terms (0.39) and (0.42) into (0.37).

$$\boxed{\gamma\frac{\mathrm{d}\dot{m}^+}{\mathrm{d}t^+} + \frac{pN_G {\dot{m}^{+}}^{2-b}}{2Re_{ss}^b} = \frac{Gr_m}{Re_{ss}^3}\oint \theta \mathrm{d}Z} \tag{0.44}$$

Dimensionless energy equation

Same procedure with momentum equation, we start with transient term of equation (0.9).

$$\frac{\mathrm{d}T}{\mathrm{d}t} = \frac{\mathrm{d}(T - T_c)}{\mathrm{d}t} = \frac{\mathrm{d}\theta}{\mathrm{d}t^+}\frac{\Delta T_{h,ss}\dot{m}_{ss}}{\rho_0 V} \tag{0.45}$$

For the cooler, we divise the second term of (0.9) by $\Delta T_{h,ss}\dot{m}_{ss}/(\rho_0 V)$.

$$\frac{\dot{m}}{\rho_0 A_c}\frac{\partial T}{\partial s}\frac{\rho_0 V}{\Delta T_{h,ss}\dot{m}_{ss}} = \frac{\dot{m}}{\rho_0 A_c}\frac{\rho_0 V}{\Delta T_{h,ss}\dot{m}_{ss}}\frac{\partial\theta\Delta T_{h,ss}}{\partial SH} = \frac{\dot{m}/\dot{m}_{ss}}{A_c H/V}\frac{\partial\theta}{\partial S} = \frac{\dot{m}^+}{a_c}\frac{\partial\theta}{\partial S} \tag{0.46}$$

Then, for the right hand side of cooler, we derive below the modified Stanton number St_m composed by modified Nusselt number Nu_m, Reynolds number Re and Prandtl number Pr with $V = L_t A_r$

$$\frac{4U_c(T - T_c)}{\rho_0 C_p D_c}\frac{\rho_0 V}{\Delta T_{h,ss}\dot{m}_{ss}} = \frac{4\frac{L_t}{D_c}\frac{U_c D_r}{\lambda}}{\frac{D_r\dot{m}_{ss}}{\mu A_r}\frac{C_p\mu}{\lambda}}\frac{T - T_c}{\Delta T_{h,ss}}, \text{ where}\begin{cases} Nu_m = 4\frac{L_t}{D_c}\frac{U_c D_r}{\lambda} \\ Re_{ss} = \frac{D_r\dot{m}_{ss}}{\mu A_r} \\ \theta = (T - T_c)/\Delta T_{h,ss} \\ Pr = \frac{C_p\mu}{\lambda} \end{cases} \tag{0.47}$$

$$\Rightarrow = -\frac{Nu_m}{Re_{ss}Pr}\theta = -St_m\theta \tag{0.48}$$

Therefore, for cooler part with the dimensionless terms of equation (0.45), (0.46) and (0.48) .

$$\boxed{\frac{\mathrm{d}\theta}{\mathrm{d}t^+} + \frac{\dot{m}^+}{a_c}\frac{\partial\theta}{\partial S} = -St_m\theta} \tag{0.49}$$

For heater part with fixed temperature T_h, same derivations are followed as cooler one. Therefore,

$$\frac{\mathrm{d}\theta}{\mathrm{d}t^+} + \frac{\dot{m}^+}{a_h}\frac{\partial\theta}{\partial S} = -St_m\left(\theta - \frac{T_h - T_c}{\Delta T_{h,ss}}\right) = St_m(\theta_{max} - \theta) \tag{0.50}$$

For heater part with fixed heat flux q_h,

$$\frac{4q_h}{\rho_0 C_p D}\frac{\rho_0 V}{\Delta T_{h,ss}\dot{m}_{ss}} = \frac{4q_h}{C_p D}\frac{V}{\frac{Q_h}{C_p\dot{m}_{ss}}\dot{m}_{ss}} = \frac{4q_h}{C_p D}\frac{V}{\frac{4q_h A_h L_h}{C_p D_h\dot{m}_{ss}}\dot{m}_{ss}} = \frac{V}{V_h} = \frac{V_t}{V_h} \tag{0.51}$$

Therefore,

$$\boxed{\frac{\mathrm{d}\theta}{\mathrm{d}t^+} + \frac{\dot{m}^+}{a_h}\frac{\partial\theta}{\partial S} = \frac{V_t}{V_h}} \tag{0.52}$$

Since from flow equation (0.30), we find out that two heating scenarios are similar by choosing adapting heat transfer coefficient U_h. Here, we compare right hand side of dimensionless equations (0.50) and (0.52).

$$St_m(\theta_{max}-\theta)=\frac{V_t}{V_h}\Rightarrow\theta=\theta_{max}-\frac{V_t}{V_h St_m} \tag{0.53}$$

We derive the dimensionless momentum equation, which combines the Grashof number, Reynolds number (Re), friction factor parameters p and b, and the geometry factor N_G. The effective length (l_{eff}) represents the total pipeline length, including the length contributed by bends and other factors. Furthermore, for dimensionless equations corresponding to different sections of the HHHC loop, the Stanton number, which quantifies the ratio of heat transferred into a fluid relative to the fluid's thermal capacity, has been determined and described the loop with normalized temperature. To streamline the analysis, we focus on the dimensionless equations at steady state where ${\dot{m}_{ss}}^{+}=1$.

$$\text{Momentum equation }\Rightarrow\boxed{\frac{pN_G}{2Re_{ss}^{b}}=\frac{Gr_m}{Re_{ss}^{3}}\oint\theta\mathrm{d}Z} \tag{0.54}$$

$$\text{Energy equation}\Rightarrow\boxed{\begin{cases}\frac{1}{a_h}\frac{\mathrm{d}\theta}{\mathrm{d}S}=St_m(\theta_{max}-\theta)=\frac{V_t}{V_h},\ S\in[0,s_h/L_t]\\ \frac{\mathrm{d}\theta}{\mathrm{d}S}=0,\ S\in(s_h/L_t,s_{hl}/L_t)\cup(s_c/L_t,1)\\ \frac{1}{a_c}\frac{\mathrm{d}\theta}{\mathrm{d}S}=-St_m\theta,\ S\in[s_{hl}/L_t,s_c/L_t]\end{cases}} \tag{0.55}$$

B.3. Derivation of Dimensionless Flow Correlations

From Equations (0.30) and (0.31), both mass flow rate and heated temperature can be estimated, given the geometry and input power, based on steady-state flow equations. To generalize the flow mechanism, the aforementioned dimensionless equations will be further investigated to obtain commonly applied flow correlations in experiments and simulations.

We notice that the integrated normalized temperature term in the momentum equation (0.54) can be deduced from the dimensionless energy equation (0.55). The same procedure will be employed to derive the normalized hot leg and cold leg temperatures at steady state.

Consequently, we begin with the heater portion of Equation (0.55).

$$\theta_{ss}(S)=\theta_{cl,ss}+\frac{V_t}{V_h}a_h S=\theta_{cl,ss}+\frac{L_t}{L_h}S \tag{0.56}$$

$$when\ S=S_h=\frac{L_h}{L_t},\ \theta_{ss}(S_h)=\theta_{hl,ss}=\theta_{cl,ss}+1 \tag{0.57}$$

Or, one can simply derive the relation from normalized temperature term of (0.34). Then, the cooler part with the outlet of cooler is the normalized temperature of coldleg

$S = S_c, \theta_{S_c} = \theta_{cl}$.

$$\frac{\mathrm{d}\theta}{\mathrm{d}S} = -St_m a_c \theta \Rightarrow \theta_{ss}(S) = \theta_{hl,ss} e^{St_m a_c (S_{hl}-S)} \tag{0.58}$$

$$\Rightarrow \theta_{ss}(S_c) = \theta_{cl,ss} = \theta_{hl,ss} e^{St_m a_c (S_{hl}-S_c)} = \theta_{cl,ss} = \theta_{hl,ss} e^{-St_m a_c \Delta S} \tag{0.59}$$

Therefore, we derive the normalized hotleg and coldleg temperature with input heating power and fixed cooling temperature at steady state.

$$\theta_{hl,ss} = \frac{1}{1 - e^{-St_m a_c \Delta S}}, \; \theta_{cl,ss} = \frac{1}{-1 + e^{St_m a_c \Delta S}} \tag{0.60}$$

Remark: If the heating temperature is utilized, the normalized temperature distribution over the heater will be as follows. Instead of exhibiting a linear temperature profile under uniform heat flux, it will display an exponential pattern, similar to the cooler temperature. Further derivations will not be elaborated upon in this context.

$$\theta_{ss}(S) = \theta_{max} + \left(\theta_{cl,ss} - \theta_{max}\right) e^{-St_m a_h \Delta S} \tag{0.61}$$

Using the above temperature distributions or directly normalized temperature term of (0.34), the integral in the momentum can be evaluated $\oint \theta \mathrm{d}Z = \theta Z \,|_0^1 = \theta_{hl,ss} - \theta_{cl,ss} = 1$.

$$\boxed{Re_{ss} = \left(\frac{2}{p}\frac{Gr_m}{N_G}\right)^{\frac{1}{3-b}} = C\left(\frac{Gr_m}{N_G}\right)^r, \text{with } C = \left(\frac{2}{p}\right)^r, r = \frac{1}{3-b}} \tag{0.62}$$

As it has been discuss in section B.4.3, the effective length for bend doesn't change over large Reynolds number in turbulent zones. However, it does changes rapidly with curvature factor k,so that it would be more enlightening to show Dean number in this correlation.

$$Re_{ss} = De_{ss}/\sqrt{k} \Rightarrow De_{ss} = C\left(\frac{Gr_m}{N_G}\right)^r \cdot \sqrt{k} = C_k\left(\frac{Gr_m}{N_G}\right)^r \tag{0.63}$$

$$\text{with } C_k = C \cdot \sqrt{k} = C \cdot \sqrt{D/2R_k}$$

Table 8. – Correlation coefficients for different flow regime

Geometry	Laminar	Transition	Turbulence f_1	Turbulence f_2
C	0.1768	1.2161	1.96	2.3446
$1/r$	2	2.584	2.75	2.8

For other source and sink orientations, further discussion can be found in Vijayan's work in **Vijayan et al. 2019.** Based on experimental studies, the correlation (0.61) for distinct flow regimes can be summarized in Table 8 with corresponding C and r values. Additionally, **Vijayan 2002** establishes correlations through experiments, along with other data presented in Figure 17, where an approximate range of Reynolds numbers can be observed for natural circulation. It is important to note that the dimensionless flow equation for a fully turbulent loop following different friction laws may yield varying correlation coefficients. For friction factor f_1, the Blasius friction law ($f = 0.316/Re^{0.25}$) is employed, and similarly, $f_2 = 0.184/Re^{0.2}$. Using these correlations, the results from simulations can be initially verified against the theory. If discrepancies exist, other geometric impacts should be considered, such as pressure drop from bends, which may influence flow behaviors.

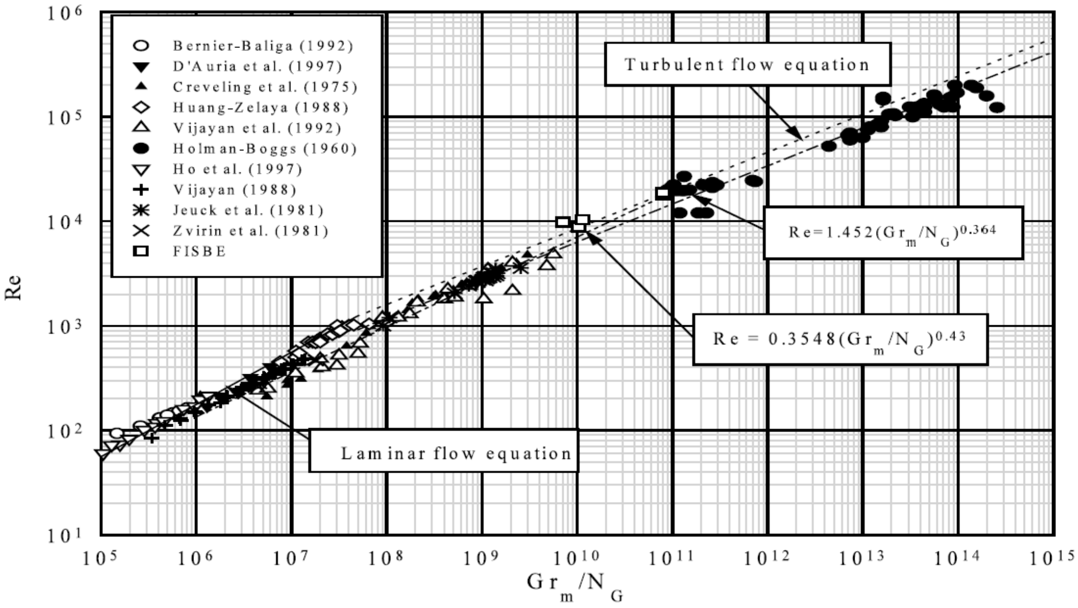

Figure 17. – Steady state natural circulation flow in uniform and non-uniform diameter closed loops by **Vijayan 2002**

B.3.1. Modified Grashof Number for NCL System

The dimensionless monmentum equation is derived in the Appendix B.2. While, the Grashof number is traditionally defined as the ratio of buoyancy to viscous force, following such structure $\rho_0^2\beta_T g L^3\Delta T/\mu^2$.

$$\rho_0\beta_T g\oint T dz\frac{\rho_0 A_r^2}{\dot{m}_{ss}^2} = \frac{Gr_m}{Re_{ss}^3}\oint \theta \mathrm{d}Z, \text{where} \begin{cases} Gr_m = \rho_0^2\beta_T g D^3\Delta T_r/\mu^2 \\ \Delta T_r = Q_h H/(A_r C_p \mu) \\ Re_{ss} = D_r\dot{m}_{ss}/(\mu A_r) \end{cases} \tag{0.64}$$

It should be noted that ΔT_r in modified Gr_m is not necessarily equivalent to **source/sink temperature difference $\boldsymbol{\Delta T_{hc}}$** or **hot/cold leg temperature difference at steady state $\boldsymbol{\Delta T_{h,ss}}$**. We can disassemble Gr_m formula as follows:

$$\begin{aligned} Gr_m &= \frac{\rho_0^2 \beta_T g D^3}{\mu^2} \Delta T_r = \frac{\rho_0^2 \beta_T g D^3}{\mu^2} \frac{Q_h H}{A_r C_p \mu} \\ &= \frac{\rho_0^2 \beta_T g D^3}{\mu^2} \frac{H}{A_r C_p \mu} C_p \rho_0 u A_r \Delta T_{h,ss} \end{aligned}$$

From the above derivation, one gets:

$$Gr_m = \frac{\beta_T g D^3 H}{\nu^3} \cdot u \cdot \Delta T_{h,ss} = \frac{\beta_T g D^3}{\nu^2} (\frac{H \cdot u}{\nu}) \cdot \Delta T_{h,ss} = \frac{\beta_T g D^3}{\nu^2} Re_H \cdot \Delta T_{h,ss} \tag{0.65}$$

To avoid confusion between the two temperature differences, we can use $\Delta T_r = Re_H \cdot \Delta T_{h,ss}$, where $Re_H = H \cdot u/\nu$. The Grashof number calculation, as shown in the Table 9, differs significantly when using classic straight pipe formula to a rectangular loop one. The Grashof number for the rectangular loop is six orders of magnitude larger, underscoring the necessity of deriving the flow equation specifically for dimensional analysis in different geometrical configurations.

Hence, in the case of a rectangular loop, it is vital to incorporate the Reynolds number, using the loop height as the characteristic length. Moreover, the temperature difference must be determined using the actual temperatures from the hot and cold legs of the system. This approach ensures an accurate representation of the physics involved in the heat and fluid flow processes.

Table 9. – Calculation values of Grashoff number under different scenario

Parameter	$\boldsymbol{\Delta T_{hc}}$	$\boldsymbol{\Delta T_{h,ss}}$	**Velocity**	$\boldsymbol{Gr(\Delta T_{hc})}$	$\boldsymbol{Gr_m(\Delta T_{h,ss})}$	**Reynolds**
$\boldsymbol{s_{1,1}}$	10	5.65	0.277	1.21E+05	1.52E+11	3.70E+04
	20	9.02	0.379	2.40E+05	3.32E+11	5.06E+04
	30	11.70	0.453	3.57E+05	5.15E+11	6.06E+04
$\boldsymbol{s_{1,2}}$	20	18.93	0.308	1.64E+04	3.53E+10	2.06E+04
	30	26.53	0.400	2.45E+04	6.43E+10	2.67E+04
	40	32.55	0.480	3.25E+04	9.48E+10	3.21E+04
$\boldsymbol{s_{1,3}}$	20	20	0.213	1.05E+03	1.62E+09	7.13E+03
	30	30	0.275	1.57E+03	3.13E+09	9.20E+03
	40	39.996	0.329	2.09E+03	4.99E+09	1.10E+04

B.3.2. Modified Rayleigh Number for NCL System

Since the study is dedicated to natural circulation, the Rayleigh number is essential for flow evaluation, especially, the critical Rayleigh number which can predict the start-up of flow. As we know, Rayleigh number Ra can be expressed by $Gr \cdot Pr$ by using the derived modified ones in equation 0.42.

$$Ra_m = Gr_m \cdot Pr = \frac{\rho_0^2 \beta_T g D^3 \Delta T_r}{\mu^2} \cdot \frac{C_p \mu}{\lambda} = \frac{\rho^2 \beta_T g D^3 H}{\mu^2 A \lambda} \cdot Q_h \tag{0.66}$$

$$\Rightarrow Ra_m = \frac{C_p \rho^3 \beta_T g D^3 H}{\mu^2 \lambda} \cdot u \cdot \Delta T_{h,ss},\ where\ Q_h = C_p \dot{m} \Delta T_{h,ss} = \rho C_p A u \Delta T_{h,ss} \tag{0.67}$$

Utilizing this formula allows for the straightforward calculation of the modified Rayleigh number (Ra_m) by incorporating the computed velocity and temperature differential between the hot leg and cold leg. Subsequently, by referencing Equation 0.30, it becomes evident that the steady-state mass flow rate exhibits proportionality to the one-third power of the heater power. As a result, it is necessary to rewrite the heater power (Q_h) accordingly.

$$\dot{m}_{ss} \propto Q_h^{1/3} = \left(C_p \dot{m}_{ss} \Delta T_{h,ss}\right)^{1/3} \leq \left(C_p \dot{m}_{ss} \Delta T_{hc}\right)^{1/3} \Rightarrow \dot{m}_{ss}^{2/3} \propto \Delta T_{h,ss}^{1/3}$$

$$\Rightarrow u^2 \propto \Delta T_{h,ss}\ or\ u^{\geq 2} \propto \Delta T_{hc} \tag{0.68}$$

Using the above correlation, we can easily recover the classic correlation between Ra and u for infinite plate with its definition.

$$\boxed{Ra = \frac{\rho \beta_T g L^3}{\mu \lambda} \cdot \Delta T_{hc} \Rightarrow Ra \propto u^{\geq 2}} \tag{0.69}$$

In the case of laminar flow, when the two temperature differences converge, we derive the proportional relationship $Ra \propto u^2$. For turbulent flow, the power coefficient is greater than 2, as indicated by empirical correlations in Table 8. Moreover, when examining the modified Rayleigh number for a high heat capacity (HHHC) natural circulation loop, comparable outcomes can be attained by referring to the definition of Q_h in Equation (0.30) and incorporating the temperature-dependent coefficient $a_T = U_h / U_{eq}$.

$$Ra_m = \frac{\rho^2 \beta_T g D^3 H}{\mu^2 A \lambda} \cdot Q_h = \frac{\rho^2 \beta_T g D^3 H}{\mu^2 A \lambda} \cdot \frac{4 q_h A L_H}{D}$$

$$\boxed{Ra_m = \frac{4 \rho^2 \beta_T g D^2 H}{\mu^2 A \lambda} \cdot a_T U_h \Delta T_{hc} L_H \propto \Delta T_{hc} \propto u^{\geq 2}} \tag{0.70}$$

Alternatively, we can simply utilize Equation (0.66). Based on the stability map proposed by **Vijayan 2002**, a linear stability analysis was conducted for three rectangular loops of identical length (6.48 m) but varying diameters of 6, 11, and 23.2 mm. The results are displayed in Figure 18(a). This analysis assumed a constant St_m. For uniform diameter loops (UDLs) with minimal local pressure losses, Figure 18(b) illustrates that when data is plotted as $(Gr_m)^{b/(3-b)}\,(D/L_t)^{3/(3-b)}$ versus St_m, a single plot can be created for all three loops.

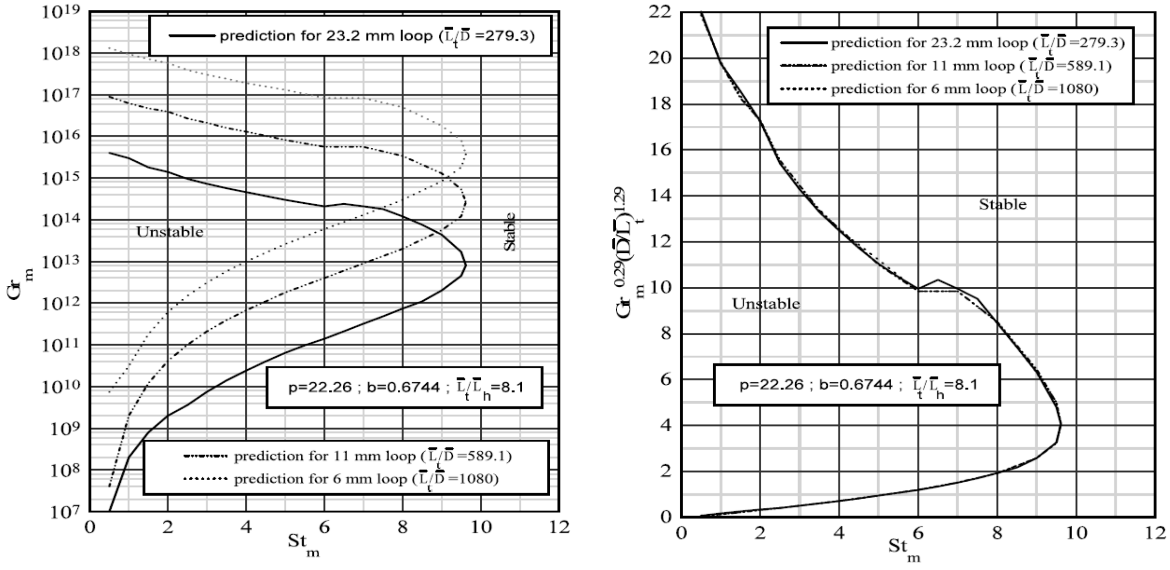

(a) $St_m \propto Gr_m$

(b) $St_m \propto (Gr_m, N_G)$

Figure 18. – Stability map for the three rectangular loops with (a) Gr_m and (b) generalised parameters (**Vijayan 2002**)

We reference the following paragraph from **Vijayan 2002** to summarize these correlations and their limitations: "Testing of the laminar flow correlation exhibited strong agreement with data from both uniform and non-uniform diameter loops. The turbulent flow correlation also displayed good alignment with data from non-uniform diameter loops. However, significant deviation was observed between turbulent UDL data and the turbulent flow correlation. This discrepancy can primarily be attributed to the neglect of local pressure losses when plotting the data. The impact of secondary flows and the undeveloped nature of the flow on the frictional resistance of the loop appear to be minimal. For $1000 < Re < 4000$, the loop is neither fully laminar nor fully turbulent, and it is recommended to employ empirical equations for flow in this region."

For the calculation of critical Rayleigh number under different scale, the correlation between Ra and velocity u has been used. By choosing a small threshold for velocity (where NCL activation time is exhaustively long), Ra_c can be calculated by extrapolation. Furthermore, by putting the uncertainty bands to replace the points, the uncertainty propagation can be done by M-C random extrapolation. As for the Ra_c and its uncertainty U_{Ra_c}, the scale effect can be shown in a demonstration of extrapolation in Figure 19. When y axis changing from velocity u to Reynolds number, the thresholds is changing with scale of diameters. Straightforward we obtain the critical Rayleigh number which increases with diameter. As for extrapolated uncertainty bands, we choose dynamic similarity where Reynolds number is kept similar (also similar numerical solution uncertainty to be propagated). Normally, if both scales share a same thresholds value, the extrapolated uncertainty bands should be similar in horizontal blue line. However, this thresholds change with diameter, therefore, the uncertainty bands for smaller diameters has larger range.

In conclusion, from this demonstration, the critical Rayleigh number increases with the diameter. Conversely, its uncertainty band reduces with increasing diameters.

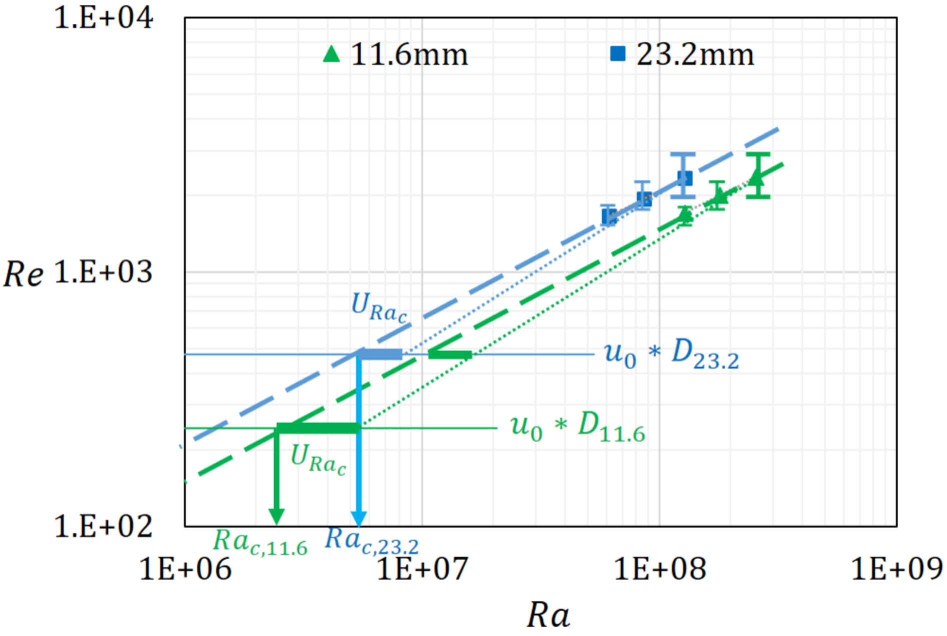

Figure 19. – Demonstration of Ra_c and U_{Ra_c} on physical correlation for dynamic similarity under scale.

B.4. Physical Confirmation for Separate Geometry Effects

B.4.1. Effect of Loop Elevation

A small increase in elevation leads to an increase in the buoyancy force, consequently augmenting the flow rate. For instance, consider geometry $s_{1,2}$ with an elevation of 2.1 m, compared to $s_{2,2}$ with an elevation of only 1.3 m. The former demonstrates a larger flow rate (around 180 to 130) under the same sink and source temperature difference, as shown in the respective Figure 5 and Figure 3.14.

Interestingly, there seems to be a compensatory region between the dominant buoyancy and friction zones where the natural circulation flow remains relatively unaltered despite changes in elevation. According to **Vijayan et al. 2019**, shown in

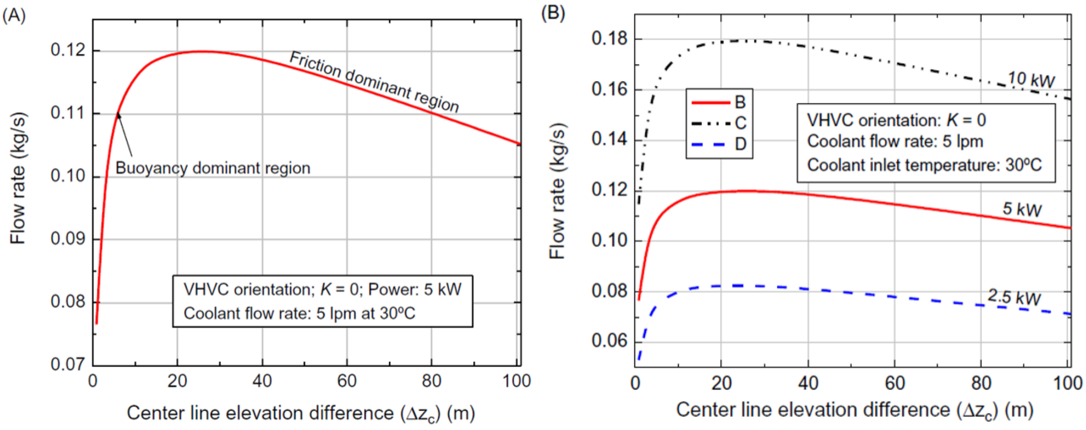

Figure 20. – Elevaltion effect on NCL loop from **Vijayan et al. 2019**.

Figure 20, this occurs between 20 m and 30 m. Additionally, this critical elevation appears to be related with the heater power, and may also vary with the loop diameter and local loss coefficient.

B.4.2. Effect of Loop Pipe Diameter

The pipe diameter plays a significant role in the functioning of a NCL. A larger diameter typically leads to an increased flow rate, predominantly owing to a reduction in local pressure loss — the energy loss primarily associated with friction, but also factors like pressure gradients and specific pipe characteristics.

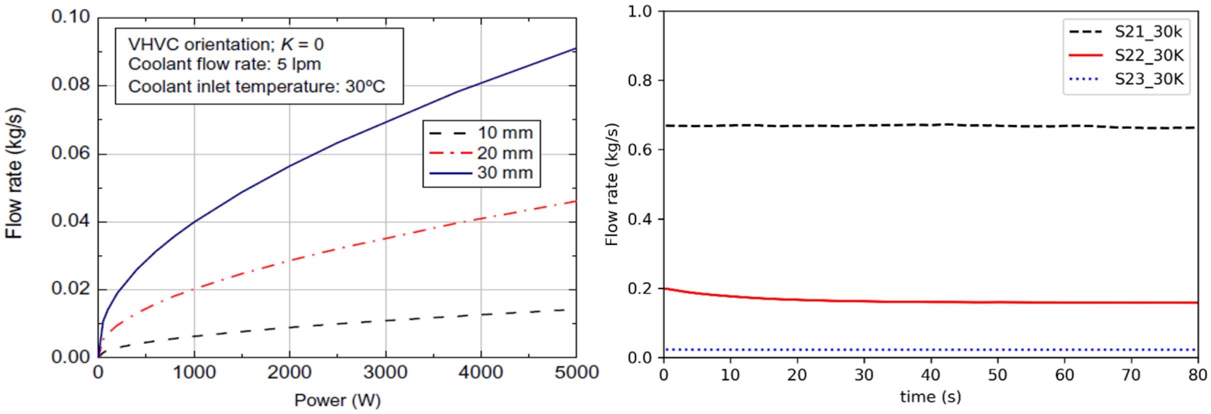

(a) Literature study

(b) CFD study

Figure 21. – Effect of loop pipe diameter in NCL system through (a) literature study (**Vijayan et al. 2019**) and (b) present CFD solutions for 3 diameters with given imposed temperature difference ΔT=30K.

This trend is evident in Figure 21, where the flow rate increases with an increase in pipe diameter. This observation is consistent with the relation derived in Equation

0.30:

— either for imposed power/heat flux

$$\dot{m} = \left(\frac{2\rho^2 \beta_T g H Q_h}{C_p R}\right)^{1/3} \Rightarrow \dot{m} = f(Q_h; 1/R)$$

where $Q_h = 4q_h A\Delta s/D$ and $1/R = A^2/(\frac{fL_t}{D} + K)$, both of which increase with diameter for a given fixed heat flux q_h. Therefore, for a given input power Q_h, a larger loop diameter effectively reduces the resistance R (plus K might reduce for smoother curvature), thus enhancing the flow rate.

— or more straightforward for imposed temperature difference

$$\dot{m} = \left(\frac{2\rho^2 \beta_T g H}{RC_p} a_T \Delta T_{hc} \frac{4U_h A\Delta s}{D}\right)^{1/3} \Rightarrow \dot{m} = f(D; U_{eq}; 1/R)$$

where U_{eq} is equivalent heat transfer coefficient defined in Equation 0.27. Therefore, for a given temperature difference, the mass flowrate is proportional directly with diameter and inverse resistance.

Hence, regardless of the heat source mechanism, increasing the diameter will typically result in an increase in flow rate. However, in certain cases, neglected factors such as resistance apart from friction and the heat transfer coefficient can have a significant impact.

B.4.3. Curvature Effect inside Natural Circulation Systems

Dimensionless effect length by friction factors

Scant attention is usually given to the exact effect of fittings in the design of piping systems. Their influence on the overall pressure drop can be significant for single phase flow. Elbow bends have proven to be difficult to both measure and represent the pressure loss. There was no reliable method of theoretically predicting pressure drop in elbow bends. Curved pipes are met in a variety of technical applications and give rise to strong secondary flows, enhanced pressure drop, as well as sometimes low-frequency oscillations. On the other hand, how the Dean vortices behave when an additional motion (swirl and pulsation) is superimposed on turbulence is an unexplored area with a limited number of studies being available (**Kalpak et al. 2016**).

Generally, the pressure drop through elbow bends is considerably larger than for the straight pipe equivalent and adds significantly to the losses sustained in piping systems. Designers usually apply the general rule that a 90 degrees elbow bend has a pressure drop equivalent of 30 to 50 pipe-diameters length of straight pipe (**Green and Perry 2008**). However, when the estimation of pressure drop can have a critical effect on operation or plant safety, such as on the downstream side of a relief value, a more exact method is desirable.

For elbow bends shown in Figure 22, the excess pressure drop due to both the separation at the inner wall and that in the tangent legs BC and DE was much greater than that observed for straight pipes with same diameter. Often the pressure drop can be presented in terms of velocity heads instead of more useful equivalent pipe length comparing to internal pipe diameter, i.e. $L_e/D = (L_{eff} - L_t)/D$. The pressure drop factor K_p can be expressed in

$$K_p = (\Delta P/\rho g)/(u^2/2g) \text{ with } L_e/D = K/(8f_{cp})$$

therefore, it's possible to quantify the specific curve pipeline friction factor from experiments or simulations. Moreover, for the theoretical analysis, a wide range of correlations are also proposed to determine such friction factor based on either Reynolds or Dean number along with curvature factor.

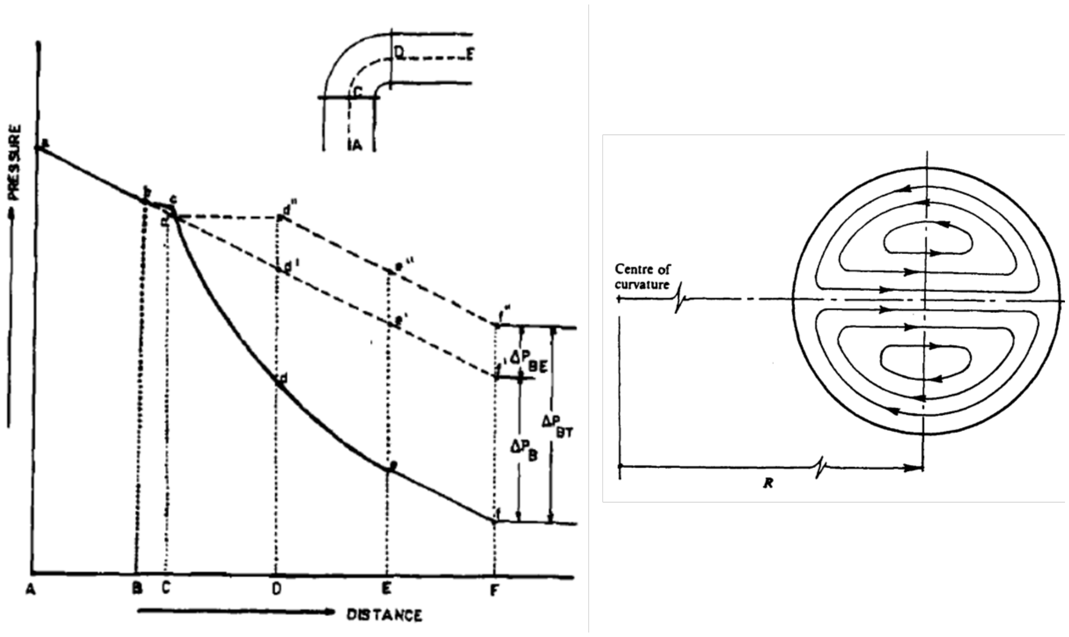

Figure 22. – Schematic diagram of ingle phase frictional pressure loss in a horizontal elbow bend with secondary flow patterns (**Spedding et al. 2004**)

As it has been referred in section B.2, the flow resistance is written with general form by effective length L_{eff} with $\frac{fL_t}{D} + K = \frac{f}{D}L_{eff}$. In order to reappear this friction factor, we break the pipeline into two parts: straight pipeline and curved pipeline to count on their effect. To be noticed, except for the consistent developed pressure drop within the curved length, there exist also inlet and outlet effects (**Rowe 1970**). Therefore, we keep extra effect as equivalent length L_{exta}.

$$\frac{fL_t}{D} + K = \frac{f_{sp}L_{sp}}{D} + \frac{f_{cp}L_{cp}}{D} + K = \frac{f_{sp}L_{eff}}{D}$$

$$\frac{fL_{eff}}{D}=\frac{fL_t}{D}l_{eff}=\frac{fL_t}{D}\left[1+\frac{L_{cp}}{L_t}\left(\frac{f_{cp}}{f}-1\right)+l_{extra}\right]$$

Therefore , we obtain the explicit expression of dimensionless effective lenth which includes all the geometry and physical effect from curve pipeline: the frictional effect, the local pressure loss due to curvature effect and the extra pressure loss due to the other effects (such as the turbulence effect). Moreover, the only unknow, except for classic friction factor for straight pipe and additional presure loss, is the f_{cp} for curved pipe which can be calculated precisely by our CFD simulation or given by correlations from other researchers.

$$\boxed{l_{eff}=1+\frac{L_{cp}}{L_t}\left(\frac{f_{cp}}{f}-1\right)+l_{extra}} \tag{0.71}$$

Equivalent length for elbow/curved pipe in literature

In order to understand easily the relations between two friction factors, an empirical example of Blasius correlations is given. For straight pipe, early approximations for smooth pipes by Blasius in terms of the Darcy–Weisbach friction factor (**Trinh 2010**): $f=0.3164Re^{-1/4}$. For curved or helically coiled tubes, **Bejan and Kraus 2003** proposed a correction taking into account directly the curve radius, R_k. $f=0.3164Re^{-1/4}+0.0075\sqrt{D/2R_k}$. As we know, by simplifying Navier-Stokes equations seeking solutions independent of longitudinal direction through the curvature of the bend for the flow driven by a pressure gradient in the same longitudinal direction, dimensionless Dean number, De, introduced as a modification to Reynolds number.

$$De=Re_b\sqrt{k}=Re_b\sqrt{D/2R_k}$$

A number of empirical relations of various forms will be shown in the Table 10 for laminar and turbulent flows. Therefore, the dimensionless effective length can be directly derived by proposed correlations for different flow regime, where either Re with k or more straight forward De need to be calculated.

Table 10. – Prediction of laminar/turbulent friction factor in curved pipes

Laminar flow	$f/f_{cp}=1-\left[1-(11.6/De)^{0.45}\right]^{1/0.45}$	(**Kapur et al. 1965**)
$13.5<De<2000$	$f/f_{cp}=21.5De/\left(1.56+logDe\right)^{5.73}$	**(Ito 1959)**
Turbulent flow	$f_{cp}/\sqrt{k}=0.003625+0.038(Re\cdot k^2)^{-0.25}$	**(Ito 1959)**
	$f_{cp}/f=\left(Re\cdot k^2\right)^{0.05}$	**(Ito 1959)**
	$f_{cp}/f=1+0.0823(1+k)k^{0.53}Re^{0.25}$	**(Schmidt 1967)**

In order to quantify and analyze this bend effect, we will start firstly from bibliography. The reliable data in Figure 23 shows some interesting fact:

1. At $R_k/D = 2.5$, it exists a minimum in the pressure drop to highlight the optimum design of an elbow bend;
2. **Ito 1960** showed that similar minimum values occurred for the 45 and 180 degree bends that were respectively below and above the 90-degree elbow bend;
3. When $R_k/D \to \infty$, the pressure drop returns to the straight pipe value;
4. With large values of R_k/D the dominant influence on excessive pressure loss was outer wall friction. As R_k/D was reduced, the length of the bend decreased, causing a steady reduction in the excess pressure drop;
    a) At $R_k/D > 10$ the elbow bend pressure drop can be predicted by equations for turbulent flow conditions in the Table 10 ;
    b) Below $R_k/D \cong 5$, the latter separation becomes the predominant cause of pressure loss . . .
5. With small values of $R_k/D (< 0.7)$, the equivalent length increase rapidly. . . .

The laminar flow region was in agreement with the data of **Beck 1944**. At high Re values in the turbulent regime, R_k/D varied very little with Reynolds number. Therefore, to better consider the curvature factor, De number can predict better the effective length better than Re number.

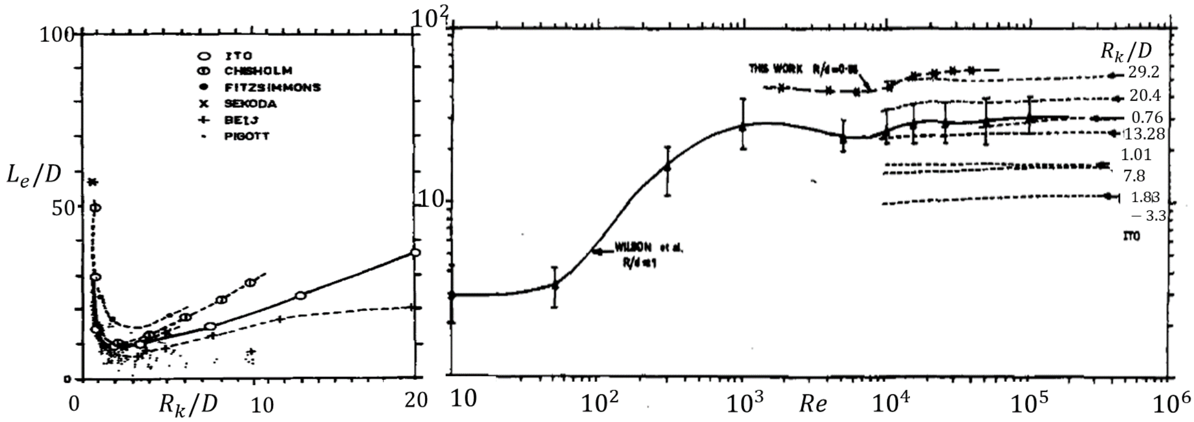

Figure 23. – Single phase equivalent length at Re = 15000 and general effect on Reynolds number for bend

In the thesis, the following empirical correlations (**Crawford et al. 2007**), also shown in Figure 24, have been applied to calculate the total equivalent length of pressure loss $(L_e/D)_{total} = (L_e/D)_{elbow} + (L_e/D)_{cp}$ due to curvature effect :

— For the curved pipe, an equivalent length can be written:

$$\boxed{(L_e/D)_{cp} = 2.4792 f_{cp} Re^{0.25}/k} \tag{0.72}$$

— For the pressure drop in an elbow bend, either these two can be used

$$(L_e/D)_{elbow} = 22.2126[Re \cdot k^2]^{0.7888} Re^{-0.71438} \tag{0.73}$$

$$\boxed{(L_e/D)_{elbow} = 1.25k^{1.5} Re^{0.35}} \tag{0.74}$$

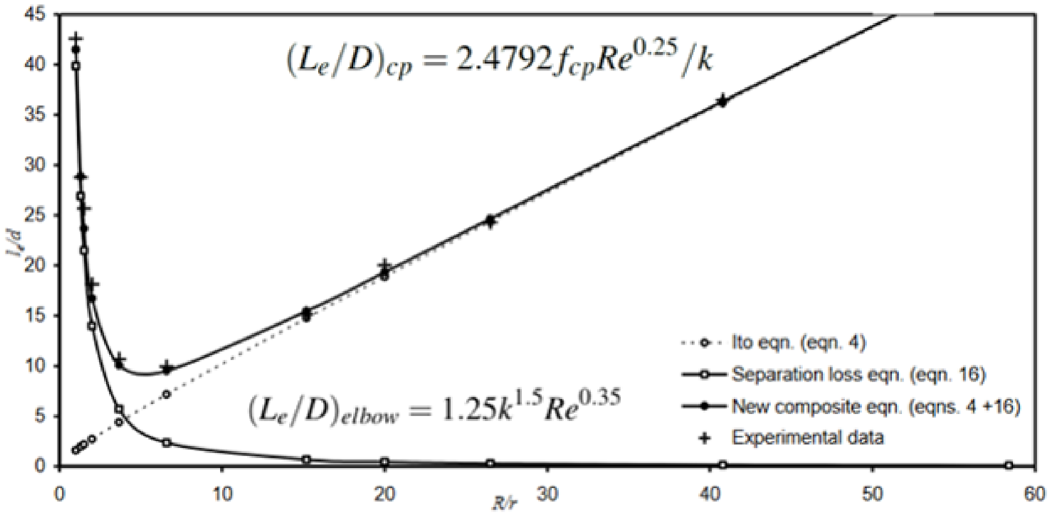

Figure 24. – Combination of elbow and curved pipe effect (**N. M. Crawford, Cunningham, and Spence 2007**).

Equivalent length for elbow/curved pipe in TrioCFD

Figure 25 displays the pressure loss in elbows for both laminar and turbulent flows. Under gravity's influence, the laminar flow exhibits a smooth slope, while the turbulent flow reveals significant pressure fluctuations. Moreover, figure 26 demonstrates that a single measurement point fails to capture the representative pressure drop resulting from acceleration at an elbow's exit. Consequently, the averaged pressure loss across the section is the most appropriate metric to assess the effect of the elbow. Accurate pressure change monitoring requires exhaustive sub-domains, as illustrated in Figure 27. Simply measuring at the entrances and exits of elbows can underestimate pressure loss over bends. Conversely, measuring only the straight pipes, inclusive of partial bend effects, might overstate the pressure loss.

Creating these exhaustive sub-domains, although essential for precision, can amplify computational and post-processing demands, particularly for scaling studies with geometrical variations. Notably, even without considering curvature effects, physical correlations can be reasonably accurate given the substantial impact of turbulent pressure loss over the loop. Hence, enhancements from literature or CFD measurements don't drastically alter the correlation relative to the laminar flow scenario.

However, as Figure 28 suggests, considering turbulent pressure loss can refine the correlation's accuracy, especially for regular flows. Literature tends to enhance accuracy, while direct CFD measurements might undervalue the friction factor between bends and straight pipes, thus compromising predictions unless measurements are comprehensive downstream of the bends.

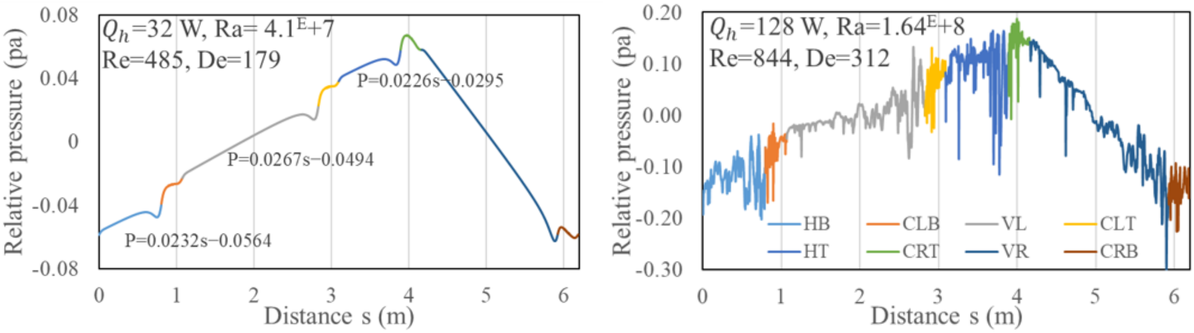

(a) Theoretical pressure loss

(b) Averaged pressure loss in TrioCFD

Figure 25. – Relative pressure over the centerline of NCL for (a)laminar flow and (b) turbulent flow in TrioCFD.

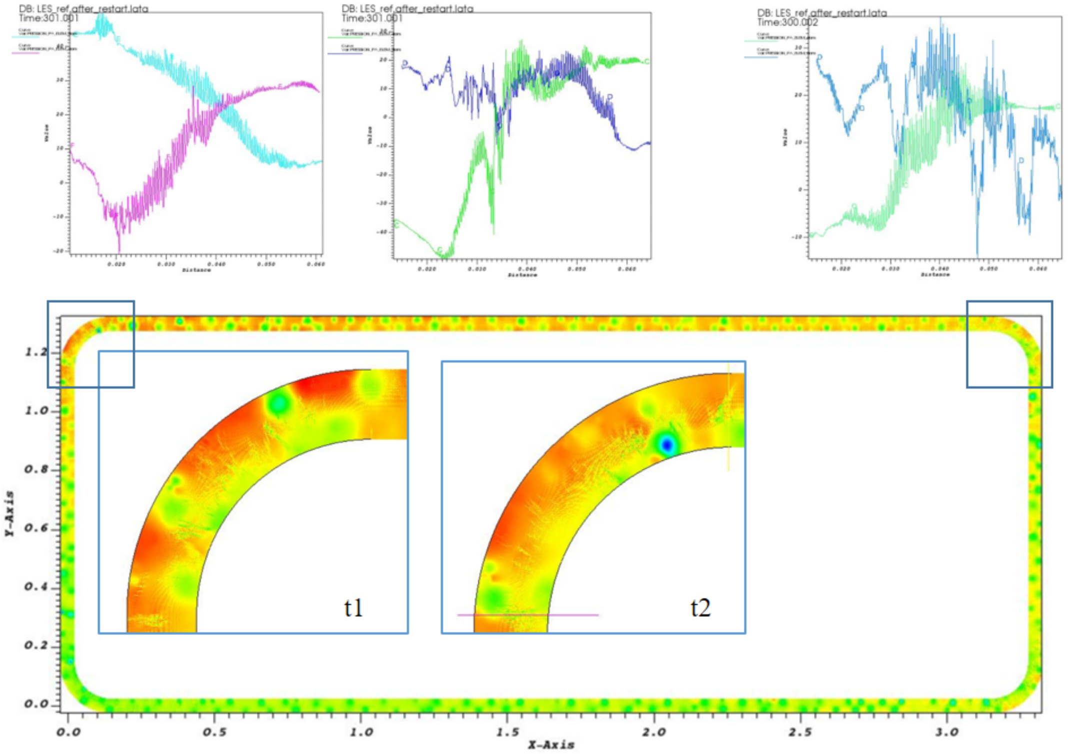

Figure 26. – Pressure field with some cross sections for a geometry $s_{2,1}$ of turbulent flow in TrioCFD.

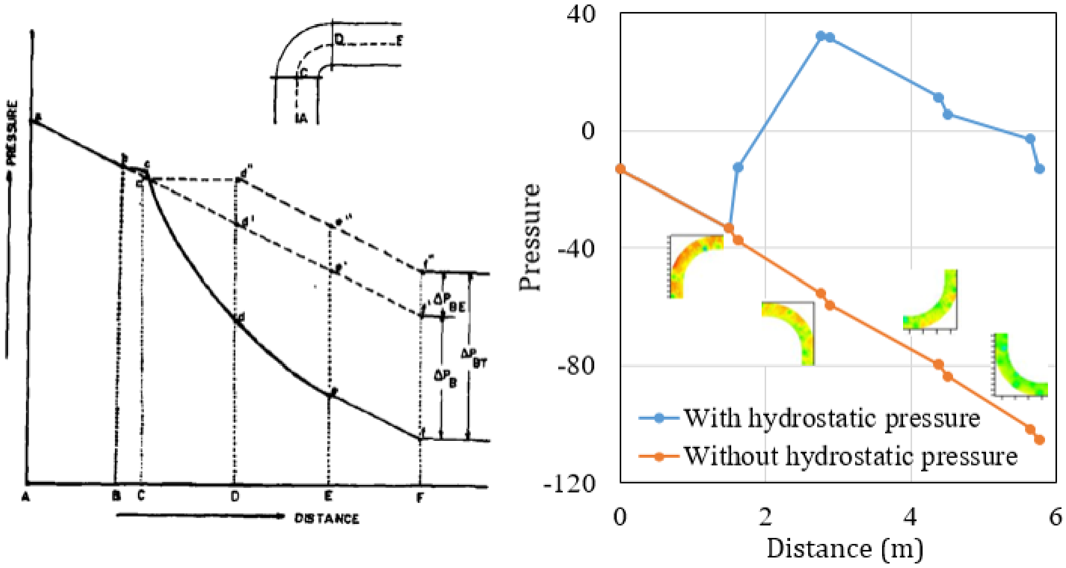

Figure 27. – Pressure loss over centerline of NCL for (left)theoretical study and (right) TrioCFD with or without gravity.

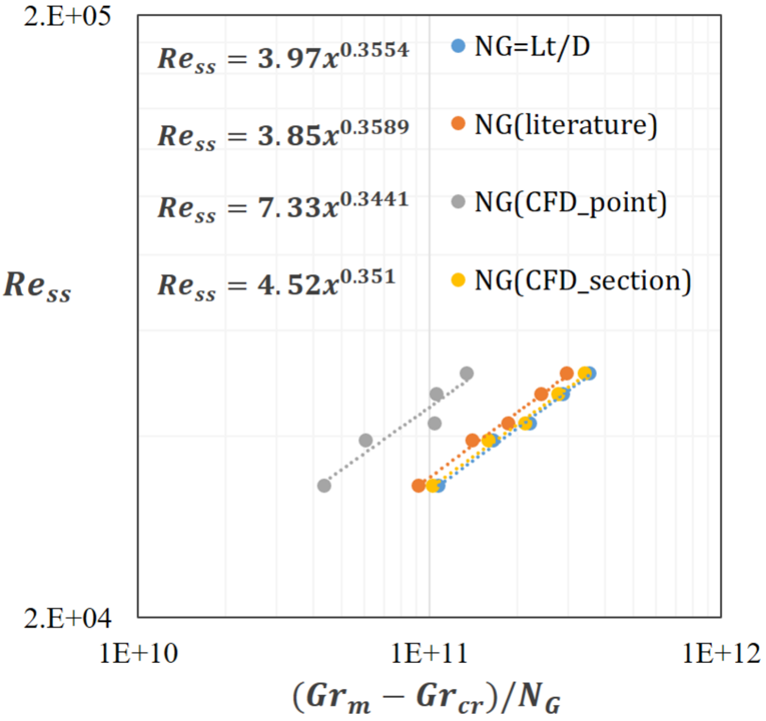

Figure 28. – Physical correlation for different approach to improve the dimensionless geometry factor.

C. Dynamical System Scaling (DSS) for Scaled Loop Design

As has been reported in first year of PhD report (**Huang** 2022), the scaling methodology Dynamical System Scaling (DSS) has been chosen as target one to launch the system scaled design for our HHHC loop.

We recall that in DSS, the normalized integral amount of conserved quantity β is firstly defined, along with the normalized sum of agent-of-change (AOC) $\omega = \mathrm{d}\beta/\mathrm{d}t$. Therefore, we obtain a process time $\tau = \beta/\omega$ other than classic clock time. Moreover, an action of process time τ_s is also created to describe $\mathrm{d}\beta/\mathrm{d}t^+ = \sum_{i=1}^{n} \Omega_i^+ = \Omega$ or $\mathrm{d}\beta/\mathrm{d}\tilde{t} = \tau_s \omega = \tilde{\Omega}$ (to distinguish with classic non-dimension analysis). Here, using mass flow rate $\dot{m}$ as an example, the superscript $\dot{m}^+$ is used for the H2TS quantity; $\dot{m}^*$ for FSA; $\tilde{\dot{m}}$ for DSS to distinguish one from another in these methods.

In the phase space of $\beta - \omega$, two parameters $\lambda_A = \beta_M/\beta_P$ and $\lambda_B = \omega_M/\omega_P$ are used to carry out the coordinate transformation for similarity criteria. Dynamic system similarity requires the dynamic process similarity of multiple state variables, **Yurko, Frepoli, and Reyes** 2015 suggests that the time ratios of different state variables in the model need to be consistent, which is expressed as equation 0.75, where $R = M/P = Model/Prototype$.

$$\tau_R^{\beta_i} = t_R^{\beta_i} = \frac{\lambda_A^{\beta_i}}{\lambda_B^{\beta_i}} = Cste\,(i = 1,2,3\ldots \text{ for different AOC}) \tag{0.75}$$

The HHHC natural circulation loops are expected to reproduce the flow and temperature responses of the prototype. The DSS analysis is carried out under a basic application framework, shown in Figure 29, so that the scaled models can be designed based on prototype.

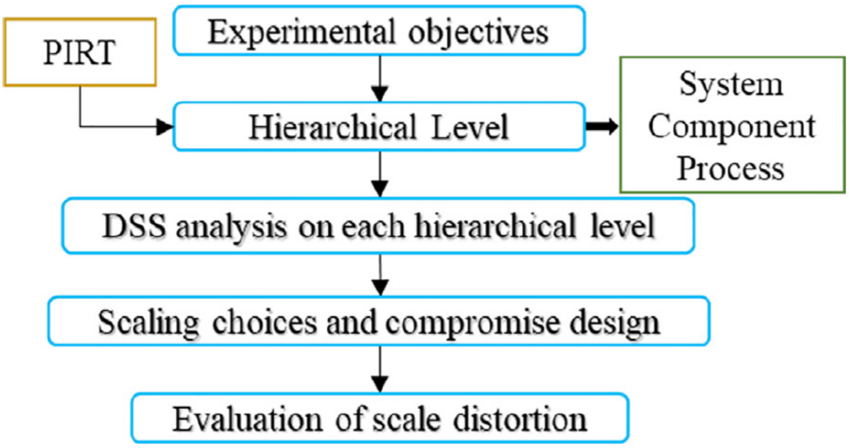

Figure 29. – The basic DSS application framework by **Liu et al.** 2022

C.1. Review of DSS Method

C.1.1. Dimensionless Coordinates

Consider a system with the same origin as H2TS and FSA, designed to incorporate the dynamic response of a thermal hydraulic process into the scaling framework. Let $\psi(\vec{x}, t)$ denote the local and instantaneous amount of a conserved quantity distributed within the system. Including all agents-of-change, ϕ_i, the integral balance equation for the system can be written as:

$$\frac{d}{dt}\int\int\int_V \psi(\vec{x}, t)dV = \frac{d\Psi}{dt} = \sum_{i=1}^{n}\phi_i. \tag{0.76}$$

Here, $\beta(t)$ is defined as the normalized integral amount of conserved quantity at a given instant:

$$\beta(t) = \frac{\Psi(t)}{\Psi_0},$$

where Ψ_0 is a time-independent maximum interval relative to a reference datum and $\phi_{i,0}$ is the reference value of AOC. Therefore, we have:

$$\frac{d\beta}{dt} = \frac{d\Psi^+}{dt}.$$

The normalized sum of the agent-of-change (AOC) is defined as:

$$\omega(t) = \frac{1}{\Psi_0}\sum_{i=1}^{n}\phi_i, \tag{0.77}$$

which gives us:

$$\frac{d\beta}{dt} = \frac{d\Psi^+}{dt} = \omega. \tag{0.78}$$

Zuber 2001 defined the process time τ as:

$$\tau = \frac{\beta}{\omega} \approx \frac{1}{FRC}, \tag{0.79}$$

which connects the concept of an externally measured reference time scale with the time scale arising from the change in the conserved quantity within a system. The process time interval represents the length of time required to produce a finite change in the conserved quantity as measured by the process clock:

$$\frac{d\tau}{dt} = \frac{1}{\omega}\frac{d\beta}{dt} - \frac{\beta}{\omega^2}\frac{d\omega}{dt} = 1 - \frac{\beta}{\omega^2}\frac{d\omega}{dt}.$$

The temporal displacement ratio D (acceleration of process) is defined as:

$$D = -\frac{\beta}{\omega^2}\frac{d\omega}{dt}. \tag{0.80}$$

Hence, we can express the differential of τ as:

$$d\tau = (1 + D)dt.$$

This equation signifies that all process time scales are relative. Every process thus creates a time scale that can be related to any reference time scale, and by extension, to any other process time scale via their process-specific temporal displacement rates.

The process action τ_S and effect parameter $\tilde{\Omega}$ are given by:

$$\tau_S = \tau_F - \tau_I = \int_{t_I}^{t_F} (1 + D)dt, \quad \tilde{\Omega} = \tau_S \omega. \tag{0.81}$$

Consider a two-parameter affine transformation, without translational components, of the β and ω coordinates:

$$\beta_M = \lambda_A \beta_P \tag{0.82}$$

$$\omega_M = \lambda_B \omega_P \tag{0.83}$$

In these equations, the transformation parameters λ_A and λ_B are constant scale factors. Importantly, the temporal displacement rate of a process, D, is invariant under affine transformation. This observation opens up new avenues for exploring the scaling distortions inherent in different dynamic systems.

C.1.2. Similarity Criteria

In these equations, the transformation parameters λ_A and λ_B are constant scale factors. Importantly, the temporal displacement rate of a process, D, is invariant under affine transformation. This observation opens up new avenues for exploring the scaling distortions inherent in different dynamic systems.

DSS represents a promising and innovative approach to capture dynamical scaling distortion, which originates from complex scientific metrics of geodesic. The strength of DSS lies in its flexibility in similarity criteria. The general two-affine method has been developed for different cases of scaling. Empirical reports suggest it is capable of encompassing previous approaches while providing a measure of the integral distortion throughout the entire transient. While the last two transformations often correspond to H2TS and the power volume method, the first three remain more theoretical and are challenging to apply to real-world facilities. The relationships between the referred parameters for different values of transformation parameter λ are shown in Table 11.

C.1.3. Scaling Distortion Measurement

Firstly, it is crucial to examine the existing scaling analyses on the target phenomena, where the vital parameters or assumptions could serve as useful references for finding appropriate decision points. Upon applying various scaling methods, the

Table 11. – Two affine similarity criteria of DSS scaling by **(Frepoli 2019)**

	$\beta-\omega$	coordinate	transformations	
2-2 affine $\beta_R=\lambda_A;\omega_R=\lambda_B$	Dilation $\beta_R=\omega_R=\lambda$	β-strain $\beta_R=\lambda;\omega_R=1$	ω-strain $\beta_R=1;\omega_R=\lambda$	Identity $\beta_R=1;\omega_R=1$
	Similarity	Criteria		
$\tilde{\Omega}_R=\lambda_A$ $\tau_R=t_R=\frac{\lambda_A}{\lambda_B}$	$\tilde{\Omega}_R=\lambda$ $\tau_R=t_R=1$	$\tilde{\Omega}_R=\lambda$ $\tau_R=t_R=\lambda$	$\tilde{\Omega}_R=1$ $\tau_R=t_R=\frac{1}{\lambda}$	$\tilde{\Omega}_R=1$ $\tau_R=t_R=1$

corresponding similarity criteria and scaling parameters will be derived. Traditional scaling analyses, which are based on initial and steady-state parameters, offer a static view as compared to dynamic analyses. Techniques such as FSA and DSS can evaluate the entire transient process of scaling distortion by considering changes in relevant parameters.

In DSS, as illustrated in Figure 30, the local separation distance is defined between the model and the prototype, both depicted in phase space. This distance connects the same process time moments of two transients:

$$\tilde{\eta}(\tilde{\tau}) = -\int_{\tilde{\tau}}^{\tilde{\tau}'} \sqrt{\epsilon D_P}\,\mathrm{d}\tilde{\tau}'$$

The total distortion over the entire reference time interval of a process is shown by

$$\tilde{\eta_T} = \int_0^1 \left|\tilde{\eta}(\tilde{\tau}^+)\right| \mathrm{d}\tilde{\tau}^+ = \int_0^1 \left| \int_{\tilde{\tau}^+}^{\tilde{\tau}'^+} \sqrt{\epsilon D_P}\,\mathrm{d}\tilde{\tau}'^+ \right| \mathrm{d}\tilde{\tau}^+$$

However, obtaining an analytical expression of a process remains impossible most of the time. The data from experiments or simulations will replace it. Therefore, the total separation with N pairs of points is given by

$$\tilde{\eta_T} = \sum_{k=1}^{N} \left|\tilde{\eta}_k\right| \tag{0.84}$$

where

$$\tilde{\eta}_k = \beta_{P_k}\sqrt{\epsilon D_{P_k}}\left[\frac{1}{\tilde{\Omega}_{P_k}} - \frac{1}{\tilde{\Omega}_{M_k}}\right]$$

With all the data, the standard error can also be determined over the whole transient:

$$\sigma_{est} = \sqrt{\frac{1}{N}\sum_{k=1}^{N}\tilde{\eta}_k^2} = \sqrt{\frac{1}{N}\sum_{k=1}^{N}\left|D_{P_k}\right|(\tilde{\tau}_{P_k}^{+} - \tilde{\tau}_{P_k}'^{+})^2} \tag{0.85}$$

As stated in **Reyes, Frepoli, and Yurko 2015**, for exact similitude, the two curves would overlay and the local separation would be zero. However, in our study, the curves M/P in Figure 30 only overlay for ω-strain and identity transformation. For the rest of the cases with $\tilde{\Omega}_R \neq 1$ in Table 11, the two curves can only be parallel. Therefore, two curves, which would be overlaid in a well-scaled case, are the simulated model curve and the ideal model curve derived from the prototype curve.

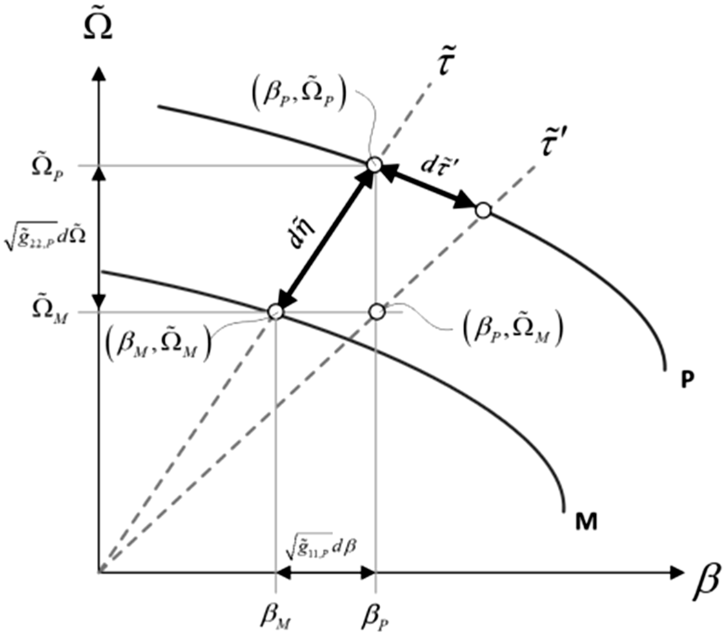

Figure 30. – Distortion quantification between model/prototype by phase space of DSS (**Reyes and Frepoli** 2019).

C.2. Comparison of H2TS, FSA and DSS Method

Several scaling methods have been developed and applied from the 1970s to the present, such as linear scaling and power to volume or power to mass scaling. It was in the 90's when the H2TS method appeared. Over the last decade, two new methodologies have been developed, the FSA and the DSS. The FSA is quite similar to the H2TS methodology. In fact, both were developed by Zuber and his coworkers (**Wulff et al.** 2005; **Catton et al.** 2009). The DSS takes a step forward and examines the scale distortions over a transient duration, but due to its short life, it has not been applied to a complex system. All these last three methods are based on the determination of a hierarchical ordering of the phenomena involved in the studied transient. A brief but informative description of the most important scaling methods has been summarized in first year report of **Huang** 2022.

Here, we can have a throughout review of three methodologies of interest: H2TS, FSA and DSS. These methodologies represent a second-generation group of assessment tools, which not only can design scaled model, but also can support the former methodologies. When some classic methodologies are applied to support the facility design to ensure its representativeness. The second generation seems to be more suitable to verify the similitude between an existing facility and the targeted prototype. An example of the latter point can be found in **Munoz-Cobo et al. 2018**, where an existing ITF undergoes the H2TS assessment. Between the H2TS, FSA, and DSS, it is important to underline two main differences:

1. First, DSS implements the rules of geometric similarity to establish process similarity. Technically, based on certain transformations, DSS method can be transformed into five different scaling methods, including the commonly used power-to-volume scaling and H2TS. Neither H2TS nor FSA, have this unique property.
2. Second, the FSA and H2TS scaling distortions are static. The distortion at different times of a transient can be approximated only by computing the dimensionless parameters through the data evaluated at various snapshots of the transient. Each snapshot would have a unique normalizing factor such as the reference value for state of variable, and thus, it is not straightforward to compare different snapshots or to integrate the distortion through time. On the other hand, DSS computes the scaling distortion as a function of dimensionless process time. This allows us to compare the trajectories of the prototype and the process curve of test facility for the entire transient as a time-dependent quantity.

We can link the internal and complex connection between them. Table 12 reports their AOC and FRC and the formalism of the final equation for further distortion analysis. Especially in the last row, each methodology shows the different philosophy for scaling analysis.

Relation of Distortion Measurements

For H2TS, the dominant terms are determined and the time characteristic is used again between the model and prototype:

$$1-\Pi_{i,R} = 1-\frac{\omega_{FRC,i,R}}{\omega_{FRC,max,R}} = 1-\frac{\frac{\omega_{FRC,i}}{\omega_{FRC,max}}_M}{\frac{\omega_{FRC,i}}{\omega_{FRC,max}}_P} \tag{0.86}$$

For FSA, the idea is similar to H2TS, but it is the effect metric for each process that will be analyzed:

$$1-\Omega_{FSA,e,R} = 1-\frac{\Omega_{FSA,e,M}}{\Omega_{FSA,e,P}} \tag{0.87}$$

For DSS, the λ value will be first chosen for different scaling similitudes. Then, the total distortion can be determined in phase space:

$$\eta_\chi(\tilde{t}) = \sqrt{1+\tilde{t}^2}(\Omega_P - \frac{\Omega_M}{\lambda_A}) \tag{0.88}$$

Table 12. – Comparison of parameters for H2TS, FSA and DSS scaling method

parameter	H2TS	FSA	DSS
Reference time	t	t	t
Conserved quantity	Ψ	Ψ	$\Phi = \beta\Psi_0$
AOC	φ_i	φ_i	φ_i
Sum of AOC	$\sum_{i=1}^{n}\varphi_i$	$\varphi_e = \sum_{i=1}^{n}\varphi_i$	$\Psi_0\omega = \sum_{i=1}^{n}\varphi_i$
Normalized AOC	$\varphi_i^+ = \frac{\varphi_i}{\varphi_{i,0}}$	$\varphi_i^* = \frac{\varphi_i}{\lvert\varphi_{e,0}\rvert}$	$-$
Normalized sum of AOC	$\frac{\varphi_{i,0}}{\Psi_0}\sum_{i=1}^{n}\varphi_i^+$	$\frac{\lvert\varphi_{e,0}\rvert}{\Psi_0}\sum_{i=1}^{n}\varphi_i^* = \frac{\lvert\varphi_{e,0}\rvert}{\Psi_0}\varphi_e^*$	ω
FRC of i-th AOC $\omega_{FRC,i,0}$	$\frac{\varphi_{i,0}}{\Psi_0}$	$\frac{\varphi_{i,0}}{\Psi_0}$	$-$
Effective FRC $\omega_{FRC,e,0}$	$\sum_{i=1}^{n}\frac{\varphi_{i,0}}{\Psi_0}$	$\frac{\varphi_{e,0}}{\Psi_0}\ or\ \frac{\lvert\varphi_{e,0}\rvert}{\Psi_0}$	$\sim\frac{1}{\tau}$
$\frac{\mathrm{d}\Psi^+}{\mathrm{d}t}$	$\sum_{i=1}^{n}\omega_{FRC,i,0}\varphi_i^+$	$\lvert\omega_{FRC,e,0}\rvert\varphi_e^+$	ω
Normalized time	$t^+ = \omega_{FRC,max}t$	$\Omega_{FSA,e} = \lvert\omega_{FRC,e,0}\rvert\ t$	$\widetilde{t} = \frac{t}{\tau_s}$
Formalism	$\frac{\mathrm{d}\Psi^+}{\mathrm{d}t} =$ $\varphi_{i,max}^+ + \sum_{i=1}^{n}\frac{\omega_{FRC,i,0}}{\omega_{FRC,max}}\varphi_i^+$	$\frac{\mathrm{d}\Psi^+}{\mathrm{d}\Omega_{FSA,e}} = \varphi_e^+$	$\frac{\mathrm{d}\beta}{\mathrm{d}\widetilde{t}} = \tau_s\omega = \widetilde{\Omega}$
Distortion factor DF	$1 - \Pi_{i,R} = 1 - \frac{(\omega_{FRC,i})_R}{(\omega_{FRC,max})_R}$ $= 1 - \frac{(\omega_{FRC,i}/\omega_{FRC,max})_M}{(\omega_{FRC,i}/\omega_{FRC,max})_P}$	$1 - (\Omega_{FSA,e})_R =$ $1 - \frac{(\Omega_{FSA,e})_M}{(\Omega_{FSA,e})_P}$	$\eta_\chi(\widetilde{t}) =$ $\sqrt{1+\widetilde{t}^2}\left(\widetilde{\Omega}_P - \frac{\widetilde{\Omega}_M}{\lambda_A}\right)$

C.2.1. Example of H2TS/DSS Analysis for a NCL

Key phenomena, such as single-phase natural circulation, heat transfer in heat source and sink, flow resistance in bends, and from local recirculation, have been identified from earlier studies. The DSS analysis will subsequently be conducted at the system, component, and process levels. To dimension the equation, quantities derived from a steady state will be utilized. The primary reason for this choice is to align the CFD simulation with the designated synthesized noise. Using noise composed of velocity and temperature from the steady state optimally reduces computational costs compared to cases utilizing initial conditions. Consequently, fewer transient phenomena will manifest in the DSS phase space. This approach, while convenient, presents challenges in situations of unstable states or when solutions are elusive.

It's essential to note that the subsequent study incorporates certain simplifications or assumptions: (1) While the flow throughout the loop is 2/3D, the analysis remains one-dimensional. (2) Fluid properties at each section are presumed uniform; however, in simulations, both μ and λ vary with temperature. (3) The fluid remains incompressible within a closed UDL. (4) Boussinesq approximation is employed, subject to constrained temperature changes.

Following the stated assumptions, the equations derived from **Reyes et al. 2015** are presented in the Table 13. Subsequently, the dimensionless momentum equations, along with their associated dimensionless parameters, are displayed. For H2TS, classic numbers such as the Richardson number, flow resistance number, and loop length number are represented as Π-groups. Conversely, for DSS, analogous terms are defined as individual normalized agents-of-change ω. This approach enables a connection between the two methods using common terms. Notably, the DSS effect parameter Ω can be expressed in terms of the H2TS dimensionless momentum equation.

The pivotal comparison hinges on the similarity criteria based on these derived dimensionless terms. In H2TS, priority is given to conserving key terms like the Richardson number, resulting in a Π-groups equated to unity. In contrast, DSS follows different similarity criteria wherein the ratio between two scales is set equal to λ for ω–strain. Upon examination of both methods, it is evident that the same Π-group for Richardson number manifests in varied expressions. Specifically, the DSS variant incorporates process time into its dimensionless term to account for time dynamics τ.

In conclusion, the main distinctions between H2TS and DSS methodologies can be outlined. Concerning normalized time, while H2TS exhibits abrupt transitions between two scales, DSS offers a more synchronized representation in phase space. In terms of similarity criteria, H2TS primarily focuses on the characteristic time ratio Π, whereas DSS offers greater flexibility by also considering normalized terms. When evaluating distortion, H2TS provides a qualitative assessment, whereas DSS enables a broader quantitative analysis and offers visual representation. This comparative analysis underscores the distinct advantages and nuances of each approach, highlighting the need to choose appropriately based on specific research requirements.

Table 13. – Scaling methods comparison for H2TS and DSS for a NCL.

Momentum equations for a NCL	$\sum\left(\frac{l_i}{a_i}\right)\cdot\frac{d\dot{m}}{dt}=B_T\rho_l g L_{th}\dot{q}_{core}-\frac{\dot{m}^2}{\rho_l a_c^2}\sum_{i=1}^{n}\left[\frac{1}{2}\left(\frac{fl}{d_h}+K_l\right)\left(\frac{a_c}{a_i}\right)^2\right]$ $\Pi_L\tau_{Loop}\frac{d\dot{m}^+}{dt}=\Pi_{Ri}\left(T_H-T_C\right)^+-\Pi_{Fl}\left(\dot{m}^+\right)^2\left(\sum_{i=1}^{n}\left[\frac{1}{2}\left(\frac{fl}{d_h}+K_l\right)\left(\frac{a_c}{a_i}\right)^2\right]\right)^+$	
Methods	**H2TS**	**DSS**
Dimensionless equations	$\frac{d\dot{m}^+}{dt^+}=\frac{\Pi_{Ri}}{\Pi_{Fl}}\left(T_H-T_C\right)^+-\left(\dot{m}^+\right)^2\left(\sum_{i=1}^{n}\left[\frac{1}{2}\left(\frac{fl}{d_h}+K_l\right)\left(\frac{a_c}{a_i}\right)^2\right]\right)^+$ $\frac{d\dot{m}^+}{dt^+}=\Pi_{NC}\varphi_{NC}^+-\varphi_{Fl}^+$	$\tau_S\frac{d\dot{m}^+}{dt}=\tau_S\left(\omega_{Ri}-\omega_{Fl}\right)$ $\frac{d\dot{m}^+}{d\left(t/\tau_S\right)}=\tilde{\Omega}_{Ri}-\tilde{\Omega}_{Fl}\rightarrow\frac{d\dot{m}^+}{d\tilde{t}}=\tilde{\Omega}$
Relationship	$\tilde{\Omega}=\frac{\Pi_L}{\Pi_{Fl}}\frac{\tau_{Loop}}{\tau_S}\frac{d\dot{m}^+}{dt^+}=\frac{\Pi_L}{\Pi_{Fl}}\frac{\tau_{Loop}}{\tau_S}\left(\Pi_{NC}\varphi_{NC}^+-\varphi_{Fl}^+\right)$	
Normalized parameters	$\Pi_{Ri}=\frac{B_T g\left(T_H-T_C\right)_0 L_{th}}{u_{c0}^2}$ $\Pi_L=\left(\frac{a_c}{l_{ref}}\right)\sum\left(\frac{l_i}{a_i}\right)$ $\Pi_{Fl}=\left(\sum_{i=1}^{n}\left[\frac{1}{2}\left(\frac{fl}{d_h}+K_l\right)\left(\frac{a_c}{a_i}\right)^2\right]\right)_0$	$\omega_{Ri}=\frac{\Pi_{Ri}}{\Pi_L\tau_{Loop}}\left(T_H-T_C\right)^+$ $\omega_{Fl}=\frac{\Pi_{Fl}}{\Pi_L\tau_{Loop}}\left(\dot{m}^+\right)^2\left(\sum_{i=1}^{n}\left[\frac{1}{2}\left(\frac{fl}{d_h}+K_l\right)\left(\frac{a_c}{a_i}\right)^2\right]\right)^+$
Similarity criteria	$\Pi_{Ri,R}=1;\ldots$	$\omega_{Ri,R}=\lambda$ for ω-strain $\Pi_{Ri,R}=\lambda\left[\frac{\Pi_L\tau_{Loop}}{\left(T_H-T_C\right)^+}\right]_R$

D. Data Storage & Codes Extracted

D.1. Dataset & Plot

D.1.1. NCL modelling by TrioCFD

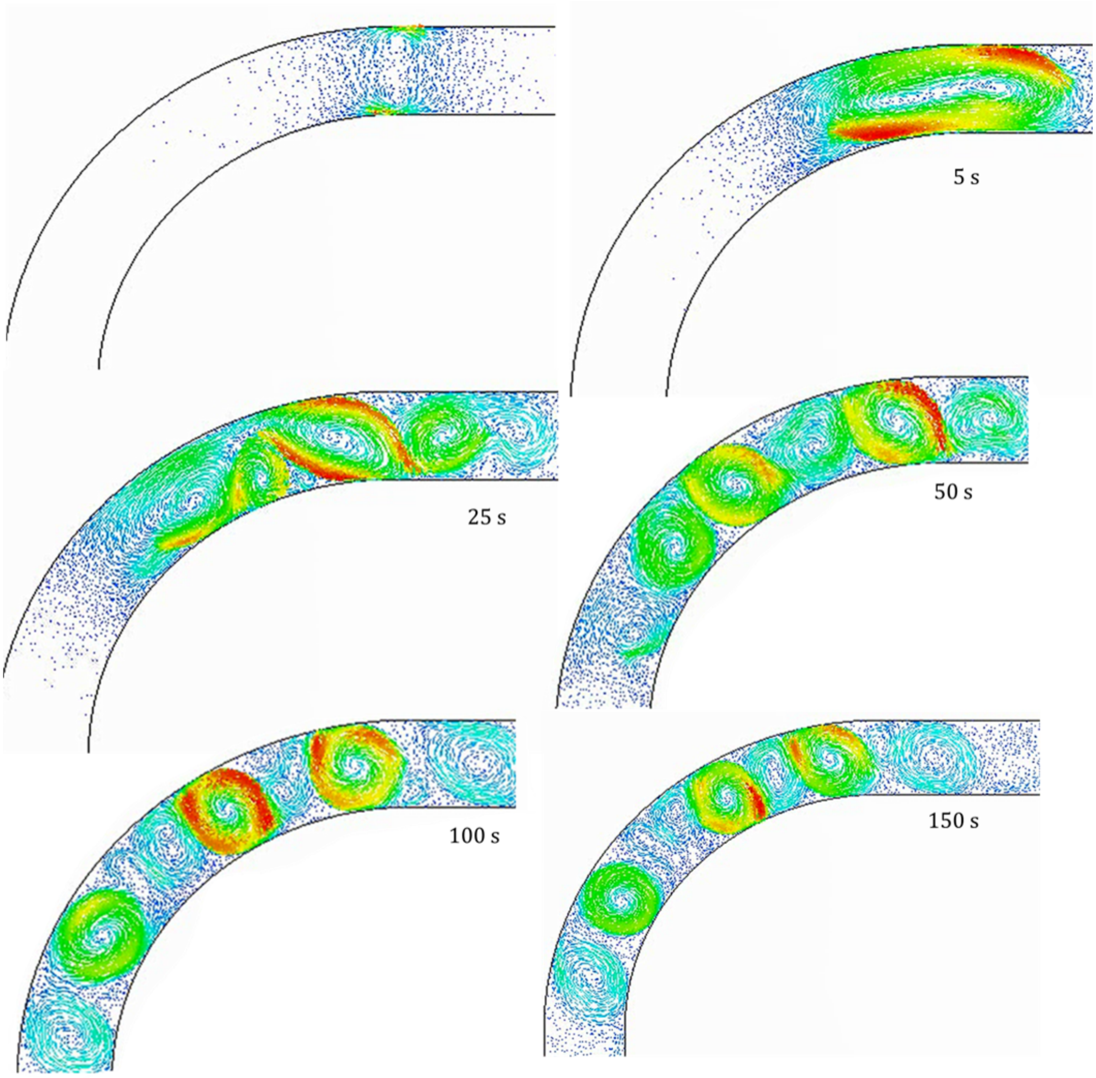

Figure 31. – Velocity profile in 2D at the elbow from stagnant state over time by TrioCFD.

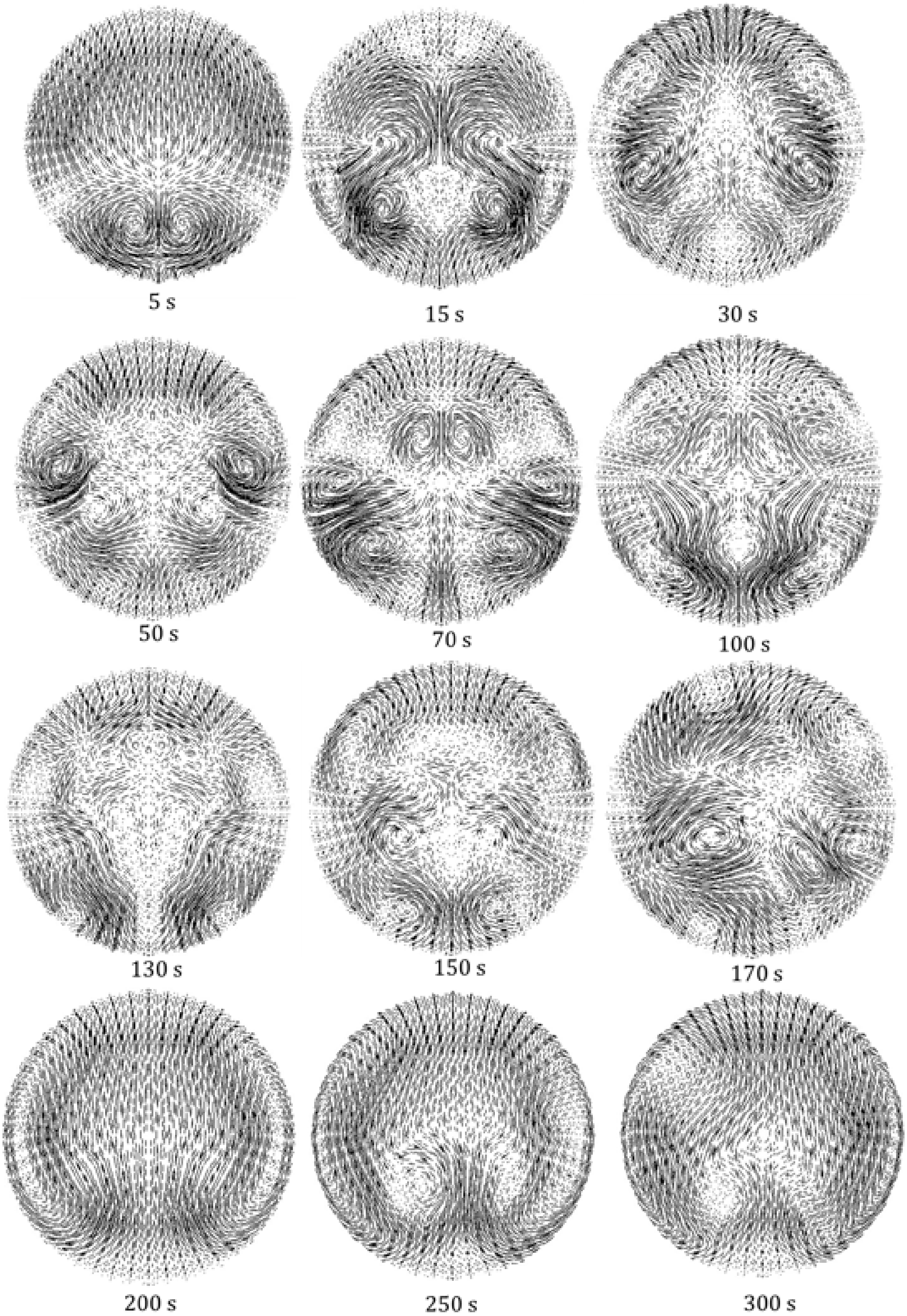

Figure 32. – Velocity profile in 3D at the downstream of elbow from stagnant state over time by TrioCFD.

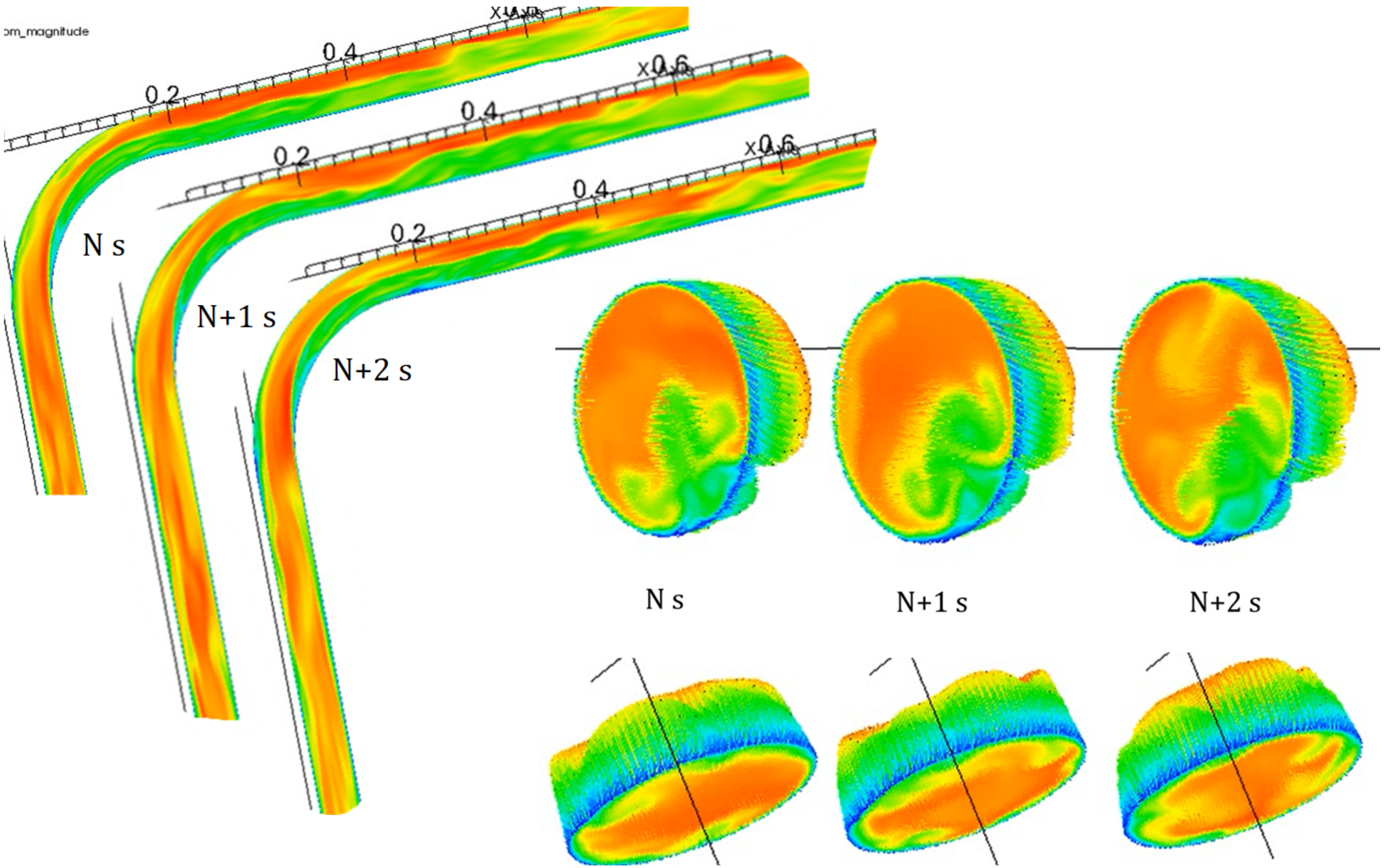

Figure 33. – Example of velocity profile in 3D at the elbow with developped turbulence over time by TrioCFD.

D.1.2. Numerical solution uncertainties using GCI method

Table 14. – Dataset: LES simulation solution convergence for global discretization under different coordinates.

Mesh	**dt**	**dt/dx**	**CFL**	**MassFlux**
M1	0.006	9.51	0.31	27.42
	0.008	12.67	0.69	46.00
	0.009	14.26	1.04	61.13
	0.01	15.84	1.30	68.98
	0.012	19.01	1.89	83.63
	0.013	20.60	2.22	90.71
	0.014	22.18	2.57	97.19
	0.015	23.76	2.87	101.60
	0.0183	29.08	4.00	115.46
M2	0.003	9.51	0.76	67.02
	0.004	12.67	1.46	96.92
	0.0045	14.26	1.94	114.04
	0.005	15.84	2.45	129.93
	0.006	19.01	3.11	137.29
	0.0065	20.60	3.43	139.94
	0.0075	23.76	4.11	145.15
M3	0.0015	9.51	1.50	132.76
	0.002	12.67	1.97	130.25
	0.00225	14.26	2.19	129.22
	0.0025	15.84	2.45	129.71
	0.003	19.01	3.02	133.59
	0.00375	23.76	4.04	142.70

Table 15. – Dataset: Effect of curvature ratio in NCL systems.

R_k/D	**3**	**4**	**5**	**6**	**7.2**	**10**
dt=1.5E-3	131.79	131.29	138.09	137.92	136.10	138.83
dt=2.25E-3	129.22	131.95	134.93	138.10	139.09	141.69
dt=3.5E-3	142.70	147.42	151.07	153.24	152.78	153.36

Table 16. – Dataset: NCL establishment from 30K to 40K with different curvature ratio for numerical solution uncertainty under scaling while CFL number keeping similar (data of Δ=30K are not fully recorded).

R_k/D	Mesh	MFlux_40k	dt_40k	Min_dx	Mean_dx	CFL_40k	Half Flux	Half Time(s)
3	M1	249.87	1.49E-02	6.31E-04	9.86E-04	7.04	232.05	8.89
	M2	330.43	5.51E-03	3.16E-04	4.93E-04	6.87	307.33	9.48
	M3	352.92	2.60E-03	1.58E-04	2.46E-04	6.92	335.30	12.32
4	M1	261.18	1.64E-02	6.68E-04	9.74E-04	7.61	242.66	8.88
	M2	346.46	5.90E-03	3.34E-04	4.87E-04	7.28	323.05	9.94
	M3	371.60	2.81E-03	1.67E-04	2.43E-04	7.44	336.39	12.51
5	M1	263.90	1.60E-02	6.91E-04	9.79E-04	7.29	245.28	9.80
	M2	354.04	6.35E-03	3.46E-04	4.89E-04	7.74	329.09	10.24
	M3	378.83	2.89E-03	1.73E-04	2.45E-04	7.53	343.73	12.54
6	M1	264.62	1.68E-02	7.08E-04	9.80E-04	7.48	245.77	10.46
	M2	355.98	6.33E-03	3.54E-04	4.90E-04	7.58	331.34	11.25
	M3	385.45	2.86E-03	1.77E-04	2.45E-04	7.41	348.19	13.79
7.2	M1	263.54	1.64E-02	7.05E-04	9.64E-04	7.30	245.15	10.21
	M2	356.42	6.26E-03	3.52E-04	4.82E-04	7.54	331.59	9.74
	M3	382.40	2.87E-03	1.76E-04	2.41E-04	7.41	344.60	18.94
10	M1	257.99	1.66E-02	7.10E-04	9.56E-04	7.17	239.43	10.91
	M2	354.02	6.41E-03	3.55E-04	4.78E-04	7.61	328.22	9.99
	M3	382.61	2.86E-03	1.78E-04	2.39E-04	7.34	343.09	44.81

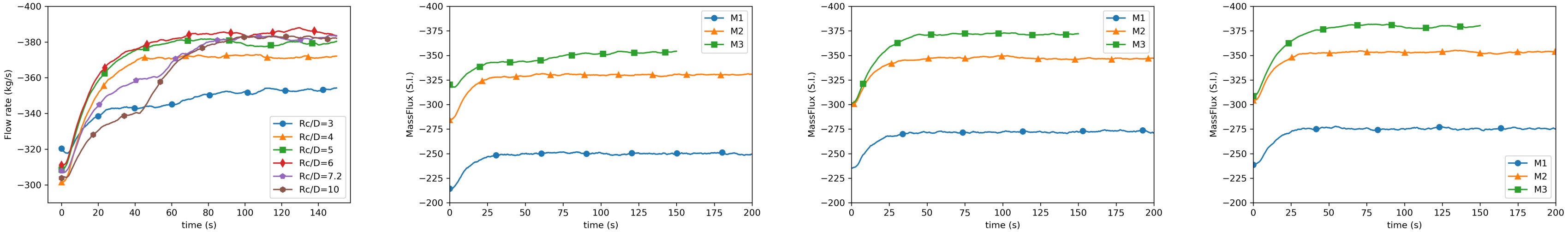

(a) M3 mesh (b) $R_k/D=3$ (c) $R_k/D=4$ (d) $R_k/D=5$

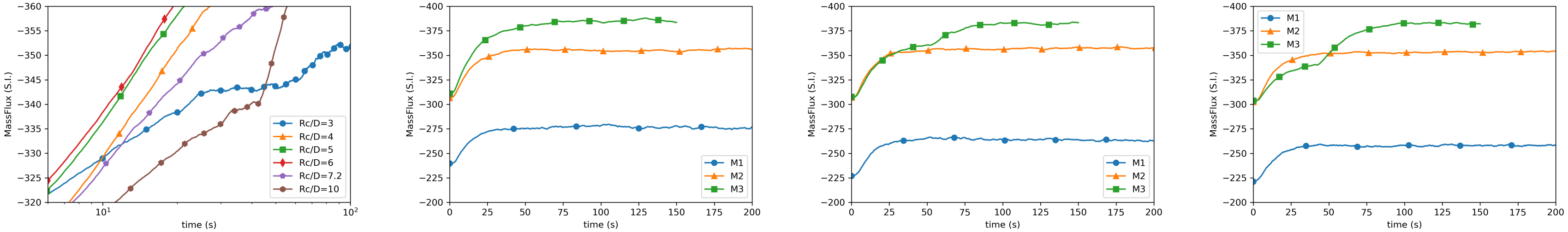

(e) M3 mesh zoom (f) $R_k/D=6$ (g) $R_k/D=7.2$ (h) $R_k/D=10$

Figure 34. – NCL establishment from Δ=30K to 40K for different curvature ratio (geometry $s_{3,i\in[1;6]}$) with mesh refinement.

Table 17. – Dataset: NCL establishment from 40K to 10K with different curvature ratio for numerical solution uncertainty under scaling while CFL number keeping similar using wall-resolved LES WALE model.

R_k/D	**Mesh**	**MFlux_40k**	**MFlux_10k**	**dt_40k**	**dt_10k**	**Min_dx**	**Mean_dx**	**CFL_40k**	**CFL_10k**	**Half Flux**	**Half Time(s)**
3	M1	259.20	115.46	1.74E-02	1.84E-02	6.31E-04	9.86E-04	8.53	4.00	187.33	11.08
	M2	341.79	142.28	6.56E-03	7.00E-03	3.16E-04	4.93E-04	8.46	3.76	242.03	12.93
	M3	375.70	144.26	3.04E-03	3.75E-03	1.58E-04	2.46E-04	8.61	4.04	259.98	14.13
4	M1	262.96	114.47	1.68E-02	1.78E-02	6.68E-04	9.74E-04	7.87	3.63	188.71	10.83
	M2	352.39	144.33	6.23E-03	7.14E-03	3.34E-04	4.87E-04	7.83	3.67	248.36	13.25
	M3	380.64	147.42	2.91E-03	3.51E-03	1.67E-04	2.43E-04	7.88	3.68	264.03	13.89
5	M1	266.48	113.71	1.62E-02	1.76E-02	6.91E-04	9.79E-04	7.43	3.45	190.09	11.20
	M2	353.60	145.16	6.18E-03	6.77E-03	3.46E-04	4.89E-04	7.52	3.38	249.38	13.47
	M3	386.05	151.07	2.88E-03	3.47E-03	1.73E-04	2.45E-04	7.66	3.61	268.56	14.17
6	M1	264.43	113.17	1.70E-02	1.87E-02	7.08E-04	9.80E-04	7.57	3.56	188.80	11.40
	M2	352.35	147.08	6.33E-03	7.01E-03	3.54E-04	4.90E-04	7.50	3.47	249.71	13.84
	M3	386.88	153.24	2.88E-03	3.48E-03	1.77E-04	2.45E-04	7.51	3.59	270.06	14.05
7.2	M1	267.65	113.36	1.66E-02	1.83E-02	7.05E-04	9.64E-04	7.50	3.51	190.51	11.48
	M2	356.56	145.72	6.14E-03	7.08E-03	3.52E-04	4.82E-04	7.40	3.49	251.14	14.17
	M3	383.60	152.78	2.87E-03	3.47E-03	1.76E-04	2.41E-04	7.43	3.58	268.19	14.41
10	M1	257.90	110.30	1.72E-02	1.90E-02	7.10E-04	9.56E-04	7.42	3.51	184.10	12.66
	M2	351.75	146.18	6.30E-03	7.19E-03	3.55E-04	4.78E-04	7.43	3.52	248.96	14.31
	M3	382.08	153.36	2.86E-03	3.48E-03	1.78E-04	2.39E-04	7.33	3.58	267.72	14.61

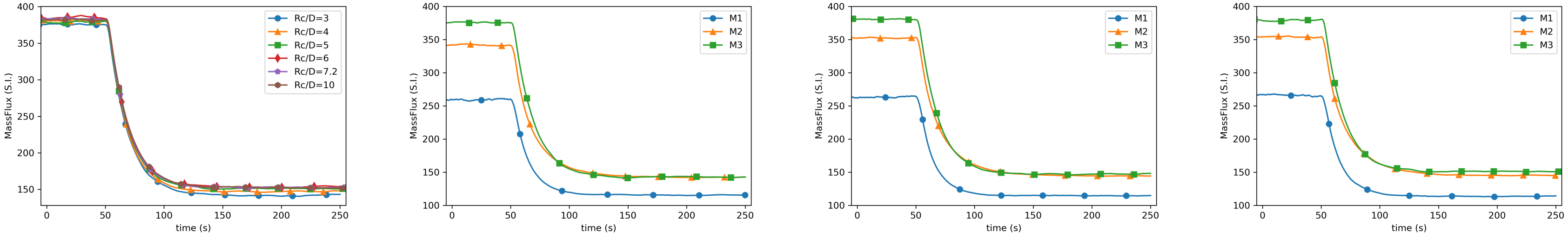

(a) M3 mesh (b) $R_k/D = 3$ (c) $R_k/D = 4$ (d) $R_k/D = 5$

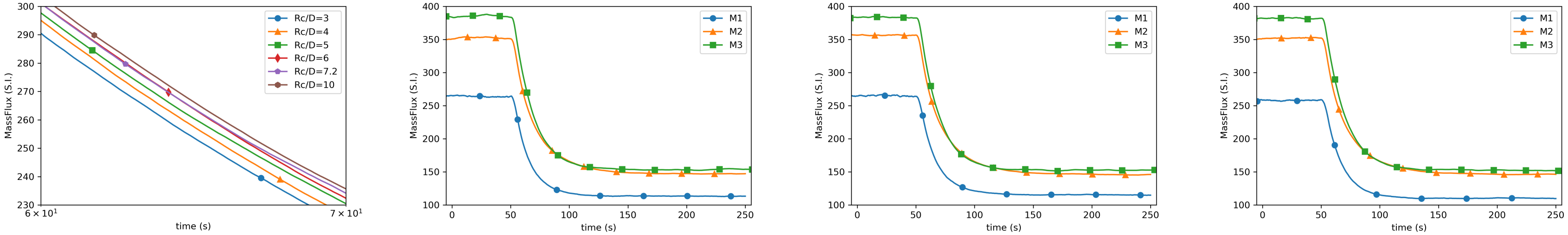

(e) M3 mesh zoom (f) $R_k/D = 6$ (g) $R_k/D = 7.2$ (h) $R_k/D = 10$

Figure 35. – NCL establishment from Δ=40K to 10K for different curvature ratio (geometry $s_{3,i\in[1;6]}$) with mesh refinement.

Table 18. – Dataset Summary: solution uncertainty of NCL establishment from 40K to 10K with different curvature ratio for numerical solution uncertainty under scaling while CFL number keeping similar.

ΔT	40k						10k					
R_k/D	3	4	5	6	7.2	10	3	4	5	6	7.2	10
Coarse	259.20	262.96	266.48	264.43	267.65	257.90	115.46	114.47	113.71	113.17	113.36	110.30
Medium	341.79	352.39	353.60	352.35	356.56	351.75	142.28	144.33	145.16	147.08	145.72	146.18
Fine	375.70	380.64	386.05	386.88	383.60	382.08	144.26	147.42	151.07	153.24	153.28	153.36
r	2	2	2	2	2	2	2	2	2	2	2	2
p_{GCI}	1.285	1.663	1.425	1.348	1.717	1.630	3.753	3.272	2.411	2.461	2.098	2.320
e_n	23.60	13.04	19.25	22.34	11.81	14.48	0.16	0.36	1.37	1.37	2.30	1.80
U_{GCI}	70.81	39.13	57.76	67.03	35.44	43.45	0.48	1.07	4.11	4.10	6.91	5.40
U_{num}	64.37	35.57	52.51	60.93	32.22	39.50	0.43	0.97	3.73	3.73	6.28	4.91
f_{ext}	399.30	393.68	405.31	409.22	395.41	396.57	144.42	147.78	152.44	154.60	155.58	155.16
CI_{low}	311.33	345.07	333.54	325.95	351.38	342.59	143.83	146.44	147.34	149.51	147.00	148.45
CI_{up}	440.07	416.21	438.56	447.81	415.82	421.58	144.70	148.39	154.81	156.97	159.56	158.27

Table 19. – Dataset Summary: solution uncertainty of NCL establishment halftime from 40K to 10K with different curvature ratio for numerical solution uncertainty under scaling while CFL number keeping similar.

$t_{1/2}$	$\Delta T = 40K \rightarrow 10K$					
R_k/D	3	4	5	6	7.2	10
Coarse	11.07882	10.826446	11.202643	11.403843	11.4757	12.66141
Medium	12.92582	13.248803	13.471039	13.838304	14.167479	14.310473
Fine	14.13117	13.888073	14.167221	14.050512	14.410201	14.614066
r	2	2	2	2	2	2
p_{GCI}	0.61573174	1.9219142	1.7041361	3.52005144	3.47118318	2.44143608
e_n	2.26426965	0.22919024	0.30827189	0.02026423	0.02405578	0.06850298
U_{GCI}	6.79280896	0.68757071	0.92481566	0.06079268	0.07216733	0.20550895
U_{num}	6.17528087	0.62506428	0.84074151	0.05526607	0.06560666	0.18682632
f_{ext}	16.3954397	14.1172632	14.4754929	14.0707762	14.4342568	14.682569
CI_{low}	7.95588913	13.2630087	13.3264795	13.9952459	14.3445943	14.4272397
CI_{up}	20.3064509	14.5131373	15.0079625	14.1057781	14.4758077	14.8008923

Table 20. – Dataset: NCL establishment from 10K to 40K with different curvature ratio for numerical solution uncertainty under scaling while dt/dx ratio keeping similar for each mesh.

R_k/D	**Mesh**	**MFlux_10k**	**MFlux_40k**	**dt_10k**	**dt_40k**	**Min_dx**	**Mean_dx**	**CFL_10k**	**CFL_40k**	**Half Flux**	**Half Time(s)**
3	M1	61.19	128.49	9.00E-03	6.00E-03	6.31E-04	9.86E-04	1.04	1.45	94.84	12.059
	M2	114.10	247.39	4.50E-03	3.00E-03	3.16E-04	4.93E-04	1.94	2.80	180.75	16.513
	M3	129.19	288.02	2.25E-03	1.50E-03	1.58E-04	2.46E-04	2.19	3.26	208.61	11.6245
4	M1	65.82	139.54	9.00E-03	6.00E-03	6.68E-04	9.74E-04	1.06	1.49	102.68	21.4349
	M2	123.33	265.82	4.40E-03	3.00E-03	3.34E-04	4.87E-04	1.93	2.84	194.57	23.248
	M3	131.95	300.09	2.25E-03	1.50E-03	1.67E-04	2.43E-04	2.12	3.21	216.02	12.2528
5	M1	62.04	132.59	9.00E-03	6.00E-03	6.91E-04	9.79E-04	0.96	1.37	97.32	22.412
	M2	121.05	264.01	4.60E-03	3.10E-03	3.46E-04	4.89E-04	1.92	2.82	192.53	24.8464
	M3	134.93	309.54	2.25E-03	1.50E-03	1.73E-04	2.45E-04	2.09	3.20	222.24	12.6491
6	M1	61.31	134.33	9.20E-03	6.20E-03	7.08E-04	9.80E-04	0.95	1.40	97.82	22.6733
	M2	118.14	261.33	4.85E-03	3.20E-03	3.54E-04	4.90E-04	1.93	2.81	189.74	25.904
	M3	138.10	318.86	2.25E-03	1.50E-03	1.77E-04	2.45E-04	2.09	3.22	228.48	12.979
7.2	M1	63.91	137.63	9.00E-03	6.00E-03	7.05E-04	9.64E-04	0.97	1.39	100.77	21.884
	M2	121.08	269.46	4.70E-03	3.10E-03	3.52E-04	4.82E-04	1.92	2.82	195.27	26.8635
	M3	139.09	324.16	2.25E-03	1.50E-03	1.76E-04	2.41E-04	2.11	3.29	231.63	13.6843
10	M1	61.49	136.40	9.20E-03	6.30E-03	7.10E-04	9.56E-04	0.95	1.44	98.95	23.3432
	M2	111.53	254.64	5.30E-03	3.30E-03	3.55E-04	4.78E-04	1.98	2.82	183.09	28.2553
	M3	141.69	329.35	2.20E-03	1.50E-03	1.78E-04	2.39E-04	2.09	3.31	235.52	14.0245

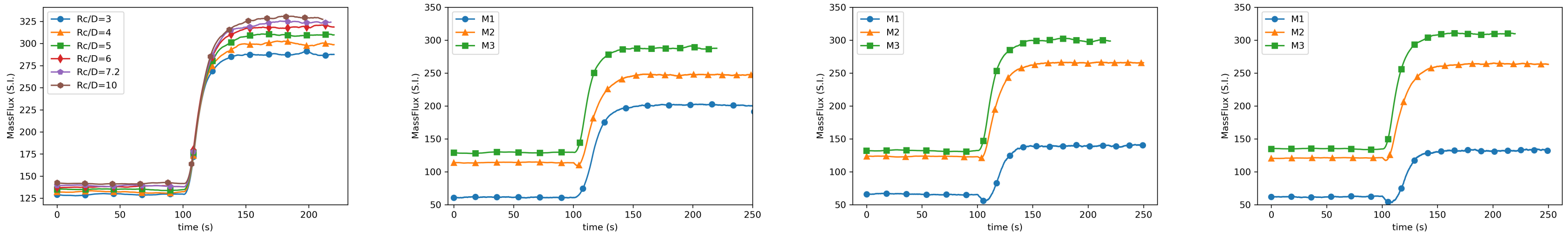

(a) M3 mesh (b) $R_k/D = 3$ (c) $R_k/D = 4$ (d) $R_k/D = 5$

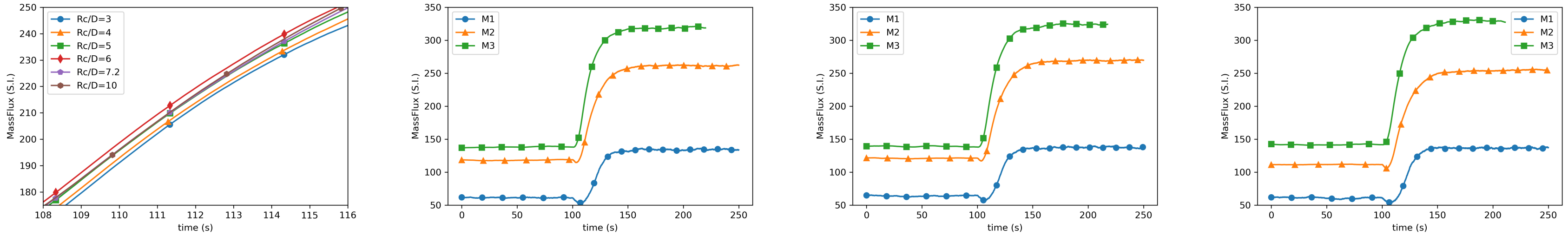

(e) M3 mesh zoom (f) $R_k/D = 6$ (g) $R_k/D = 7.2$ (h) $R_k/D = 10$

Figure 36. – NCL establishment from Δ=10K to 40K for different curvature ratio (geometry $s_{3,i\in[1;6]}$) with mesh refinement.

Table 21. – Dataset Summary: solution uncertainty of NCL establishment from 10K to 40K with different curvature ratio for numerical solution uncertainty under scaling while dt/dx ratio keeping similar for each mesh.

ΔT	**10k**						**40k**					
R_k/D	3	4	5	6	7.2	10	3	4	5	6	7.2	10
Coarse	61.19	65.82	62.04	61.31	63.91	61.49	128.49	139.54	132.59	134.33	137.63	136.40
Medium	114.10	123.33	121.05	118.14	121.08	111.53	247.39	265.82	264.01	261.33	269.46	254.64
Fine	129.19	131.95	134.93	138.10	139.09	141.69	288.02	300.09	309.54	318.86	324.16	329.35
r	2	2	2	2	2	2	2	2	2	2	2	2
p_{GCI}	1.809	2.738	2.088	1.510	1.667	0.730	1.549	1.881	1.529	1.142	1.269	0.662
e_n	6.03	1.52	4.27	10.80	8.28	45.78	21.09	12.77	24.15	47.65	38.80	128.22
U_{GCI}	18.08	4.56	12.81	32.41	24.84	137.35	63.27	38.31	72.44	142.94	116.41	384.67
U_{num}	16.43	4.15	11.64	29.46	22.58	124.87	57.52	34.82	65.85	129.94	105.82	349.70
f_{ext}	135.22	133.47	139.20	148.90	147.37	187.47	309.11	312.86	333.69	366.51	362.97	457.58
CI_{low}	112.76	127.80	123.29	108.64	116.51	16.82	230.50	265.27	243.69	188.92	218.34	-20.34
CI_{up}	145.63	136.09	146.57	167.56	161.67	266.56	345.54	334.91	375.40	448.80	429.99	679.05

D.1.3. Numerical model uncertainty using Uranie-PCE

Table 22. – Dataset: PCE of NCL establishment from 30K to 40K by URANS for input parameters Von Karman Vk and turbulent Prandtl number Prdt to FoM massflux with geometry $s_{1,2}$.

Case	Vk	Prdt	CFD TrioCFD	PCE (URANIE)	PCE (UQLab)
Training data					
1	0.3003	1.8794	469.20	469.67	469.72
2	0.3670	2.1911	378.89	380.65	381.28
3	0.3420	2.8983	412.01	412.22	412.46
4	0.3405	3.0731	414.00	413.12	414.23
5	0.4259	2.3398	334.54	335.86	335.12
6	0.4019	2.0269	356.14	354.64	355.44
7	0.3793	2.8063	374.82	374.12	374.15
8	0.4492	3.4285	310.67	310.82	310.47
9	0.3537	2.4121	397.83	395.66	395.15
10	0.3947	2.6774	361.68	361.79	361.27
11	0.3541	1.5760	396.82	396.75	395.72
12	0.3336	2.1243	414.36	415.32	415.76
13	0.4120	3.2961	347.84	347.27	348.35
14	0.4300	2.2365	331.19	331.43	331.47
15	0.4035	2.4547	354.64	354.94	354.03
16	0.4376	2.9228	320.56	320.40	320.37
17	0.4155	1.6632	345.68	345.93	345.82
18	0.3647	2.6968	386.02	387.07	386.62
19	0.3070	1.9339	457.28	456.42	456.69
20	0.3879	2.5382	367.60	366.83	366.18
21	0.4434	2.3083	315.49	314.88	315.52
22	0.3139	2.4985	451.31	451.29	450.71
23	0.3775	3.1462	373.53	374.68	375.76
24	0.3237	2.7757	436.74	437.62	437.92
25	0.3292	2.6084	429.07	428.53	427.71
Validation data					
1	0.4056	3.6096	352.73	360.23	354.37
2	0.3700	2.3640	383.96	379.87	379.67
3	0.3007	2.5029	472.45	475.42	476.09
4	0.4414	1.9220	317.28	315.92	320.00
5	0.3481	2.8710	404.63	404.98	405.03

Table 23. – Dataset: PCE of NCL establishment from 30K to 40K by LES for input parameters SGS coefficient Cw and turbulent Prandtl number Prdt with geometry $s_{1,2}$.

Case	**Cw**	**Prdt**	**CFD MassFlux**	**CFD T_{hl}**	**CFD T_{cl}**	**CFD $T_{h,ss}$**
Training data						
1	0.4315	2.9325	422.06	645.92	613.82	32.10
2	0.3292	2.8682	428.01	646.11	613.69	32.41
3	0.5015	1.4190	413.66	646.01	613.73	32.28
4	0.5981	2.8290	417.41	645.93	613.81	32.12
5	0.6143	3.4433	418.58	646.29	613.47	32.82
6	0.3331	2.2623	427.34	645.85	613.93	31.92
7	0.3667	2.0325	423.74	646.02	613.74	32.29
8	0.4638	2.5636	420.18	646.05	613.72	32.33
9	0.5796	3.1839	418.58	645.81	613.94	31.86
10	0.3931	2.2936	422.77	646.04	613.76	32.28
11	0.4862	3.0417	420.52	646.33	613.45	32.88
12	0.6703	3.2115	418.92	646.22	613.56	32.66
13	0.3059	2.7560	430.21	645.95	613.81	32.14
14	0.4112	2.5981	422.51	645.95	613.82	32.13
15	0.5469	2.3625	417.42	646.30	613.49	32.81
16	0.6445	1.7105	411.85	646.03	613.79	32.24
17	0.6583	1.9624	412.53	645.75	613.99	31.76
18	0.6227	2.1074	414.22	645.85	613.90	31.96
19	0.3558	2.4615	426.63	646.10	613.68	32.42
20	0.4264	2.1873	420.63	646.19	613.54	32.65
21	0.5237	2.6924	418.87	645.84	613.92	31.92
22	0.5356	2.4872	417.60	646.07	613.67	32.40
23	0.5679	2.6773	417.43	646.08	613.68	32.40
24	0.6921	2.4016	415.12	646.10	613.67	32.44
25	0.4458	1.8370	418.60	646.03	613.69	32.34
Validation data						
26	0.6562	2.9604	416.42	646.14	613.62	32.52
27	0.5037	2.5823	417.50	646.05	613.71	32.34
28	0.3977	2.6631	422.93	646.27	613.53	32.74
29	0.3727	2.3043	424.93	646.06	613.69	32.37
30	0.6010	1.9596	413.73	645.88	613.83	32.05
Extra data						
31	0.65	2.4	415.37	645.85	613.90	31.95
32	0.475	2.25	419.13	645.92	613.81	32.11
33	0.525	2	416.01	646.17	613.60	32.56
34	0.6	2.5	416.92	646.08	613.68	32.40
35	0.37	2.9	425.91	646.18	613.60	32.57
36	0.32	1.9	427.37	645.99	613.76	32.23

Table 24. – Dataset: PCE from 30K to 40K by LES for input parameters SGS coefficient Cw and turbulent Prandtl number Prdt - PSD & DTW based FoMs - Mean PD(T), Min Freq(eps) and Cost(vit) are mean/minimum/average value of power density/frequency/DTW cost for near wall temperature/dissipated energy/velocity at the exit of elbow with geometry $s_{1,2}$.

Case	Cw	Prdt	Mean PD (T)	Min Freq (eps)	Cost (vit)
1	0.4315	2.9325	45.73	294.12	46.54
2	0.3292	2.8682	68.89	289.02	47.33
3	0.5015	1.4190	77.84	335.57	46.76
4	0.5981	2.8290	54.40	310.56	48.44
5	0.6143	3.4433	51.80	306.75	47.50
6	0.3331	2.2623	67.46	290.70	46.56
7	0.3667	2.0325	68.40	292.40	47.22
8	0.4638	2.5636	45.72	297.62	47.39
9	0.5796	3.1839	71.16	306.75	46.83
10	0.3931	2.2936	67.05	292.40	46.20
11	0.4862	3.0417	42.83	297.62	47.31
12	0.6703	3.2115	49.62	324.68	46.71
13	0.3059	2.7560	46.15	289.02	47.29
14	0.4112	2.5981	75.56	294.12	47.00
15	0.5469	2.3625	67.03	314.47	47.56
16	0.6445	1.7105	65.89	352.11	47.07
17	0.6583	1.9624	67.17	342.47	47.17
18	0.6227	2.1074	71.35	331.13	47.33
19	0.3558	2.4615	86.41	290.70	47.15
20	0.4264	2.1873	67.10	304.88	46.35
21	0.5237	2.6924	73.99	304.88	47.00
22	0.5356	2.4872	76.92	310.56	47.06
23	0.5679	2.6773	68.82	308.64	46.78
24	0.6921	2.4016	70.78	335.57	47.02
25	0.4458	1.8370	82.94	303.03	46.47
26	0.6562	2.9604	46.89	314.47	46.97
27	0.5037	2.5823	62.13	304.88	47.41
28	0.3977	2.6631	88.50	292.40	47.02
29	0.3727	2.3043	78.40	294.12	47.59
30	0.6010	1.9596	49.58	337.84	46.91
31	0.65	2.4	67.20	331.13	47.63
32	0.475	2.25	76.30	304.88	48.20
33	0.525	2	50.14	318.47	51.70
34	0.6	2.5	78.95	318.47	48.55
35	0.37	2.9	47.84	290.70	46.94
36	0.32	1.9	57.00	294.12	46.96

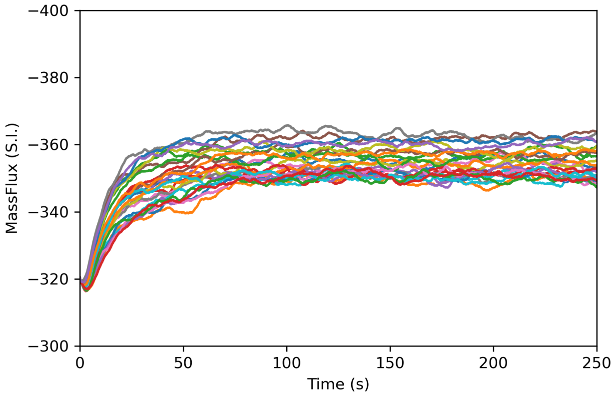

(a) R_k/D=3

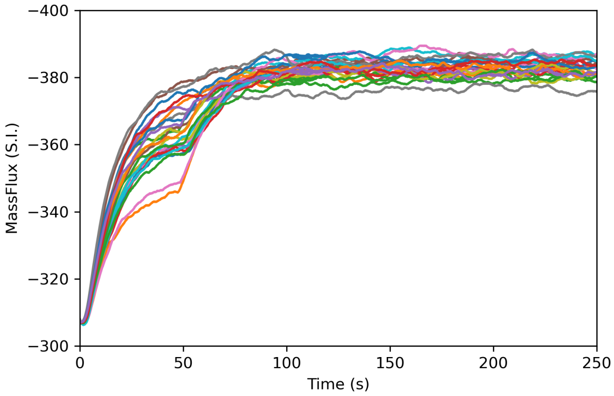

(b) R_k/D=7.2

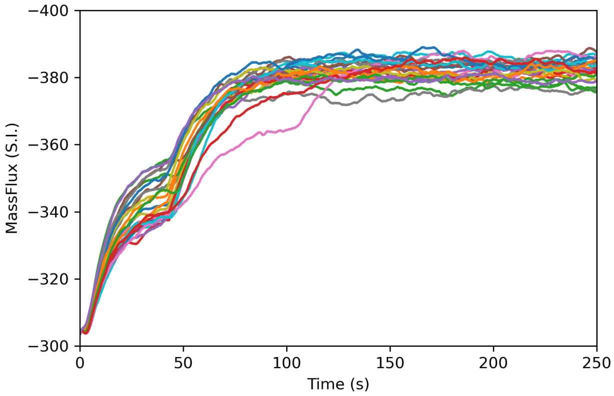

(c) R_k/D=10

Figure 37. – NCL establishment for MassFlux from 30K to 40K for different curvature ratio with geometry $s_{3,i}$.

Table 25. – NCL establishment for MassFlux from 40K to 10K for different curvature ratio with geometry $s_{3,i}$.

			$R_k/D = 3$			**$R_k/D = 7.2$**			**$R_k/D = 10$**		
Case	**Cw**	**Prdt**	**MFlux 40K**	**MFlux 10K**	**HalfTime**	**MFlux 40K**	**MFlux 10K**	**HalfTime**	**MFlux 40K**	**MFlux 10K**	**HalfTime**
1	0.4928	3.0184	355.34	134.97	13.31	383.17	153.20	14.37	384.19	152.83	14.73
2	0.3893	1.9475	349.52	130.10	12.90	381.15	148.09	14.30	382.34	147.74	14.61
3	0.6893	1.6510	357.56	146.33	12.97	378.67	162.38	13.46	377.87	162.29	14.10
4	0.4176	2.5200	351.08	132.10	12.92	382.47	150.00	14.30	381.50	149.93	14.63
5	0.4478	2.7253	352.04	132.75	13.20	383.90	151.03	14.19	382.67	150.82	14.32
6	0.6495	2.9549	362.00	144.76	13.16	384.92	160.22	14.26	383.52	159.77	14.47
7	0.4903	2.4693	354.02	134.77	12.70	382.51	153.02	14.16	381.40	151.89	14.42
8	0.5522	1.4680	351.06	137.78	12.89	376.28	155.25	13.66	376.60	154.23	14.01
9	0.5321	2.1601	354.41	136.94	13.20	380.18	154.61	14.09	380.55	153.91	14.40
10	0.3004	2.5929	350.77	126.85	13.32	386.54	144.95	14.75	386.44	145.61	15.14
11	0.3615	2.8184	350.87	129.34	13.14	384.09	147.05	14.61	384.07	147.69	14.72
12	0.5084	2.3328	354.27	136.15	13.07	381.97	153.29	14.26	381.42	153.23	14.19
13	0.5898	2.0916	355.82	140.70	13.08	380.68	157.69	13.62	379.27	157.31	14.30
14	0.4666	2.2174	351.65	133.21	13.02	381.65	151.21	14.30	381.45	151.72	14.46
15	0.4015	2.3155	351.08	130.82	12.96	381.36	148.34	14.70	382.33	149.81	14.57
16	0.5700	3.2331	357.47	140.17	13.14	384.37	156.85	13.88	384.27	155.76	14.41
17	0.3189	3.7368	351.68	128.53	12.85	386.99	145.85	14.90	386.98	146.03	14.92
18	0.6687	2.8689	362.67	146.04	13.17	385.70	161.86	14.20	384.23	161.17	14.68
19	0.6109	2.4058	358.60	141.90	13.32	381.90	158.21	13.90	381.26	158.25	14.45
20	0.3349	2.6521	350.13	127.82	13.00	384.37	146.57	14.55	384.18	147.25	14.92
21	0.6295	3.1411	361.27	142.85	13.07	385.38	159.58	14.08	384.09	159.81	14.37
22	0.5768	2.7673	357.29	140.54	13.00	383.03	156.67	13.88	382.85	156.59	14.31
23	0.4401	1.8559	350.12	132.52	12.99	380.17	150.28	14.17	378.30	150.19	14.55
24	0.3708	2.5672	350.90	129.15	13.08	383.33	147.52	14.67	383.98	146.70	14.96
25	0.6643	2.0757	359.97	145.46	13.03	381.76	161.05	13.80	379.81	160.24	14.29

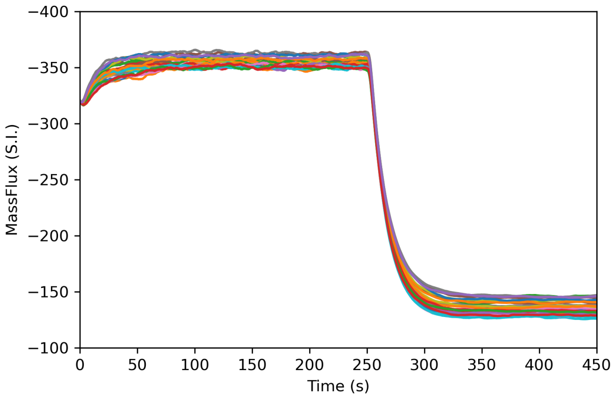

(a) R_k/D=3

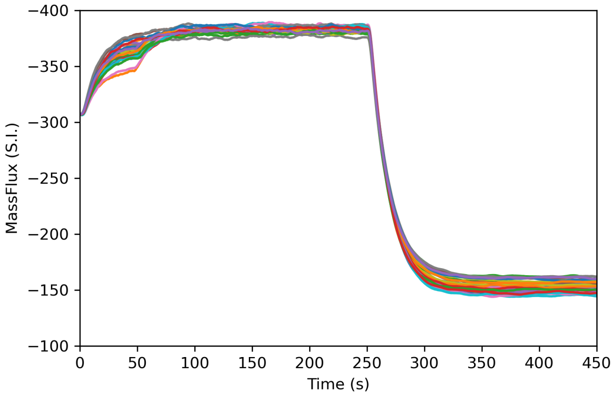

(b) R_k/D=7.2

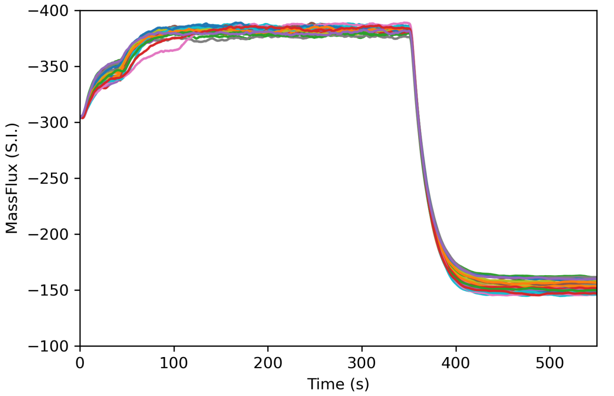

(c) R_k/D=10

Figure 38. – NCL establishment for MassFlux from 30K to 40K then 10K for different curvature ratio with geometry $s_{3,i}$.

Table 26. – NCL establishment for MassFlux from 10K to 40K for different curvature ratio with geometry $s_{3,i}$.

$\boldsymbol{R_k/D=3}$			$\boldsymbol{R_k/D=5}$			$\boldsymbol{R_k/D=7.2}$			$\boldsymbol{R_k/D=10}$		
MFlux 10K	MFlux 40K	HalfTime	MFlux 10K	MFlux 40K	HalfTime	MFlux 10K	MFlux 40K	HalfTime	MFlux 10K	MFlux 40K	HalfTime
128.61	288.86	11.74	135.24	310.16	12.65	139.16	323.09	13.45	141.95	326.37	13.80
126.01	283.59	11.49	130.75	305.56	12.71	134.60	319.81	13.42	138.26	318.34	14.21
138.48	312.56	12.46	146.38	332.61	13.49	150.45	341.61	13.94	152.28	345.75	14.36
127.13	283.87	11.62	130.95	306.77	12.53	136.17	321.49	13.56	138.70	319.89	14.89
126.70	285.61	11.61	133.14	306.74	12.48	137.02	322.45	13.42	140.07	322.35	13.75
136.50	305.26	12.18	144.15	326.49	13.13	148.59	336.57	13.88	150.23	341.93	14.47
128.36	288.62	11.80	134.65	308.98	12.62	139.15	323.64	13.52	141.41	326.79	13.93
131.25	294.03	11.75	137.64	315.79	12.94	142.34	326.15	13.53	144.86	333.01	14.05
130.82	290.16	11.70	136.78	313.47	12.82	140.67	325.40	13.53	143.87	330.58	13.94
123.69	283.63	11.73	128.28	306.97	12.71	131.53	319.48	13.45	135.90	312.00	15.04
124.74	282.23	11.67	129.57	306.04	12.59	133.16	321.04	13.62	136.82	315.50	14.31
128.88	290.48	11.74	135.13	311.48	12.68	139.58	323.41	13.51	143.15	329.62	14.01
132.92	297.99	11.94	140.03	317.93	12.95	144.41	329.52	13.58	147.31	336.91	14.16
128.26	287.05	11.79	134.05	308.86	12.71	137.72	321.40	13.53	141.13	326.02	13.85
125.07	284.66	11.63	131.14	305.22	12.64	135.28	320.70	13.50	138.30	318.74	14.22
131.75	295.33	12.03	139.45	316.00	12.79	143.28	328.12	13.55	145.43	333.99	14.12
124.29	282.95	11.60	128.16	305.64	12.91	131.78	319.98	13.48	135.74	312.86	14.21
137.77	308.41	12.26	145.21	328.98	13.23	148.97	339.00	13.74	150.74	342.97	14.26
133.90	300.30	11.93	141.36	320.95	12.92	145.58	333.07	13.76	147.95	337.74	14.19
124.02	283.08	11.62	128.45	305.90	12.64	132.07	320.96	13.68	136.49	314.81	14.86
135.13	304.16	12.20	142.08	324.34	12.97	146.54	334.41	13.66	148.82	338.95	14.08
132.29	296.88	11.96	139.66	317.13	12.88	144.04	329.21	13.83	146.27	334.33	14.03
127.04	284.71	11.68	132.83	307.19	12.97	135.97	321.62	13.41	139.34	322.11	13.80
125.26	282.68	11.62	130.02	306.22	12.66	133.40	320.34	13.63	137.72	314.75	13.79
137.38	307.62	12.26	145.32	328.36	13.39	148.43	338.42	13.85	150.76	343.45	14.34

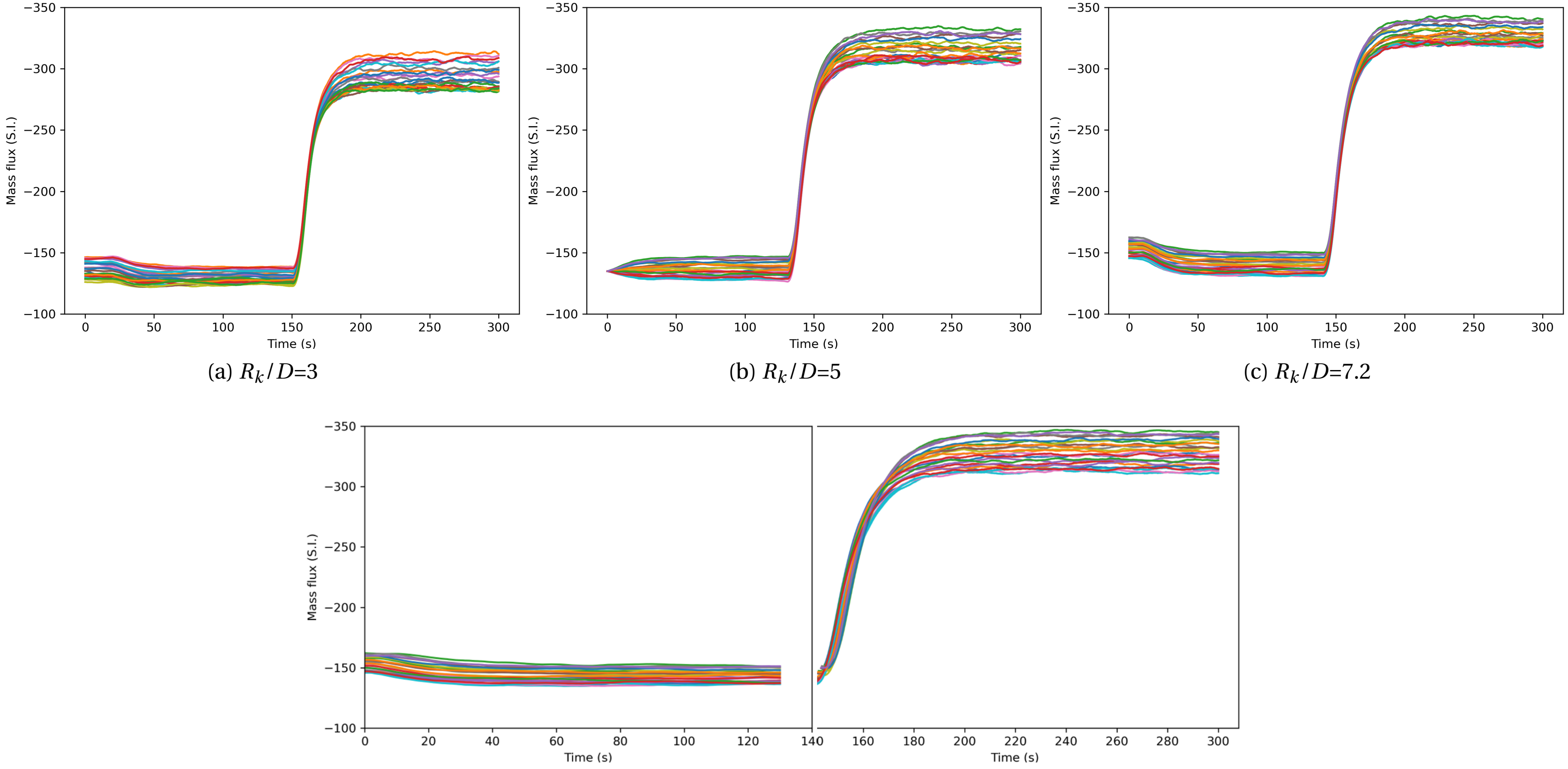

(a) R_k/D=3

(b) R_k/D=5

(c) R_k/D=7.2

(d) R_k/D=10

Figure 39. – NCL establishment for MassFlux from 10K to 40K for different curvature ratio with geometry $s_{3,i}$.

Table 27. – Dataset Summary: mdoel uncertainty of NCL establishment for different curvature ratio with geometry $s_{3,i}$ by Uranie.

R_k/D	ΔT	Mean	Var	1st Ord.[1]	1st Ord.[2]	Total Ord.[1]	Total Ord.[2]	MSELOO	Quant[0]	Quant[1]
$\Delta T = 40K \rightarrow 10K$										
10	40	382.65	6.35	0.382	0.344	0.656	0.618	12.721	379.26	386.80
	10	152.82	30.39	0.853	0.084	0.916	0.147	6.411	145.79	161.34
	HalfTime	14.41	0.87	0.028	0.568	0.432	0.973	0.259	14.25	15.15
7.2	40	383.49	20.82	0.156	0.391	0.609	0.844	6.235	379.39	387.43
	10	153.64	28.04	0.973	0.013	0.987	0.027	6.666	145.55	162.90
	HalfTime	14.11	0.45	0.097	0.500	0.500	0.903	0.757	13.75	14.72
3	40	354.68	19.64	0.829	0.105	0.895	0.171	7.181	349.63	363.38
	10	136.02	38.82	0.987	0.004	0.996	0.013	1.681	126.99	147.45
	HalfTime	13.01	0.45	0.004	0.735	0.265	0.996	1.100	12.95	13.34
$\Delta T = 10K \rightarrow 40K$										
10	10	142.89	26.36	0.955	0.025	0.975	0.045	3.101	136.04	151.33
	40	327.90	109.60	0.993	0.005	0.995	0.007	62.586	312.59	345.62
	HalfTime	14.20	0.15	0.345	0.521	0.479	0.655	0.857	13.84	14.96
7.2	10	140.03	33.25	0.982	0.002	0.998	0.018	1.645	131.74	150.01
	40	326.61	51.01	0.914	0.045	0.956	0.087	6.009	318.34	342.16
	HalfTime	13.50	0.22	0.119	0.384	0.616	0.881	0.085	13.15	13.94
5	10	135.88	35.55	0.914	0.042	0.958	0.087	1.598	128.26	147.49
	40	313.62	73.82	0.993	0.002	0.998	0.008	3.320	304.89	332.39
	HalfTime	12.73	0.37	0.154	0.439	0.561	0.846	0.620	12.47	13.52
3	10	129.91	21.19	0.996	0.002	0.998	0.004	3.160	123.93	139.32
	40	292.48	89.01	0.953	0.031	0.969	0.047	17.831	282.23	311.51
	HalfTime	11.78	0.13	0.595	0.150	0.850	0.406	0.040	11.36	12.41

D.2. Procedures of SCTs

D.2.1. Example of MedCoupling in SALOME

Objective: Interpolate the physical fields between different meshes.

```
# Load the SALOME environment
source /...location/env_launch.sh
# Launch following codes in SALOME command box or as a python file to launch in Linux command line
import MEDLoader as ml
import medcoupling as mc
from MEDCouplingRemapper import MEDCouplingRemapper
import numpy as np
srcMesh = ml.ReadUMeshFromFile("source.med")
# refined mesh where field is interpolated
trgMesh = ml.ReadUMeshFromFile("target.med")
srcField=mc.ReadFieldCell("source.med","dom",0,"TEMPERATURE_ELEM_dom",0,-1)
print(srcField.getArray())
remap = MEDCouplingRemapper()
remap.prepare(srcMesh,trgMesh,"P0P0")
# Temperature as intensive parameter
srcField.setNature(mc.IntensiveMaximum)
trgFieldCV = remap.transferField(srcField,1e300)
integSource = srcField.integral(True)[0]
integTarget = trgFieldCV.integral(True)[0]
print ("IntensiveMaximum – integrals: %lf == %lf" % (integSource, integTarget))
accSource = srcField.getArray().accumulate()[0]
accTarget = trgFieldCV.getArray().accumulate()[0]
print ("IntensiveMaximum – sums: %lf != %lf" % (accSource, accTarget))
ml.WriteField("target_interpo.med",trgFieldCV,True)
print(trgFieldCV.getArray())
```

D.2.2. Example of applying Uranie

Objective: Obtain the numerical model uncertainty through surrogate model, along with sensitivity study and data assimilation (calibration).

Step 0: Load the ROOT/URANIE ENVIRONMENT

```
# Install the Uranie platform for the OS
https://gitlab.com/uranie_tma/publication/-/wikis/home#linux-bash
# Choose your path of environment file thisroot.sh location
source /Haifu/uranie/bin/thisroot.sh
# Maybe the link of models are necessary, one doesn't want to use the header
```

```
ln -s ../rootlogon.py # to import the modules in one single file
```

Step 1: Sampling

```
# Launch Sampling_VkPrdt.py
python3 -i Sampling_VkPrdt.py
# or using C script
root -l xx.C
```

Step 2: KEY Launch External Code

```
# If the sequential calculation is not too long
# Otherwise, Launch parallel and collect results in the *.dat file
# Example: launch a TrioCFD code
source /...localtion/TRUST-1.9.1/env_TRUST.sh
source /...location/trust-trio/TrioCFD-1.9.1/env_TrioCFD.sh
# Launch a xx.data file using 40 processors or better using validation file in TrioCFD/TRUST to launch massively similar calculations in a cluster of HPC
trust xx.data 40
```

Step 3: Data-Driven PCE Meta-Modelling

```
python3 -i PCEVkPrdt_data.py
# output -> KEpsVonKarmanPrdt30.C as PCE model
```

Step 4: Quantile

```
python3 -i Quantile_VkPrdt.py
# output -> quantile wilks & Keps_Quantile_Histo.png
```

Step 5: Sensitivity

```
# Multi SA can be done, recommend Brute-Force and Sobol method
python3 -i Sensitivity_BruitForce_VK_Prdt.py
# output -> Figure of individual input on QoI
python3 -i Sensitivity_Morris_VK_Prdt.py
python3 -i Sensitivity_Regression_VK_Prdt.py
python3 -i Sensitivity_Sobol_VK_Prdt.py
# Output -> quantile of input
```

Step 6: Calibration

```
# Choose your reference data and target parameter
python3 -i CalibrationRejABC_VkPrdt.py
# Output -> Cali Parameter & Fig Histo
```

Bibliography

[AV12] Abdulle, A. and Vilmart, G. “A Priori Error Estimates for Finite Element Methods with Numerical Quadrature for Nonmonotone Nonlinear Elliptic Problems”. In: *Numerische Mathematik* 121.3 (July 2012), pp. 397–431. ISSN: 0945-3245. DOI: 10.1007/s00211-011-0438-4. (Visited on 06/23/2023) (cit. on p. 108).

[Alp+16] Alpy, N., Marsault, P., Anderhuber, M., et al. “Phenomenological Investigation of Sodium Boiling in a SFR Core during a Postulated ULOF Transient with CATHARE 2 System Code: A Stabilized Boiling Case”. In: *Journal of Nuclear Science and Technology* 53.5 (2016), pp. 692–697. ISSN: 00223131. DOI: 10.1080/00223131.2015.1111778 (cit. on p. 64).

[Amb+04] Ambrosini, W., Forgione, N., Ferreri, J. C., et al. “The Effect of Wall Friction in Single-Phase Natural Circulation Stability at the Transition between Laminar and Turbulent Flow”. In: *Annals of Nuclear Energy* 31.16 (2004), pp. 1833–1865. ISSN: 03064549. DOI: 10.1016/j.anucene.2004.05.011 (cit. on pp. 34, 68).

[ABF15] Angeli, P. E., Bieder, U., and Fauchet, G. “Overview of the TrioCFD Code: Main Features, VetV Procedures and Typical Applications to Nuclear Engineering”. In: *NURETH 16 - 16th International Topical Meeting on Nuclear Reactor Thermalhydraulics*. Aug. 2015. (Visited on 06/02/2023) (cit. on pp. 65, 77, 173, 190, 191).

[AP16] Angeli, P. E. and Peybernes, M. “CFD Analysis of the Turbulent Flow in a PWR 5x5 Rod Bundle with Staggered Structural Grids”. In: *CFD4NRS-6 - The 6th Workshop on Computational Fluid Dynamics for Nuclear Reactor Safety Applications*. OCDE ; NEA, Sept. 2016. (Visited on 06/03/2023) (cit. on pp. 90, 93).

[ABN16] Asch, M., Bocquet, M., and Nodet, M. *Data Assimilation*. Fundamentals of Algorithms. Society for Industrial and Applied Mathematics, Dec. 2016. ISBN: 978-1-61197-453-9. DOI: 10.1137/1.9781611974546. (Visited on 07/07/2023) (cit. on p. 147).

[ASM09] ASME. *ASME V&V 20-2009 Standard for Verification and Validation in Computational Fluid Dynamics and Heat Transfer*. Jan. 2009 (cit. on pp. 28, 102, 107, 109–111, 119, 121).

[AI17] ASN and IRSN. *Qualification Des Outils de Calcul Scientifique Utilisés Dans La Démonstration de Sûreté Nucléaire - 1re Barrière, GUIDE N°28*. Tech. rep. 2017 (cit. on pp. 27–29, 33, 41, 102, 111).

[Bac+20] Baccou, J., Zhang, J., Fillion, P., et al. “SAPIUM: A Generic Framework for a Practical and Transparent Quantification of Thermal-Hydraulic Code Model Input Uncertainty”. In: *Nuclear Science and Engineering* 194.8-9 (Sept. 2020), pp. 721–736. ISSN: 0029-5639. DOI: 10.1080/00295639.2020.1759310 (cit. on pp. 56, 57).

[BZS22] Baccou, J., Zhang, J., and Skorek, T. “From PREMIUM to SAPIUM: Towards a Practical and Systematic Approach for Model Input Uncertainty Quantification of Thermal Hydraulic Codes”. In: *OECD/NEA/CSNI Specialists Meeting on Transient Thermal-hydraulics in Water Cooled Nuclear Reactors (SM-TH)*. Virtual, Mar. 2022 (cit. on p. 56).

[Bad+14] Badillo, A., Niceno, B., Fokken, J., et al. “Uncertainty Quantification of the Effect of Random Inputs on Computational Fluid Dynamics Simulations of the GEMIX Experiment Using Metamodels”. In: *CFD4NRS-5*. Zurich, Sept. 2014 (cit. on p. 139).

[BN05] Baglietto, E. and Ninokata, H. “A Turbulence Model Study for Simulating Flow inside Tight Lattice Rod Bundles”. In: *Nuclear Engineering and Design* 235.7 (2005), pp. 773–784. ISSN: 0029-5493. DOI: 10.1016/j.nucengdes.2004.10.007 (cit. on p. 90).

[BNM06] Baglietto, E., Ninokata, H., and Misawa, T. “CFD and DNS Methodologies Development for Fuel Bundle Simulations”. In: *Nuclear Engineering and Design* 236.14 (2006), pp. 1503–1510. ISSN: 0029-5493. DOI: 10.1016/j.nucengdes.2006.03.045 (cit. on p. 92).

[Bar22] Barletta, A. “The Boussinesq Approximation for Buoyant Flows”. In: *Mechanics Research Communications* 124 (Sept. 2022), p. 103939. ISSN: 0093-6413. DOI: 10.1016/j.mechrescom.2022.103939. (Visited on 06/14/2023) (cit. on p. 81).

[BBD14] Basu, D. N., Bhattacharyya, S., and Das, P. K. “A Review of Modern Advances in Analyses and Applications of Single-Phase Natural Circulation Loop in Nuclear Thermal Hydraulics”. In: *Nuclear Engineering and Design* 280 (2014), pp. 326–348. ISSN: 0029-5493. DOI: 10.1016/j.nucengdes.2014.09.011 (cit. on pp. 59, 60).

[Bat+21] Battistini, A., Cammi, A., Lorenzi, S., et al. “Development of a CFD – LES Model for the Dynamic Analysis of the DYNASTY Natural Circulation Loop”. In: *Chemical Engineering Science* 237 (June 2021), p. 116520. ISSN: 0009-2509. DOI: 10.1016/j.ces.2021.116520. (Visited on 05/19/2022) (cit. on p. 68).

[BT81] Bau, H. H. and Torrance, K. E. “Transient and Steady Behavior of an Open, Symmetrically-Heated, Free Convection Loop”. In: *International Journal of Heat and Mass Transfer* 24.4 (1981), pp. 597–609. ISSN: 00179310. DOI: 10.1016/0017-9310(81)90004-1 (cit. on p. 115).

[Bec44] Beck, C. “Laminar Flow Pressure Losses in 90 Degree Constant Circular Cross-Section Bends”. In: *Journal of the American Society for Naval Engineers* 56.3 (1944), pp. 366–388. ISSN: 1559-3584. DOI: `10.1111/j.1559-3584.1944.tb01637.x`. (Visited on 09/18/2022) (cit. on p. 212).

[Bec+21] Bect, J., Zio, S., Perrin, G., et al. “On the Quantification of Discretization Uncertainty: Comparison of Two Paradigms”. In: *14th World Congress in Computational Mechanics and ECCOMAS Congress 2020 (WCCM-ECCOMAS)*. Jan. 2021. DOI: `10.23967/wccm-eccomas.2020.260`. (Visited on 08/05/2022) (cit. on p. 106).

[BK03] Bejan, A. and Kraus, A. D. *Heat Transfer Handbook*. John Wiley & Sons, June 2003. ISBN: 978-0-471-39015-2 (cit. on p. 211).

[BRK19] Bertocchi, F., Rohde, M., and Kloosterman, J. L. “Experimental Investigation on the Influence of Gap Vortex Streets on Fluid-Structure Interactions in Hexagonal Bundle Geometries”. In: *International Journal of Heat and Fluid Flow* 79 (Oct. 2019), p. 108443. ISSN: 0142-727X. DOI: `10.1016/j.ijheatfluidflow.2019.108443`. (Visited on 04/14/2022) (cit. on p. 151).

[Bes+17] Bestion, D., D’Auria, F., P., L., et al. *Scaling in System Thermal-Hydraulics Applications to Nuclear Reactor Safety and Design: A State-of-the-Art Report*. Tech. rep. Mar. 2017 (cit. on pp. 41, 43, 48, 55, 65).

[Bes17] Bestion, D. “System Thermalhydraulics for Design Basis Accident Analysis and Simulation: Status of Tools and Methods and Direction for Future R&D”. In: *Nuclear Engineering and Design* 312 (2017), pp. 12–29. ISSN: 00295493. DOI: `10.1016/j.nucengdes.2016.11.010` (cit. on pp. 33, 36, 37).

[Bes+16] Bestion, D., de Crécy, A., Camy, R., et al. *Review of Uncertainty Methods for Computational Fluid Dynamics Application to Nuclear Reactor Thermal Hydraulics*. Tech. rep. NEA/CSNI/R(2016)4. 2016 (cit. on pp. 28, 51, 66, 102).

[Bes22] Bestion, D. “Proposals to Improve Thermal Hydraulic Codes”. In: *OECD/NEA/CSNI Specialists Meeting on Transient Thermal-hydraulics in Water Cooled Nuclear Reactors (SM-TH)*. Virtual, Mar. 2022 (cit. on pp. 55, 56).

[BD16] Bestion, D. and De Crecy, A. “Review of Uncertainty Methods for CFD Application to Nuclear Reactor Thermalhydraulics”. In: *NUTHOS-11*. Gyeongjum,Korea, 2016 (cit. on pp. 51, 53, 66, 103, 138, 141, 158).

[Bhu+22] Bhushan, S., Elmellouki, M., Walters, D. K., et al. “Analysis of Turbulent Flow and Thermal Structures in Low-Prandtl Number Buoyant Flows Using Direct Numerical Simulations”. In: *International Journal of Heat and Mass Transfer* 189 (June 2022), p. 122733. ISSN: 0017-9310. DOI: `10.1016/j.ijheatmasstransfer.2022.122733`. (Visited on 08/25/2022) (cit. on p. 89).

[Bie+19] Bieder, U., Maillard, J., Gorsse, Y., et al. "CFD Analysis of the Flow in the MICAS Experimental Facility, a Water Model of the Hot Pool of a Sodium Cooled Fast Reactor". In: *Nuclear Engineering and Design* 350.April (2019), pp. 67–77. ISSN: 00295493. DOI: `10.1016/j.nucengdes.2019.04.033` (cit. on p. 90).

[BR19] Bieder, U. and Rodio, M. G. "Large Eddy Simulation of the Injection of Cold ECC Water into the Cold Leg of a Pressurized Water Reactor". In: *Nuclear Engineering and Design* 341 (Jan. 2019), pp. 186–197. ISSN: 0029-5493. DOI: `10.1016/j.nucengdes.2018.10.026`. (Visited on 06/03/2023) (cit. on p. 90).

[BON21] BONNEFOY, O. *Mécanique Des Fluides et Transferts*. l'Ecole Nationale Supérieure des Mines de Saint-Etienne, June 2021 (cit. on p. 42).

[Bor+17] Borreani, W., Chersola, D., Lomonaco, G., et al. "Assessment of a 2D CFD Model for a Single Phase Natural Circulation Loop". In: *International Journal of Heat and Technology* (2017). ISSN: 03928764. DOI: `10.18280/ijht.35Sp0141` (cit. on p. 68).

[BD93] Bovalini, R. and D'Auria, F. "Scaling of the Accuracy of the Relap5/Mod2 Code". In: *Nuclear Engineering and Design* 139.2 (1993), pp. 187–203. ISSN: 00295493. DOI: `10.1016/0029-5493(93)90156-4` (cit. on p. 64).

[Boy+89] Boyack, B., Duffey, R., Griffith, P., et al. *Quantifying Reactor Safety Margins: Application of Code Scaling, Applicability, and Uncertainty Evaluation Methodology to a Large-Break, Loss-of-Coolant Accident*. 1989 (cit. on pp. 51, 52).

[BK92] Bremhorst, K. and Krebs, L. "Experimentally Determined Turbulent Prandtl Numbers in Liquid Sodium at Low Reynolds Numbers". In: *International Journal of Heat and Mass Transfer* 35.2 (Feb. 1992), pp. 351–359. ISSN: 0017-9310. DOI: `10.1016/0017-9310(92)90273-U`. (Visited on 08/29/2023) (cit. on p. 143).

[Buc14] Buckingham, E. "On Physically Similar Systems; Illustrations of the Use of Dimensional Equations". In: *Physical Review* 4.4 (Oct. 1914), pp. 345–376. DOI: `10.1103/PhysRev.4.345`. (Visited on 06/09/2023) (cit. on p. 42).

[CCE02] Calvin, C., Cueto, O., and Emonot, P. "An Object-Oriented Approach to the Design of Fluid Mechanics Software". In: *ESAIM: Mathematical Modelling and Numerical Analysis - Modélisation Mathématique et Analyse Numérique* 36.5 (2002), pp. 907–921. ISSN: 0764-583X. (Visited on 06/22/2023) (cit. on p. 76).

[Cat+09] Catton, I., Wulff, W., Zuber, N., et al. "Application of Fractional Scaling Analysis to Loss of Coolant Accidents: Component Level Scaling for Peak Clad Temperature". In: *Journal of Fluids Engineering, Transactions of the ASME* 131.12 (2009), pp. 1214011–1214018. ISSN: 00982202. DOI: `10.1115/1.4000370` (cit. on p. 220).

[CEA12] CEA. *Les Réacteurs à Neutrons Rapides de 4e Génération à Caloporteur Sodium Le Démonstrateur Technologique ASTRID*. Paris, 2012 (cit. on p. 81).

[CEA22a] CEA. *Internal Note: Comment Appliquer et Décliner I'approche VVQI-T Au Multiphysique En Fonction Du Niveau de Simulation et Du Besoin ?* Tech. rep. DES/IRESNE/DIR2022 - 16. CEA Cadarache, Aug. 2022 (cit. on p. 63).

[CEA22b] CEA. *User Manual for Uranie v4.7.0*. Oct. 2022 (cit. on p. 141).

[ÇK20] Çobanoğlu, N. and Karadeniz, Z. H. "Effect of Nanofluid Thermophysical Properties on the Performance Prediction of Single-Phase Natural Circulation Loops". In: *Energies* 13.10 (Jan. 2020), p. 2523. ISSN: 1996-1073. DOI: `10.3390/en13102523`. (Visited on 02/17/2022) (cit. on p. 58).

[Col92] Coleman, G. "Direct Simulation of Compressible Wall-Bounded Turbulence". In: -1 (Dec. 1992), pp. 139–144 (cit. on p. 100).

[CCS07] Crawford, N. M., Cunningham, G., and Spence, S. W. T. "An Experimental Investigation into the Pressure Drop for Turbulent Flow in 90° Elbow Bends". In: *Proceedings of the Institution of Mechanical Engineers, Part E: Journal of Process Mechanical Engineering* 221.2 (May 2007), pp. 77–88. ISSN: 0954-4089. DOI: `10.1243/0954408JPME84`. (Visited on 03/15/2023) (cit. on pp. 115, 212, 213).

[DAu23] D'Auria, F. "Scaling, Passive Systems, and the AP-1000". In: *Nuclear Science and Engineering* 0.0 (Mar. 2023), pp. 1–13. ISSN: 0029-5639. DOI: `10.1080/00295639.2023.2178874`. (Visited on 03/24/2023) (cit. on pp. 34, 35).

[DG10] D'Auria, F. and Galassi, G. M. "Scaling in Nuclear Reactor System Thermal-Hydraulics". In: *Nuclear Engineering and Design* 240.10 (2010), pp. 3267–3293. ISSN: 00295493. DOI: `10.1016/j.nucengdes.2010.06.010` (cit. on p. 40).

[Dau+87] D'auria, F., Galassi, G. M., Oriolo, F., et al. "Assessment of Scaling Principles for the Simulation of Small Break LOCA Experiments in PWRs". In: *Nuclear Engineering and Design* (1987). DOI: `10.1016/0029-5493(87)90245-7` (cit. on p. 48).

[DAu+91] D'Auria, F., Galassi, G. M., Vigni, P., et al. "Scaling of Natural Circulation in PWR Systems". In: *Nuclear Engineering and Design* 132.2 (Dec. 1991), pp. 187–205. ISSN: 0029-5493. DOI: `10.1016/0029-5493(91)90265-J`. (Visited on 06/13/2023) (cit. on pp. 60, 61).

[DDG95] D'Auria, F., Debrecin, N., and Galassi, G. M. "Outline of the Uncertainty Methodology Based on Accuracy Extrapolation". In: *Nuclear Technology* 109.1 (1995), pp. 21–38. ISSN: 00295450. DOI: `10.13182/nt109-21` (cit. on p. 53).

[DAu+97] D'Auria, F., Galassi, G., Leonardi, M., et al. "Application of Fast Fourier Transform Method to Evaluate the Accuracy of SBLOCA Data Base". In: *NURETH-8*. Kyoto, Japon, 1997 (cit. on p. 53).

[DG00] D'Auria, F. and Giannotti, W. "Development of a Code with the Capability of Internal Assessment of Uncertainty". In: *Nuclear Technology* 131.2 (2000), pp. 159–196. ISSN: 00295450. DOI: 10.13182/NT00-5 (cit. on p. 53).

[de +08] de Crécy, A., Bazin, P., Glaeser, H., et al. "Uncertainty and Sensitivity Analysis of the LOFT L2-5 Test: Results of the BEMUSE Programme". In: *Nuclear Engineering and Design* 238.12 (2008), pp. 3561–3578. ISSN: 0029-5493. DOI: 10.1016/j.nucengdes.2008.06.004 (cit. on pp. 48, 57, 139).

[de 12] de Rocquigny, E. *Modelling Under Risk and Uncertainty: An Introduction to Statistical, Phenomenological and Computational Methods*. 2012. ISBN: 978-1-119-96949-5. (Visited on 02/09/2022) (cit. on p. 180).

[DPT17] De Saint Jean, C., Palau, J., and Tommasi, J. "Description Des Méthodes de Transposition Employées En Neutronique". 2017 (cit. on p. 36).

[DPS86] De Santi, G., Piplies, L., and Sanders, J. "Mass Flow Instabilities in LOBI Steam Generator U-tubes Array under Natural Circulation Conditions". In: *Proceedings of Second International Topical Meeting on Nuclear Power Plant Thermal Hydraulics and Operations*. Japon, 1986 (cit. on p. 59).

[DH59] Dean, W. R. and Hurst, J. M. "Note on the Motion of Fluid in a Curved Pipe". In: *Mathematika* 6.1 (1959), pp. 77–85. DOI: 10.1112/S0025579300001947 (cit. on pp. 59, 60).

[Dow16] Dowding, K. "Overview of ASME V&V 20-2009 Standard for Verification and Validation in Computational Fluid Mechanics and Heat Transfer". In: *2016 Inverse Problems Symposium Virginia Military Institute*. US: Sandia National Laboratories, 2016 (cit. on p. 109).

[Due+22] Duenas, A., Wachs, D., Mignot, G., et al. "Dynamical System Scaling Application to Zircaloy Cladding Thermal Response During Reactivity-Initiated Accident Experiment". In: *Nuclear Science and Engineering* (Feb. 2022), pp. 193–208. ISSN: 0029-5639. (Visited on 02/21/2022) (cit. on p. 50).

[Dup+14] Duponcheel, M., Bricteux, L., Manconi, M., et al. "Assessment of RANS and Improved Near-Wall Modeling for Forced Convection at Low Prandtl Numbers Based on LES up to Reτ=2000". In: *International Journal of Heat and Mass Transfer* 75 (Aug. 2014), pp. 470–482. ISSN: 0017-9310. DOI: 10.1016/j.ijheatmasstransfer.2014.03.080. (Visited on 12/04/2021) (cit. on p. 89).

[Dzo16] Dzodzo, M. *Overview of Scaling Methodologies*. Tech. rep. Vienna, Sept. 2016. DOI: 10.13140/RG.2.2.14247.65449 (cit. on p. 45).

[Dzo+19] Dzodzo, M. B., Oriolo, F., Ambrosini, W., et al. “Application of Fractional Scaling Analysis for Development and Design of Integral Effects Test Facility”. In: *Journal of Nuclear Engineering and Radiation Science* 5.4 (Sept. 2019). ISSN: 2332-8983. DOI: 10.1115/1.4042496 (cit. on p. 45).

[EH06] Eça, L. and Hoekstra, M. “Discretization Uncertainty Estimation Based on a Least Squares Version of the Grid Convergence Index”. In: (Jan. 2006) (cit. on p. 108).

[Fok+17] Fokken, J., Krohn, R., Kapulla, R., et al. *Computational Fluid Dynamic Prediction and Uncertainty Quantification of a GEMIX Mixing Layer Test*. Tech. rep. 2017. (Visited on 07/05/2023) (cit. on pp. 121, 139).

[FSK07] Forrester, A. I., Sóbester, A., and Keane, A. J. “Multi-Fidelity Optimization via Surrogate Modelling”. In: *Proceedings of the Royal Society A: Mathematical, Physical and Engineering Sciences* 463.2088 (Oct. 2007), pp. 3251–3269. DOI: 10.1098/rspa.2007.1900. (Visited on 07/06/2023) (cit. on p. 139).

[Fre19] Frepoli, C. “Scaling Analysis of Thermal-Hydraulic Integral Systems: Insights from Practical Applications and Recent Advancements”. In: *18th International Topical Meeting on Nuclear Reactor Thermal Hydraulics, NURETH 2019* (2019), pp. 1075–1079 (cit. on pp. 44, 219).

[FYR15] Frepoli, C., Yurko, J. P., and Reyes, J. N. “Experimental Test Facility Data Synthesis with the Dynamical System Scaling Methodology”. In: *NURETH-16*. Chicago, USA, 2015 (cit. on pp. 45, 48).

[Gau09] Gauthe, P. “Compte Rendu d’essai Scienifique, Convection Naturelle”. 2009 (cit. on p. 64).

[Gef+17] Geffray, C., Gerschenfeld, A., Gorsse, Y., et al. *Multi-Scale Modelling of the ASTRID Reactor*. Tech. rep. DM2S/STMF, 2017 (cit. on p. 82).

[Ger+17] Gerschenfeld, A., Li, S., Gorsse, Y., et al. “Development and Validation of Multi-Scale Thermal-Hydraulics Calculation Schemes for SFR Applications at CEA”. In: *FR17 Conference*. Yekaterinburg, Russian Federation, 2017, pp. 1–10 (cit. on pp. 34, 58, 64).

[Gla08] Glaeser, H. *Results from the Application of Uncertainty Methods in the CSNI Uncertainty Methods Study (UMS)*. Tech. rep. Garching, Germany: Gesellschaft für Anlagen- und Reaktorsicherheit (GRS) mbH, 2008, pp. 305–316 (cit. on p. 57).

[GYA21] Gomez, J., Yu, H., and Andreopoulos, Y. “Role of Flow Reversals in Transition to Turbulence and Relaminarization of Pulsatile Flows”. In: *Journal of Fluid Mechanics* 917 (June 2021). ISSN: 0022-1120, 1469-7645. DOI: 10.1017/jfm.2021.269. (Visited on 01/12/2022) (cit. on p. 59).

[GG76] Gray, D. D. and Giorgini, A. “The Validity of the Boussinesq Approximation for Liquids and Gases”. In: *International Journal of Heat and Mass Transfer* 19.5 (May 1976), pp. 545–551. ISSN: 0017-9310. DOI: `10.1016/0017-9310(76)90168-X`. (Visited on 01/30/2023) (cit. on pp. 81–83).

[GP08] Green, D. W. and Perry, R. H. *Perry’s Chemical Engineers’ Handbook, Eighth Edition*. McGraw-Hill Education, 2008. ISBN: 978-0-07-142294-9. (Visited on 07/29/2022) (cit. on p. 209).

[GG82] Grewal, S. and Gluekler, E. “Water Simulation of Sodium Reactors”. In: *Chemical Engineering Communications* 17.1-6 (Sept. 1982), pp. 343–360. ISSN: 0098-6445. DOI: `10.1080/00986448208911637`. (Visited on 06/13/2023) (cit. on p. 62).

[Gue+07] Guelfi, A., Bestion, D., Boucker, M., et al. “NEPTUNE: A New Software Platform for Advanced Nuclear Thermal Hydraulics”. In: *Nuclear Science and Engineering* 156.3 (July 2007), pp. 281–324. ISSN: 0029-5639. DOI: `10.13182/NSE05-98`. (Visited on 07/11/2023) (cit. on p. 65).

[GP21] Guo, W. and Prasser, H.-M. “Mixed Convection Study on the Influence of Low Prandtl Numbers and Buoyancy in Turbulent Heat Transfer Using DNS”. In: *Annals of Nuclear Energy* 158 (Aug. 2021), p. 108258. ISSN: 0306-4549. DOI: `10.1016/j.anucene.2021.108258`. (Visited on 11/20/2022) (cit. on p. 58).

[Has+19] Hashemi-Tilehnoee, M., Sahebi, N., Dogonchi, A. S., et al. “Simulation of the Dynamic Behavior of a Rectangular Single-Phase Natural Circulation Vertical Loop with Asymmetric Heater”. In: *International Journal of Heat and Mass Transfer* (2019). ISSN: 00179310. DOI: `10.1016/j.ijheatmasstransfer.2019.05.076` (cit. on p. 68).

[HFR19] Heagy, S. A., Frepoli, C., and Reyes, J. N. “Investigation of Scaling Distortions for NRELAP5 Model of NIST Facility Realized Using the Dynamical Systems Scaling Methodology”. In: *18th International Topical Meeting on Nuclear Reactor Thermal Hydraulics, NURETH 2019*. 2019, pp. 6083–6095 (cit. on p. 50).

[Hei82] Heisler, M. P. “Development of Scaling Requirements for Natural Convection Liquid-Metal Fast Breeder Reactor Shutdown Heat Removal Test Facilities”. In: *Nuclear Science and Engineering* 80.3 (1982), pp. 347–359. ISSN: 00295639. DOI: `10.13182/NSE82-A19819` (cit. on p. 60).

[Hou+18] Hourcade, E., Mihara, T., Dauphin, A., et al. “ASTRID Nuclear Island Design Update in French-Japanese Joint Team Development of Decay Heat Removal Systems”. In: *2018 International Congress on Advances in Nuclear Power Plants (ICAPP 18)*. Apr. 2018. (Visited on 08/12/2023) (cit. on pp. 35, 36).

[HYR13] Houser, R., Young, E., and Rasmussen, A. *Overview of NuScale Testing Programs*. Tech. rep. Washington, D.C.: American Nuclear Society, 2013 (cit. on p. 44).

[Hua22] Huang, H. *Contribution to the Multi-Scale Thermal-Hydraulics Modeling in Mixed Convection and Methodologic Impact on the Scaling Process in VVUQ, Based on Cliff-Edge Effects. DES/IRESNE/DER/SESI/LEMS/NT/DO02.* Feb. 2022 (cit. on pp. 216, 220).

[Hua+22] Huang, X., Pang, B., Chai, X., et al. "Proposal of a Turbulent Prandtl Number Model for Reynolds-averaged Navier–Stokes Approach on the Modeling of Turbulent Heat Transfer of Low-Prandtl Number Liquid Metal". In: *Frontiers in Energy Research* 10 (2022). ISSN: 2296-598X. (Visited on 02/16/2023) (cit. on p. 142).

[IAE00] IAEA. *Natural Circulation Data and Methods for Advanced Water Cooled Nuclear Power Plant Designs*. Text. Vienna: International Atomic Energy Agency, July 2000, pp. 1–254. (Visited on 06/14/2023) (cit. on p. 74).

[IAE05] IAEA. *Natural Circulation in Water Cooled Nuclear Power Plants: Phenomena Models and Methodology for System Reliability Assessments*. International Atomic Energy Agency, 2005. ISBN: 978-92-0-110605-6 (cit. on p. 34).

[IAE11] IAEA. *Stress Corrosion Cracking in Light Water Reactors: Good Practices and Lessons Learned*. Text. International Atomic Energy Agency, 2011, pp. 1–100. (Visited on 06/28/2023) (cit. on p. 130).

[IS12] Imke, U. and Sanchez, V. H. "Validation of the Subchannel Code SUBCHANFLOW Using the NUPEC PWR Tests (PSBT)". In: *Science and Technology of Nuclear Installations* 2012 (Aug. 2012), e465059. ISSN: 1687-6075. DOI: `10.1155/2012/465059`. (Visited on 07/05/2023) (cit. on p. 64).

[IOS93] IOS. *International Vocabulary of Basic and General Terms in Metrology (VIM)*. Geneva, Switzerland: International Organization for Standardization, 1993. ISBN: 978-9989-868-00-9 (cit. on p. 109).

[IJ76] Ishii, M. and Jones, O. C. "Derivation and Application of Scaling Criteria for Two-phase Flows". In: *Proc. Conf. Two-Phase Flows and Heat Transfer* (1976), pp. 163–185 (cit. on p. 44).

[IK83] Ishii, M. and Kataoka, I. *Similarity Analysis and Scaling Criteria for LWR'S Under Single-Phase and Two-Phase Natural Circulation*. Tech. rep. D.C., US: USNRC, 1983 (cit. on p. 60).

[IK84] Ishii, M. and Kataoka, I. "Scaling Laws for Thermal-Hydraulic System under Single Phase and Two-Phase Natural Circulation". In: *Nuclear Engineering and Design* 81 (1984), pp. 411–425 (cit. on p. 60).

[Ish+98] Ishii, M., Revankar, S. T., Leonardi, T., et al. “The Three-Level Scaling Approach with Application to the Purdue University Multi-Dimensional Integral Test Assembly (PUMA)”. In: *Nuclear Engineering and Design* 186.1 (1998), pp. 177–211. ISSN: 0029-5493. DOI: `10.1016/S0029-5493(98)00222-2` (cit. on pp. 43, 48, 60).

[Ito59] Ito, H. “Friction Factors for Turbulent Flow in Curved Pipes”. In: *Journal of Basic Engineering* 81.2 (June 1959), pp. 123–132. ISSN: 0021-9223. DOI: `10.1115/1.4008390`. (Visited on 07/29/2022) (cit. on p. 211).

[Ito60] Ito, H. “Pressure Losses in Smooth Pipe Bends”. In: *Journal of Basic Engineering* 82.1 (Mar. 1960), pp. 131–140. ISSN: 0021-9223. DOI: `10.1115/1.3662501`. (Visited on 09/18/2022) (cit. on p. 212).

[Jam19] Jamelot, E. “TrioCFD: Code & Numerical Schemes”. In: *POEMs 2019 - POlytopal Element Methods in Mathematics and Engineering*. Apr. 2019. (Visited on 06/05/2023) (cit. on p. 108).

[Jul+12] Julbe, A., Muñoz-Cobo, J. L., Escrivá, A., et al. *Analysis with TRACE Code of ROSA Test 1.1: ECCS Water Injection Under Natural Circulation Condition*. Tech. rep. NUREG/IA-0419. Oct. 2012. (Visited on 07/05/2023) (cit. on p. 64).

[KÖA16] Kalpakli Vester, A., Örlü, R., and Alfredsson, P. H. “Turbulent Flows in Curved Pipes: Recent Advances in Experiments and Simulations”. In: *Applied Mechanics Reviews* 68.5 (Sept. 2016). ISSN: 0003-6900. DOI: `10.1115/1.4034135` (cit. on p. 209).

[KTS65] Kapur, J. N., Tyagi, V. P., and Srivastava, R. C. “Streamline Flow through a Curved Annulus”. In: *Applied Scientific Research, Section A* 14.1 (Jan. 1965), pp. 253–267. ISSN: 1573-1987. DOI: `10.1007/BF00382249`. (Visited on 09/17/2022) (cit. on p. 211).

[Kat+22] Katsamis, C., Craft, T., Iacovides, H., et al. “Use of 2-D and 3-D Unsteady RANS in the Computation of Wall Bounded Buoyant Flows”. In: *International Journal of Heat and Fluid Flow* 93 (Feb. 2022), p. 108914. ISSN: 0142-727X. DOI: `10.1016/j.ijheatfluidflow.2021.108914`. (Visited on 05/19/2022) (cit. on p. 68).

[Kay94] Kays, W. M. “Turbulent Prandtl Number. Where Are We?” In: *ASME Journal of Heat Transfer* 116 (May 1994), pp. 284–295. ISSN: 0022-1481. (Visited on 08/25/2022) (cit. on p. 89).

[KKT82] Kelly, J., Kohrt, R., and Thurgood, M. *Assessment of the COBRA-TF Subchannel Code*. Tech. rep. United States, 1982, pp. 944–959 (cit. on p. 64).

[Kim+08] Kim, Y.-s., Choi, K.-y., Park, H.-s., et al. “Annals of Nuclear Energy Commissioning of the ATLAS Thermal-Hydraulic Integral Test Facility”. In: 35 (2008), pp. 1791–1799. DOI: `10.1016/j.anucene.2008.05.010` (cit. on p. 48).

[KB16] Krishnani, M. and Basu, D. N. “On the Validity of Boussinesq Approximation in Transient Simulation of Single-Phase Natural Circulation Loops”. In: *International Journal of Thermal Sciences* 105 (2016), pp. 224–232. ISSN: 12900729. DOI: `10.1016/j.ijthermalsci.2016.03.004` (cit. on p. 68).

[Kud+16a] Kudariyawar, J. Y., Srivastava, A. K., Vaidya, A. M., et al. “Computational and Experimental Investigation of Steady State and Transient Characteristics of Molten Salt Natural Circulation Loop”. In: *Applied Thermal Engineering* 99 (2016), pp. 560–571. ISSN: 13594311. DOI: `10.1016/j.applthermaleng.2015.12.114` (cit. on pp. 59, 60).

[Kud+16b] Kudariyawar, J. Y., Vaidya, A. M., Maheshwari, N. K., et al. “Computational Study of Instabilities in a Rectangular Natural Circulation Loop Using 3D CFD Simulation”. In: *International Journal of Thermal Sciences* 101 (2016), pp. 193–206. ISSN: 12900729. DOI: `10.1016/j.ijthermalsci.2015.11.003` (cit. on p. 68).

[Kun12] Kunes, J. *Dimensionless Physical Quantities in Science and Engineering*. Elsevier, Feb. 2012. ISBN: 978-0-12-416013-2 (cit. on p. 42).

[LS74a] Launder, B. E. and Sharma, B. I. “Application of the Energy-Dissipation Model of Turbulence to the Calculation of Flow near a Spinning Disc”. In: *Letters in Heat and Mass Transfer* 1.2 (1974), pp. 131–137. ISSN: 0094-4548. DOI: `10.1016/0094-4548(74)90150-7` (cit. on p. 67).

[LS74b] Launder, B. E. and Spalding, D. B. “The Numerical Computation of Turbulent Flows”. In: *Computer Methods in Applied Mechanics and Engineering* 3.2 (1974), pp. 269–289. ISSN: 0045-7825. DOI: `10.1016/0045-7825(74)90029-2` (cit. on pp. 67, 90).

[LM95] Levin, A. E. and McPherson, G. D. “A Practical View of the Insights from Scaling Thermal-Hydraulic Tests”. In: *NURETH-7*. United States, 1995 (cit. on p. 65).

[Lev99] Levy, S. *Two-Phase Flow in Complex Systems*. John Wiley & Sons, 1999. ISBN: 978-0-471-32967-1 (cit. on p. 48).

[Li18] Li, N. *Application of Dynamical System Scaling on Single-Phase Natural Circulation*. Tech. rep. North China Electric Power University, 2018 (cit. on p. 50).

[Li+18] Li, X., Li, H., Li, N., et al. “DSS Application on Single-Phase Natural Circulation in a Simple Rectangular Loop”. In: *Annals of Nuclear Energy* 119 (2018), pp. 214–228. ISSN: 0306-4549. DOI: `10.1016/j.anucene.2018.05.004` (cit. on pp. 45, 50).

[Li+17] Li, X., Li, N., Wu, Q., et al. “Application of Dynamical System Scaling Method on Simple Gravity-Driven Draining Process”. In: *Journal of Nuclear Science and Technology* 55.1 (Jan. 2017), pp. 11–18. ISSN: 0022-3131. DOI: `10.1080/00223131.2017.1372231` (cit. on p. 45).

[Lia+22] Liang, C.-H., Sun, M.-B., Huang, Y.-h., et al. “Mechanism of Development of Turbulent Boundary Layer in a Curved Circular Pipe under Supersonic Conditions”. In: *AIP Advances* 12 (Mar. 2022), p. 035039. DOI: `10.1063/5.0085586`. (Visited on 03/21/2023) (cit. on p. 95).

[LS15] Liao, Z.-J. and Su, W.-D. “Kolmogorov’s Hypotheses and Global Energy Spectrum of Turbulence”. In: *Physics of Fluids* 27.4 (Apr. 2015), p. 041701. ISSN: 1070-6631. DOI: `10.1063/1.4916964`. (Visited on 03/30/2022) (cit. on p. 151).

[Liu+20] Liu, L., Peterson, P., Zhang, D., et al. “Scaling and Distortion Analysis Using a Simple Natural Circulation Loop for FHR Development”. In: *Applied Thermal Engineering* 168 (2020), p. 114849. ISSN: 1359-4311. DOI: `10.1016/j.applthermaleng.2019.114849` (cit. on pp. 50, 60, 62).

[Liu+22a] Liu, Z., Bai, T., Peng, C., et al. “A Method of Scaling Distortion Assessment Based on Dynamic Time Warping”. In: *Annals of Nuclear Energy* 177 (Nov. 2022), p. 109304. ISSN: 0306-4549. DOI: `10.1016/j.anucene.2022.109304`. (Visited on 04/04/2023) (cit. on p. 45).

[Liu+22b] Liu, Z., Guo, Y., Bao, H., et al. “The Dynamical System Scaling Analysis for Single-Phase Integral Test Facilities”. In: *Annals of Nuclear Energy* 165 (2022), p. 108682. ISSN: 0306-4549. DOI: `10.1016/j.anucene.2021.108682` (cit. on p. 216).

[Luz+17] Luzzi, L., Misale, M., Devia, F., et al. “Assessment of Analytical and Numerical Models on Experimental Data for the Study of Single-Phase Natural Circulation Dynamics in a Vertical Loop”. In: *Chemical Engineering Science* 162 (2017). ISSN: 00092509. DOI: `10.1016/j.ces.2016.12.058` (cit. on p. 68).

[Mah+07] Mahaffy, J., Chung, B., Song, C., et al. “Best Practice Guidelines for the Use of CFD in Nuclear Reactor Safety Applications”. Nuclear Energy Agency of the OECD (NEA), 2007 (cit. on p. 66).

[Mah+15] Mahaffy, J., Chung, B., Song, C., et al. *Best Practice Guidelines for the Use of CFD in Nuclear Reactor Safety Applications.* Tech. rep. Nuclear Energy Agency of the OECD (NEA), 2015, p. 176 (cit. on p. 66).

[Mai+16] Mai, C., Spiridonakos, M., Chatzi, E., et al. “Surrogate Modeling for Stochastic Dynamical Systems by Combining Nonlinear Autoregressive with Exogenous Input Models and Polynomial Chaos Expansions”. In: 6 (Jan. 2016), pp. 313–339 (cit. on p. 153).

[Mar+18] Marfaing, O., Guingo, M., Laviéville, J., et al. “Comparison and Uncertainty Quantification of Two-Fluid Models for Bubbly Flows with NEPTUNE_CFD and STAR-CCM+”. In: *Nuclear Engineering and Design* 337.May (2018), pp. 1–16. ISSN: 00295493. DOI: `10.1016/j.nucengdes.2018.05.028` (cit. on p. 65).

[MIC22] Marrel, A., Iooss, B., and Chabridon, V. “The ICSCREAM Methodology: Identification of Penalizing Configurations in Computer Experiments Using Screening and Metamodel—Applications in Thermal Hydraulics”. In: *Nuclear Science and Engineering* 196.3 (Mar. 2022), pp. 301–321. ISSN: 0029-5639. DOI: `10.1080/00295639.2021.1980362`. (Visited on 07/06/2023) (cit. on p. 139).

[Mar17] Martinez, J. *Formalisation de La Méthode de Transposition*. Tech. rep. CEA-Saclay: Séminaire Multi-Physiques, 2017 (cit. on p. 36).

[Mar11] Martinez, J. *Analyse de Sensibilité Globale Par Décomposition de La Variance*. Tech. rep. Institut Henri Poincaré, 2011 (cit. on pp. 146, 147).

[Mar14] Martinez Quiroga, V. M. “Scaling-up Methodology, a Systematical Procedure for Qualifying NPP Nodalizations. Application to the OECD/NEA ROSA-2 and PKL-2 Counterpart Test”. PhD thesis. Universitat Politècnica de Catalunya, 2014 (cit. on p. 48).

[Men94] Menter, F. R. “Two-Equation Eddy-Viscosity Turbulence Models for Engineering Applications”. In: *AIAA Journal* 32.8 (Aug. 1994), pp. 1598–1605. ISSN: 0001-1452, 1533-385X. DOI: `10.2514/3.12149`. (Visited on 06/20/2023) (cit. on p. 67).

[Mis+07] Misale, M., Garibaldi, P., Passos, J. C., et al. “Experiments in a Single-Phase Natural Circulation Mini-Loop”. In: *Experimental Thermal and Fluid Science* 31.8 (Aug. 2007), pp. 1111–1120. ISSN: 0894-1777. DOI: `10.1016/j.expthermflusci.2006.11.004`. (Visited on 07/06/2022) (cit. on p. 115).

[Mis14] Misale, M. “Overview on Single-Phase Natural Circulation Loops”. In: Sept. 2014 (cit. on pp. 74, 123).

[Mod+02] Modro, S. M., Fisher, J. E., Weaver, K. D., et al. *Multi-Application Small Light Water Reactor Final Report*. Tech. rep. U.S. Department of Energy, 2002, p. 116 (cit. on p. 44).

[MMN12] Mohanty, S., Majumdar, S., and Natesan, K. “A Review of Stress Corrosion Cracking / Fatigue Modeling for Light Water Reactor Cooling System Components”. In: (2012). (Visited on 06/28/2023) (cit. on p. 130).

[Mor19] Morton, T. J. *Primary System Test Facility Review*. Tech. rep. INL/EXT-19-55536-Rev000. Idaho National Lab. (INL), Idaho Falls, ID (United States), Aug. 2019. DOI: `10.2172/1562115`. (Visited on 06/21/2023) (cit. on p. 48).

[Mou+04] Mousavian, S. K., Misale, M., D’Auria, F., et al. “Transient and Stability Analysis in Single-Phase Natural Circulation”. In: *Annals of Nuclear Energy* 31.10 (July 2004), pp. 1177–1198. ISSN: 0306-4549. DOI: `10.1016/j.anucene.2004.01.005`. (Visited on 09/12/2023) (cit. on p. 115).

[Mun+14] Munoz-Cobo, J. L., Escrivá, A., Mendizabal, R., et al. "CSAU Methodology and Results for an ATWS Event in a BWR Using Information Theory Methods". In: *Nuclear Engineering and Design* 278 (2014), pp. 445–464. ISSN: 00295493. DOI: `10.1016/j.nucengdes.2014.07.036` (cit. on pp. 51, 139).

[MBE18] Muñoz-Cobo, J. L., Berna, C., and Escrivá, A. "Top-down Scaling Methodology from the LSTF Facility to a Three Loop PWR Plant Applied to a SBLOCA Event – The ROSA 1.2 Test". In: *Nuclear Engineering and Design* 327.December 2017 (2018), pp. 248–273. ISSN: 00295493. DOI: `10.1016/j.nucengdes.2017.12.011` (cit. on pp. 44, 45, 48, 60, 61, 221).

[NC08] Nagib, H. M. and Chauhan, K. A. "Variations of von Kármán Coefficient in Canonical Flows". In: *Physics of Fluids* 20.10 (Oct. 2008), p. 101518. ISSN: 1070-6631. DOI: `10.1063/1.3006423`. (Visited on 03/30/2023) (cit. on pp. 94, 142).

[NCM79] Nahavandi, A. N., Castellana, F. S., and Moradkhanian, E. N. "Scaling Laws for Modeling Nuclear Reactor Systems". In: *Nuclear Science and Engineering* 72.1 (Oct. 1979), pp. 75–83. ISSN: 0029-5639. DOI: `10.13182/NSE79-A19310` (cit. on p. 43).

[Naj09] Najm, H. N. "Uncertainty Quantification and Polynomial Chaos Techniques in Computational Fluid Dynamics". In: *Annual Review of Fluid Mechanics* 41.1 (Jan. 2009), pp. 35–52. ISSN: 0066-4189, 1545-4479. DOI: `10.1146/annurev.fluid.010908.165248`. (Visited on 07/06/2023) (cit. on p. 141).

[Nat+21] Nathalie, S.-M., Li, S., Marrel, A., et al. "VVUQ of a Thermal-Hydraulic Multi-Scale Tool on Unprotected Loss of Flow Accident in SFR Reactor". In: *EPJ Nuclear Sciences & Technologies* 7 (Jan. 2021), p. 3. DOI: `10.1051/epjn/2021002` (cit. on p. 67).

[Nav+14] Naveen, K., Iyer, K. N., Doshi, J. B., et al. "Investigations on Single-Phase Natural Circulation Loop Dynamics. Part 2: Role of Wall Constitutive Laws". In: *Progress in Nuclear Energy* 75 (2014), pp. 105–116. ISSN: 0149-1970. DOI: `10.1016/j.pnucene.2014.04.011` (cit. on p. 94).

[ND99] Nicoud, F. and Ducros, F. "Subgrid-Scale Stress Modelling Based on the Square of the Velocity Gradient Tensor". In: *Flow, Turbulence and Combustion* 62.3 (Sept. 1999), pp. 183–200. ISSN: 1573-1987. DOI: `10.1023/A:1009995426001`. (Visited on 02/07/2023) (cit. on pp. 67, 90).

[Nis+00] Nishimura, M., Kamide, H., Hayashi, K., et al. "Transient Experiments on Fast Reactor Core Thermal-Hydraulics and Its Numerical Analysis: Inter-subassembly Heat Transfer and Inter-Wrapper Flow under Natural Circulation Conditions". In: *Nuclear Engineering and Design* 200.1 (Aug. 2000), pp. 157–175. ISSN: 0029-5493. DOI: `10.1016/S0029-5493(99)00324-6`. (Visited on 10/31/2022) (cit. on pp. 58, 74).

[NES13] Noorani, A., El Khoury, G. K., and Schlatter, P. “Evolution of Turbulence Characteristics from Straight to Curved Pipes”. In: *International Journal of Heat and Fluid Flow* 41 (2013), pp. 16–26. ISSN: 0142-727X. DOI: `10.1016/j.ijheatfluidflow.2013.03.005` (cit. on pp. 59, 60).

[Nop+22] Nop, R., Bruneton, A., Darona, J., et al. *High Performance Calculation Enhancement Using Massive Parallelization with TRUST and TrioCFD*. Tech. rep. CEA-Saclay, June 2022 (cit. on pp. 76, 77, 172, 178).

[OR10] Oberkampf, W. L. and Roy, C. J. *Verification and Validation in Scientific Computing*. Cambridge, Massachusettes, 2010. ISBN: 978-0-511-76039-6. DOI: `10.1017/CBO9780511760396` (cit. on p. 175).

[OEC17] OECD/NEA. *Post-BEMUSE Reflood Model Input Uncertainty Methods (PREMIUM) Benchmark*. Tech. rep. NEA/CSNI/R(2016)18. 2017 (cit. on p. 57).

[ONO+20] ONO, A., TANAKA, M., MIYAKE, Y., et al. “Preliminary Analysis of Sodium Experimental Apparatus PLANDTL-2 for Development of Evaluation Method for Thermal-Hydraulics in Reactor Vessel of Sodium Fast Reactor under Decay Heat Removal System Operation Condition”. In: *Mechanical Engineering Journal* 7.3 (2020), pp. 19–546. DOI: `10.1299/mej.19-00546` (cit. on p. 67).

[Os00] Osterlund, J. and sterlund, J. “Experimental Studies of Zero Pressure-Gradient Turbulent Boundary Layer Flow”. In: (July 2000) (cit. on pp. 94, 142).

[Pal+ew] Pallec, J. C. L., Ivanov, E., Dehart, M., et al. *Novel Multiphysics M&S Tools and Uncertainty Quantification*. Tech. rep. Report 2, Sub-Task 2, Task Force 1. OCDE/EGMPEBV, under review (cit. on pp. 62, 63).

[Pér+14] Pérez Mañes, J., Sánchez Espinoza, V. H., Chiva Vicent, S., et al. “Validation of NEPTUNE-CFD Two-Phase Flow Models Using Experimental Data”. In: *Science and Technology of Nuclear Installations* 2014 (2014). ISSN: 16876083. DOI: `10.1155/2014/185950` (cit. on p. 65).

[Phi+21] Phillips, D. R., Furnstahl, R. J., Heinz, U., et al. “Get on the BAND Wagon: A Bayesian Framework for Quantifying Model Uncertainties in Nuclear Dynamics”. In: *Journal of Physics G: Nuclear and Particle Physics* 48.7 (May 2021), p. 072001. ISSN: 0954-3899. DOI: `10.1088/1361-6471/abf1df`. (Visited on 07/06/2023) (cit. on p. 139).

[Pil+07] Pilkhwal, D. S., Ambrosini, W., Forgione, N., et al. “Analysis of the Unstable Behaviour of a Single-Phase Natural Circulation Loop with One-Dimensional and Computational Fluid-Dynamic Models”. In: *Annals of Nuclear Energy* 34.5 (May 2007), pp. 339–355. ISSN: 0306-4549. DOI: `10.1016/j.anucene.2007.01.012`. (Visited on 06/20/2023) (cit. on p. 68).

[PCL16] Pini, A., Cammi, A., and Luzzi, L. “Analytical and Numerical Investigation of the Heat Exchange Effect on the Dynamic Behaviour of Natural Circulation with Internally Heated Fluids”. In: *Chemical Engineering Science* 145 (2016). ISSN: 00092509. DOI: `10.1016/j.ces.2016.01.014` (cit. on p. 68).

[Pou09] Pourgol-Mohammad, M. “Thermal-Hydraulics System Codes Uncertainty Assessment: A Review of the Methodologies”. In: *Annals of Nuclear Energy* 36.11-12 (2009), pp. 1774–1786. ISSN: 03064549. DOI: `10.1016/j.anucene.2009.08.018` (cit. on pp. 50, 52).

[PL11] Proek, A. and Leskovar, M. *Application of Fast Fourier Transform for Accuracy Evaluation of Thermal-Hydraulic Code Calculations.* 2011. DOI: `10.5772/15735` (cit. on p. 53).

[Rey94] Reyes, J. N. “Scaling Single-State Variable Catastrophe Functions: An Application to Two-Phase Natural Circulation”. In: *Nuclear Engineering and Design* (1994). DOI: `10.1016/0029-5493(94)90032-9` (cit. on pp. 60, 61).

[Rey15] Reyes, J. N. “The Dynamical System Scaling Methodology”. In: *NURETH-16*. Chicago, USA, 2015. ISBN: 978-85-7811-079-6 (cit. on p. 48).

[Rey20] Reyes, J. N. *Application of Dynamical System Scaling to Bubble Dynamics.* Tech. rep. DOE-NuScale-08928. NuScale Power, LLC, Corvallis, OR (United States), Dec. 2020. (Visited on 01/11/2022) (cit. on p. 50).

[RF19] Reyes, J. N. and Frepoli, C. “Similarity and Scaling”. In: *Design-Basis Accident Analysis Methods For Light-water Nuclear Power Plants.* Singapore: World Scientific, 2019. ISBN: 978-981-327-566-9 (cit. on p. 220).

[RFY15] Reyes, J. N., Frepoli, C., and Yurko, J. P. “The Dynamical System Scaling Methodology: Comparing Dimensionless Governing Equations with the H2TS and FSA Methodologies”. In: *International Topical Meeting on Nuclear Reactor Thermal Hydraulics 2015, NURETH 2015* 1 (2015), pp. 192–206 (cit. on pp. 45, 47, 219, 223).

[Rey+10] Reyes, J. N., Groome, J. T., Woods, B. G., et al. “Scaling Analysis for the High Temperature Gas Reactor Test Section (GRTS)”. In: *Nuclear Engineering and Design* 240.2 (2010), pp. 397–404. ISSN: 00295493. DOI: `10.1016/j.nucengdes.2009.03.020` (cit. on p. 62).

[RH98] Reyes, J. N. and Hochreiter, L. “Scaling Analysis for the OSU AP600 Test Facility (APEX)”. In: *Nuclear Engineering and Design* 186.1-2 (1998), pp. 53–109. ISSN: 00295493. DOI: `10.1016/S0029-5493(98)00218-0` (cit. on p. 65).

[Roa01] Roache, P. J. “Code Verification by the Method of Manufactured Solutions”. In: *Journal of Fluids Engineering* 124.1 (Nov. 2001), pp. 4–10. ISSN: 0098-2202. DOI: `10.1115/1.1436090`. (Visited on 03/01/2022) (cit. on pp. 97, 102).

[Roa09] Roache, P. J. *Fundamentals of Verification and Validation.* hermosa publ., 2009. ISBN: 978-0-913478-12-7 (cit. on p. 103).

[Roa16] Roache, P. J. "Verification and Validation in Fluids Engineering: Some Current Issues". In: *Journal of Fluids Engineering* 138.10 (Aug. 2016). ISSN: 0098-2202. DOI: `10.1115/1.4033979`. (Visited on 09/12/2022) (cit. on p. 108).

[RAC17] Rodio, M. G., Abgrall, R., and Congedo, P. M. "Numerical Simulation of Cavitating Flows under Uncertainty". In: *Journal of Physics: Conference Series* 821.1 (Mar. 2017), p. 012009. ISSN: 1742-6596. DOI: `10.1088/1742-6596/821/1/012009`. (Visited on 06/17/2023) (cit. on pp. 77, 139).

[RB19] Rodio, M. G. and Bieder, U. "Comparison between Compressible, Dilatable and Incompressible Fluid Hypotheses Efficiency in Liquid Conditions at High Pressure and Large Temperature Differences". In: *European Journal of Mechanics - B/Fluids* 76 (2019), pp. 32–49. ISSN: 0997-7546. DOI: `10.1016/j.euromechflu.2018.12.001` (cit. on p. 78).

[RJT15] Röhrig, R., Jakirlić, S., and Tropea, C. "Comparative Computational Study of Turbulent Flow in a 90° Pipe Elbow". In: *International Journal of Heat and Fluid Flow* 55 (2015), pp. 120–131. ISSN: 0142-727X. DOI: `10.1016/j.ijheatfluidflow.2015.07.011` (cit. on p. 58).

[Row70] Rowe, M. "Measurements and Computations of Flow in Pipe Bends". In: *Journal of Fluid Mechanics* (1970). (Visited on 09/17/2022) (cit. on p. 210).

[RO11] Roy, C. J. and Oberkampf, W. L. "A Comprehensive Framework for Verification, Validation, and Uncertainty Quantification in Scientific Computing". In: *Computer Methods in Applied Mechanics and Engineering* 200.25 (2011), pp. 2131–2144. ISSN: 0045-7825. DOI: `10.1016/j.cma.2011.03.016` (cit. on pp. 50, 102).

[Sch67] Schmidt, E. "Heat Flow and Pressure Loss in Spiral Pipe". In: *Chem. Ing Tech 39* (1967), pp. 781–789 (cit. on p. 211).

[SK89] Schwartzbeck, R. K. and Kocamustafaogullari, G. "Similarity Requirements for Two-Phase Flow-Pattern Transitions". In: *Nuclear Engineering and Design* 116.2 (Sept. 1989), pp. 135–147. ISSN: 0029-5493. DOI: `10.1016/0029-5493(89)90232-X`. (Visited on 06/13/2023) (cit. on pp. 60, 61).

[SZL93] Shih, T.-H., Zhu, J., and Lumley, J. L. "A Realizable Reynolds Stress Algebraic Equation Model". In: *Symposium on Turbulence Shear Flows.* Kyoto, Jan. 1993. (Visited on 03/15/2023) (cit. on p. 67).

[Shy+02] Shyy, W., Garbey, M., Appukuttan, A., et al. "Evaluation of Richardson Extrapolation in Computational Fluid Dynamics". In: *Numerical Heat Transfer, Part B: Fundamentals* 41.2 (2002), pp. 139–164. ISSN: 10407790. DOI: `10.1080/104077902317240058` (cit. on p. 108).

[Sma22] Smart, G. “A Base for the Log Law and von Karman’s Constant Problem”. In: *Journal of Hydraulic Research* 60.6 (Nov. 2022), pp. 935–943. ISSN: 0022-1686. DOI: `10.1080/00221686.2022.2076164`. (Visited on 08/29/2023) (cit. on p. 142).

[Son01] Sonin, A. A. *The Physical Basis of Dimensional Analysis*. 2nd. Department of Mechanical Engineering, MIT, Cambridge, 2001 (cit. on p. 42).

[SBM04] Spedding, P., Benard, E., and Mcnally, G. “Fluid Flow through 90 Degree Bends”. In: *Developments in Chemical Engineering and Mineral Processing* 12.1-2 (2004), pp. 107–128. ISSN: 1932-2143. DOI: `10.1002/apj.5500120109`. (Visited on 09/16/2022) (cit. on pp. 114, 210).

[Str19] Strogatz, S. H. *Nonlinear Dynamics and Chaos: With Applications to Physics, Biology, Chemistry, and Engineering*. 2nd ed. Boca Raton: CRC Press, May 2019. ISBN: 978-0-429-49256-3. DOI: `10.1201/9780429492563` (cit. on p. 74).

[Tal16] Taler, D. “Heat Transfer in Turbulent Tube Flow of Liquid Metals”. In: *Procedia Engineering*. Selected Papers from IX International Conference on Computational Heat and Mass Transfer (ICCHMT2016) 157 (Jan. 2016), pp. 148–157. ISSN: 1877-7058. DOI: `10.1016/j.proeng.2016.08.350`. (Visited on 06/17/2022) (cit. on p. 143).

[Tar05] Tarantola, A. *Inverse Problem Theory and Methods for Model Parameter Estimation*. Society for Industrial and Applied Mathematics, Jan. 2005. ISBN: 978-0-89871-572-9. DOI: `10.1137/1.9780898717921`. (Visited on 07/07/2023) (cit. on p. 147).

[Ten+12] Tenchine, D., Barthel, V., Bieder, U., et al. “Status of TRIO-U Code for Sodium Cooled Fast Reactors”. In: *Nuclear Engineering and Design* 242 (2012), pp. 307–315. ISSN: 00295493. DOI: `10.1016/j.nucengdes.2011.10.026` (cit. on p. 76).

[Tou+00] Toumi, I., Bergeron, A., Gallo, D., et al. “FLICA-4: A Three-Dimensional Two-Phase Flow Computer Code with Advanced Numerical Methods for Nuclear Applications”. In: *Nuclear Engineering and Design* 200.1 (Aug. 2000), pp. 139–155. ISSN: 0029-5493. DOI: `10.1016/S0029-5493(99)00332-5`. (Visited on 07/05/2023) (cit. on p. 64).

[Tri10] Trinh, K. T. *On the Blasius Correlation for Friction Factors*. July 2010. DOI: `10.48550/arXiv.1007.2466`. arXiv: `1007.2466 [physics]`. (Visited on 09/17/2022) (cit. on p. 211).

[Tru+06] Trucano, T. G., Swiler, L. P., Igusa, T., et al. “Calibration, Validation, and Sensitivity Analysis: What’s What”. In: *Reliability Engineering & System Safety*. The Fourth International Conference on Sensitivity Analysis of Model Output (SAMO 2004) 91.10 (Oct. 2006), pp. 1331–1357. ISSN: 0951-8320. DOI: `10.1016/j.ress.2005.11.031`. (Visited on 07/07/2023) (cit. on p. 147).

[USN89] USNRC. *Best-Estimate Calculations of Emergency Core Cooling System Performance.* Tech. rep. May 1989 (cit. on p. 62).

[VRS23] Vaglio-Gaudard, C., Ramière, I., and Seiler, N. "Overview of Multiphysics R&D Activities at the CEA/IRESNE Institute". In: *Annals of Nuclear Energy* 192 (Nov. 2023), p. 109957. ISSN: 0306-4549. DOI: `10.1016/j.anucene.2023.109957`. (Visited on 06/27/2023) (cit. on p. 66).

[VG22] Vaux, S. R. de and Grosjean, B. "Effect of Upstream and Downstream Pressure Losses on Flow Reversals in Low-Pressure Natural Circulation Loops". In: *Advances in Thermal Hydraulics 2022.* June 2022. (Visited on 06/16/2023) (cit. on p. 59).

[Ver89] Vertes, C. M. *Passive Safeguards Design Optimization Studies for the Westinghouse AP600.* United States: American Nuclear Society, 1989. ISBN: 0-89448-150-9 (cit. on p. 44).

[Vij+08] Vijayan, P. K., Nayak, A. K., Saha, D., et al. "Effect of Loop Diameter on the Steady State and Stability Behaviour of Single-Phase and Two-Phase Natural Circulation Loops". In: *Science and Technology of Nuclear Installations* 2008 (2008). Ed. by Cleveland, J., p. 672704. ISSN: 1687-6075. DOI: `10.1155/2008/672704` (cit. on p. 115).

[Vij02] Vijayan, P. K. "Experimental Observations on the General Trends of the Steady State and Stability Behaviour of Single-Phase Natural Circulation Loops". In: *Nuclear Engineering and Design* 215.1-2 (2002), pp. 139–152. ISSN: 00295493. DOI: `10.1016/S0029-5493(02)00047-X` (cit. on pp. 59, 60, 203, 206).

[VA94] Vijayan, P. K. and Austregesilo, H. "Scaling Laws for Single-Phase Natural Circulation Loops". In: *Nuclear Engineering and Design* 152.1-3 (1994), pp. 331–347. ISSN: 00295493. DOI: `10.1016/0029-5493(94)90095-7` (cit. on pp. 60, 61, 115).

[Vij+02a] Vijayan, P. K., Bhojwani, V. K., Bade, M. H., et al. *Investigations on the Effect of Heater and Cooler Orientation on the Steady State, Transient and Stability Behaviour of Single-Phase Natural Circulation in a Rectangular Loop.* Tech. rep. India, 2002 (cit. on p. 57).

[Vij+02b] Vijayan, P. K., Nayak, A., Bade, M., et al. "Scaling of the Steady State and Stability Behaviour of Single-Phase Natural Circulation Systems". In: *Proceedings of a Technical Committee meeting* (2002) (cit. on p. 114).

[VSS07] Vijayan, P. K., Sharma, M., and Saha, D. "Steady State and Stability Characteristics of Single-Phase Natural Circulation in a Rectangular Loop with Different Heater and Cooler Orientations". In: *Experimental Thermal and Fluid Science* 31.8 (2007), pp. 925–945. ISSN: 08941777. DOI: `10.1016/j.expthermflusci.2006.10.003` (cit. on p. 115).

[VNK19] Vijayan, P. K., Nayak, A. K., and Kumar, N. *Single-Phase, Two-Phase and Supercritical Natural Circulation Systems*. Woodhead Publishing, 2019. ISBN: 978-1-62623-977-7 (cit. on pp. 58, 111, 112, 192, 203, 207, 208).

[Wan07] Wan, P. T. "A Derivation of the Fractional Scaling Analysis (FSA) Method for Time-Dependent Complex Problems". In: *Proceedings - 12th International Topical Meeting on Nuclear Reactor Thermal Hydraulics, NURETH-12*. Jan. 2007 (cit. on p. 45).

[WCF13] Wang, J. Y., Chuang, T. J., and Ferng, Y. M. "CFD Investigating Flow and Heat Transfer Characteristics in a Natural Circulation Loop". In: *Annals of Nuclear Energy* (2013). DOI: `10.1016/j.anucene.2013.01.015` (cit. on p. 68).

[WFC97] Weigand, B., Ferguson, J. R., and Crawford, M. E. "An Extended Kays and Crawford Turbulent Prandtl Number Model". In: *International Journal of Heat and Mass Transfer* 40.17 (Oct. 1997), pp. 4191–4196. ISSN: 0017-9310. DOI: `10.1016/S0017-9310(97)00084-7`. (Visited on 08/25/2022) (cit. on p. 89).

[Wil13] Wilkinson, R. D. "Approximate Bayesian Computation (ABC) Gives Exact Results under the Assumption of Model Error". In: *Statistical Applications in Genetics and Molecular Biology* 12.2 (May 2013), pp. 129–141. ISSN: 1544-6115. DOI: `10.1515/sagmb-2013-0010`. (Visited on 07/07/2023) (cit. on p. 147).

[Wil41] Wilks, S. "Determination of Sample Sizes for Setting Tolerance Limits". In: *Ann. Math. Stat.* 12 (1941), pp. 91–96 (cit. on p. 145).

[WIC23] Wilson, D., Iacovides, H., and Craft, T. "LES and Unsteady RANS Computations of Natural Convection Cooling Loops". In: *Chemical Engineering Research and Design* 194 (June 2023), pp. 211–224. ISSN: 0263-8762. DOI: `10.1016/j.cherd.2023.04.025`. (Visited on 06/20/2023) (cit. on p. 68).

[WR98] Wulff, W. and Rohatgi, U. S. *System Scaling for the Westinghouse AP600 Pressurized Water Reactor and Related Test Facilities*. Tech. rep. 1998 (cit. on p. 48).

[Wul+05] Wulff, W., Zuber, N., Rohatgi, U. S., et al. "Application of Fractional Scaling Analysis to Loss of Coolant Accidents, System Level Scaling for System Depressurization". In: *The 11th International Topical Meeting on Nuclear Reactor Thermal-Hydraulics (NURETH-11)*. Avignon, France, 2005. DOI: `10.1115/1.3155994` (cit. on p. 220).

[Xie+22] Xie, X., Samaei, A., Guo, J., et al. "Data-Driven Discovery of Dimensionless Numbers and Governing Laws from Scarce Measurements". In: *Nature Communications* 13.1 (Dec. 2022), p. 7562. ISSN: 2041-1723. DOI: `10.1038/s41467-022-35084-w`. (Visited on 06/09/2023) (cit. on p. 43).

[XK03] Xiu, D. and Karniadakis, G. “Modeling Uncertainty in Flow Simulations via Generalized Polynomial Chaos”. In: *Journal of Computational Physics* 187 (May 2003), pp. 137–167. DOI: `10.1016/S0021-9991(03)00092-5` (cit. on p. 138).

[YWW23] Yan, L., Wang, D., and Wu, H. “Numerical Study on the Influence of Input Power and Tube Shape on a Single-Phase Natural Circulation for Passive Residual Heat Removal Heat Exchanger”. In: *Progress in Nuclear Energy* 159 (May 2023), p. 104643. ISSN: 0149-1970. DOI: `10.1016/j.pnucene.2023.104643`. (Visited on 06/20/2023) (cit. on p. 68).

[YEM21] Yoshiura, R. K., Epiney, A. S., and M Mostafa Abdo, M. G. *Integration of Dynamical System Scaling to RAVEN and Facility Application*. Tech. rep. INL/EXT-21-64507-Rev000. Idaho National Lab. (INL), Idaho Falls, ID (United States), Sept. 2021. (Visited on 01/11/2022) (cit. on p. 50).

[YC17] Yu, X.-G. and Choi, K.-Y. “Heat Transfer Scaling Analysis of the Single-Phase Natural Circulation Flow System”. In: *Applied Thermal Engineering* 126 (2017), pp. 237–244. ISSN: 1359-4311. DOI: `10.1016/j.applthermaleng.2017.07.023` (cit. on p. 61).

[YKZ17] Yuquan, L., Kai, Y., and Zishen, Y. “Thermal Stratification in SBLOCA Simulated on the AMCE Test Facility”. In: *17th International Topical Meeting on Nuclear Reactor Thermal Hydraulics, NURETH 2017*. Vol. 2017-Septe. 2017 (cit. on p. 48).

[YFR15] Yurko, J. P., Frepoli, C., and Reyes, J. N. “Demonstration of Test Facility Design Optimization with the Dynamical System Scaling Methodology”. In: *International Topical Meeting on Nuclear Reactor Thermal Hydraulics 2015, NURETH 2015* 6 (2015), pp. 5152–5168 (cit. on pp. 45, 50, 216).

[ZDN03] Zanoun, E.-S., Durst, F., and Nagib, H. “Evaluating the Law of the Wall in Two-Dimensional Fully Developed Turbulent Channel Flows”. In: *Physics of Fluids* 15.10 (2003), pp. 3079–3089. ISSN: 1070-6631. DOI: `10.1063/1.1608010` (cit. on p. 142).

[Zha19] Zhang, J. “The Role of Verification & Validation Process in Best Estimate plus Uncertainty Methodology Development”. In: *Nuclear Engineering and Design* 355.December 2018 (2019), p. 110312. ISSN: 00295493. DOI: `10.1016/j.nucengdes.2019.110312` (cit. on p. 51).

[ZM12] Zhao, H. and Mousseau, V. A. “Use of Forward Sensitivity Analysis Method to Improve Code Scaling, Applicability, and Uncertainty (CSAU) Methodology”. In: *Nuclear Engineering and Design* 249 (2012), pp. 188–196. ISSN: 00295493. DOI: `10.1016/j.nucengdes.2011.09.042` (cit. on p. 51).

[Zha+18] Zhao, P., Zhu, J., Ge, Z., et al. “Direct Numerical Simulation of Turbulent Mixed Convection of LBE in Heated Upward Pipe Flows”. In: *International Journal of Heat and Mass Transfer* 126 (Nov. 2018), pp. 1275–1288. ISSN: 0017-9310. DOI: `10.1016/j.ijheatmasstransfer.2018.05.104`. (Visited on 08/25/2022) (cit. on p. 89).

[ZYZ19] Zhu, G., Yang, X., and Zhu, H. “Reduction of Flow Oscillation of Natural Circulation in Non-Inertial System”. In: *International Journal of Heat and Mass Transfer* 139 (Aug. 2019), pp. 720–724. ISSN: 0017-9310. DOI: `10.1016/j.ijheatmasstransfer.2019.05.062`. (Visited on 06/20/2023) (cit. on p. 68).

[Zub+90] Zuber, N., Wilson, G. E., Boyack, B. E., et al. “Quantifying Reactor Safety Margins Part 5: Evaluation of Scale-up Capabilities of Best Estimate Codes”. In: *Nuclear Engineering and Design* 119.1 (1990), pp. 97–107. ISSN: 00295493. DOI: `10.1016/0029-5493(90)90075-9` (cit. on p. 52).

[Zub91] Zuber, N. *An Integrated Structure and Scaling Methodology for Severe Accident Technical Issue Resolution*. 1991 (cit. on p. 44).

[Zub01] Zuber, N. “The Effects of Complexity, of Simplicity and of Scaling in Thermal-Hydraulics”. In: *Nuclear Engineering and Design* 204.1 (2001), pp. 1–27. ISSN: 0029-5493. DOI: `10.1016/S0029-5493(00)00324-1` (cit. on p. 217).

[Zub+07] Zuber, N., Rohatgi, U. S., Wulff, W., et al. “Application of Fractional Scaling Analysis (FSA) to Loss of Coolant Accidents (LOCA). Methodology Development”. In: *Nuclear Engineering and Design* 237.15-17 SPEC. ISS. (2007), pp. 1593–1607. ISSN: 00295493. DOI: `10.1016/j.nucengdes.2007.01.017` (cit. on p. 44).

Abstract

In order to enhance safety, nuclear reactors in the design phase consider natural circulation as a means to remove residual power. The simulation of this passive mechanism must be qualified between the validation range and the scope of utilisation (typically reactor case), introducing potential physical and numerical distortion effects. In this study, the flow of liquid sodium is simulated using the TrioCFD code, with both LES (high-fidelity, HF) and URANS (best-effort, BEF) models applied. After defining the validity of the Boussinesq approximations, we tackle respectively numerical uncertainties through the Grid Convergence Index method, and physical modelling uncertainties through Polynomial Chaos Expansion method on the URANIE platform. In a threshold configuration, we demonstrate that HF simulations are resilient to physical distortion effects, with numerical uncertainties being intricately correlated. Conversely, the BEF approach (the only one applicable at the reactor scale) can experience a degradation in its predictability due to physical distortion effects. While the HF approach proves effective in pinpointing these weaknesses: the growth of uncertainty associated with these distortion effects introduces the concept of scaling uncertainty. Ultimately, we propose a methodology named MUSQ - Modelling Uncertainties with Scaling Quantification, which tentatively introduces the recent Dynamical System Scaling technique in the validation domain to manage distortion effects, aiding in calibrating the scaling uncertainty.

Résumé

Afin d'accroître la sûreté, les réacteurs nucléaires en conception considèrent la circulation naturelle pour évacuer la puissance résiduelle. La simulation de ce mécanisme passif doit être qualifiée entre le domaine de validation et celui d’utilisation (typiquement le cas réacteur) : cette transposition met en jeu des effets de distorsion physiques et numériques. Dans l’étude, l’écoulement de sodium liquide est simulé par TrioCFD, les modèles LES (haute-fidélité, HF) et URANS (« best-effort », BEF) étant appliqués. Après cadrage de la validité de l’approximation de Boussinesq, les incertitudes numériques et de modélisation physique sont établies respectivement par les techniques d'Indice de Convergence de Grille et d’Expansion du Chaos Polynômial (sous URANIE). Dans une configuration à seuil, nous démontrons que les simulations HF sont résilientes à des effets de distorsion physique, les incertitudes numériques y étant complexement corrélées. A contrario, l'approche BEF (seule applicable à l’échelle réacteur) doit voir une dégradation de sa prédictivité selon des effets de distorsion physiques et l’approche HF s’avère un moyen efficace d’en localiser les faiblesses : la croissance de l’incertitude associée à ces effets de distorsion met en avant le concept d’incertitude de transposition. Une proposition de méthodologie nommée MUSQ - *Modelling Uncertainties with Scaling Quantification*, est in fine exploratoirement avancée et propose originalement l’utilisation de la technique récente de Dynamical System Scaling dans le domaine de validation pour piloter des effets de distorsions, utiles pour la calibration de l’incertitude de transposition.